RESEARCH & DEVELOPMENT

Field Verification of Undercut Criteria and Alternatives for Subgrade Stabilization in the Piedmont Area

S. Hamed Mousavi, M. A. Gabr, Ph.D., P.E., and R. H. Borden, Ph.D, P.E.

Department of Civil, Construction, and Environmental Engineering
North Carolina State University

NCDOT Project 2011-05

FHWA/NC/2011-05

November 2016

Field Verification Of Undercut Criteria And Alternatives For Subgrade Stabilization In The Piedmont Area

By

S. Hamed Mousavi, M. A. Gabr, Ph.D., P.E., and Roy H. Borden, Ph.D, P.E.

Department of Civil, Construction, and Environmental Engineering

North Carolina State University

In Cooperation with

The North Carolina Department of Transportation

Raleigh, North Carolina

November 21, 2016

1. Report No. *FHWA/NC/2011-05*	2. Government Accession No.	3. Recipient's Catalog No.
4. Title and Subtitle Filed Verification Of Undercut Criteria And Alternatives For Subgrade Stabilization In The Piedmont Area		5. Report Date February 15, 2016 6. Performing Organization Code
7. Author(s) S. Hamed Mousavi, Mohammed A. Gabr, Ph.D., P.E., and Roy H. Borden, Ph.D, P.E.		8. Performing Organization Report No.
9. Performing Organization Name and Address Department of Civil, Construction, and Environmental Engineering North Carolina State University Campus Box 7908 Raleigh, NC 27695		10. Work Unit No. (TRAIS) 11. Contract or Grant No.
12. Sponsoring Agency Name and Address North Carolina Department of Transportation Research and Analysis Group Raney Building, 104 Fayetteville Street Raleigh, North Carolina 27601		13. Type of Report and Period Covered Final Report *September 01, 2013 – November 21, 2016* 14. Sponsoring Agency Code *2011-05*
Supplementary Notes:		

16. Abstract

Work performed in this research project was in support of the effort by the North Carolina Department of Transportation to develop criteria to discern the need for undercutting soft soils and the adequacy of the subgrade after stabilization measures are implemented. The work was specifically focused on performing field testing and collecting data at a site located in the North Carolina Piedmont geologic area. Three test pads were constructed on comparable subgrade conditions with subgrade stabilization measures that included the use of select fill material and geosynthetic reinforcement coupled with a relatively thin layer of Aggregate Base Coarse (ABC). Field loading was applied using 1000 passes of a loaded construction truck. Several parameters were monitored during loading including stresses, deformation, and moisture and suction levels. A fourth pad was also constructed to test lime stabilization; however loading of this pad was not performed since the lime used for stabilization did not meet NCDOT's specifications. A surface profiler (Lidar-based surveying) was used at periodic intervals to monitor plastic deformation and wheel path rutting with loading cycles. The field testing also included collection of data from Light Weight Deflectometer (LWD) and Dynamic Cone Penetrometer (DCP) to assess subgrade properties. Results indicated that the measured vertical stress near the interface of the subgrade for the geosynthetics-reinforced sections initially increased, but then decreased with increasing number of truck passes This decrease was attributed to progressive densification of the aggregate base course and the mobilization of the reinforced layer tensile strength. The reinforced sections experienced surface deformation on the order of 0.5-0.7 inches and the select fill-stabilized section showed a 1.2 inches of deformation after 1000 truck passes. In addition to the field data, two models were developed for the estimation of the resilient modulus (Mr) on the basis of the Light Weight Deflectometer (LWD) and Dynamic Cone Penetrometer (DCP) data. Mr values from these models can be used along with the subgrade's shear strength to discern the need for undercutting. Using the monitored data, the proposed undercut criteria by Borden et al 2010 were deemed to be valid at the site with the Piedmont residual subgrade soil. Sections with stabilized measures met the criteria for adequate subgrade. Guidelines regarding thickness of the ABC layer with various subgrade strength values were proposed based on the results of dynamic 3-D numerical analyses. A chart was proposed to enable the selection of an appropriate thickness of ABC layer based on the measured DCPI of the subgrade soil.

17. Key Words *geosynthetics, numerical, proof roller, resilient modulus, subgrade undercut, unsaturated*	18. Distribution Statement		
19. Security Classif. (of this report) Unclassified	20. Security Classif. (of this page) Unclassified	21. No. of Pages 210	22. Price

Form DOT F 1700.7 (8-72) **Reproduction of completed page authorized**

DISCLAIMER

The contents of this report reflect the views of the author(s) and not necessarily the views of the University. The author(s) are responsible for the facts and the accuracy of the data presented herein. The contents do not necessarily reflect the official views or policies of either the North Carolina Department of Transportation or the Federal Highway Administration at the time of publication. This report does not constitute a standard, specification, or regulation.

ACKNOWLEDGEMENTS

The authors would like to thank the members of the NCDOT Geotechnical, Materials, and Construction divisions who worked on this project. The time, expertise and guidance of NCDOT engineers were invaluable to this project. Special thanks are due to the members of the steering and implementation committee:

- John L. Pilipchuk, P.E., L.G. (Chair)
- J. Dean Hardister, P.E
- Kyung J. Kim, Ph.D., P.E.
- Chris Kreider, P.E.
- Kevin Sebold
- Eric Williams, P.E.
- Ernest Morrison, P.E.

Executive Summary

Work perofred in this resuearch project was in support of the effort by North Carolina Department of Transportation to develop criteria to discern the need for undercutting soft soils and the adequacy of the subgrade after stabilization measures are implemented. The work was specifically focused on performing field testing and collecting data at a site located in the North Carolina Piedmont geologic area. The objective was to validate guidelines regarding the depth of undercutting and the use of supplemental and/or additional stabilization measures to develop subgrade soils with adequate bearing capacity to support traffic loading. The perofrmed work encompassed small scale and large scale laboratory testing, field testing, and numerical analyses and modeling.

Three test pads were constructed on comparable subgrade conditions with subgrade stabilization measures that included the use of select fill material and geosynthetic reinforcement coupled with a relatively thin layer of Aggregate Base Coarse (ABC). Field loading was applied using 1000 passes of a loaded construction truck. Several parameters were monitored during loading including stresses, deformation, and moisture and suction levels. A fourth pad was also constructed to test lime stabilization; however loading of this pad was not performed since the lime used for stabilization did not meet NCDOT's standards. A surface profiler (Lidar-based surveying) was used at periodic intervals to monitor plastic deformation and wheel path rutting with loading cycles. Sensors were installed and used to monitor moisture and suction variation at the subgrade. The field testing results also included collection of data from Light Weight Deflectometer (LWD) and Dynamic Cone Penetrometer (DCP) to assess subgrade properties. Numerical analyses were performed using the dynamics module of PLAXIS 2D and 3D software, in order to study the deformation performance and stress distribution in reinforced unsaturated subgrade soil layer under cyclic traffic loading.

Results indicated that the measured vertical stress near the interface of the subgrade for the geosynthetics-reinforced sections initially increased, but then decreased with increasing number of truck passes. This decrease was attributed to progressive densification of the aggregate base

course and the mobilization of reinforced layer tensile strength. In addition, this decrease might be attributed to the increase in matric suction in the subgrade layer, from 25 kPa to 35 kPa, as a result of the "hot" summer weather during testing. The geosynthetics-reinforced sections experienced surface deformation on the order of 0.5-0.7 inches and the select fill-stabilized section showed a 1.2 inches of deformation after 1000 truck passes. In addition to the field data, two models were developed for the estimation of the resilient modulus (Mr) on the basis of the Light Weight Deflectometer (LWD) and Dynamic Cone Penetrometer (DCP) data. The proposed LWD and DCP models were shown to be capable of predicting the resilient modulus of low plasticity soils SM, ML, and SC (A-4a and A-4), with PI<5, and 40%<P200<55%; as a function of the stress state. Such values can be used along with the subgrade's shear strength to discern the need for undercutting based on the criteria presented in Borden et al 2010.

Using the monitored stresses and deformation as well as subgrade and ABC properties, the proposed undercut criteria, previously developed in an earlier phase of the research program, were deemed to be valid at the site with the Piedmont residual subgrade. Sections with stabilized measures met the criteria for adequate subgrade. Guidelines regarding thickness of the ABC layer under various subgrade strength values were proposed based on the results of the numerical analyses. These guidelines are shown on a chart that enables the selection of an appropriate thickness of ABC layer based on the measured DCPI of the subgrade soil.

The results presented herein are intended to assist NCDOT and their contractors with a tool for decision making to systematically determine whether undercutting and stabilization measures are needed. It was demonstrated that the proposed undercut criteria can be used to assess the adequacy of the subgrade soils to support traffic loading on the criteria basis of 1-inch deformation limit, and performance capacity factor of 1.5 or higher. In this case, the 1-inch limit addresses issues related to deep layers "pumping" while the performance capacity factor addresses issues related to localized bearing failure. Implementation of the research project is recommended along the following tracks:

i. Use of the data and approach presented in this report to discern whether undercutting of the perceived soft soils is necessary for the construction of the roadway. The results from field testing indicated that the criteria proposed by Borden et al 2010 in terms of the strength and stiffness of the subgrade soils is valid for defining situations in which undercut is needed based on quantifiable criteria presented.

ii. Use the recommended approach utilizing data from DCP, LWD, resilient modulus testing, and conventional geotechnical testing to make a determination regarding the need for undercut during the design phase. In addition, the results indicated that the NCDOT criterion using the DCP Index of 38mm/blow is valid and can be used if expedient determination is needed during the construction phase.

iii. Estimate the depth of undercut and the corresponding thickness of the select fill or ABC layer, depending on the stabilization measure to be implemented. It should be mentioned that these layers (select fill or ABC) are a part of the subgrade stabilization measure and should not be included during the design as a part of the pavement section layers (base, subbase, and asphalt)

iv. Provide information on the stabilized section properties that will inform the design process of the pavement section.

v. Determining the depth of undercut required in the case where no other additional means of stabilization is to be used. The depth of undercut should be established based on strength and modulus properties as assessed from the DCP data or conventional engineering properties of soils determined from laboratory testing.

TABLE OF CONTENTS

LIST OF FIGURES

LIST OF TABLES

CHAPTER 1: INTRODUCTION

With increased construction activities associated with the development of North Caolina's road network, it is common to encounter soft subgrade soils, which pose a challenge to the engineers and contractors. The long term serviceability of a given road not only depends on the performance of the asphalt layer, but is also tied to the quality of the subgrade layer. In situ subgrade soil layers should be able to support heavy construction vehicles to enable a given project to be completed on schedule. In addition to the short term stability, soft subgrade layers need to sustain the lifetime traffic loading without experiencing excessive deformation. Excessive deformation can lead to accelerated degradation of the asphalt layer and the need for emergency repairs and maintenance. One example where problem soils are often found is within the Triassic basin area of the Piedmont Physiographic region of North Carolina. In general, NCDOT's practice for addressing these situations is to excavate (undercut) the undesirable soil and replace it with materials that meet high quality specifications or, alternatively, use chemical stabilization to reduce soil plasticity and improve strength and workability. The need to properly engineer undercutting the soil approach as a stabilization measure is well recognized by NCDOT and the agency has supported the development of "undercut criteria" to assist in avoiding cost overruns in construction projects where undercut is implemented.

The NCDOT has supported two prior research studies, which will be referred to as Phase I and II studies, to establish criteria for defining the need for undercut in expansive and loose or soft soils. These criteria included means to define the need for and depth of undercut, and guidelines for alternative or supplemental stabilization approaches including the use of geosynthetics and chemical stabilization to limit volume change and improve properties of the subgrade layer. The Phase I study (Borden et al., 2010) was focused on the development of undercut criteria based on Dynamic Cone Penetrometer (DCP) testing, and included the performance of large-scale laboratory model tests using various stabilization measures. In addition, numerical modeling of field configurations typically encountered in situations where an undercut approach is implemented was performed. The undercut criteria based on the use of DCP, and the performance of alternative stabilization measures are documented in the Phase I report (Borden et al., 2010).

The Phase II study (Cowell et al., 2012) was focused on validating the findings from the Phase I study through implementation of the proposed undercut criteria and stabilization approaches at a site within the Coastal Plain region of North Carolina. Rut depth and stress increase on the top of the subgrade were monitored during the full-scale testing, which also included performance of in-situ tests for estimating the shear strength and stiffness properties of subgrade soil. Based on the field results, the proposed undercut criteria were assessed with regards to ability to identify the need for undercut and ability to predict the performance of the stabilized sections. It was concluded that the proposed criteria established in phase I provides a reliable approach for determining whether or not subgrade soil stabilization is required, and for discerning the efficacy of the stabilization measure in rendering the subgrade layer able to meet the undercut criteria.

In general, soft subgrade soils are typically detected during the initial site investigation so that the associated costs of stabilization can be anticipated prior to construction. The properties of subgrade soil can be evaluated by conventional in-situ tests such as Dynamic Cone Penetrometer and Light Weight Deflectometer, or by static and dynamic laboratory tests including monotonic triaxial and resilient modulus tests. Once the subgrade is prepared in the field for the placement of the base and asphalt layers, its stability is evaluated by subjectively observing a proof rolling process to identify areas of excessive pumping and/or rutting. The magnitude of pumping and/or rutting that is considered "excessive," however, is left to the discretion of the proof roll inspector. In previous work. Borden et al. (2010) and Cowell et al. (2012) provided an approach for using the results from the DCP tesing to determine the need for subgrade soil improvement and also the properties of the stabilized layer (by correlating the DCP data to shear strength and modulus values.)

Work in this report is focused the performance of constructed test pads at a site in the Piedmont geologic area to validate the undercut guidelines previously developed from testing and numerical modeling. The field testing results presented herein included collection of data from Light Weight Deflectometer (LWD) and Dynamic Cone Penetrometer (DCP) to assess subgrade properties. Three test pads were constructed on comparable subgrade conditions with different subgrade stabilization measures including the use of select fill material and geosynthetic reinforcement coupled with relatively thin layer of Aggregate Base Coarse (ABC). Field loading was applied using 1000 passes of a loaded construction truck. Several parameters were

monitored during loading including stresses, deformation, and moisture and suction levels. A fourth pad was also constructed to test lime stabilization; however loading of this pad was not performed since the lime used for stabilization did not meet NCDOT's standards. The results from the field testing are used to assess the extent to which the use of each stabilization measure is effective in rendering the soft soil layer as meeting the criteria for a stable subgrade.

Objectives

In many cases, NCDOT uses the "undercut" approach as a means for facilitating construction in areas with unstable soils. In order to verify and validate findings from the Phase I research study, as discussed above, the main research objective herein is to perform field testing on instrumented road-under-construction sections in the Piedmont area. The results are used to validate the previously developed undercut criteria, and verify performance of stabilization measures under construction loading. The objectives of this study are expressed as follows:

i. Identify a test site in the Piedmont Physiographic region for implementation of alternative or supplemental approaches to undercut, including the use of geosynthetics and/or chemical stabilization. Perform complete characterization of the site soils to define their physical and engineering properties.
ii. Perform Light Weight Deflectometer (LWD) and Dynamic Cone Penetrometer (DCP) testing, and develop correlation with soil strength parameters. Use the estimated properties to validate proposed undercut criteria for the test site, including the validity of defining the depth of undercut and quality of replacement material.
iii. Instrument the test pads at the identified site and monitor performance in terms of induced rutting and stress attenuation with depth under repeated construction truck loading.
iv. Through field monitoring, verify the performance of alternative or supplemental approaches to undercut including the use of geosynthetics, and/or chemical stabilization to limit volume change and improve soil properties and workability.

Scope of Work

Four full-scale road sections (each 50 ft. long by 16 ft width) were constructed on poor subgrade soil where undercutting is normally needed. One test section incorporated 31 inches of undercut and replacement with select fill material (Class II), the second and third test sections included reinforcement using a geogrid and geotextile, respectively, in conjunction with excavating and replacement with 9 inches ABC (Class IV), and the fourth test section included lime stabilization of the top 8 inches soft subgrade soil. The type of lime used in construction of the fourth section, however, did not meet the NCDOT standards for materials used in this application, and will therefore was not loaded; no response results from this section are presented in this report.

Full-scale field testing consisted of 1,000 consecutive passes of a fully loaded tandem axle dump truck over each of the test pads. The goal was to have all 1,000 passes conducted within approximately the same wheel path. Four Earth Pressure Cells (EPC) were embedded within the wheel paths (two in each wheel path) of each the test sections to monitor stress variations with traffic loading. A surface profiler (Lidar-based surveying) was used at periodic intervals to monitor plastic deformation and wheel path rutting with loading cycles. Moisture and suction sensors were embedded in the subgrade to monitor moisture and suction variation. These data were collected to discern impact of moisture variation on the strength properties of the subgrade as might be relevant to the interpretation of the field data. The construction and instrumentation of the test pads were performed with the assistance of the NCDOT engineers and contractors.

Light Weight Deflectometer (LWD), Dynamic Cone Penetrometer, and SPT tests were performed at various stages of the full scale testing, along with laboratory resilient modulus and monotonic triaxial tests. In addition sampling using Shelby tubes was alos performed. The testing results and samples were used to collect data on the strength and modulus characteristics of the subgrade prior to and after roadway construction and full scale testing. The experimental results were used to assess performance of the proposed undercut criteria as were detailed in the Phase I of this study.

Report Layout

The results and finding of this study are presented within 9 chapters as follows:

Chapter 2. Review of the related literature.

Chapter 3. Details of the full scale testing, including site description, subgrade, aggregate base course, and reinforced sections' properties and instrumentations.

Chapter 4. Laboratory and in-situ testing program results including tested material properties, resilient modulus test results, and LWD and DCP field measured data are presented.

Chapter 5. Two subgrade resilient modulus prediction models from DCP and LWD measurements are introduced in this chapter. The proposed models are validated by data reported herein and in the literature.

Chapter 6. The applicability of the proposed undercut criteria by Borden at el (2010) is evaluated for the Piedmont residual soils.

Chapter 7. The full scale testing results, including field observations during vehicle loading, earth pressure cell measurements, Lidar Scan data, and moisture and suction sensors readings are presented in this chapter.

Chapter 8. Numerical analyses predicting the deformation behavior and stress distribution within the reinforced unsaturated subgrade soil under cyclic loading. The performance of the subgrade soil under proof roller loading is also investigated through numerical analysis in Plane strain and 3D mode in Plaxis 2D and 3D, respectively.

Chapter 9. A summary of the research results and findings and conclusions of the study.

CHAPTER 2: LITERATURE REVIEW

A comprehensive summary of the findings of previous studies relevant to this project, including geosynthetic-reinforced subgrades, full-scale roadway testing, Dynamic Cone Penetrometer (DCP), and chemical stabilization, can be found in the NCDOT research reports by Borden et al. (2010) and Cowell et al. (2012). A summary of the recent findings related to full scale testing, resilient modulus prediction from in-situ testing, and numerical analyses of reinforced soft subgrades are presented in this chapter.

2.1 Full Scale Testing

Based on a review of the literature, most design criteria for unreinforced/reinforced unpaved roads are derived from physical testing including small-scale and large-scale laboratory testing and full-scale field testing. Despite the good quality control obtainable in laboratory testing, boundary effects can influence the results (Cote 2009). In addition, the load conditions produced by full scale moving tires cannot be perfectly replicated in most laboratory settings. Therefore, full-scale testing is carried out to simulate the actual load condition and eliminate the influence of boundary effects on the results.

The performance of geosynthetic-reinforced subgrades has been evaluated and compared to that of unreinforced sections through several full-scale testing programs over the past two decades. It was observed from field-scale testing results that the inclusion of geosynthetic reinforcement reduces the magnitude of permanent deformation and the magnitude of applied stress transferred onto the reinforced subgrade (Fannin and Sigurdsson, 1996; Tingle and Webster, 2003; Hufenus et al., 2006; Tingle and Jersey, 2009; Cowell et al., 2012). Early on, it was also observed that the use of geosynthetics can potentially reduce the necessary base layer thickness (Fannin and Sigurdsson, 1996). Geosynthetic inclusions have been shown to be more beneficial with thinner ABC layers, and with increasing thicknesses of ABC, the contribution of the geosynthetic inclusion to the reduction of rut depth development decreases (Fannin and Sigurdsson, 1996; Hufenus et al., 2006). Tingle and Jersey (2009) observed that the base layer material became stiffer after trafficking, due to the densification of the base materials and mobilization of the geosynthetic reinforcement. Cowell et al. (2012) reported that a small difference in base-layer thickness can cause a significant effect on the measured stress at the subgrade surface. Cowell et

al. applied the analysis approach by Giroud and Han (2004) to the measured field data. Based on their analyses, it was reported that their proposed model underestimated the required thickness of ABC.

2.2 Dynamic Cone Penetrometer (DCP)

The Dynamic Cone Penetrometer (DCP) is a portable instrument that has been used widely in geotechnical and pavement design for estimating the shear strength and stiffness properties of soils in the field (AASHTO, 1993; Gabr et al., 2000; Gabr et al., 2001; Chen et al., 2005). As shown in Figure 2-1, the DCP consists of an 8 kg sliding hammer, 57.5 cm (22.6 in) drop height, 111 cm (44 in) driving shaft and a cone tip with 60^o angle, ASTM D6951. During the DCP test, the sliding hammer falls 57.5 cm vertically and drives the cone tip attached to the bottom of the DCP rod into the ground. The penetration depth is recorded after each drop (blow) on the vertical stake positioned next to the DCP rod. Dynamic cone penetration index (DCPI) for the soil layer is expressed as inches per blow or mm/blow. Several correlations have been proposed in the literature that relate DCPI of soils to the shear strength and stiffness properties, such as the California Bearing Ratio, CBR, (NCDOT, 1998; Gabr et al., 2000), undrained shear strength, s_u, (Ayres, 1989) elastic modulus, E, (Chai and Roslie, 1998; Abu-Farsakh et al., 2004; Chen et al., 2005) and resilient modulus, Mr, (AASHTO, 1993; Hassan, 1996; Herath et al., 2005).

DCP data need to be interpreted to obtain a representative value of dynamic cone penetration index (DCPI) for each layer. Allbright (2002) suggested using a weighted average over arithmetic average to calculated DCPI, presented in Eq. 2-1, because of a smaller standard deviation and better observed correlation with other field tests. By defining the DCPI of each soil layer, the CBR, resilient modulus and undrained shear strength can be estimated by applying existing empirical correlations.

$$DCPI_{wt.\,avg.} = \frac{1}{H}\sum_{i=1}^{N}(DCPI_i \times z_i) \qquad \text{Eq. (2-1)}$$

Which,

z = Depth of penetration per blow (mm/in)

H = Total depth of the soil layer (mm/in)

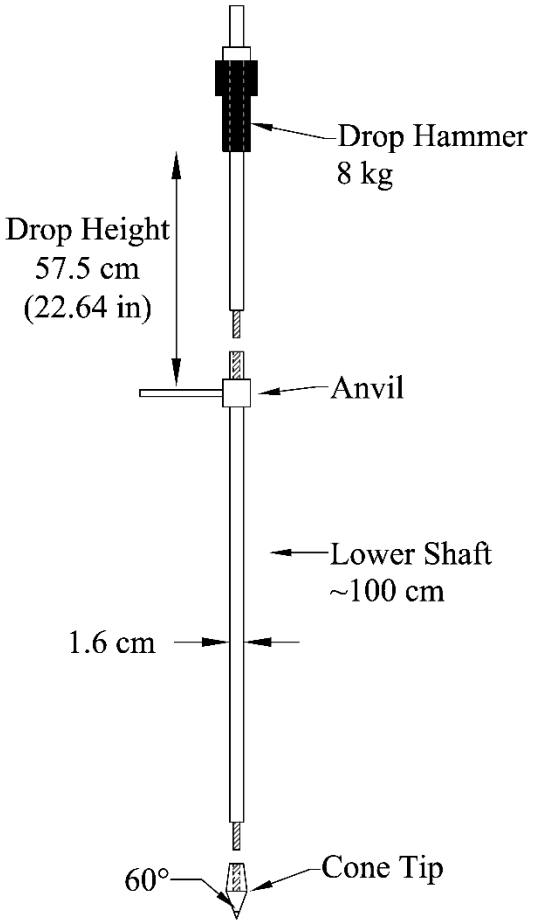

Figure 2-1. Dynamic cone penetrometer sketch (after ASTM D6951).

2.2.1 Correlation of DCP data with CBR

There are different empirical correlations for estimating CBR of soils as a function of DCPI, however each equation has been developed on a specific type of soil. Coonse et al. (1999) proposed Eq. 2-2 for estimating the CBR of Piedmont Residual soil. Eq. 2-3, proposed by Norwegian Road Research (Ese et al. 1995), is used in this study for estimating CBR value of the aggregate base course.

Coonse's 1999 (residual soil):

$$Log(CBR) = 2.53 - 1.14 \times \log(DCPI) \qquad \text{Eq. (2-2)}$$

Norwegian Road Research (1995) (ABC):

$$\log(CBR) = 1.4 - 0.55 \times \log(DCPI) \quad \text{Eq. (2-3)}$$

2.2.2 Correlation of DCP data with undrained shear strength

Undrained shear strength of the subgrade soil can be estimated from the CBR value by Danistan and Vipulanandan's correlation (2009) as expressed in Eq. 2-4:

$$Su_{subgrade\ soil} = -0.282 \times (CBR)^2 + 14.97 \times (CBR) \quad \text{Eq. (2-4)}$$

Ayers (1989) proposed Eq. 2-5 to estimate undrained shear strength of select fill material and aggregate base coarse as a function of DCPI and maximum aggregate size:

$$Su_{ABC} = \frac{1}{2}(37.0 - 9.0 \times DCPI + 7.8MAS) \quad \text{Eq. (2-5)}$$

Where,

$DCPI$: Penetration rate (in/blow)

MAS : Maximum aggregate size (in)

2.3 Light Weight Deflectometer (LWD)

The LWD is a portable falling weight deflectometer for measuring the in-situ modulus of soil (Fleming 2007). Compared to the falling weight deflectometer (FWD), the LWD is less expensive and more convenient to perform. The device used in this study was a Priam 100, as shown in Figure 2-2, and consisted of a 10 kg falling weight, which can induce a 15-20 ms pulse load producing a contact stress up to 450 kPa, with its 20-cm diameter plate (r = 10 cm). A geophone is used to measure surface deflection. Surface deflection and applied load are monitored and recorded through Prima 100 software. Figure 2-3 shows an example of the calculated applied stress and surface deflection for one drop.

The modulus is calculated based on Boussineq's elastic half space theory by assuming a homogeneous isotropic soil layer (Fleming 2007). Therefore Poisson's ratio and a shape factor are assigned as input parameters to the software to calculate the modulus per Eq. 2-6 (Fleming 2007).

$$E_{LWD} = \frac{f.(1-\nu^2).\sigma.\mathrm{r}}{\delta} \qquad \text{Eq. (2-6)}$$

Where:

E_{LWD} : surface layer modulus (MPa)

σ : applied stress (kPa)

δ : surface deflection (μm)

f : shape factor

ν : Poisson's ratio

r : radius of plate (mm)

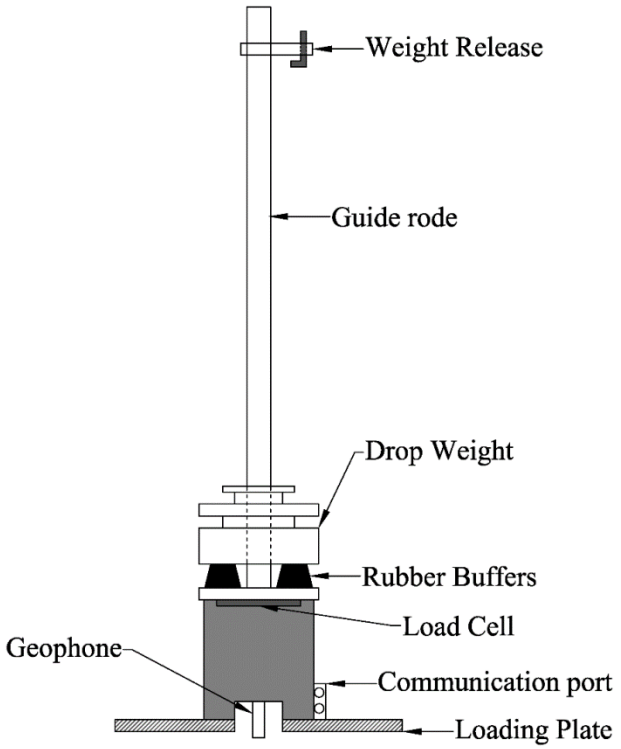

Figure 2-2. Prima 100 sketch (after Vennapusa, 2008)

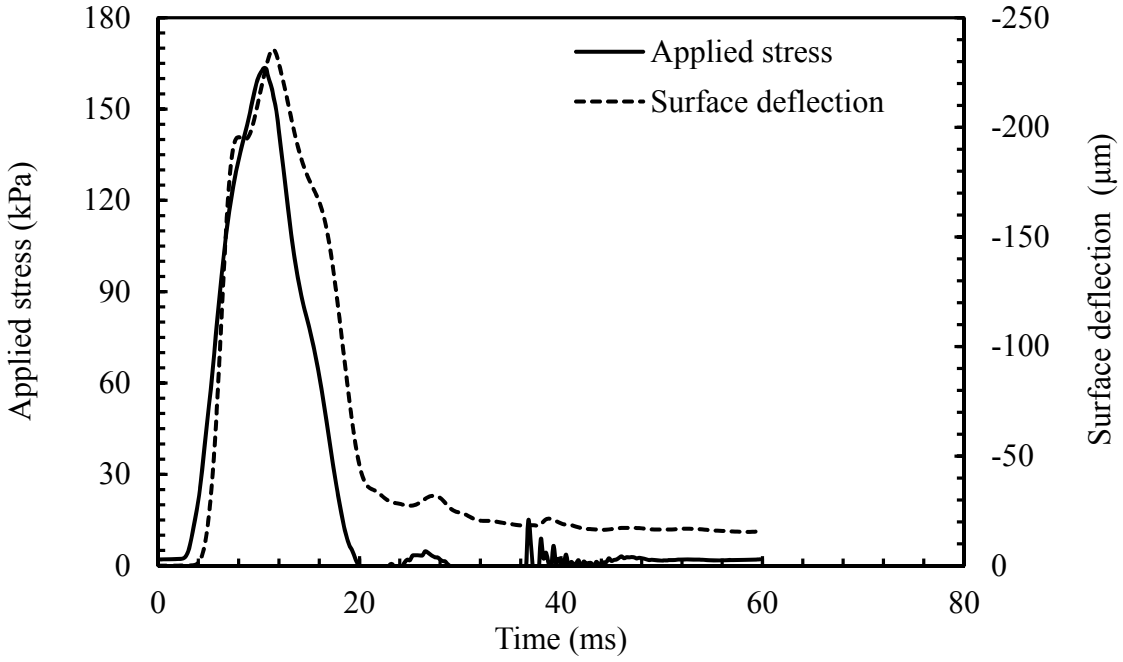

Figure 2-3. Example of recorded applied stress and surface deflection during LWD testing

Poisson's ratio values between 0.2 to 0.5 are recommended in the literature (Bishop 1977) based on soil type. Shape factor under the plate is a function of both plate rigidity and soil types similar to Terzaghi and peck (1968) approach for interpretation of plate load test data. Various shape factors are recommended for different scenarios. The shape factor can be varied between $\frac{\pi}{2}$ for a rigid loading plate, 1.33 and 2.67 for parabolic contact stress distribution in cohesive soils and granular soils, respectively, and 2 for a uniform contact stress distribution (Terzaghi and Peck, 1967; Mooney and Miller, 2007; White et al., 2007; Prima 100 software).

2.4 Resilient Modulus Determination

The use of the resilient modulus (Mr) has been substituted for the California Bearing Ratio (CBR) in pavement design in order to consider the deformation behavior of base and subgrade layers under cyclic loading conditions (AASHTO, 1993; MEPDG, 2004). The magnitude of M_r depends on soil physical properties, such as density and water content, as well as the applied stress state (Li, 1994). The value of Mr is defined as the ratio of the cyclic axial stress to the

recoverable or resilient axial strain (NCHRP project 1-28A, 2004), as expressed in Eq. 2-7 and shown in Figure 2-4:

$$M_r = \frac{\sigma_{cyclic}}{\varepsilon_r} \qquad \text{Eq. (2-7)}$$

Where:

σ_d : applied deviatoric stress

σ_{cyclic} : cyclic axial stress ($0.9\sigma_d$)

ε_r : resilient strain

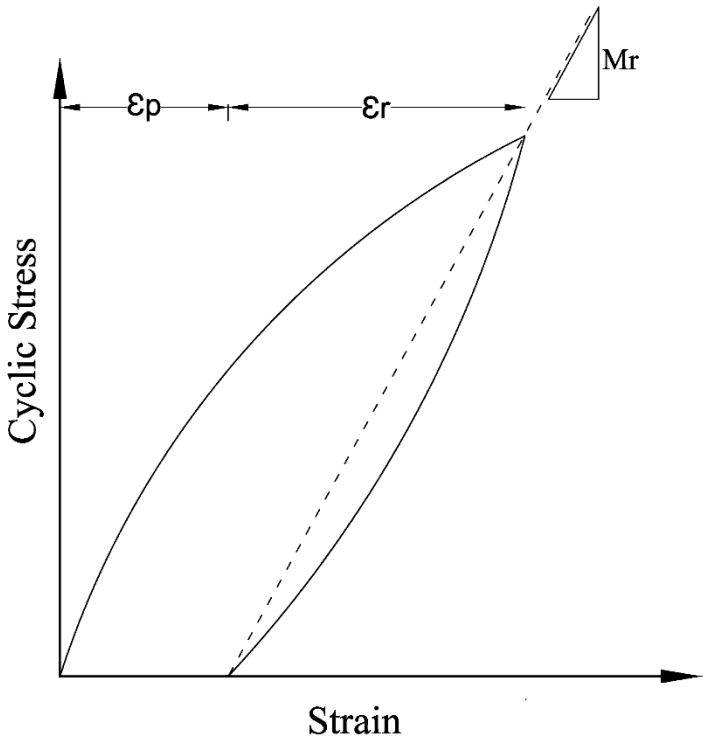

Figure 2-4. Definition of resilient modulus

The resilient modulus of a subgrade layer can be determined from laboratory testing following AASHTO T-307 test protocol, which uses fifteen load combinations: five deviatoric stress levels 13.8, 27.6, 41.4, 55.2 and 69 kPa (2, 4, 6, 8 and 10 psi) at three confining pressures 41.4, 57.6

and 13.8 kPa (6, 4 and 2 psi). Different forms of constitutive models can be found in the literature that calculate the resilient modulus as a function of one, two or three stress parameters such as confining pressure, deviatoric stress, bulk stress and octahedral shear stress (e.g. Dunlap, 1963; Seed et al., 1967; Witczak and Uzan, 1988; Pezo, 1993; NCHRP project 1-28A, 2004). The most recent universal constitutive model proposed in NCHRP 1-28A (MEPDG) is expressed as Eq. 2-8:

$$M_r = k_1.Pa.(\frac{\theta}{Pa})^{k_2}.(\frac{\tau}{Pa}+1)^{k_3} \qquad \text{Equ. (2-8)}$$

Where:

M_r : resilient modulus

P_a : atmospheric pressure

$\sigma_1, \sigma_2, \sigma_3$: principal stresses

$\theta = \sigma_1 + 2\sigma_3$: bulk stress

$\tau_{oct} = \frac{\sqrt{2}}{3}(\sigma_1 - \sigma_3)$: octahedral shear stress

k_i : regression constants

Although laboratory tests can provide high quality results, they require a well-trained operator and substantial time as well as an advanced apparatus to perform. An alternative to laboratory testing is empirical correlations developed from statistical analyses on mechanical and physical properties of soils and laboratory-measured resilient modulus. Carmichael et al., 1985; Elliott et al., 1988; Drumm et al., 1990; Farrar and Turner, 1991; and Hudsun et al., 1994 have all proposed models to estimate the resilient modulus of subgrade soils from index properties of soils. A shortcoming of these models is that they are not capable of capturing stress dependency of the resilient modulus. As an alternative, Hasan et al. 1994; MEPDG 2004; Herath et al. 2005; George et al. 2006; and Mohammad et al. 2008 have proposed correlations to predict M_r from in situ testing using the DCP, which are summarized in Table 2-1.

Table 2-1. Previous direct DCP models.

Researcher	Correlation equation	Unit
Hassan (1996)	M_r=7013.065-2040.783ln(DCPI)	M_r: psi, DCPI: in/blow
MEPDG (Powel) (2004)	CBR=$\frac{292}{DCPI^{1.12}}$ (Webster 1994) M_r=17.58(CBR)$^{0.64}$	M_r: MPa, DCPI: mm/blow
Herath et al. (2005)	M_r=16.25+$\frac{928.24}{DCPI}$	M_r: MPa, DCPI: mm/blow
George and Uddin (2000)	M_r=235.3(DCPI)$^{-0.48}$	M_r: MPa, DCPI: mm/blow
Mohammad et al. (2008)	M_r=$\frac{1045.9}{DCPI^{1.096}}$	M_r: MPa, DCPI: mm/blow

There are few empirical correlations to approximate the resilient modulus of subgrade soil from LWD measurements. Although a main advantage of these models is that they can capture actual conditions of a soil layer, they are mostly limited to one specific stress state. White et al. (2007) proposed the following model, presented in Eq. 2-9, to predict resilient modulus of subgrade soil from E_{LWD} with an assumed Poisson's ratio of 0.35 and shape factor of $\frac{\pi}{2}$ and 2 for cohesive and cohesionless soils, respectively, at confining pressure = 41.4 kPa (6 psi) and deviatoric stress = 69 kPa (10 psi).

$$M_r = \frac{(E_{LWD} + 45.3)}{1.24} \quad \text{Eq. (2-9)}$$

With M_r, E_{LWD} in MPa

Mohammad et al (2008) presented the model in Eq. 2-10 in order to estimate resilient modulus from LWD data by assuming a Poisson's ratio of 0.4 and a shape factor of $\frac{\pi}{2}$ for cohesive soil and 2 for cohesionless soils, at confining pressure = 13.8 kPa (2 psi) and deviatoric stress = 41.4

kPa (6 psi). These values represent the stress state at the top of the subgrade layer under standard single axle loading of 80 kN (18 kips) and tire pressure of 689 kPa (100 psi) with a 50-mm asphalt wearing course, 100-mm asphalt binder course and 200-mm aggregate base course (Mohammad et al., 2008; Rahim, 2004; Asphalt Institute, 1989).

$$M_r = 27.75 \times E_{LWD}^{0.18} \qquad \text{Eq. (2-10)}$$

With M_r, E_{LWD} in MPa

The validity of these models at just one specific stress state, makes them ineffectual for other loading combinations. Many studies have been performed over the past two decades to model the stress dependency of the resilient modulus by predicting the coefficients of the universal constitutive models (e.g. Dunlap, 1963; Seed et al., 1967; Witczak and Uzan, 1988; Pezo, 1993; NCHRP project 1-28A, 2004) using basic soil properties such as water content, plastic limit, liquid limit, P_4, P_{200} etc. For example, Yau and Von Quintus, 2002; Elias and Titi, 2006; and Nazzal and Mohammad, 2010 each proposed different models to estimate "NCHRP project 1-28A" constitutive model coefficients (k_1, k_2 and k_3) from the physical properties of soils taking into account mean and deviatoric stress dependency.

2.5 Numerical Analyses

2.5.1 Various soil constitutive models

In order to study the deformation behavior of test sections under cyclic loading, the subgrade and base layer have been modeled in Plaxis 2D and 3D using Mohr-Coulomb, Hardening Soil, and Hardening Soil small strain constitutive models.

2.5.1.1 Mohr-Coulomb

The Mohr-Coulomb or elastic perfectly-plastic constitutive model uses Hooke's law and the Mohr-Coulomb failure envelope. The deformation behavior of the soils below the failure envelope is assumed to be linear elastic following Hooke's law. The linear elastic stiffness is modeled by a constant elastic modulus and Poisson's ratio. The failure behavior is captured by the Mohr-Coulomb criterion. Hence, the model is not capable of capturing the non-linear deformation behavior of soil before failure.

The model required two stiffness properties: elastic modulus, E, and Poisson's ratio, ν ; and three shear strength properties in drained condition: the cohesion, c, friction angle, ϕ, and dilatancy angle, ψ

2.5.1.2 Hardening Soil

The Hardening Soil model is an advanced soil constitutive model, which is capable of simulating the stiffness hardening of soils with an increase of confining pressure and stiffness softening due to vertical strain increase. The relationship between axial deviatoric stress and axial strain was formulated with the hyperbolic relationship first by Konder (1963), as shown in Figure 2-5, and later implemented to the constitutive model by Duncan and Chang (1970). Compared to the Mohr-Coulomb model, the Hardening Soil model involves more stiffness parameters, as stated below:

m: Stress dependent stiffness according to a power law.

E_{50}^{ref} : plastic straining due to primary deviatoric loading

E_{oed}^{ref} : Plastic straining due to primary compression

E_{ur}^{ref} : elastic unloading/reloading

ν_{ur} : unloading/reloading Poisson's ratio

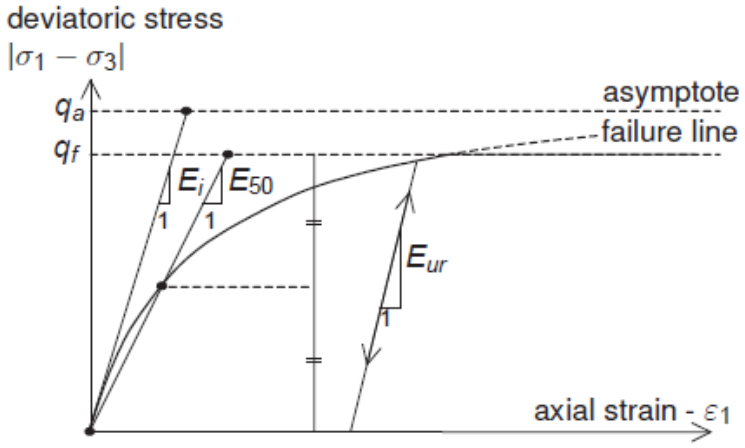

Figure 2-5. Hyperbolic stress-strain relation (Plaxis 2010 manual)

The strain-stress relation and stress dependency of stiffness properties are formulated for standard drained triaxial test as follow:

$$-\varepsilon_1 = \frac{1}{E_i}\frac{q}{1-q/q_a} \qquad q<q_f \qquad \text{Eq. (2-11)}$$

Where q_a and E_i are defined as:

$$q_a = \frac{q_f}{R_f} \qquad \text{Eq. (2-12)}$$

$$E_i = \frac{2E_{50}}{2-R_f} \qquad \text{Eq. (2-13)}$$

The E_{50} is the stress dependent stiffness modulus which is given by Eq. 2-14:

$$E_{50} = E_{50}^{ref}\left(\frac{c\cos\varphi - \sigma_3^{'}\sin\varphi}{c\cos\varphi + p^{ref}\sin\varphi}\right)^m \qquad \text{Eq. (2-14)}$$

The stress dependency of the stiffness modulus is expressed by the power *m*. The value of m can be directly calculated from a series of triaxial tests conducted at various effective confining pressures or estimated from reported values in the literature. The m value is recommend between 0.5 for sand and silt to 1 for soft clayey soil.

In case of unloading/reloading stress paths, the E_{ur} is formulated as a stress dependent stiffness modulus by Eq. 2-15:

$$E_{ur} = E_{ur}^{ref}\left(\frac{c\cos\varphi - \sigma_3^{'}\sin\varphi}{c\cos\varphi + p^{ref}\sin\varphi}\right)^m \qquad \text{Eq. (2-15)}$$

2.5.1.3 Hardening Soil small strain (HS small model)

The Hardening Soil model considers elastic behavior during unloading/reloading, however only within the small strain range. As shown in Figure 2-6, stiffness of soils reduce due to the increase of strain level. It can be seen that for the conventional laboratory measured strain, (i.e. $\varepsilon > 10^{-3}$), soil stiffness is reduced to half of its initial value.

It can be concluded that for geotechnical or soil-structure analyses, an appropriate stiffness incorporating the soil's non-linear dependency on strain level should be used. The Hardening Soil Small Strain (HS Small Strain) model is capable of considering this characteristic of soil stiffness, as well as the other features included in the Hardening Soil model.

In order to describe the variation of stiffness with strain, the HS Small Strain model requires two more parameters in addition to HS model parameters:

G_0: initial shear modulus.

$\gamma_{0.7}$: shear strain level at which G_s is reduced to 70% of G_0

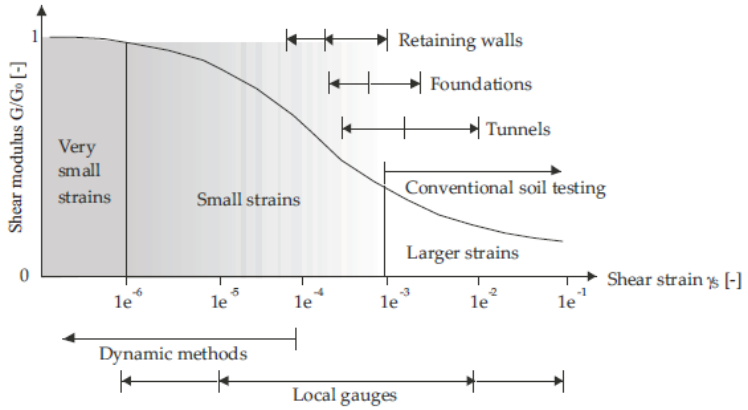

Figure 2-6. Stiffness-strain behavior of soil (after Atkinson & Sallfors (1990))

Hardin and Drnevich (1972) proposed Eq. 2-16 to capture the strain dependency of shear modulus:

$$\frac{G_s}{G_0} = \frac{1}{1 + \left| \frac{\gamma}{\gamma_r} \right|} \qquad \text{Eq. (2-16)}$$

Where γ_r, threshold shear strain, is defined as:

$$\gamma_r = \frac{\tau_{max}}{G_0} \qquad \text{Eq. (2-17)}$$

Santos and Correia (2001) suggested Eq. 2-18, to use $\gamma_{0.7}$, instead γ_r to eliminate the error involved with selecting the threshold shear strain:

$$\frac{G_s}{G_0}=\frac{1}{1+0.385\left|\frac{\gamma}{\gamma_{0.7}}\right|} \qquad \text{Eq. (2-18)}$$

Benz (2007) defined the stress-strain relationship in context of HS Small Strain model, as expressed in Eqs. 2-19 and 2-20;

$$\tau = G_s\gamma=\frac{G_0}{1+0.385\left|\frac{\gamma}{\gamma_{0.7}}\right|} \qquad \text{Eq. (2-19)}$$

$$\gamma=\frac{3}{2}\varepsilon_q \qquad \text{Eq. (2-20)}$$

Where ε_q is the second deviatoric strain invariant.

Figure 2-7 shows the stiffness properties of the HS Small Strain model. In contrast to the HS model, it can been seen that within the HS Small Strain model, E_{ur} is not linear and also E_{ur} is different than the initial E_0 value.

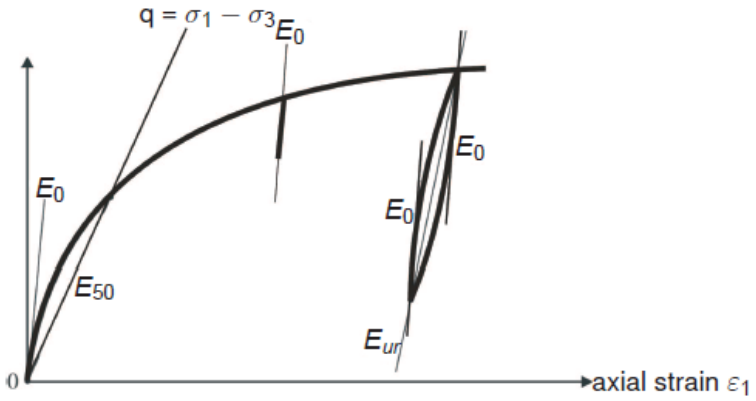

Figure 2-7. Stiffness parameter of HS Small strain model (Plaxis 2010 manual).

The stress dependency of shear modulus is given by Eq. 2-21:

$$G_0 = G_0^{ref}\left(\frac{c\cos\varphi - \sigma_3^{'}\sin\varphi}{c\cos\varphi + p^{ref}\sin\varphi}\right)^m \quad \text{Eq. (2-21)}$$

And the initial elastic modulus is defined by Eq. 2-22:

$$E_0 = 2G_0(1+\nu_{ur}) \quad \text{Eq. (2-22)}$$

2.5.2 Previous numerical studies

Several numerical studies have been performed over the past decades to evaluate the performance of reinforced unpaved and paved roads using finite element/difference analyses. Different constitutive soil models were used to model the deformation behavior of ABC and subgrade soils. Dondi (1994) obtained results from numerical analyses that were in a good agreement with field observations and indicated a significant increase in bearing capacity of the reinforced subgrade compare to the unreinforced section. Dondi (1994), and Wathugala et al. (1996) showed through numerical analyses that geosynthetic inclusions produced up to a 20% reduction in vertical deformation compared to an unreinforced subgrade. Barksdale et al. (1989) reported that the most beneficial location of the reinforcement is between the top of the subgrade and 1/3 up into the base layer. Leng and Gabr (2005) showed that the contribution of geosynthetic reinforcement to reducing rut depth increased as the modulus ratio of the ABC to the subgrade decreased. Nazzal et al. (2010) found the benefit of reinforcement is more pronounced in reducing permanent deformation rather than recoverable strain.

A summary of the numerical investigations on the performance of reinforced subgrades is presented in Table 2-2. From an analysis of these studies, it was concluded that the deformation behavior and stress distribution within reinforced unsaturated base/subgrade materials under cyclic loading have not been fully addressed. Furthermore, no explicit consideration for the base/subgrade matric suction seems to have been taken into account in evaluating the deformation behavior of the pavement system.

Table 2-2. Summary of Finite Element Studies of Reinforced un/Pavements

Author(s)	Software	Analysis mode	Asphalt layer model	Base layer model	Subgrade layer model	Load
Miura et al (1990)	-	Axi-sym	LE[1]	LE	LE	Monotonic
Dondi (1994)	ABAQUS	3D	LE	D-P[2]	None	Monotonic
Whathugala et al. (1996)	ABAQUS	Axi-sym	D-P	D-P	Hiss δ_0	Single Cycle
Perkin et al. (2001)	ABAQUS	3D	MC[3]	BS[4]	BM	Monotonic
Leng and Gabr (2001)	ABAQUS	Axi-sym	None	D-P	D-P	Monotonic
Kwon et al. (2005)	ABAQUS	Axi-sym	LE	MC	LE	Monotonic
Abu-Farsakh et al. (2009)	ABAQUS	Axi-sym	MC	D-P	D-P	100 load cycles
Nazzal et al. (2010)	ABAQUS	Axi-sym	MC	CS[5]	Cam-Clay	Monotonic

[1]LE: Linear Elastic
[2]D-P: Drucker-Prager
[3]Mohr-Coulomb
[4]BS : Bounding Surface
[5]CS : Critical State

2.6 Soil Water Characteristic Curve

The soil water characteristic curve (SWCC), correlates the soil matric suction state and volumetric/gravimetric water content or degree of saturation. Several mathematical models have been developed over the last decades in order to develop the soil SWCC from a limited number of points. Fredlund and Xing (1994) proposed Eq. 2-23:

$$\theta(\psi, a, n, m) = C(\psi)\frac{\theta_s}{\{\ln[e+(\frac{\psi}{a})^n]\}^m} \qquad \text{Eq. (2-23)}$$

Where:

$$C(\psi) = 1 - \frac{\ln[1 + (\frac{\psi}{\psi_r})]}{\ln[1 + (\frac{10^6}{\psi_r})]} \quad \text{Eq. (2-24)}$$

Van Genuchten (1980) proposed Eq. 2-24 for developing soil the SWCC. Plaxis software uses Van Genuchten's model for unsaturated soil analysis.

$$\theta = \theta_r + \frac{\theta_s - \theta_r}{[1 + (a\psi)^n]^m} \quad \text{Eq. (2-25)}$$

Where:

$$m = 1 - 1/n \quad \text{Eq. (2-26)}$$

Ba et al. (2013) reported results which looked into the SWCC of different types of ABC. The SWCC curves were developed and constructed from laboratory suction measurements and using Frendlund and Xing's and also Van Genuchten's models. The presented results by Ba et al. (2013) were used in numerical analyses, to estimate the SWCC of the aggregate base materials utilized in the present study.

Wang (2014) performed a comprehensive study on the SWCC of Piedmont residual soils from Greensbro, North Carolina. A series of pressure plate tests and tensiometer suction measurements were performed to develop the SWCC of the natural A-7-5 soils. Since the location of the full-scale testing in this project was located in same geologic region, the developed SWCC for A-7-5 soil by Wang (2014) was used for numerical analyses in this study. The developed SWCC was validated by laboratory tensiometer matric suction measurements on field-obtained Shelby tubes.

Since developing the SWCC curve through laboratory testing (pressure plate test, etc.) is time consuming and requires advanced equipment, empirical correlations have been proposed in the literature to estimate Fredlund and Xing's or Van Genuchten's model coefficients (a, n, m), from soil grain size distribution data. In order to develop a SWCC for the A-4 soil, with PI<4, the

proposed model by Zapata et al. (2000), that predicts the SWCC from index properties of soils with PI=0, was used. Eqs. 2-27 to 2-30 predict the Frendlund and Xing's model coefficients for soils with PI=0:

$$a = 0.8627(D_{60})^{-0.751} \quad \text{Eq. (2-27)}$$

$$n = 7.5 \quad \text{Eq. (2-28)}$$

$$m = 0.1772\ln(D_{60}) + 0.7734 \quad \text{Eq. (2-29)}$$

$$\frac{\psi_r}{a} = \frac{1}{D_{60} + 9.7e^{-4}} \quad \text{Eq. (2-30)}$$

2.7 Summary

In summary, there is consensus that the inclusion of geosynthetics reinforcements reduces deformation and applied stresses on the top of the subgrade compared with unreinforced unpaved section. The contribution of the geosynthetics reinforcement intensified with smaller thicknesses of the ABC layer. Existing empirical correlations for prediction the resilient modulus either do not simulate field stress conditions and are generally not capable of calculating the resilient modulus at various stress state. The modulus and shear strength properties of soils depend on matric suction state, which in turn affect deformation behavior of the base and subgrade layers. The contributions of the matric suction to the deformation behavior of the reinforced or stabilized subgrade, under static and cyclic loading, are not well addressed in literature.

CHAPTER 3: FIELD TESTING

3.1 Site Description:

The test site was part of a NCDOT road widening project (State Project R-2413C) located in Rockingham & Guilford, north of Greensboro, North Carolina. The specific test area was located on ramp B that connects US 65 East to US 220 South at the coordinates of 36.268082 and-79.93053, as marked on Figure 3-1.

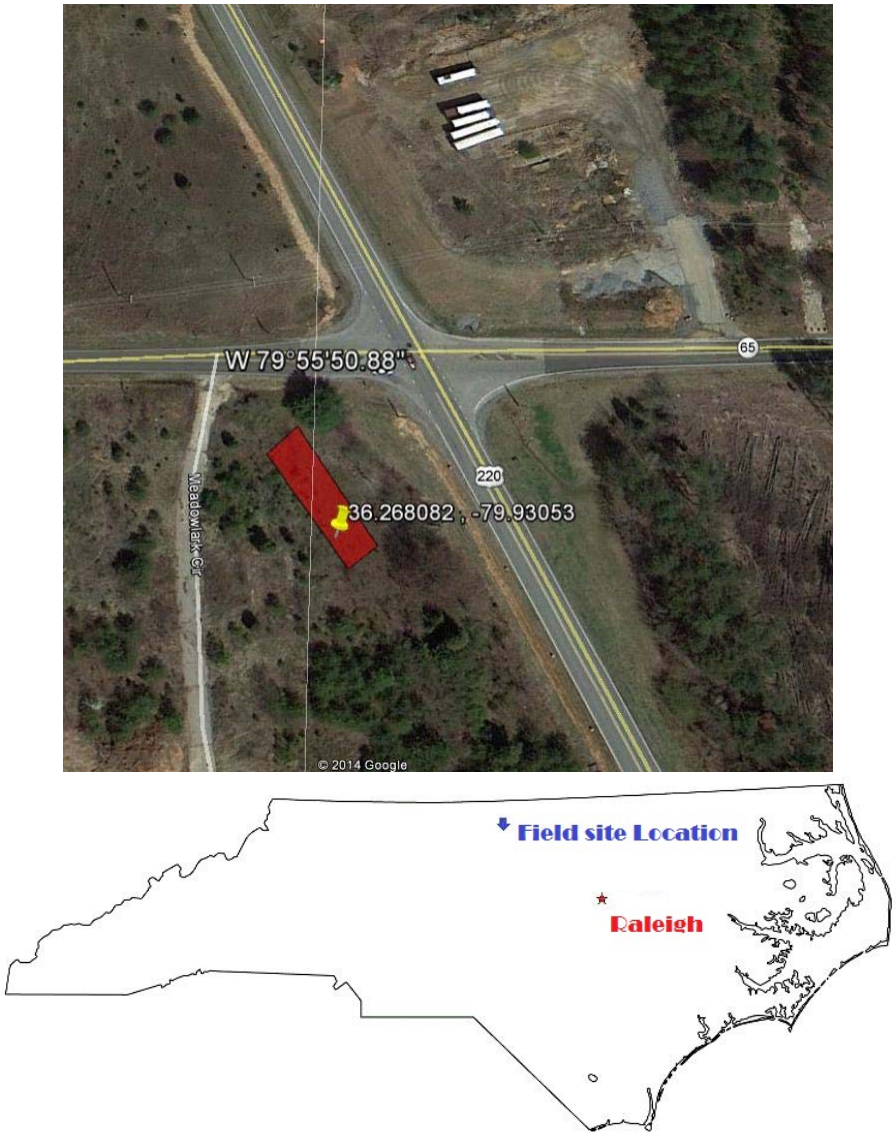

Figure 3-1. Site Location

Guilford County is located in the Piedmont region, which encompasses approximately the middle one third of the state of North Carolina. The chosen test area used to be a trailer park, with four to six septic tanks installed into the ground. During the first phase of the project (drilling boreholes, sampling and SPT testing) which occurred in the middle of March 2014, the ground surface was completely covered by mud, water and grass, as shown in Figure 3-2.

Figure 3-2. Field site on March 19th 2014

3.2 Test Pads Configuration

Table 3-1 provides descriptive information for the test sections and Figure 3-3 shows a plan view and section of the test pad area. The area encompassing the four test section was 200 ft long by 16 ft wide and was divided to four sections of 50ft long pads in order to compare the performance of different types of subgrade soil stabilization. The test pads were constructed in the following order:

I) Section 1 was designed to be undercut by 31" and backfilled with type II select fill material. After analyzing Lidar scan data, it was observed that 29" to 31" was excavated and backfilled with 30" to 33" of select fill.

II) Section 2 was excavated 9” and reinforced with biaxial geogrid (BX 1200). The section was backfilled with 9” of class IV aggregate base course.

III) Section 3 was undercut by 9” and backfilled with 9” of class IV aggregate base course on the top of high strength polyester woven geotextile.

IV) Section 4 was designed to be treated by lime stabilization for the top 8 inches.

Table 3-1. Test pads description

Section No.	Depth of Undercut/Treatment	Backfill Martial	Reinforcement	Tensile Strength, MD, (at 5% strain), lbs/ft
1	30”~33”	Select Material (Class II)	None	-
2	7.5”~11”	ABC (Class IV)	Tensar® BX1200 Geogrid	810
3	10”~11.5”	ABC (Class IV)	Mirafi® HP570 Geotextile	2400
4	8”	1.5 ton of lime per 600 ft^3	None	-

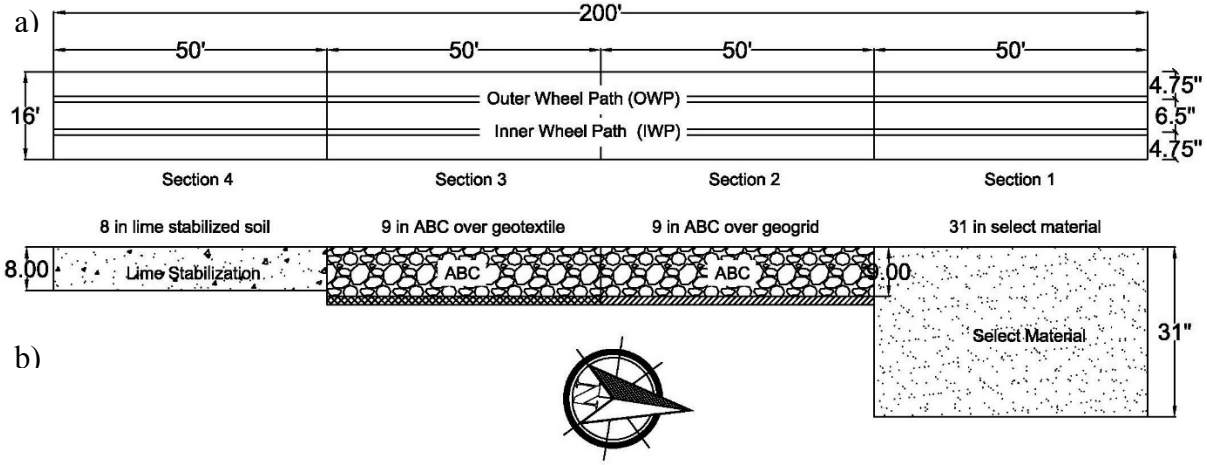

Figure 3-3. Plan view (a) and section (b) of the test pads.

3.3 Sensor Installation and Pad Construction

3.3.1 Moisture and suction sensors

As shown in Figure 3-4 and Figure 3-5(d), two moisture and one suction sensors were installed in the middle of each test pad to monitor and record the volumetric water content and matric suction of the subgrade layer. One 10HS Decagon® moisture sensor, Figure 3-5(a), was installed horizontally at a depth of 3" and one vertically at the depth of 6" below the stabilized zone, Figure 3-5(f). One MPS-2 Decagon® suction sensor, Figure 3-5(b), was installed 3" below the undercut/treated depth, and 2" away from the horizontal moisture sensor, Figure 3-5(e). Figure 3-5(d) shows the depth of sensor installation in the section 4. The suction sensors were calibrated at the North Carolina State University geomechanics lab, the results are presented in Appendix A.

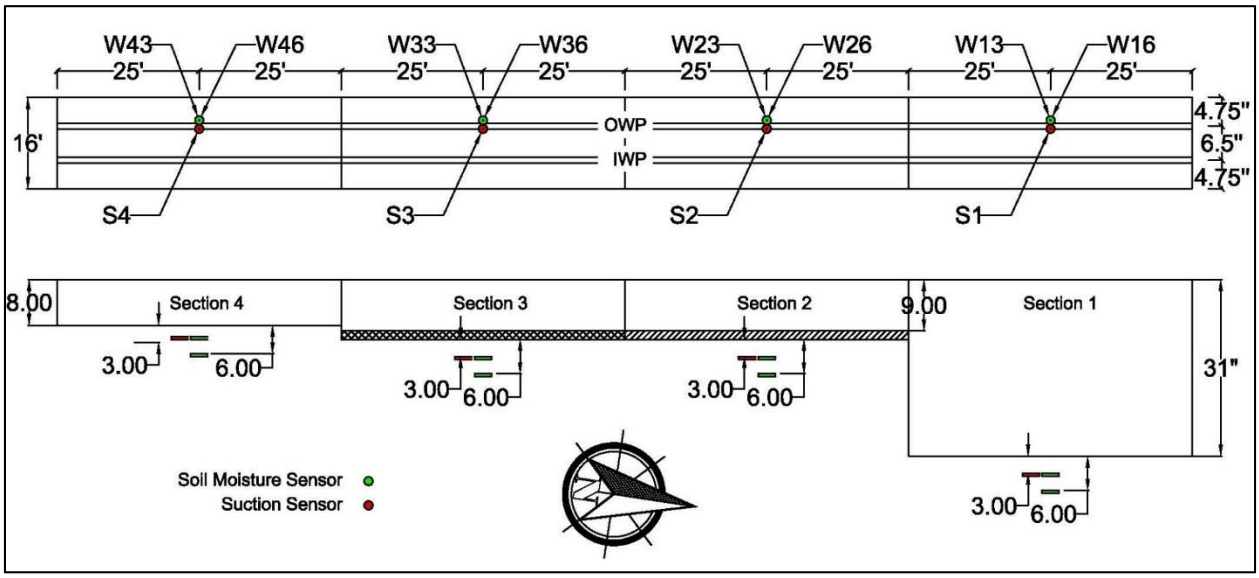

Figure 3-4. Moisture and suction sensors layout

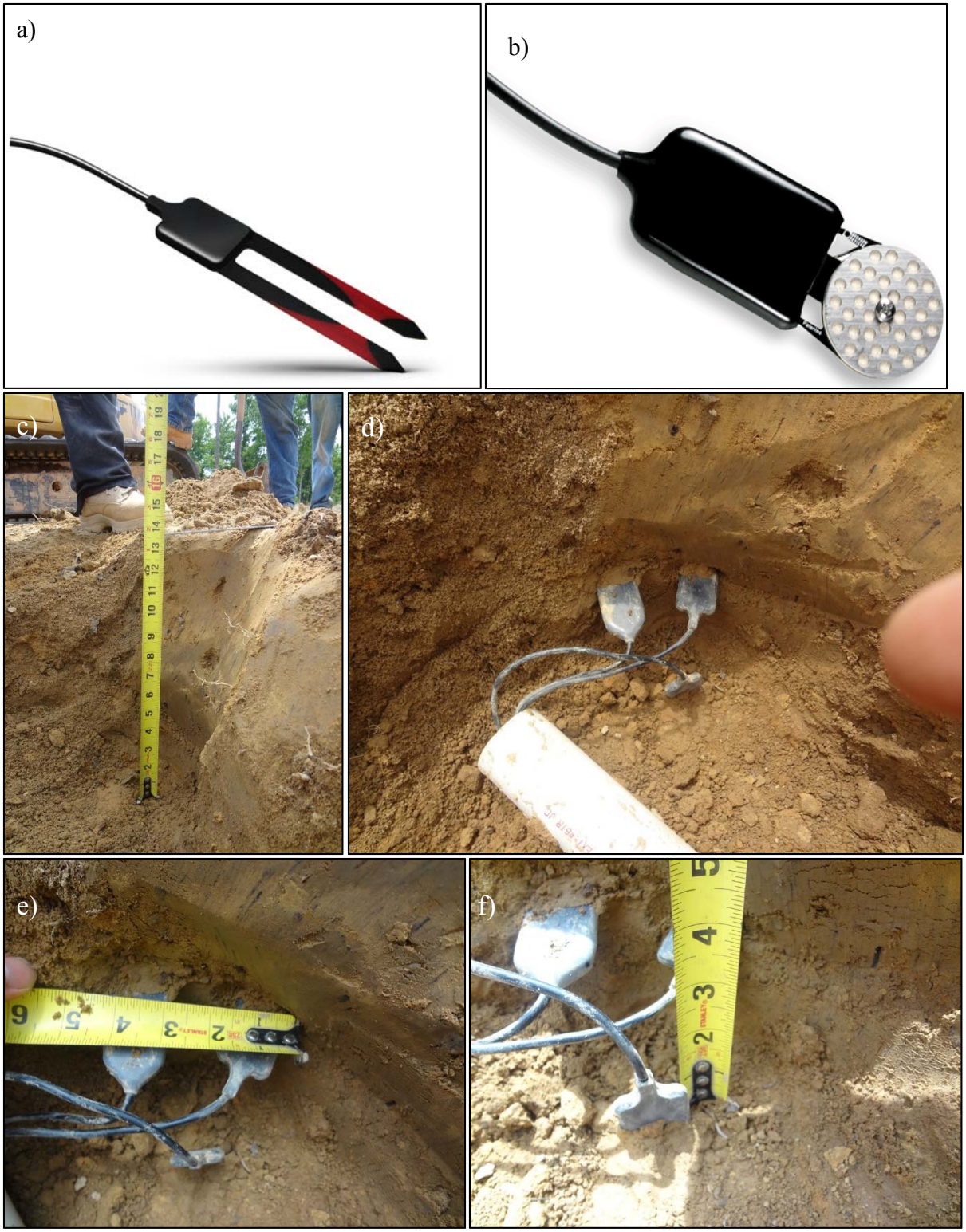

Figure 3-5. a) 10HS Decagon® moisture sensor; b) MPS-2 Decagon® suction sensor; c) depth of sensors in section; and d, e, f) two moisture and one suction sensor.

3.3.2 Earth pressure cell installation

Figure 3-6 shows the location of earth pressure cells (EPC) in each test section. A combination of 9 inch- diameter EPC Geokon® -model # 3500-2 and 3500-3 with pressure transducer with voltage 0-5 VDC and current 4-20 mA output, respectively (instruction manual 3500 EPCs, Geokone, 2013), were used. The EPC were located to measure applied stress by traffic load near the interface of stabilized layer and subgrade. The EPC model # 3500-2 is manufactured with readout cable that consists of four individually shielded pairs of cable; two pairs directly connected to the semiconductor and one pair for long cable remote sense, which make this model suitable for long cable (>50m). However for shorter cables, model 3500-3 with readout cable consisting of two pairs of cable, was used. The EPCs were calibrated in the air chamber in the North Carolina State University structure lab, CFL. The results are presented in Appendix B.

On each test pad, four pressure cells were installed 3" below the undercut/stabilized depth, two on each wheel path. In order to install the pressure cells, after undercutting to the pre-determined grade, a hole with 10"~11" diameter and 6" depth was dug out, as shown in Figure 3-7(a-b), and backfilled using 3" hand-compacted silica sand, Figure 3-7(c). Each pressure cell was then placed as shown in Figure 3-7(d), and 1" soil (fraction that passed sieve No. 10) was compacted on the top of it, Figure 3-7(e-f).

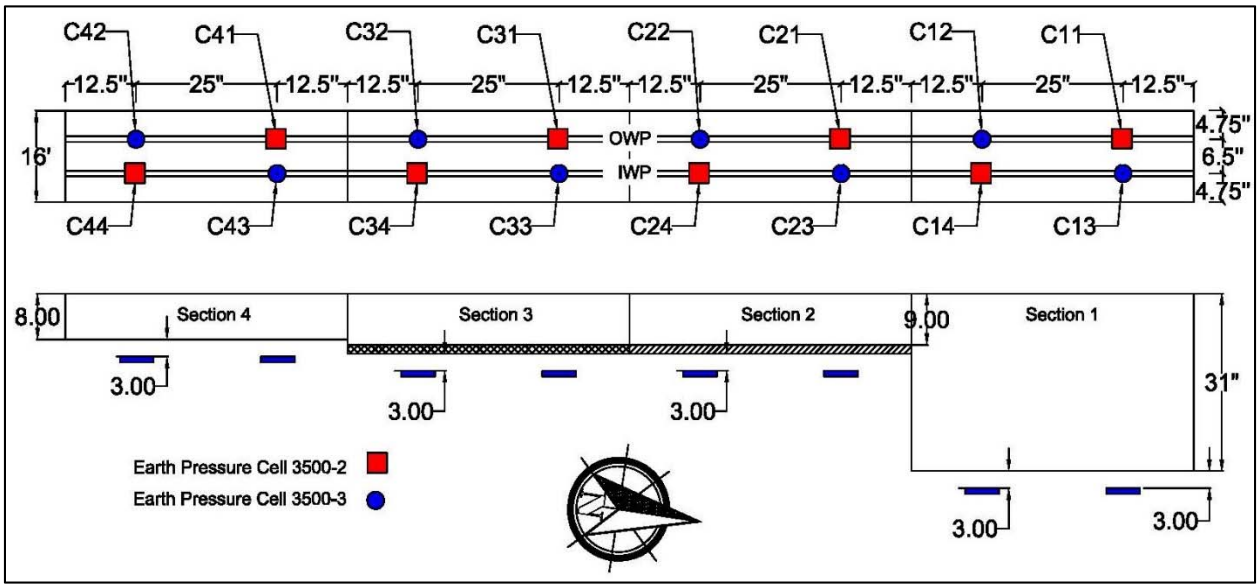

Figure 3-6. Earth Pressure Cells layout

Figure 3-7. a) Depth of the EPC below the stabilized layer; b) 10”~11” hole; c, d) 3” hand-compacted silica sand; and e, f) 1” soil (fraction that passed sieve No. 10).

3.3.3 Data acquisition

Applied stress was measured by the EPCs. These data were recorded by using Vishay Micro-Measurements® through 16 channels, Figure 3-8(a). Data acquisition was connected to a laptop to record and save the data by StrainSmart© software. Recording rate was set on 1000 reading per second.

The volumetric water content and matric suction were recorded using four EM 50 data loggers, shown in Figure 3-8(b). The data loggers were set to record volumetric water content and suction every one hour. At the end of the full scale testing, the data loggers were connected to a laptop and the stored data were transferred and saved on the laptop by Decagon's ECH2O Utility software.

a)

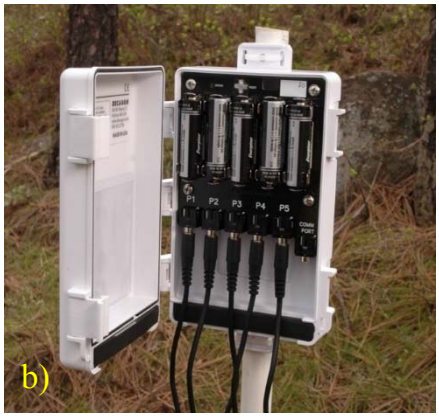

Figure 3-8. a) Data Acquisition System Vishay 7000 and b) EM 50 data loggers

3.3.4 Construction of test sections

As shown in Figure 3-9(a), Section 1 was undercut 31" and backfilled by select material class II that was compacted in four and one-half lifts to reach relative compaction greater than 95%, Figure 3-9(b). The physical properties of the select fill are summarized in Table 3-2.

Table 3-2 Mechanical properties of select fill.

LL	PL	PI	G_s	P_4%	P_{200}%	USCS	AASHTO
32	30	2	2.71	83%	42%	SM	A-4a

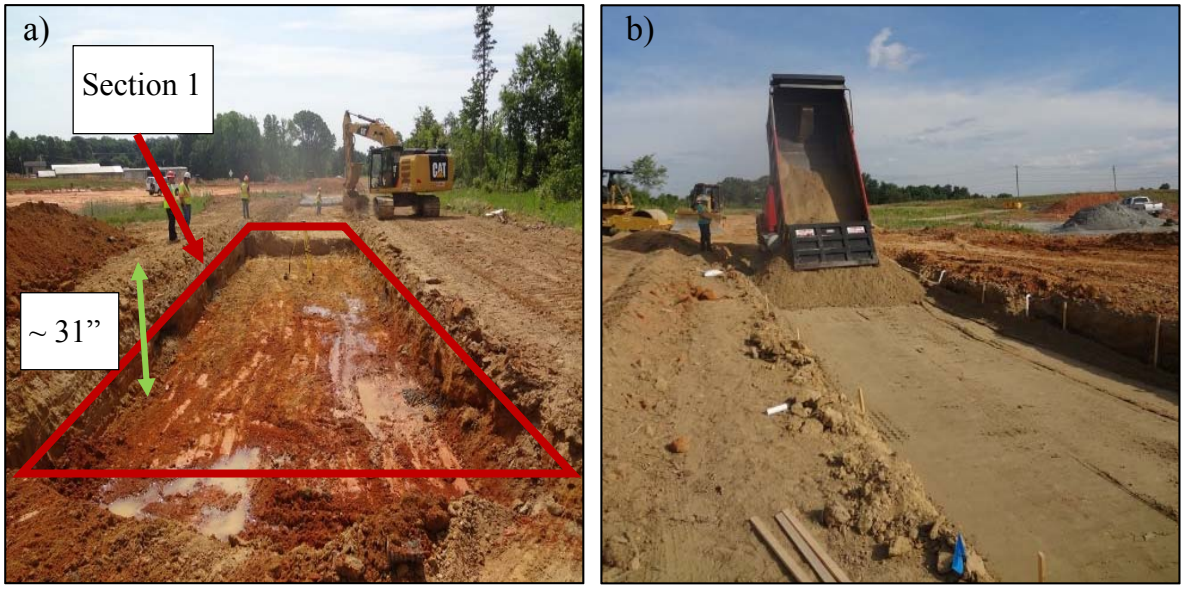

Figure 3-9. (a)Undercutting section 1 and (b) Backfilling section 1

Test sections 2 and 3 were stabilized by excavating 9 inches of in-place soil and installing geogrid BX1200 manufactured by Tensar ® and geotextile Mirafi® HP570 on section 2 and 3, respectively, as shown in Figures 3-10 and 3-11. The geosynthetic materials were stapled into the ground and tighten as much as possible to minimize required strain for mobilizing tensile strength, Figure 3-11. After installing the geosynthetic layers, 9 inches of ABC class IV were backfilled and compacted to relative compaction greater than 91% based on AASHTO T180.

Figure 3-10. Geogrid Tensar ® BX1200 on section 2 and geotextile Mirafi® HP570 on section 3

Figure 3-11. Stapling geogrid Tensar ® BX1200 into the ground in section 2

3.3.5 Density testing

Two rubber balloon density tests were performed on section 1 with the select fill material. One test was conducted right after the select fill was placed and compacted and one test 4 days later, before full scale testing, Figure 3-12(a). Four nuclear gage density tests were carried out on sections 2 and 3 in order to measure relative compaction of aggregate base course, Figure 3-12(b). Two density tests were performed (one on each section) one day after the ABC was placed and compacted and two tests before starting traffic on the pads. The relative compaction values were calculated based on a maximum dry unite weight of 115 and 134 pcf for select fill and ABC materials, from presented laboratory proctor test results in Chapter 4. The density testing results are summarized in Table 3-3.

Table 3-3. Measured Relative Compaction

Pad No.	1	2	3
Description	31" Select Material type II	9" ABC over Geogrid	9" ABC over Geotextile
Method	Rubber Balloon	Nuclear gage	Nuclear gage
% Compaction	95.4 (95)[1]	95.7 (97.1)[1]	96.3 (96.3)[1]
Water content	14%	6.4% (3.4%)[2]	6.4% (3.9%)[2]

1: Relative compaction before full scale testing

2: water content before full scale testg

Figure 3-12. a) Rubber balloon density and b) nuclear gage density

3.4 Test Load and Deformation Surveys

3.4.1 Truck configuration

A tri-axle dump truck was loaded with stone and weighed on a certified truck scale in order to determine the load distribution on each axel. The total gross weight was determined as 54980 lbs. By comparing the truck weight and load distribution on each axle to one used in a similar project (Cowell et al. 2012), the front and two rear axles load were estimated as 16500 and 38500 lbs, respectively, which were assumed evenly distributed among the tires for each axle. Tire pressure was checked before, intermittently during and after testing, and set to ~85 psi. a) Figure 3-13 shows the truck tire configuration and dimensions.

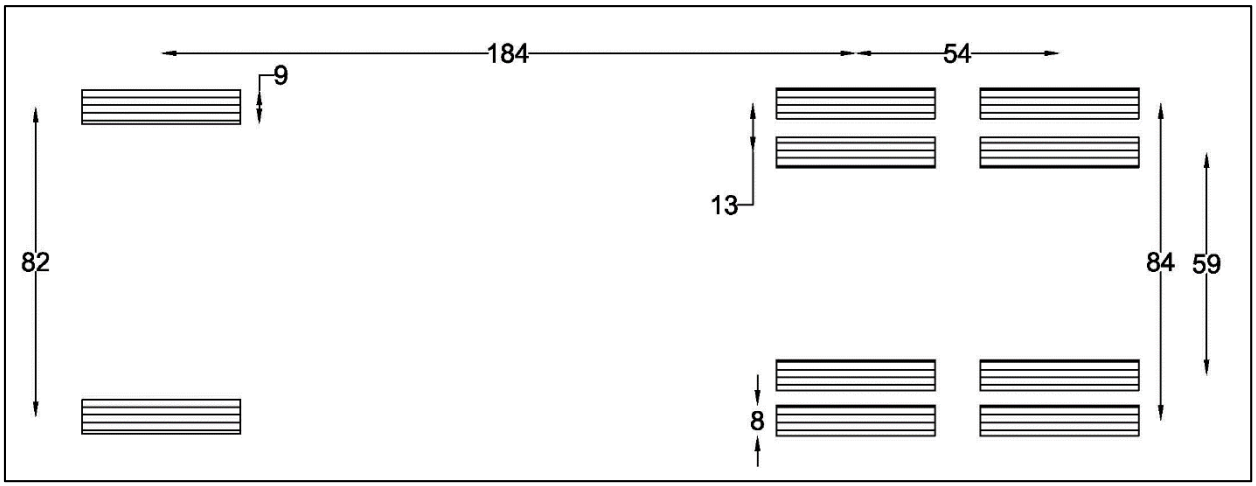

Figure 3-13. Truck configuration (Dimensions in inches)

3.4.2 Lidar scan

To monitor the cumulative permanent deformation induced by traffic loading, Lidar Scan surveys (see Figure 3-14) were performed before starting the test, after 1, 5, 10, 50, 100, 200, 300, 500, 700, 800, 900 and 1000 truck passes. Surveys were also conducted before and after excavation to determine exact depth of the stabilization measure. Since the accuracy of survey is dependent on distance of objects, and for the sake of consistency, surveys were carried out from two stations, at the interface of sections 1 and 2 and the interface of sections 3 and 4.

Figure 3-14. Survey from interface of section 3 and 4

3.5 Summary

In summary, a site located in the Piedmont Physiographic region, Greensbro, North Carolina state was selected, in order to evaluate proposed undercut criteria in the Phase I, as well as performance of several subgrade stabilization alternatives included select fill materials, geosynthetics reinforcement and chemical treatment. Four full-scale road sections (each 50 ft. long by 16 ft width) were constructed on poor subgrade soil where undercutting is normally needed. One test section incorporated 31 inches of undercut and replacement with select fill material (Class II), the second and third test sections included reinforcement using a geogrid and geotextile, respectively, in conjunction with excavating and replacement with 9 inches ABC (Class IV), and the fourth test section included lime stabilization of the top 8 inches soft subgrade soil. Four Earth Pressure Cells (EPC) were embedded within the wheel paths (two in each wheel path) of each the test sections to monitor stress variations with traffic loading. A surface profiler (laser-based surveying) was used at periodic intervals to monitor plastic deformation and wheel path rutting with loading cycles. Moisture and suction sensors were embedded in the subgrade to monitor moisture and suction variation; to investigate impacts of

such variation on the strength properties of the subgrade, and therefore to enhance interpretation of the field data.

CHAPTER 4: LABORATORY AND IN-SITU TESTING

During field construction of the test pads, in-situ tests including DCP and LWD were carried out to evaluate shear strength and stiffness properties of the encountered soils. Laboratory tests included index properties, monotonic triaxial compression testing and Resilient Modulus testing. These tests were performed on samples retrieved from the test site using Shelby tubes.

4.1 Sampling and Testing

Shelby tube samples were obtained at eight locations, with 3 tubes retrieved per location. As shown in Figure 4-1, the locations of the holes from which Shelby tubes were retrieved were along the centerline of each test section, with samples retrieved 12.5 ft from the two ends of each test pad. In total, 24 Shelby tubes were recovered. The samples were then taken to the Constructed Facilities Laboratory (CFL) at NCSU for further testing.

A series of laboratory and in-situ tests were performed to evaluate subgrade soil modulus properties of the four test pads. In this case, SPT, LWD and DCP testing was conducted to monitor the variation of subgrade modulus across the test sections. The LWD and DCP tests were performed four locations within each test section, as shown in Figure 4-1, both before and after excavation and full scale testing. The test locations were offset 1-m (3.3-ft) away from the boreholes from which Shelby tubes were obtained. In parallel, a laboratory testing program including physical properties characterization, monotonic triaxial, and resilient modulus testing was performed on undisturbed samples retrieved from within the LWD influence zone (a depth of 1~1.5 diameter of the LWD loading plate, as was specified by Mooney and Miller 2007).

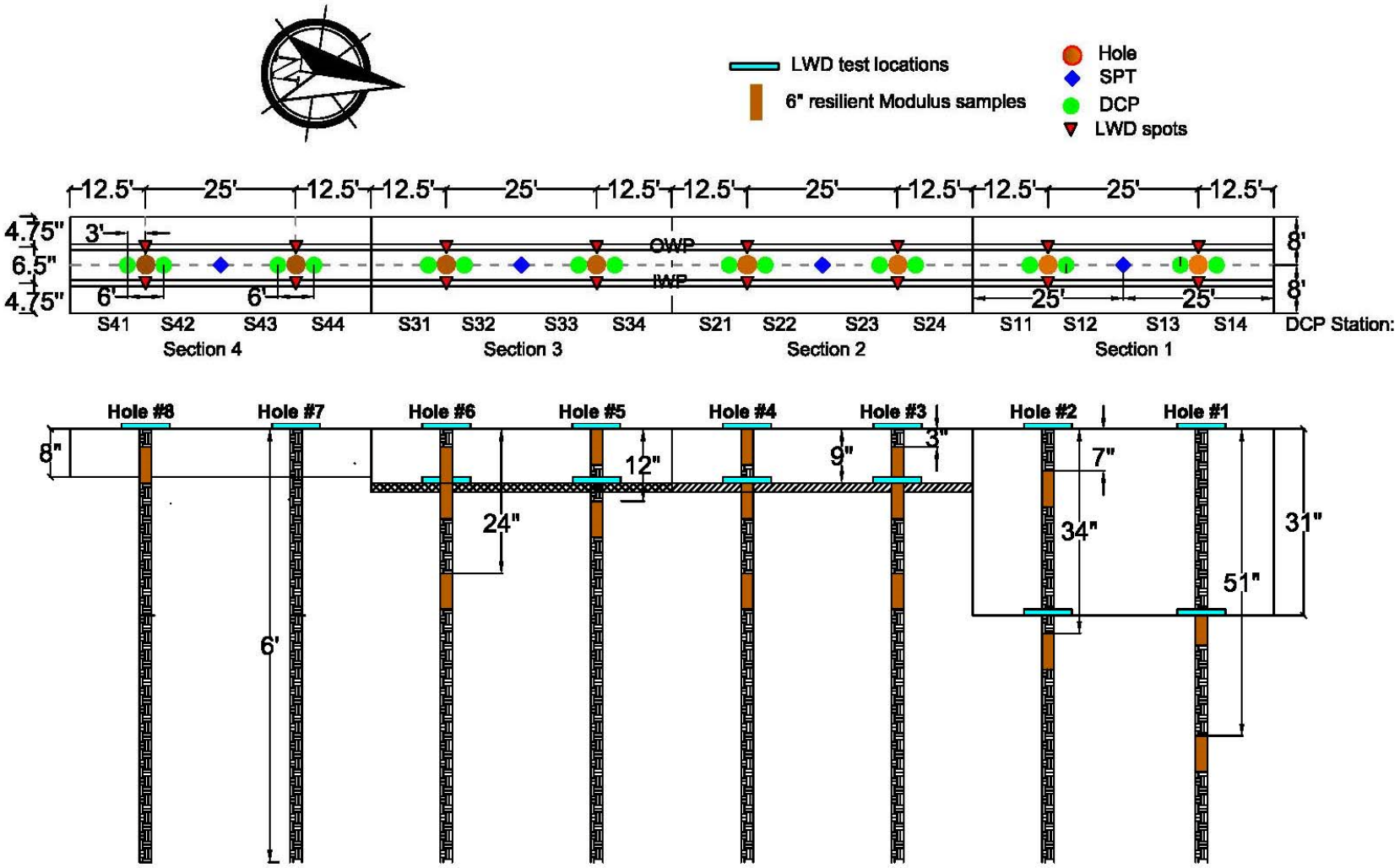

Figure 4-1. Location of Shelby tubes, resilient modulus specimens, and in-situ tests

4.2. Laboratory Testing

4.2.1 Material properties

Index property tests included specific gravity, grain size distribution, Atterberg limits and standard compaction, which were performed following ASTM D854, D2216, D4318 and D698, respectively, on the specimens retrieved from the Shelby tubes, select fill material and aggregate base course.

4.2.1.1 Subgrade soil

Index properties of the subgrade soil specimens are summarized in Table 4-1. Figure 4-2 shows the grain size distribution of the four different type subgrade soils encountered, as determined from index properties. According to the AASHTO engineering soil classification system (Unified Soil Classification System-USCS) the compacted fill subgrade soils are classified as A-4 (SM, ML, CL), and the natural Piedmont residual soil as A-7-5 (MH).. Based on the index properties test results, it was determined that the top 32 inches of soft low plasticity subgrade soil (A-4) was compacted fill, which was underlain by the natural stiff high plasticity Piedmont residual soil (A-7-5).

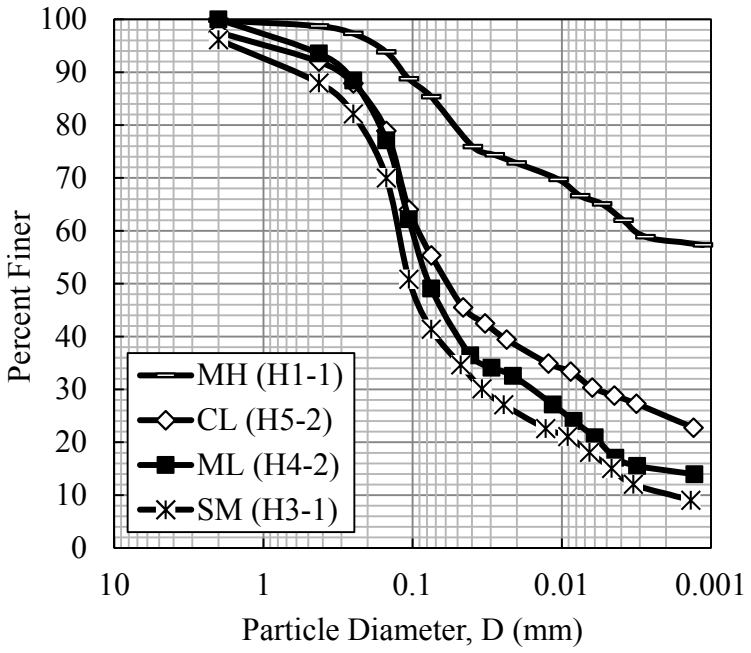

Figure 4-2. Grain size distribution of the subgrade materials.

Table 4-1. Index properties of the subgrade soil specimens

Section No.	*Hole No.*	*Depth*	*w (%)*	*γ (pcf)*	*e*	*Gs*	*LL*	*PI*	*P_{200} (%)*	*% Clay[1]*	*USCS.*	*AASHTO*
Section 1	H1	*30″-36″*	34	113	0.98	2.7	72	25	80	65	MH	A-7-5
		51″-57″	32	121	0.84	2.68	75	24	85	69	MH	A-7-5
	H2	*7″-13″*	14	125	0.51	2.64	15	4	41	15	SM	A-4a
		34″-40″	28	118	0.8	2.66	57	22	71	46	MH	A-7-5
Section 2	H3	*3″-9″*	17	120	0.61	2.64	20	3	49	18	SM	A-4a
		9″-15″	16	125	0.51	2.61	18	2	51	16	ML	A-4a
		24″-30″	19	121	0.63	2.63	17	5	50	28	SM	A-4a
	H4	*0″-6″*	22	124	0.63	2.60	20	3	54	19	ML	A-4a
		9″-15″	15	129	0.47	2.62	19	3	54	20	ML	A-4a
		24″-30″	21	117	0.74	2.63	17	4	51	25	ML	A-4a
Section 3	H5	*0″-6″*	13	130	0.46	2.61	21	2	51	20	ML	A-4a
		12″-18″	16	131	0.44	2.64	25	8	42	16	CL	A-4a
	H6	*3″-9″*	17	122	0.58	2.65	13	3	42	14	SM	A-4a
		9″-15″	21	125	0.59	2.61	19	4	48	19	ML	A-4a
		24″-30″	21	1120	0.7	2.63	18	5	40	17	SM	A-4a
Section 4	H8	*3″-9″*	16	125	0.52	2.61	19	2	54	14	ML	A-4

[1]Clay <5μm

4.2.1.2 Aggregate Base Course

As mentioned in Chapter 3, aggregate base course class IV, with specific gravity 2.7, was used in this project. Figure 4-3 shows the grain size distribution of ABC material. The index properties of the ABC material are presented in Table 4-2. Modified proctor compaction results, performed according to ASTM D1577, are presented in Figure 4-4. According to AASHTO engineering soil classification system (USCS) the ABC is classified as an A-1 (GW), a well-graded gravel with silt and sand. or .

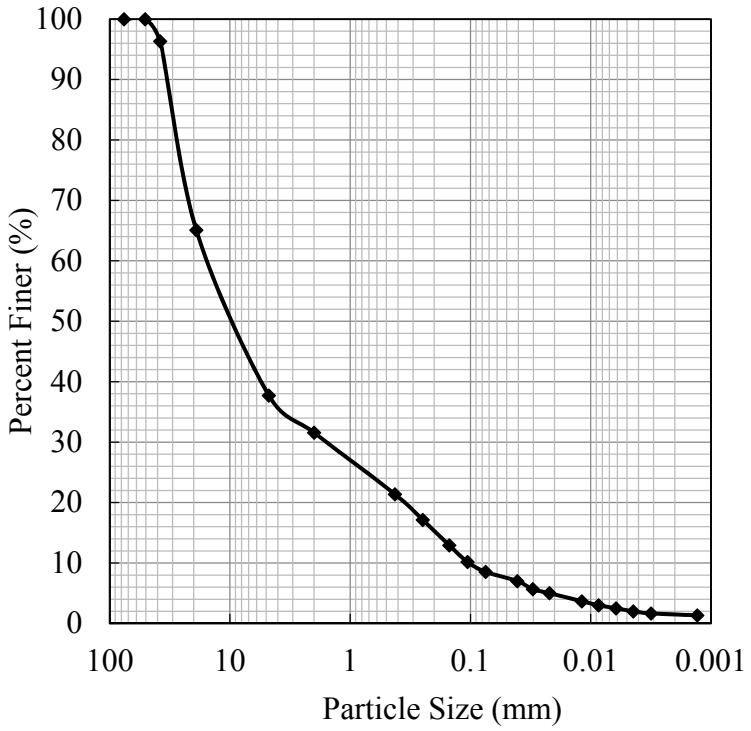

Figure 4-3. Grain size distribution of ABC

Table 4-2. Index properties of ABC material

Soil Sample	G.s.	Maximum dry unit weight (pcf)	Optimum water content	USCS	AASHTO
32	2.7	134	7.5	GW	A-1

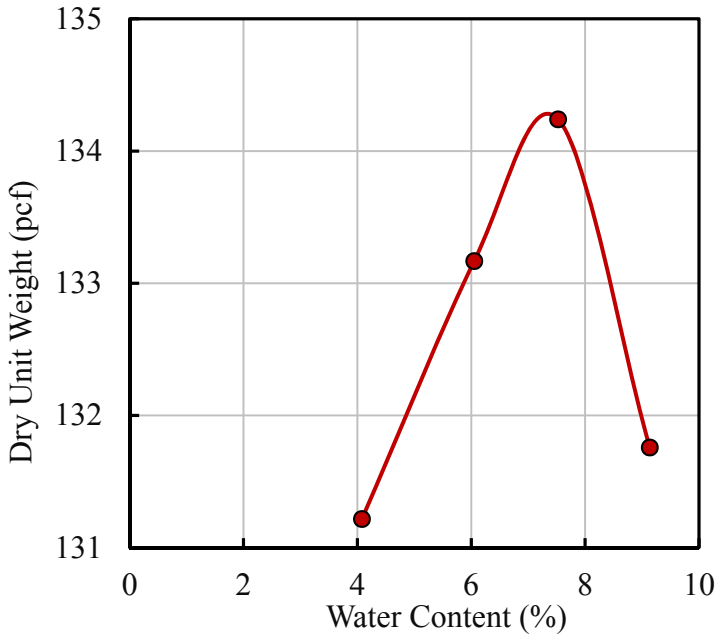

Figure 4-4. ABC modified proctor compaction results

4.2.1.3 Select Material

Test section 1 was stabilized by undercutting 32 inches of soft soil and backfilling with select fill material. The index properties and grain size distribution of the select material are summarized in Table 4-3 and Figure 4-5, respectively. The standard proctor test result are plotted in Figure 4-6. Based on the index properties, the select material was classified as A-4 and met the NCDOT specification for class II select material. According to USCS the select material is classified as a silty sand (SM)

Table 4-3. Index properties of select material

LL	PI	G_s	Maximum dry unit weight (pcf)	Optimum water content (%)	USCS	AASHTO
32	2	2.71	117	14.5	SM	A-4a

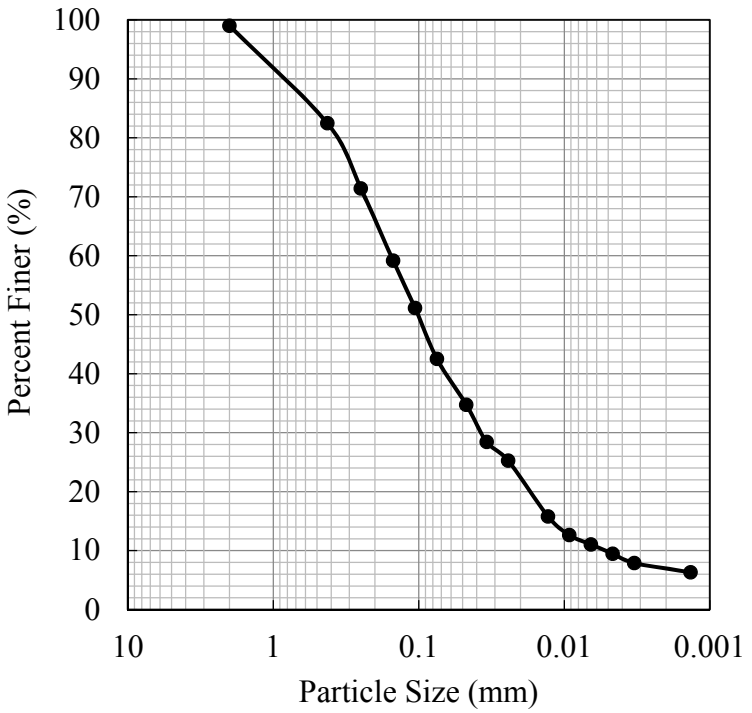

Figure 4-5. Grain size distribution of select material

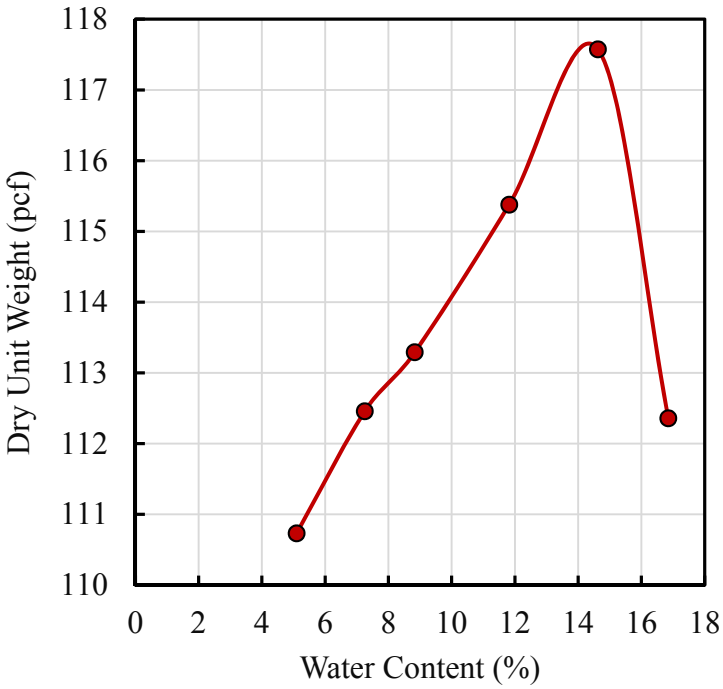

Figure 4-6. Select material standard proctor compaction results

4.2.2 Monotonic triaxial testing

Monotonic CU triaxial compression tests were also carried out on the undisturbed samples retrieved from the Shelby tubes, following ASTM 4767-04. The CU tests were performed on saturated specimens at effective confining pressures of 8 and 14.5 psi. The undrained shear strength parameters of the subgrade soils are summarized in Table 4-4. Figure 4-7(a) and (b) show the A-4 and A-7-5 specimens at the end of the CU triaxial test. It can be seen that A-4 specimens bulged at the failure point, while the shear band can be clearly seen in the stiff A-7-5 specimen. More details can be found in Appendix C.

Table 4-4. Shear strength parameters of the subgrade soil layers

Subgrade	Total Stress Parameters		Effective Stress Parameters	
	C (psi)	φ	C' (psi)	φ'
A4-a	15	4	2	25
A-7-5	10	13	3	25

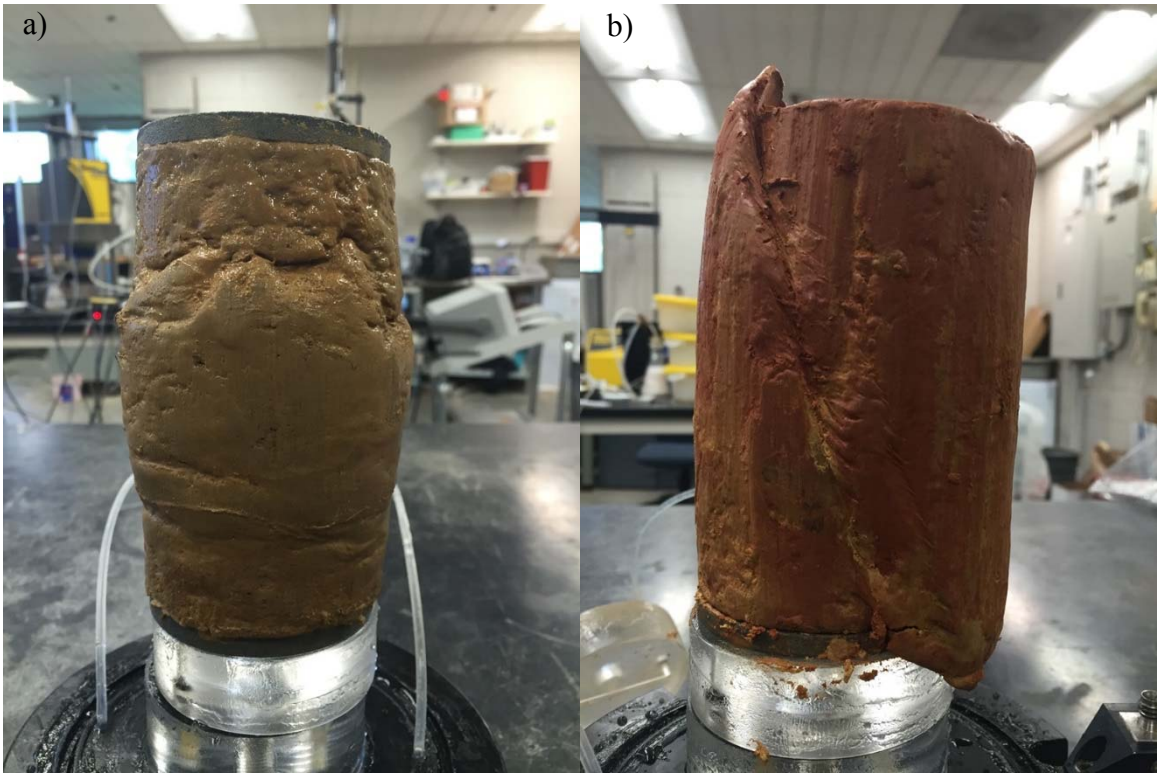

Figure 4-7. CU triaxial specimens at failure state a) A-4 soil & b) A-7-5 soil.

4.2.3 Resilient modulus test results

Resilient modulus tests were performed on sixteen 15.24-cm (6-in) long, undisturbed specimens retrieved from Shelby tubes, as shown in Figure 4-1, by following the AASHTO T-307 protocol. According to AASHTO T-307, the resilient modulus of cylindrical specimens is measured under the repeated deviatoric stress with 0.1 sec load duration and 0.9 sec resting time. As shown in Fig. 4-8, the deviatoric stress (σ_d) consists of the fixed contact stress ($\sigma_{Contact}: 0.1\sigma_d$) and the cyclic stress ($\sigma_{Cyclic}: 0.9\sigma_d$). The resilient modulus test begins by applying 1000 conditioning load cycles at 13.79 kPa (6 psi) confining pressure, followed by 15 stress combinations including five deviatoric stress levels 13.79, 27.58, 41.37, 55.16 and 68.95 kPa (2, 4, 6, 8 and 10 psi) at the three confining pressures of 41.37, 57.58 and 13.79 kPa (6, 4 and 2 psi). The resilient modulus is defined as the cyclic stress divided by the average resilient strain for the last 5 of the 100 applied load cycles at each stress state. The laboratory-measured resilient moduli were analyzed in the context of the NCHRP 1-28A (MEPDG) constitutive model. The model coefficients (k_1, k_2, and k_3) of all specimens, which were determined from curve fitting in Matlab, are presented in Table 4-5. Further details are presented in Appendix D.

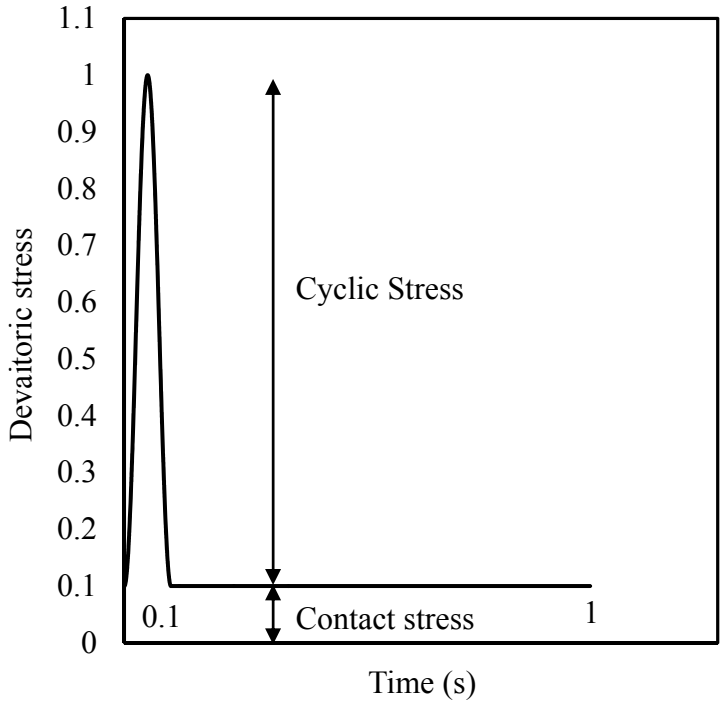

Figure 4-8. Resilient modulus test cyclic load example.

Table 4-5. Resilient modulus test results

Section No.	*Hole No.*	*Depth*	k_1	k_2	k_3	*R2*
Section 1	H1	*30"-36"*	1310	0.230	-1.04	0.97
		51"-57"	750	0.270	-0.62	0.99
	H2	*7"-13"*	634	0.882	-2.50	0.94
		34"-40"	1444	0.329	-2.44	0.99
Section 2	H3	*3"-9"*	513	0.970	-3.08	0.96
		9"-15"	593	0.874	-3.09	0.95
		24"-30"	488	0.897	-4.25	0.8
	H4	*0"-6"*	666	0.879	-3.28	0.94
		9"-15"	646	0.895	-2.44	0.97
		24"-30"	803	0.697	-3.86	0.96
Section 3	H5	*0"-6"*	680	0.910	-2.82	0.96
		12"-18"	897	0.897	-4.26	0.92
	H6	*3"-9"*	567	0.808	-2.11	0.96
		9"-15"	717	0.673	-4.39	0.86
		24"-30"	812	0.679	-4.57	0.95
Section 4	H8	*3"-9"*	555	0.924	-2.81	0.96

4.3 In-situ Testing

Light Weight Deflectometer (LWD), Dynamic Cone Penetrometer (DCP), and Standard Penetration (SPT) tests were performed at various stages of the full scale testing, along with laboratory tests, to collect data on the strength and modulus characteristics of the subgrade prior to and after roadway grading and full scale testing.

4.3.1 SPT test results

SPT tests, to a depth of 6ft below grade, were performed at the middle of each test section before excavation. As shown in Figure 4-9, the top 3 ft of the profile was composed of soft compacted soil with low N_{60}-values, underlain by stronger natural Piedmont residual soil.. It can be concluded that the soft A-4 soil layer is located at shallow depth in section 1, compared with the other sections, which is consistent with laboratory soil classification and index property tests results. A summary of the collected soil sample description and SPT tests results, along with calculated N_{60} values incorporating rod-length correction factors, are presented in Table 4-6.

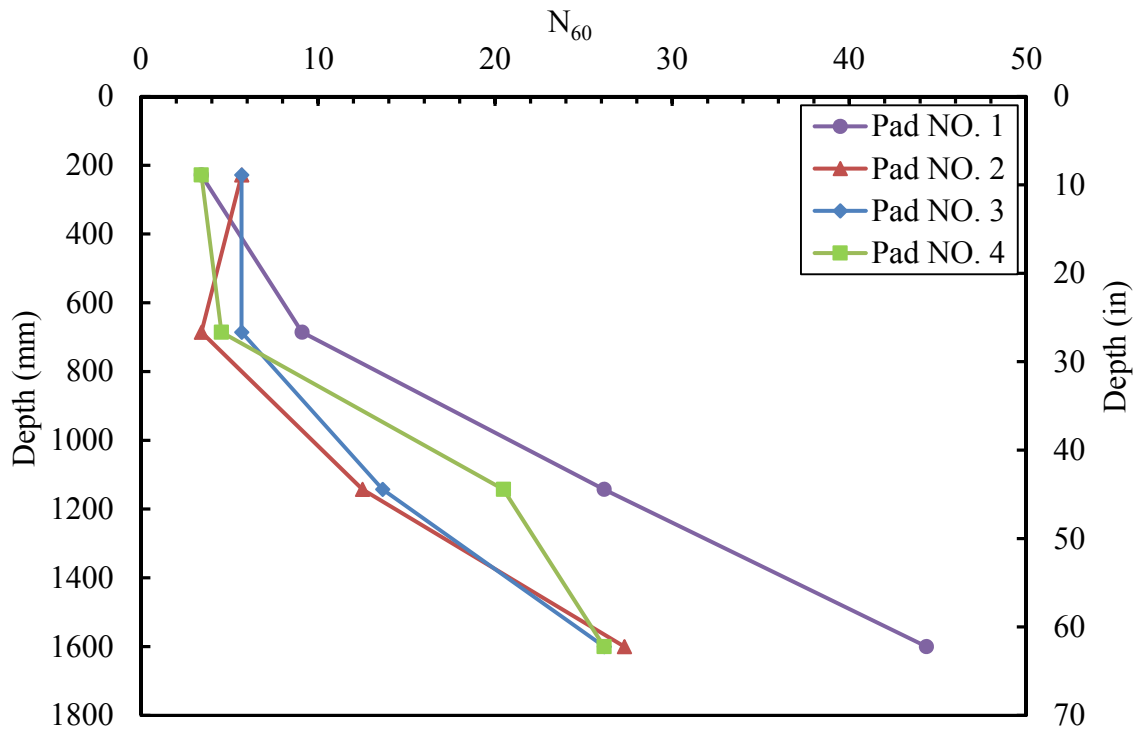

Figure 4-9. SPT test results

Table 4-6. SPT test results

Section	Depth		Description	Soil type	N	N_{60}
	From	To				
1	0	1.5	Loose, Tan to Brown	Silty Sand	3	3.4
	1.5	3	Medium Stiff, Tan to Brown	Silty Clay	8	9.1
	3	4.5	Very Stiff, Red to Brown	Silty Clay	23	26.2
	4.5	6	Hard, Red to Brown	Silty Clay	39	44.4
2	0	1.5	Loose, Tan to Brown	Silty Sand	5	5.7
	1.5	3	Soft, Tan to Brown	Sandy silt	3	3.4
	3	4.5	Stiff, Tan to Brown	Silty Clay	11	12.5
	4.5	6	Very Stiff, Red to Brown	Silty Clay	24	27.3
3	0	1.5	Medium Stiff, Tan to Brown	Sandy silt	5	5.7
	1.5	3	Medium Stiff, Tan to Brown	Silty Clay	5	5.7
	3	4.5	Stiff, Red to Brown	Silty Clay	12	13.6
	4.5	6	Very Stiff, Red to Brown	Silty Clay	23	26.2
4	0	1.5	Soft, Tan to Brown	Sandy silt	3	3.4
	1.5	3	Medium Stiff, Tan to Brown	Silty Clay	4	4.5
	3	4.5	Very Stiff, Red to Brown	Silty Clay	18	20.5
	4.5	6	Very Stiff, Red to Brown	Silty Clay	23	26.2

4.3.2 DCP tests measurements

As previously stated, DCP tests were performed during the project at different time steps. DCP tests were carried out at four locations in each test section, as shown in Figure 4-1, before and after excavation, and after traffic loading. To establish the interface between soil layers from DCP data, ASTM D6951 recommends to plot the cumulative blow counts vs penetration depth and find the intersection of tangent lines. From this plot, as shown in Figure 4-10, the thickness or respective layers can be found.

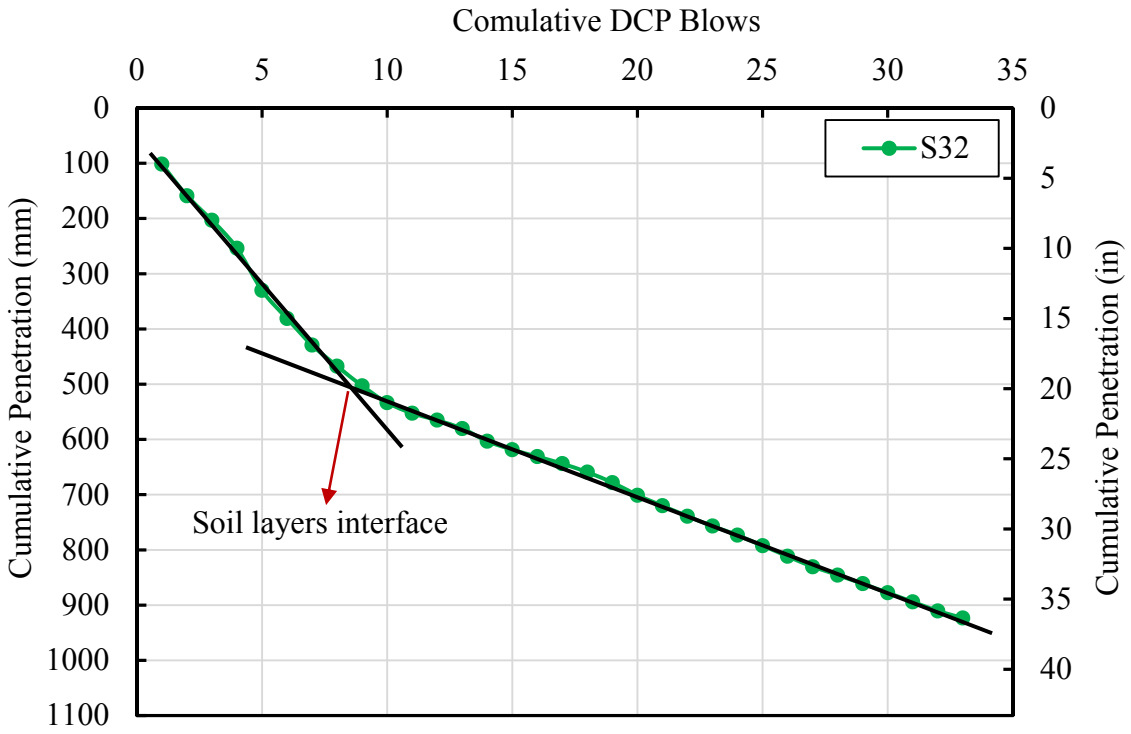

Figure 4-10. Soil layer interface determination by DCP data

After locating the interface of layers, the weighted average DCP Index of each soil layer was calculated using Eq. 4-1. By defining the DCPI of each soil layer, the CBR, resilient modulus and undrained shear strength can be estimated by inserting DCPI into the existing empirical correlations, as presented in Chapter 2.

$$DCPI_{wt.\,avg.} = \frac{1}{H}\sum_{i=1}^{N}(DCPI_i \times z_i) \qquad \text{Eq. (4-1)}$$

Which,

z = Depth of penetration per blow (mm/in)

H = Total depth of the soil layer (mm/in)

The DCP measurements are summarized in Tables 4-7 to 4-10.

Table 4-7. DCP test results prior to excavation.

Test Section	Station	Depth[1]	DCPI[2]	CBR[3]	Su[4]
1	S11	0~21	60	3	45
		21~34	25	8	107
	S12	0~6	33	6	82
		6~21	43	5	64
		21~35	18	18	143
	S13	0~25	48	4	57
		25~36	15	15	160
	S14	0~9	27	8	100
		9~22	16	15	158
		22~35	6	41	140
2	S21	0~9	37	5	73
		9~28	54	4	50
		29~32	16	14	155
	S22	0~12	126	1	20
		12~27	56	3	48
		27~31	17	13	148
	S23	0~8	35	6	79
		8~28	57	3	47
		28~35	37	5	73
	S24	0~28	57	3	47
		28~37	17	13	149
3	S31	0~1	51	4	53
		1~8	21	10	124
		8~26	43	5	64
		26~38	21	11	129
	S32	0~17	56	3	48
		17~34	18	13	147
	S33	0~4	43	5	64
		4~17	19	12	137
		17~28	40	5	69
		28~37	15	16	165
	S34	0~15	46	4	59
		15~25	28	8	97
		25~33	17	13	150

[1]Inches
[2]mm/blow
[3]Eq. (2-2)
[4]Eq. (2-4), kPa

Table 4-8. DCP test results after excavation.

Test Section	Station	Depth[1]	DCPI[2]	CBR[3]	Su[4]
1	S11	32~40	48	4	57
		40~52	16	14	158
		52~59	7	40	149
	S12	32~50	22	10	123
		50~58	8	33	187
	S13	32~50	20	11	132
		50~57	6	45	98
	S14	32~44	15	16	164
		44~54	10	25	198
2	S21	9~13	24	9	113
		13~39	60	3	45
		39~346	27	8	101
	S22	9~14	19	12	137
		14~38	55	4	49
		38~45	27	8	102
	S23	9~38	58	3	47
		38~45	25	9	109
	S24	9~17	22	10	123
		17~31	45	4	61
		31~44	20	11	132
3	S31	9~31	48	4	56
		31~45	25	9	108
	S32	9~30	47	4	59
		30~47	20	11	131
	S33	9~25	47	4	58
		25~47	23	10	119
	S34	9~31	48	4	57
		31~44	18	13	143

[1]Inches
[2]mm/blow
[3]Eq. (2-2)
[4]Eq. (2-4), kPa

Table 4-9. DCP test results prior to traffic loading.

Test Section	Station	Depth[1]	DCPI[2]	CBR[3,4]	Su[5,6]
1	S11	0~29	13	18	238
	S12	0~34	14	17	237
	S13	0~14	13	18	238
	S14	0~33	13	18	238
2	S21	0~6	4	56	341
		6~10	13	17	175
	S22	0~11	4	53	341
		11~14	14	17	173
	S23	0~7	4	55	341
		7~13	19	12	139
	S24	0~14	6	43	339
3	S31	0~7	6	43	338
		7~10	17	13	150
	S32	0~8	6	39	337
	S33	0~11	5	47	340
	S34	0~8	5	48	340
		8~10	14	16	171

[1]Inches
[2]mm/blow
[3,4]Eq. (2-2) for subgrade, Eq. (2-3) for ABC
[5,6]Eq. (2-4) for subgrade, Eq. (2-6) for ABC and select material, kPa

Table 4-10. DCP test results after traffic loading.

Test Section	Station	Depth[1]	DCPI[2]	CBR[3,4]	Su[5,6]
1	S11	0~24	8	31	251
		24~28	4	68	262
		28~32	20	11	220
	S12	0~17	12	19	270
		17~32	6	43	327
	S13	0~33	11	21	244
	S14	0~16	12	19	240
		16~30	6	41	256
2	S21	0~6	5	53	341
		6~12	13	18	178
		12~31	37	6	74
	S22	0~6	4	69	344
		6~10	12	21	189
		10~29	32	7	87
	S23	0~10	5	47	340
		10~28	36	6	77
		28~31	14	17	171
	S24	0~7	5	53	340
		7~23	25	9	110
		23~29	13	19	180
3	S31	0~3	5	53	341
		3~31	34	6	80
	S32	0~7	5	51	341
		7~21	34	6	81
	S33	0~9	4	74	345
		9~16	20	12	135
	S34	0~5	4	66	343
		5~31	30	7	92

[1]Inches
[2]mm/blow
[3,4]Eq. (2-2) for subgrade, Eq. (2-3) for ABC
[5,6]Eq. (2-4) for subgrade, Eq. (2-6) for ABC and select material, kPa

4.3.3 LWD tests measurements

Light weight deflectometer (LWD) tests were carried out at the different points in time, in order to monitor the variation of the subgrade and ABC modulus during the project duration. The LWD tests were performed at four locations in each test section, two on each wheel path, as shown in the Figure 4-11. The Prima 100 LWD device was used in this study. Since the effective zone of the LWD measurement has been estimated to be approximately 1~1.5D, where D= the diameter of LWD plate (Mooney and Miller, 2007), in order to minimize the effect of the stiffness of the underlying layers on the measured E_{LWD}, a plate diameter of 20 cm (8 inches) similar to the thickness of the ABC layer was used. E_{LWD} values were calculated by using Eq. 2-6 with a Poisson's ratio of 0.35 and shape factor of $\frac{\pi}{2}$ was selected for the MH soil, and 2 for the ML, SM, and CL soil, (Mooney and Miller, 2007; White et al., 2007). LWD tests were performed at four stages of the project, before and after the excavation, and prior to and after traffic loading. The results of the LWD tests are presented in the Tables 4-11 to 14.

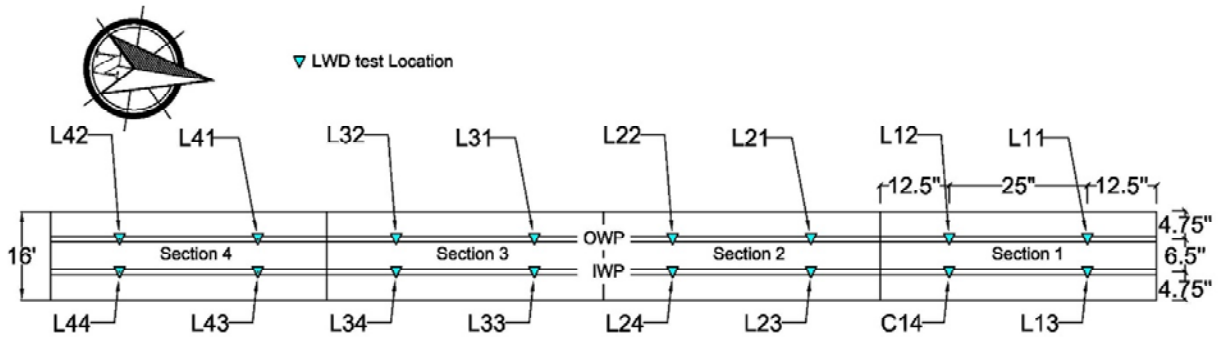

Figure 4-11. LWD test locations.

Table 4-11. LWD measurements prior to excavation.

Test Section	Station	E_{LWD} (MPa)	Std. (MPa)	C.V. %
1	L11	55	2.25	2.04
	L12	71	9.37	6.56
	L13			
	L14	56	3.08	2.76
2	L21	38	1.03	1.35
	L22	16	1.79	5.42
	L23	43	2.80	3.24
	L24	25	2.08	4.20
3	L31	31	2.95	4.70
	L32	40	3.03	3.79
	L33	64	11.12	8.67
	L34	25	4.56	9.23
4	L41	32	5.32	8.38
	L42			
	L43	38	3.05	4.00
	L44			

Table 4-12. LWD measurements after excavation.

Test Section	Station	E_{LWD} (MPa)	Std. (MPa)	C.V. %
1	L11	117	8.92	3.80
	L12	155	4.32	1.39
	L13	190	14.09	3.71
	L14	67	7.08	5.28
2	L21	33	2.40	3.65
	L22	32	2.93	4.58
	L23	71	3.38	2.38
	L24	28	1.72	3.08
3	L31	37	6.79	9.08
	L32	27	1.86	3.49
	L33	18	3.31	9.24
	L34	12	0.51	2.09

Table 4-13. LWD measurements prior to traffic loading.

Test Section	Station	E_{LWD} (MPa)	Std. (MPa)	C.V. %
1	L11	54	1.79	1.83
	L12	59	3.73	3.45
	L13	66	2.75	2.27
	L14	64	3.27	2.80
2	L21	178	7.52	2.31
	L22	115	4.97	2.35
	L23	80	9.96	6.79
	L24	176	4.46	1.38
3	L31	149	9.88	3.63
	L32	135	10.40	4.22
	L33	145	13.11	4.93
	L34	110	10.12	5.08

Table 4-14. LWD measurements after traffic loading.

Test Section	Station	E_{LWD} (MPa)	Std. (MPa)	C.V. %
1	L11	28	9.16	17.61
	L12	51	3.86	4.21
	L13	34	13.57	22.08
	L14	41	7.13	9.54
2	L21	60	20.15	18.50
	L22	105	14.27	7.48
	L23	63	14.90	13.10
	L24	53	17.68	18.38
3	L31	48	12.66	14.65
	L32	57	17.27	16.79
	L33	58	24.10	23.03
	L34	71	29.52	23.02

4.4 Summary

In summary, a series of the laboratory tests including basic index property, monotonic triaxial axial compression, and resilient modulus were performed on the undisturbed specimens, along in-situ tests included SPT, DCP, and LWD. Based on the basic index property tests results, the top 32 inches subgrade soil was determined as A-4 (SM, ML, CL); which is lied on the top of the natural Piedmont residual soil A-7-5 (MH). The monotonic triaxial axial compression CU tests were performed on the subgrade specimens. The resilient modulus tests were carried on sixteen undistributed specimens on their natural water content state. SPT test results confirmed the soil classification from index property tests, which indicated top 32 inches soft compacted fill soil. The in-situ DCP and LWD data before/after excavation and traffic loading were also presented.

CHAPTER 5: PROPOSED MODELS FOR PREDICTING RESILIENT MODULUS

As previously mentioned a series of the resilient modulus, DCP and LWD tests were performed in this project. The performance of the existing empirical models; which predict the resilient modulus from in-situ DCP and LWD data were examined by applying measured DCP, LWD and resilient modulus test data. In this chapter, two proposed models are presented that are capable of calculating the resilient modulus of subgrade soil by estimating the coefficients of MEPDG model (k_1, k_2, and k_3) from in-situ DCP and LWD data.

5.1 Proposed LWD Model

As stated before, subgrade modulus values were measured at the test site by Prima 100 LWD device (with 20 cm plate) following the ASTM E2583-07. The E_{LWD} was calculated using Eq. 2-6 and assuming a Poisson's ratio of 0.35. A shape factor of $\frac{\pi}{2}$ was selected for the MH soil, and 2 for the ML, SM, and CL soil, (Mooney and Miller 2007, White et al. 2007). The LWD tests were located about 2 m apart on the both sides of the boreholes, from which samples for resilient modulus testing were collected. Hence for comparison sake, the average of two E_{LWD} values was used to estimate the Mr from LWD. The calculated Mr value was compared to the laboratory-evaluated resilient modulus for samples retrieved from the corresponding borehole within the LWD effective zone, as summarized in Table 5-1.

As previously mentioned, the assumption of Poisson's ratio and shape factor can lead to various estimates of E_{LWD}. In order to overcome the ambiguities with which values to use, the ratio of the applied stress to surface deflection, $\frac{\sigma}{\delta}$, from LWD direct measurements; which is representative of soil layer elasticity, is directly used herein in the proposed model development, instead of computing the E_{LWD} by Eq. 2-6. The applied stress to surface deformation ratios from the LWD measurements are summarized in Table 5-1 and are shown associated with the Sample Number upon which the subsequent resilient modulus tests were performed.

Table 5-1. Summary of LWD Measurements and Mr Model Parameters

Soil Classification	Sample No.	E_{LWD} [a]	*Std.* MPa	C_v%	$\frac{\sigma}{\delta}$ [b,c]	k_1	k_2	k_3	R^2
MH (A-7-5)	H1-1	154	8.92	3.8	0.87	1310	0.230	-1.04	0.96
	H2-2	111	4.32	1.4	0.63	1440	0.329	-2.44	0.99
SM (A-4a)	H6-1	32	3.03	3.8	0.18	567	0.808	-2.11	0.96
	H3-1	41	1.03	1.3	0.23	513	0.970	-3.08	0.96
	H2-1	64	3.07	2.7	0.36	634	0.882	-2.50	0.94
ML(A-4a)	H5-1	48	2.94	4.7	0.27	680	0.910	-2.82	0.96
	H4-1	21	2.07	4.2	0.12	666	0.879	-3.28	0.94
	H8-1	35	3.05	4.0	0.20	555	0.925	-2.82	0.96
	H4-2	30	1.72	3.08	0.17	646	0.896	-2.44	0.97
	H6-2	20	0.51	2.1	0.11	717	0.673	-4.39	0.86
	H3-2	56	2.40	3.6	0.32	593	0.874	-3.09	0.95
CL(A-4a)	H5-2	20	3.31	9.2	0.11	897	0.897	-4.26	0.92

[a] $E_{LWD}(MPa)$

[b] $\sigma(kPa)$

[c] $\delta(\mu m)$

5.1.1 Evaluating existing LWD models

There are few empirical correlations to approximate the Mr of subgrade soil from LWD measurements. Although a main advantage of these models is that they can capture actual moisture and density conditions of the soil layer, they are mostly limited to one specific stress state. As mentioned in chapter 2, White et al. (2007) and Mohammad et al (2008) proposed the empirical models, to predict resilient modulus of subgrade soil from E_{LWD}.

The performance of the White et al. (2007) and Mohammad et al. (2010) correlations in estimating laboratory-measured M_r values are both shown in Figure 5-1. It can be seen that both correlations have generally overpredicted the measured values; however the Mohammad et al. correlation underestimates the Mr of the more highly plastic soils.

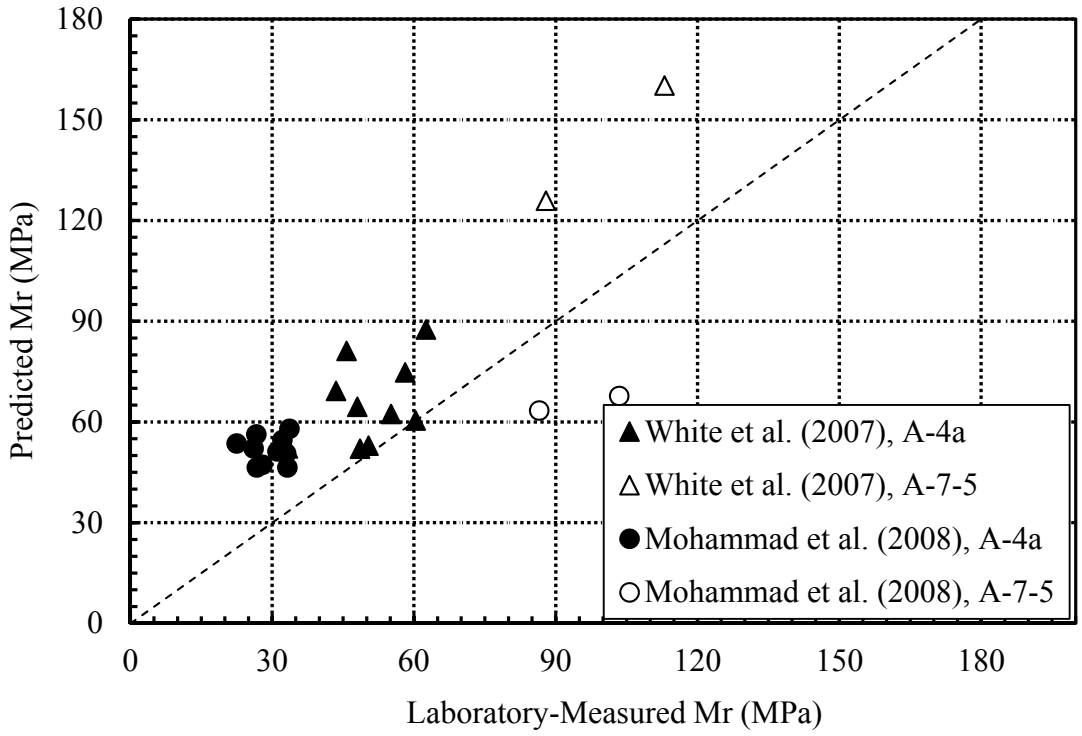

Figure 5-1, Laboratory-measured vs predicted Mr from existing models

5.1.2 Development of LWD correlation

As previously noted, the existing models for subgrade Mr determination from LWD data are limited to a specific stress level. A change in pavement structure layer thickness, axial load and tire pressure can lead to changes in stresses within the layers. In order to overcome this restriction and eliminate uncertainties associated with selecting appropriate Poison's ratio and shape factor values, the ratio of applied stress to surface deflection as measured during LWD testing was used. The coefficients of the MEPDG model are functionally related to the elastic modulus (k1), stiffness hardening (k2) and strain softening (k3) behavior of the soil (Yau and Quintus, 2002). Accordingly, the proposed model was developed to correlate k1, k2 and k3 to the ratio of obtained from LWD measurements, with the advantage of having the ability to estimate Mr. at other stress levels once these parameters are defined. The new model was developed from regression analyses on the laboratory and field measurement data from the cohesive (A-7-5) and cohesionless (A-4a) soils

Multilinear regression analyses was performed on three quarters of the data set to develop a model to indirectly calculate resilient modulus at any stress level from LWD data through estimating the MEPDG formula coefficients. The proposed correlation is presented in Eq. 5-1, with the definition of constants presented in Table 5-2. The analyses results illustrated in Figure 5-2 show that the proposed model is able to compute the laboratory-measured Mr with a coefficient of determination (R^2)= 0.83.

$$k_i = C_1 + C_2(\frac{\sigma}{\delta}) \qquad \text{Eq. (5-2)}$$

$i: 1, 2, 3$

Table 5-2. Constant Coefficients of Developed Model

	C_1	C_2
k_1	480	1040
k_2	1.0	-0.9
k_3	-3.7	2.8

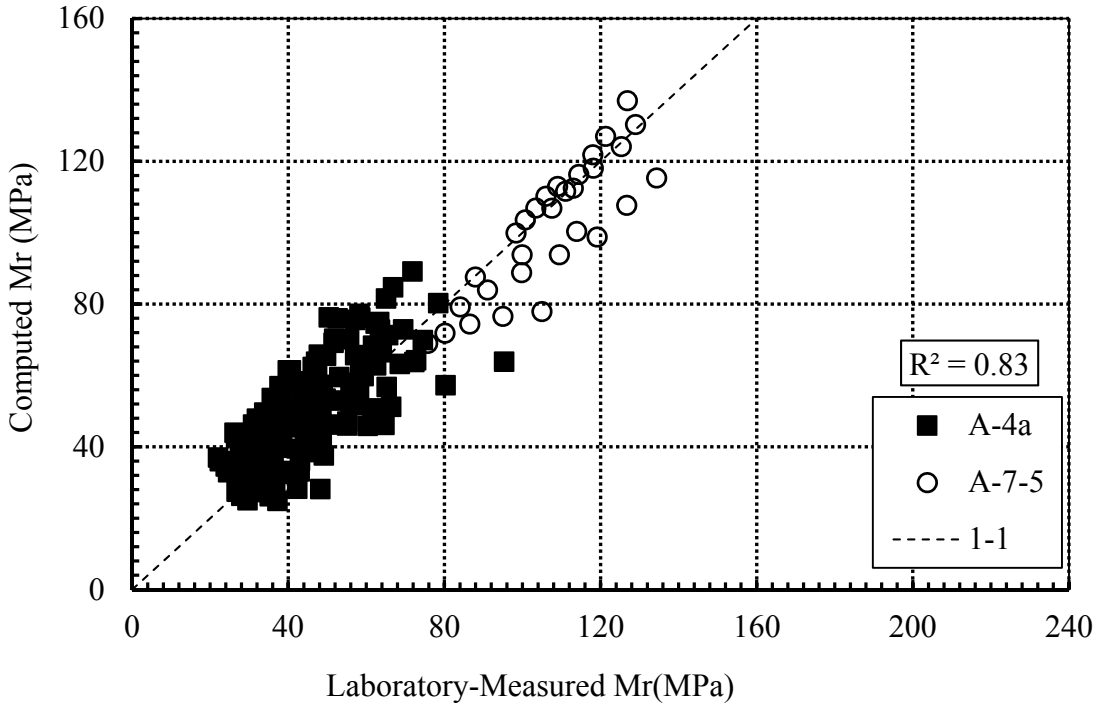

Figure 5-2, Laboratory-measured vs computed Mr prediction

5.1.3 Model validation

Figure 5-3 shows laboratory-measured vs model-computed resilient modulus values using the remaining quarter of the data set which was not used in the initial statistical correlations. The best-fit line for the data plotted shows that the proposed model slightly underestimates resilient modulus by 7% with a coefficient of determination of 0.83. The performance of the proposed model was also evaluated by utilizing data available from two other studies by White et al. (2007) and Mohammad et al. (2008). Data from White et al. (2007) included LWD measurements as well as laboratory-measured Mr data for A-6 (CL), sandy lean clay; and A-1-b (SP) soil, poorly graded sand with silt and gravel. Mohammad et al. (2007) presented LWD and Mr measurements for A-4(CL-ML) and A-6 (CL-ML) soils. In order to be able to utilize this data from the literature, the ratio of values were back calculated using Equation 3. The parameters utilized in the back calculation were Poisson's ratio of 0.35 and 0.4, for White et al. (2007) and Mohammad et al. (2008), respectively, and shape factors of for cohesive soils and 2 for cohesionless soils, as originally reported by the authors. As shown in Figure 10, the proposed model underestimates laboratory-measured Mr by 11% with a coefficient of determination of 0.96.

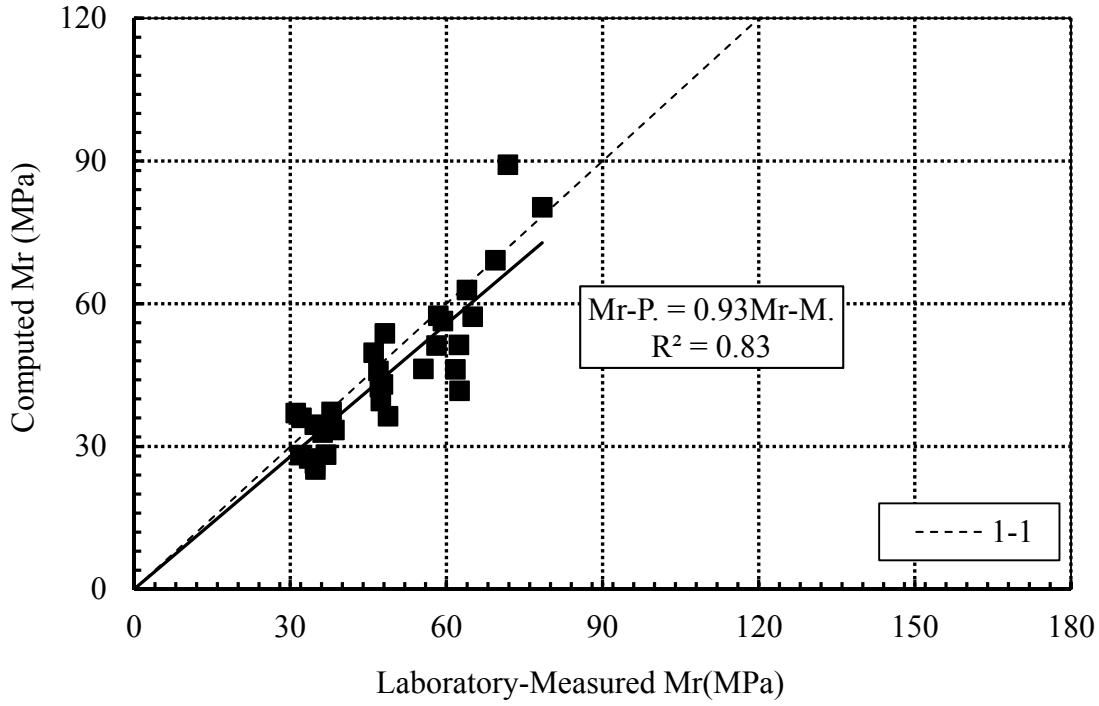

Figure 5-3, Laboratory-measured vs predicted Mr for one quarter of data set.

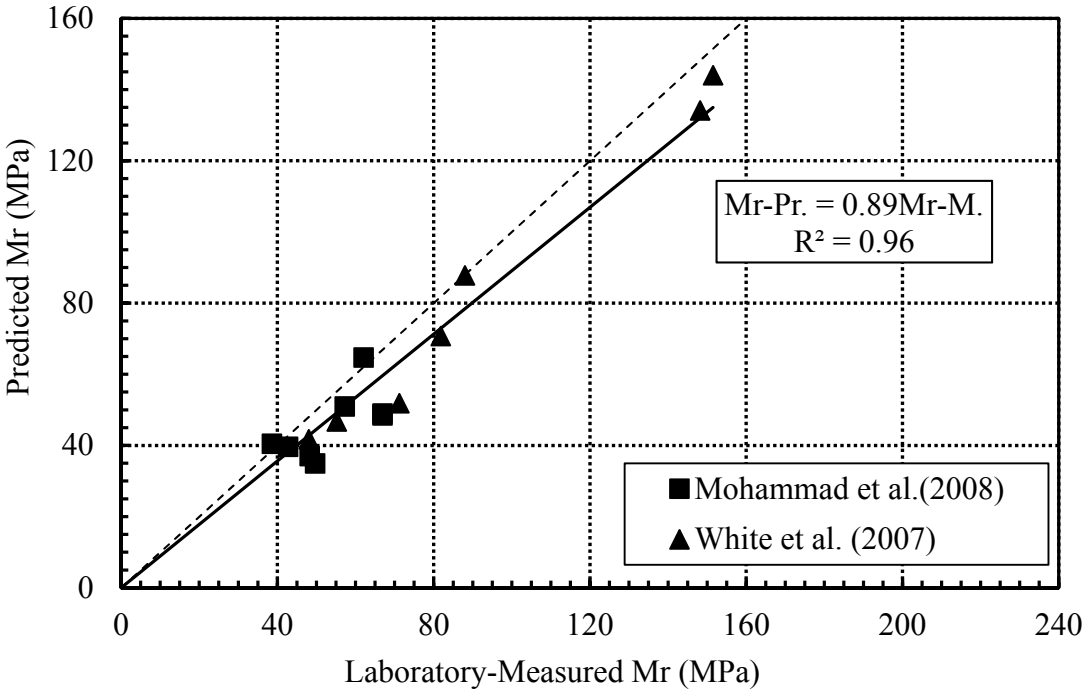

Figure 5-4, Laboratory-measured vs predicted Mr from other studies.

5.2 Proposed DCP Model

The DCP tests were performed at the four locations on the centerline of each test section, as shown in Fig. 4-1. The DCPI values, corresponding to the location of resilient modulus specimens and the MEPDG coefficients (k_1, k_2, and k_3), calculated from Mr. laboratory results, are summarized in Table 5-3.

Table 5-3. DCP measurement and resilient modulus model parameters

Classification	Sample Number	DCPI[a]	k_1	k_2	k_3	R^2
SM A-4a	H2-1	52	634	0.882	-2.50	0.94
	H3-1	46	513	0.970	-3.08	0.96
	H3-3	57	488	0.897	-4.25	0.86
	H4-3	55	803	0.698	-3.86	0.96
	H6-1	39	567	0.808	-2.11	0.96
	H6-3	30	812	0.679	-4.58	0.95
ML (A-4a)	H3-2	57	593	0.874	-3.09	0.95
	H4-1	82	666	0.879	-3.28	0.94
	H4-2	55	646	0.895	-2.44	0.97
	H5-1	44	680	0.910	-2.82	0.96
	H6-2	49	717	0.673	-4.39	0.86
	H8-1	46	554	0.924	-2.82	0.96

[a] mm/blow

5.2.1 Applicability of previous DCP models

The laboratory-measured M_r and DCP data were implemented in the existing models, presented in chapter 2, Table 2-1, to evaluate their performance in resilient modulus prediction from in-situ DCP measurements. As shown in Figure 5-5, existing models have generally over-predicted the resilient modulus, except Mohammad et al.'s correlation which underestimates the resilient modulus. The inconsistency in predicting the measured Mr values might be attributed to the fact that these correlations are empirical in nature, and they are most applicable to soil types similar to those for which the models were developed.

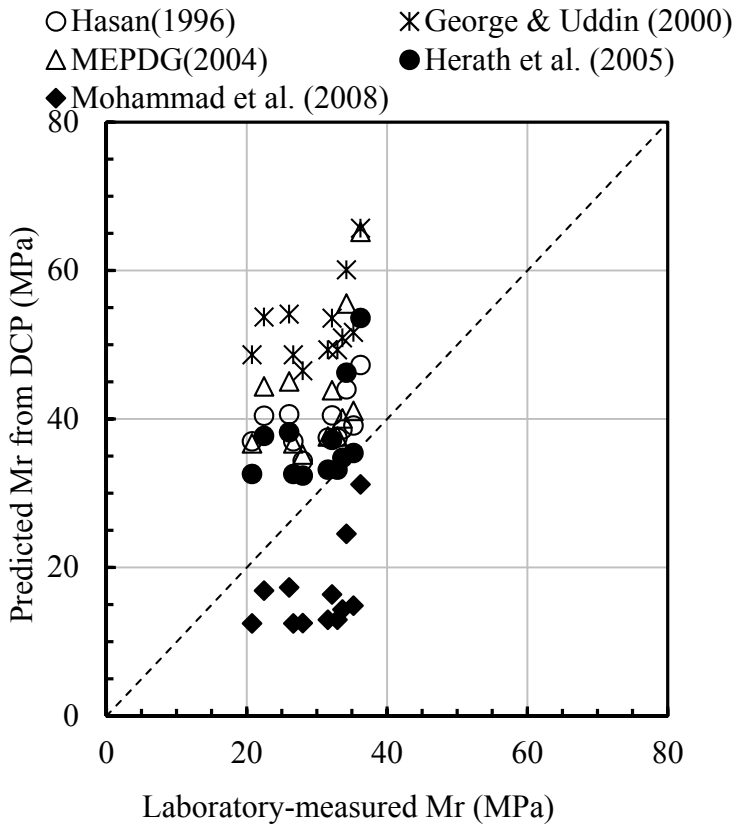

Figure 5-5. Laboratory-measured vs predicted vs Mr from existing direct DCP models.

5.2.2 Proposed of DCP correlation

Extensive statistical analyses were performed to develop an approach in the resilient modulus prediction from in situ testing DCP data. As noted above, in the MEPDG model, Mr is linearly influenced by k1, while the exponents k2 and k3 define the rate of increase and decrease, respectively, of stiffness hardening and soil softening (Yau and Quintus, 2002) with respect to the confining and deviatoric stresses

Multilinear statistical analyses were performed to develop an approach to calculate the resilient modulus by predicting k1, k2, and k3 from the insitu DCP test data. The multilinear regression analyses were performed on three quarters of the data set to develop a model that indirectly computes the resilient modulus at any desired stress state.

The proposed model is presented in Eq. 5-3, with the model constants presented in Table 5-4. As shown in Figure 5-6, the calculated Mr values by the proposed model and laboratory-measured resilient modulus are correlated with a coefficient of determination, R2, equal to 0.70.

$$k_i = C_1 + C_2 Ln(DCPI), \quad i:1,2,3 \qquad \text{Eq. (5-3)}$$

Table 5-4, model coefficients.

Coefficients	C_1	C_2
k_1	2310 (911)[1]	-377
k_2	-0.3 (0.7)[1]	0.3
k_3	-10 (-4.5)[1]	1.7

[1] English Unit

SI Unit: DCPI: mm/blow,

English Unit: DCPI: in/blow,

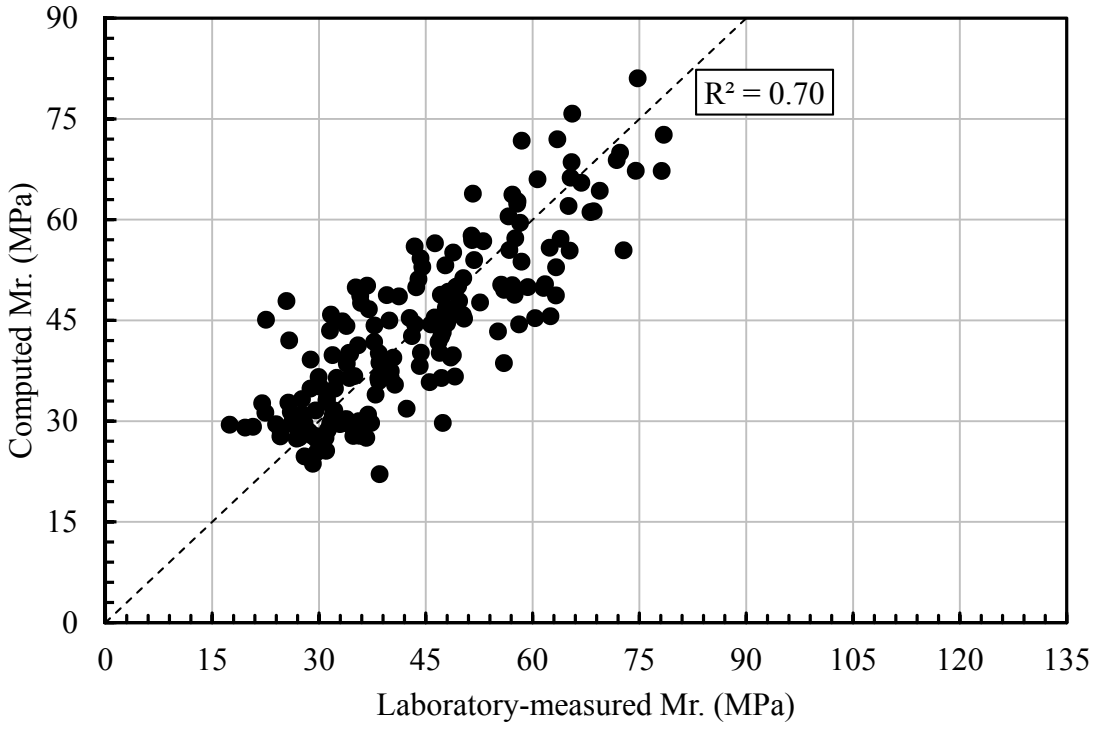

Figure 5-6. Laboratory-measured vs calculated Mr by the proposed model.

5.2.3 Proposed model validation

The validity of the proposed model was examined using the quarter of the data set which was not used in the statistical analyses and was selected arbitrarily, as well as additional data from the literature. The performance of the proposed model in predicting the resilient modulus of the quarter of the data is shown in Figure 5-7. The line of equality is added for clarity. It can be seen that the proposed model slightly underestimate the resilient modulus by 4% and the data are correlated with an R2 = 0.73.

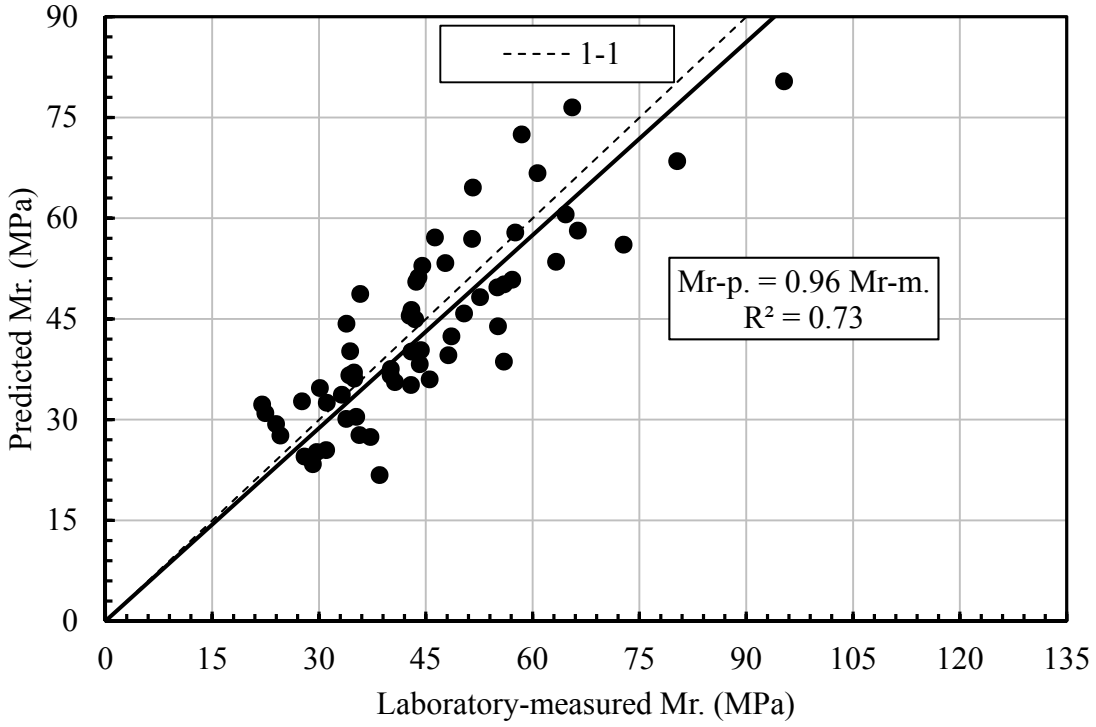

Figure 5-7. Laboratory-measured vs predicted M_r by the proposed model for the quarter of the data set.

The data set from Cowell et al. (2012) was also used to test the proposed model. The subgrade soil for this project consisted of low plasticity SM and SC (A-4). The data set by Cowell et al. (2012) included Mr values from tests on undisturbed specimens collected from the Coastal Plain of North Carolina, and *insitu* DCP measurements, summarized in Table 5-5. As shown in Fig. 5-8, the predicted Mr by the proposed model show reasonably good agreement with the laboratory-measured Mr values.

The performance of the proposed model was also investigated through the use of data presented by Mohammad et al. (2007, 2008). The reported data include laboratory and field DCP measurements, summarized in Table 5-5, and laboratory Mr test data on the low plasticity soil specimens tested at a confining pressure of 13.8 kPa (2 psi) and deviatoric stress of 41.4 kPa (6 psi).

The data plotted in Fig. 5-8 shows that the proposed model underestimates Mr of this data set by 8% with an R^2 of 0.53. By comparing the performance of the proposed model to that of existing Mr predicting correlations, Figure 5-5, it can be seen that the proposed model provides significantly improved predictive capability, with values slightly less than laboratory-measured values and with a higher coefficient of determination.

Table 5-5. DCP data in the literature with corresponding predicted coefficients by proposed model

Authors	Sample ID	DCPI(mm/blow)	k_1	k_2	k_3
Cowell et al. (2012)	ST7	24	933	0.682	-4.62
	ST6	17	1063	0.578	-5.20
	ST5	36	780	0.804	-3.94
	ST4	77	494	0.995	-2.66
	ST3	37	770	0.813	-3.89
	ST2	65	558	0.983	-2.94
Mohammad et al. (2007)	Clayey silt-1	26.1	902	0.707	-4.48
	Clayey silt-2	18.8	1025	0.609	-5.04
	Clayey silt-3	27	889	0.718	-4.42
	Clayey silt (ALF)	29	862	0.739	-4.30
	LA-182	36	780	0.804	-3.94
	LA-334C(2)	18.2	1037	0.599	-5.09
	LA-334C(5)	19.3	1015	0.616	-4.99
	LA-334C(8)	18.6	1029	0.605	-5.05

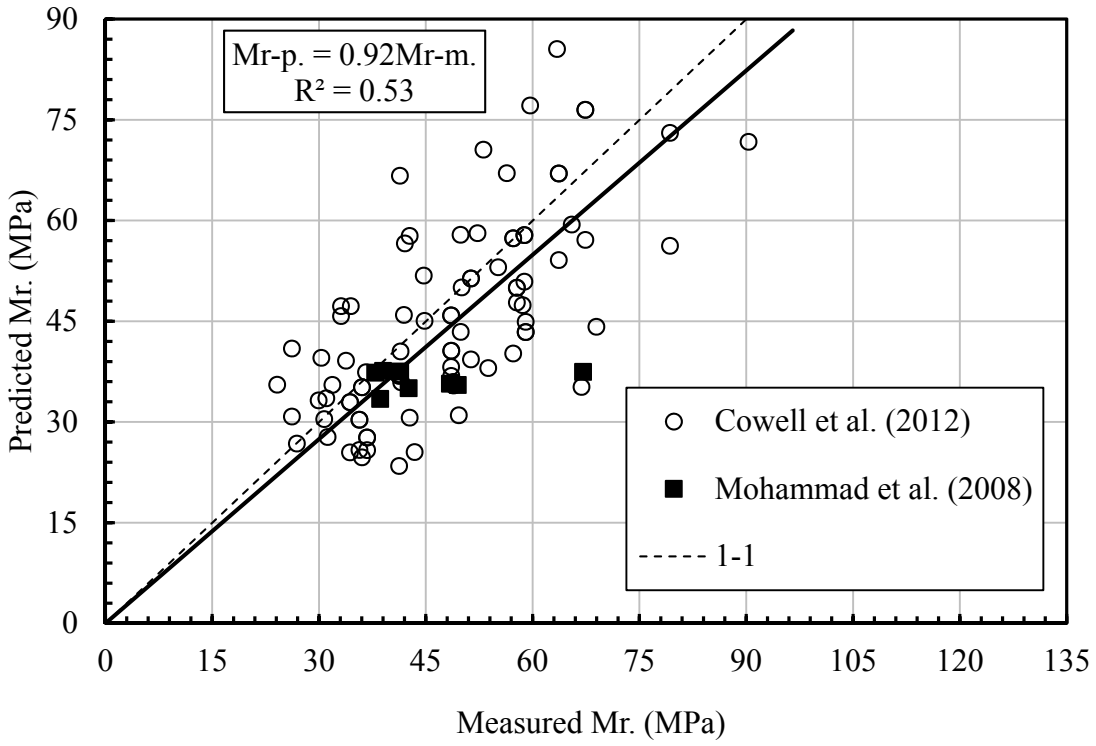

Figure 5-8. Laboratory-measured vs predicted Mr by the proposed model for data presented in the literature.

5.3 Summary

In summary, Good agreement was obtained between calculated Mr values from the proposed models and the laboratory-measured resilient modulus data. Examination of the performance of the proposed model with a quarter of the data set which was not included in the statistical analyses, indicated that, on average, the proposed model slightly underestimated the Mr. Predicted Mr values by the proposed model were seen to be in reasonably good agreement with the laboratory-measured Mr presented in the literature, however with a rather lower coefficient of determination. The evaluation of existing models which directly estimate the Mr of soils from the DCP and LWD measurements showed that they overestimated measured Mr values. In addition, the validity of these models only at one determined stress level limits their applicability to one particular pavement structure. The assessment of existing empirical models that predict the universal constitutive model fitting coefficients from basic physical properties of soils, yielded poor predictions of Mr for the soils tested in this study. The proposed model is capable of

predicting the resilient modulus of low plasticity soils SM, ML, and SC (A-4a and A-4), with PI<5, and 40%<P_{200}<55%; at any stress state.

CHAPTER 6: ASSESSMENT OF UNDERCUT CRITERIA

As previously stated, investigating the performance of the NCDOT undercut criteria and that proposed by Borden et al. (2010) is one of the major objectives of this study. The applicability of the undercut criteria by Borden et al. (2010) was examined by applying the measured DCP data presented in Chapter 4 to estimate the subgrade properties before and after stabilization. The performance of the subgrade under the traffic loading is then used to demonstrate the applicability of the undercut criteria.

6.1 NCDOT Undercut Criteria

Prior to field construction, a series of DCP tests was carried out to assess the need for site improvement. Obtained DCP data were plotted as cumulative penetration resistance as a function of number of blows, as shown in Figures 6-1, 6-2 and 6-3, and compared to the NCDOT's cut-off value of 38 mm/blow, indicating the need for undercutting the weak subgrade soil and replacement with select fill. The NCDOT undercut criteria is specified by the shaded triangle shown in each of the three figures. The data indicated that sections 1, 2, and 3 needed improvement to a varying degree to different depths.

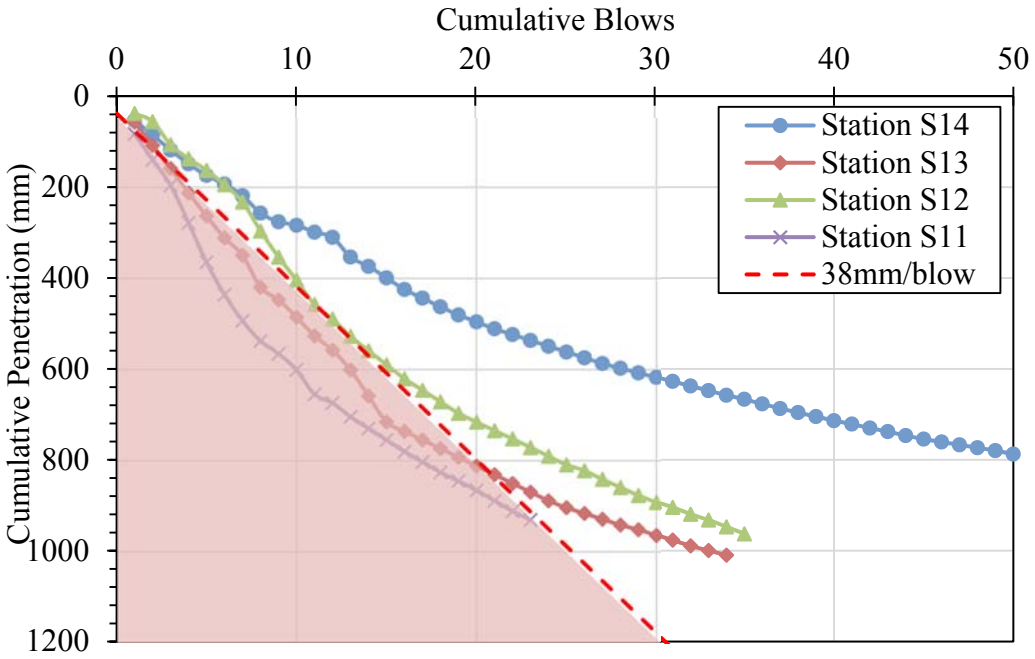

Figure 6-1. NCDOT's undercut criteria on section 1

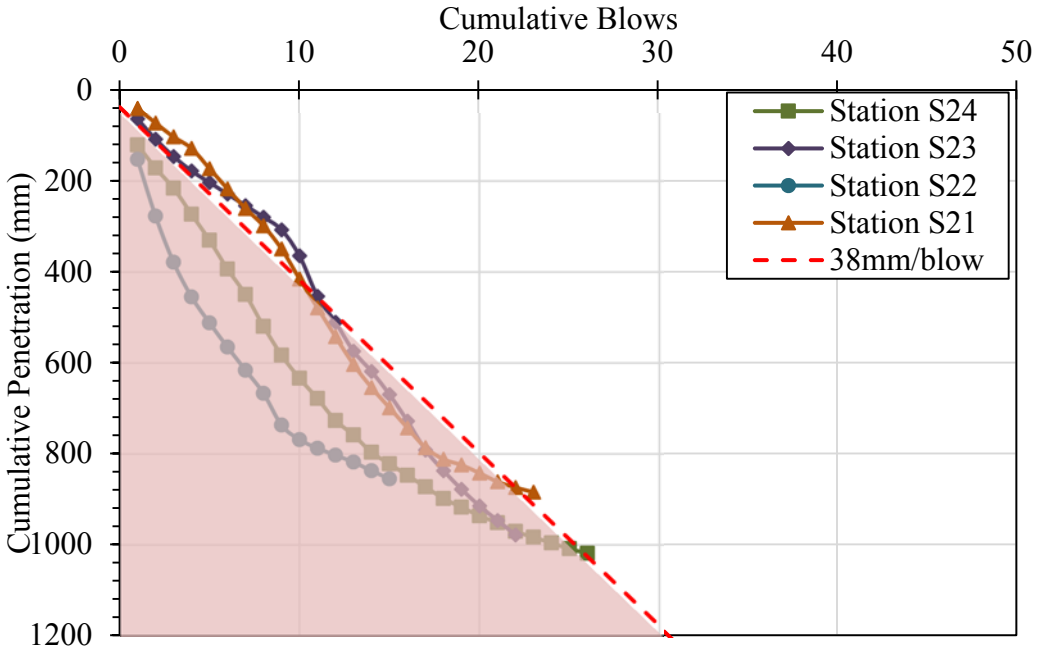

Figure 6-2. NCDOT's undercut criteria on section 2

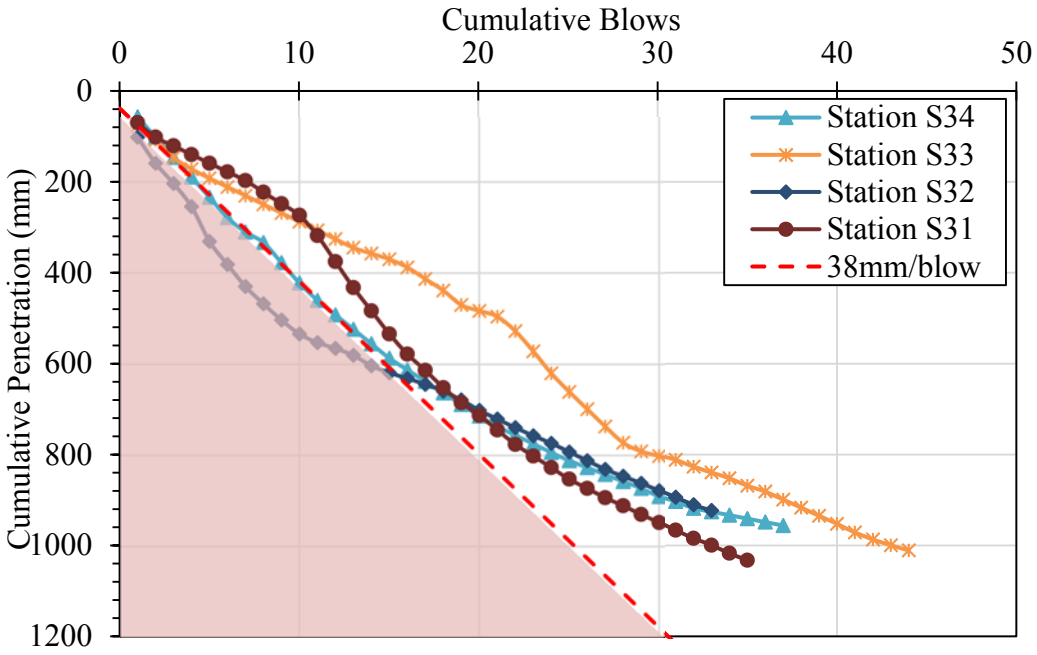

Figure 6-3. NCDOT's undercut criteria on section 3

6.2 Undercut Criteria by Borden et al. (2010)

Borden et al. (2010) proposed criteria indicating the need for undercut based on the results of prototype laboratory scale testing and extensive numerical analyses. Plain strain and axisymmetric numerical models were used to evaluate effect of the stiffness of a deep layer on pumping and the shear strength properties of shallow layers on surface rutting. The undercut criteria proposed by Borden et al. (2010) was based on the acceptable rut of less than 1" and acceptable performance capacity ratio equal to 1.5, where the performance capacity ratio was defined as:

$$\xi = \frac{Performance\ Capacity}{70\,psi}$$

The performance capacity was defined as the pressure corresponding to the asymptotic value of the pressure-deformation curve under wheel loading. Two undercut criteria charts were proposed, one for axisymmetric loading and the second for the plane strain condition, simulating the conditions of local bearing capacity failure, and deep layer pumping, respectively. The normalized settlement at the center of the loaded area is estimated by Eq. 6-1 for axisymmetric loading condition. More details can be found in the final report by Borden et al. (2010).

$$(\frac{\delta}{B}) = \{-2.13\times10^{-6} + 3.61(\frac{E}{p_a})^{-1}\} + (0.085 + 1.32\,e^{-0.25\phi})(\frac{E}{p_a})^{-1}(\frac{C}{p_a})^{0.22-7.75e^{-0.046\phi}} \quad \text{Eq. (6-1)}$$

6.2.1 Evaluation of undercut criteria

The proposed undercut criteria was utilized to assess the need for site improvement, as well as performance of the stabilized materials. To do so, the laboratory and in-situ measured shear strength and stiffness parameters of subgrade and stabilized materials are imposed to the proposed undercut criteria.

6.2.1.1 Undercut criteria results - subgrade

Laboratory resilient modulus results and measured DCP data were utilized to determine subgrade soil stiffness and shear strength properties. As previously mentioned, the resilient modulus value depends on both confining and deviatoric stress. Hence the resilient modulus value at the

confining pressure of 2 psi and deviatoric stress of 6 psi was selected as a representative Mr value for the subgrade (Mohammad et al., 2008; Rahim, 2004; Asphalt Institute, 1989). The undrained shear strength of subgrade was calculated by using Danistan and Vipulanandan (2009) and Coonse's proposed equations, as expressed in Eqs. 6-2 and 6-3 and presented in Table 6-1:

$$S_u(\text{kPa}) = 0.282 \times \text{CBR}^2 + 14.97 \times \text{CBR} \qquad \text{Eq. (6-2)}$$

$$Log(CBR) = 2.53 - 1.14 \times \log(DCPI) \qquad \text{Eq. (6-3)}$$

The subgrade soil undrained shear strength (s_u) and Modulus values, presented in Table 6-1, were used as inputs to Eq. 6-1 assuming the friction angle as zero. The resulting values of δ/B are presented in Table 6-1 and plotted in Figure 6-4. Based on the acceptance line in the chart (ξ =1.5), the unstabilized subgrade soils were identified as unstable. In this case, the proposed criteria by Borden et al. (2010) is in a good agreement with the NCDOT's criteria of the need for undercut for cases with DCPI > 38 mm/blow.

Table 6-1. Subgrade soil properties

Section	Station	Avg. DCPI	Undrained Shear Strength		Resilient Modulus		$\frac{\delta}{B}$
		mm/blow	s_u[1] (kPa)	s_u/Pa	Mr[2] (MPa)	Mr/Pa	
1	S14	21	123.9	1.24	103	1034	0.004
	S13	48	57.4	0.57	103	1034	0.092
	S12	38	71.9	0.72	34	336	0.061
	S11	60	44.7	0.45	34	336	1.793
2	S24	57	47.4	0.47	22	224	1.738
	S23	46	59.4	0.59	22	224	0.331
	S22	91	28.6	0.29	28	279	63
	S21	46	59.6	0.60	28	279	0.256
3	S34	39	70.0	0.70	32	321	0.075
	S33	24	114.3	1.14	32	321	0.013
	S32	56	48.3	0.48	31	311	1.091
	S31	35	78.2	0.78	31	311	0.040

[1] From Eq. (6-2)
[2] Mr. value at confining stress 2 psi (13.8 kPa) and deviatoric stress 6 psi (41.4 kPa)

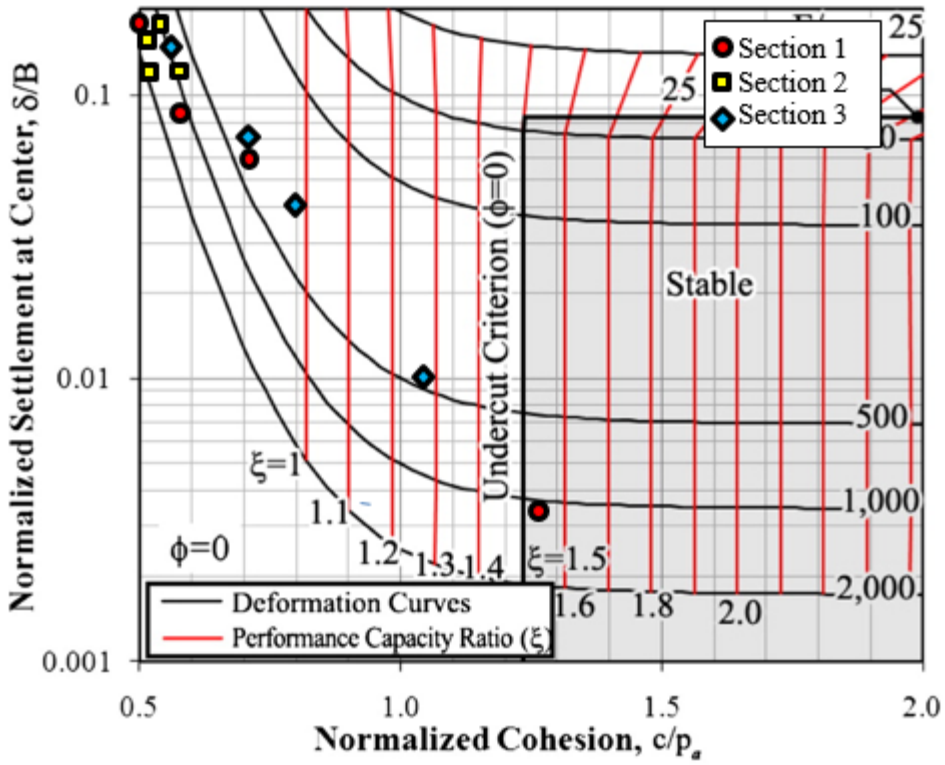

Figure 6-4. Application of undercut criteria (Borden et al. 2010) for the subgrade

6.2.1.2 Undercut criteria results - stabilized materials

In order to select appropriate select fill and ABC properties, the laboratory resilient modulus test results presented by Cowell et al. (2012) were utilized in this study. Figure 6-5 shows the select fill material grain size distribution used in this study and Cowell et al. (2012). The select fill material in both studies are Class II based on NCDOT specification and classified as A-2-4 (SM). According to the resilient modulus test results presented by Cowell et al. (2012), the resilient modulus of select fill material is determined by Eq. 6-4:

$$Mr = 1.7358\theta^{0.6704} \qquad \text{Eq. (6-4)}$$

Where, Mr. is in ksi, and θ in psi.

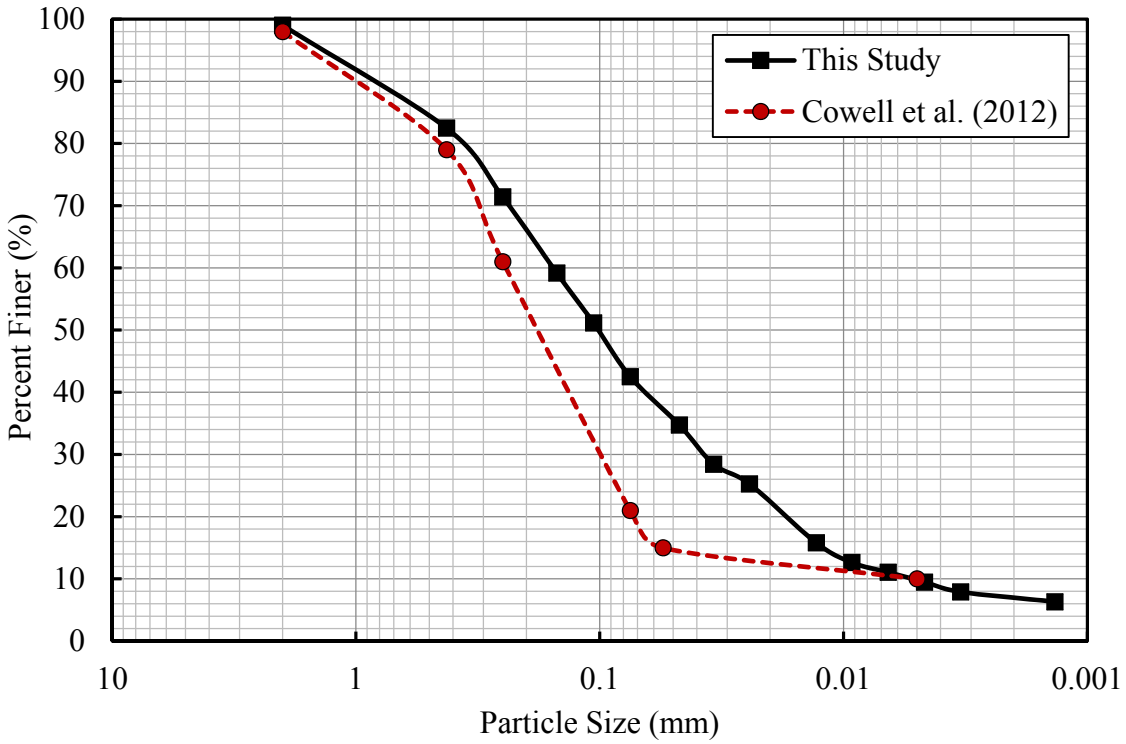

Figure. 6-5. Grain size distribution of select fill material used in this study vs Cowell et al. (2012)

Cowell et al. also presented the laboratory resilient modulus test results performed on the ABC Class IV. The resilient modulus tests were performed on ABC specimens at their 95% and 98% relative compaction. Figure 6-6, shows the grain size distribution of the ABC materials used in this study and by Cowell et al. (2012). The ABC materials is classified as A-1-a (GW). Based on the resilient modulus test results, the Mr value of the ABC at 95% relative compaction is determined by Eq. 6-5, where Mr is in ksi, and θ in psi:

$$Mr = 4.1046\theta^{0.6085} \qquad \text{Eq. (6-5)}$$

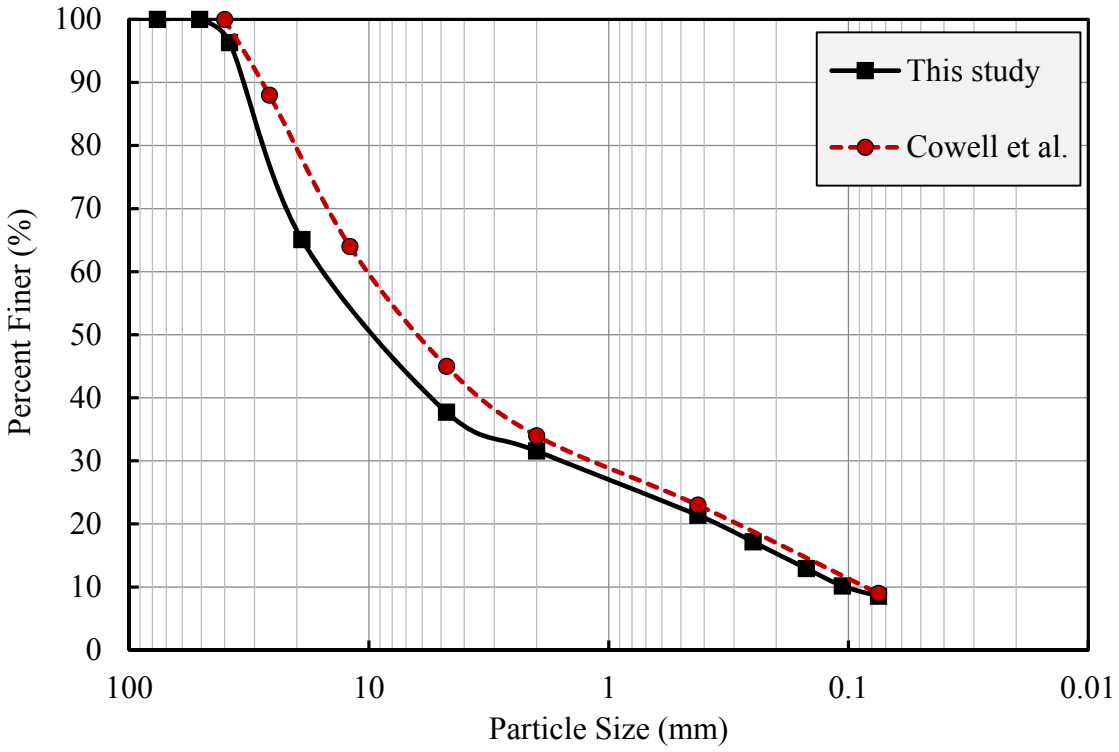

Figure 6-6. Grain size distribution of ABC used in this study vs Cowell et al. (2012)

Based on the presented equations, the resilient modulus of select fill materials and ABC are a function of the bulk stress. A deviatoric stress of 15 psi (103.35 kPa) and a confining pressure of 5 psi (34.45 kPa) were selected (NCHRP, Project 1-28 A; Mohammad et al., 2008) as the field representative stress state to interpolate the corresponding Mr value of the select fill and ABC materials from the resilient modulus test results.

The undrained shear strength value of the select fill and ABC materials were calculated by Ayers's equation, as expressed in Eq. 6-6, as a function of DCPI and maximum aggregate size:

$$Su_{ABC} = \frac{1}{2}(37.0 - 9.0 \times DCPI + 7.8MAS) \qquad \text{Eq. (6-6)}$$

Where,

$DCPI$: Penetration rate (in/blow)

MAS : Maximum aggregate size (in)

The calculated resilient modulus and undrained shear strength values of select fill and ABC materials are presented in Table 6-2. These calculated parameters were implemented in Eq. 6-1 proposed by Borden et al. (2010) by assuming a friction angle of zero. The results are summarized in Table 6-2 and plotted in Figure 6-7. It can be seen that the all data points plot within the stable zone of the chart.

This is consistent with field observations to be discussed later. In this case, after 1000 traffic passes, the maximum rut depth in the three stabilized section were less than the failure criterion (75mm). Hence, it can be concluded that the charts accurately gauge the effectiveness of the stabilization measure when subjected to less than 1000 truck passes.

Table 6-2. Base layer properties

Section	Station	Soil Type	Avg. DCPI	Undrained Shear Strength		Resilient Modulus		$\frac{\delta}{B}$
			mm/blow	s_u[3] (kPa)	s_u/Pa	Mr[4] (MPa)	Mr/Pa	
1	S14	S.F.[1]	13	240	2.40	117	1170	0.003
	S13	S.F.	13	240	2.40	117	1170	0.003
	S12	S.F.	14	237	2.37	117	1170	0.003
	S11	S.F.	13	238	2.38	117	1170	0.003
2	S24	ABC[2]	6	338	3.38	224	2240	0.002
	S23	ABC	5	341	3.41	224	2240	0.002
	S22	ABC	5	340	3.40	224	2240	0.002
	S21	ABC	5	341	3.41	224	2240	0.002
3	S34	ABC	5	340	3.40	224	2240	0.002
	S33	ABC	5	340	3.40	224	2240	0.002
	S32	ABC	6	337	3.37	224	2240	0.002
	S31	ABC	6	389	3.89	224	2240	0.002

[1] Select fill material type II,
[2] Aggregate base course type IV
[3] From Eq. (6-6)
[4] Mr. value at confining stress 5 psi (34.5 kPa) and deviatoric stress 15 psi (103.5 kPa)

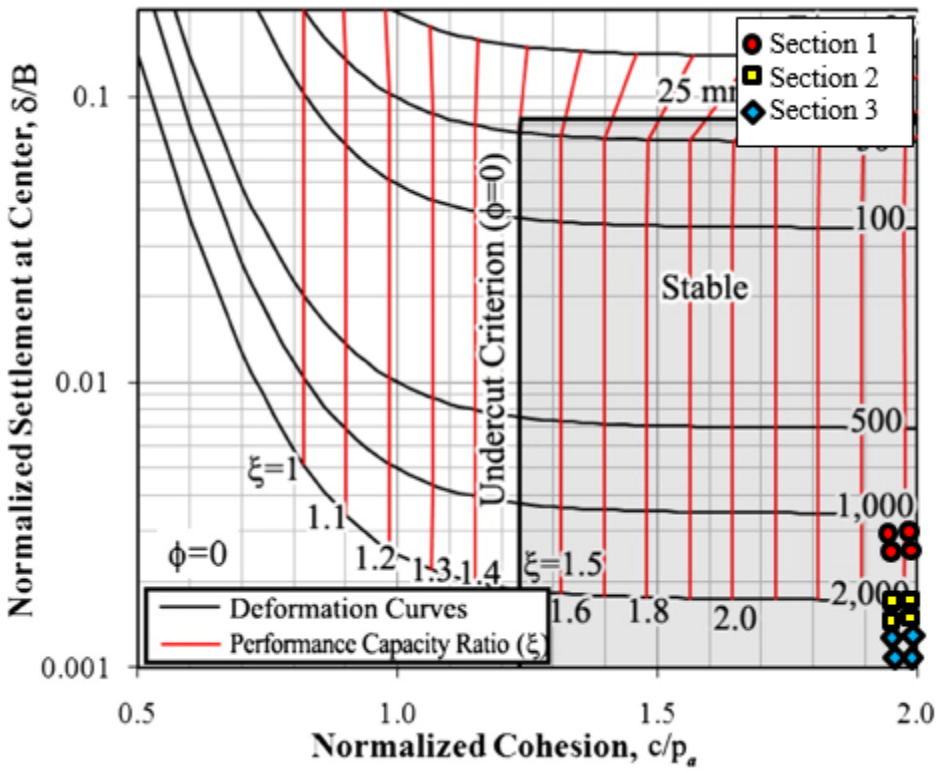

Figure 6-7. Application of undercut criteria (Borden et al. 2010) to the stabilized materials

6.3 Summary

This chapter investigated the ability of the NCDOT criterion and that proposed by the NC State research team reported in Borden et al. (2010) to predict the need for undercut at the research project test site. In summary, the applicability of the undercut criteria for the Piedmont residual subgrade soils was validated using soil properties estimated from test data that included triaxial and resilient modulus and/or DCP testing. The proposed undercut criteria based on deformation performance of the subgrade soil after traffic loading indicated the adequacy of the stabilized subgrade layer to support the road section when geosynthetic reinforcement was used in conjunction with ABC or when the excavated material was replaced with select fill.

CHAPTER 7: DEFORMATION AND STRESS UNDER TRAFFIC LOADING

The deformation and stress results from traversing the test pads with the proof roll truck are presented herein. As previously mentioned, four earth pressure cells were installed in each stabilized section to monitor and record the applied pressure near the top of the subgrade. Two moisture and one suction sensors, embedded at the middle of each test section, were used to record the variation of moisture and matric suction of the subgrade soil during the full scale testing. Lidar scans were frequently conducted, with the survey data imported into Matlab and analyzed, to assess surface plastic deformation as a function of the number of load applications.

7.1 Equivalent Single Axle Load (ESAL)

ESAL is used to convert the loading from various axle configurations and load magnitudes into an equivalent number of standard single axle 18 kips loads for pavement design. The ESAL for each test section was calculated by following the AASHTO 1993 procedure, assuming a terminal serviceability index of 2.5. The ESAL value was calculated for each test section based on the load distribution on each truck axle, and calculated structure number (SN) of each test section. A summary of the ESAL calculation for each test section is provided below, where a_1 and D_1 are the layer coefficient, and thickness of layer (inches), respectively:

Front axle load: 16,500 lbs

Combined rear axles load: 38,500 lbs

Section 1:

$a_1 = 1,\ D_1 = 32"$
$M_1 : Engineered\ fill = 0.1$
$SN = 3.2$
$ESAL = 0.73 + 1.78 = 2.51$

Sections 2 and 3:

$a_1 = 1,\ D_1 = 9"$
$\mathrm{M}_1 : ABC = 0.13$
$SN = 1.17$
$ESAL = 0.7 + 1.86 = 2.56$

7.2 Speed of Truck

The influence of the speed of truck for each pass on the measured stress was explored based on the time interval between the recorded first and second pressure peak (which were associated with the front and back axle load, and the distance between the front and second rear axle). As shown in Figure 7-1, the speed of truck was also categorized based on the drivers. It was observed that driver No.1, who started the traffic, drove between 9-13 mph at the beginning until he reduced the speed down to 6-9 mph after about 300 passes. Driver No.2 drove at speeds ranging from 8-12 mph. Driver No.3 drove at slightly higher speed compared with driver No. 1 final speed, about 8-9 mph. It was concluded that the average speed of the truck was about 8 mph during the test.

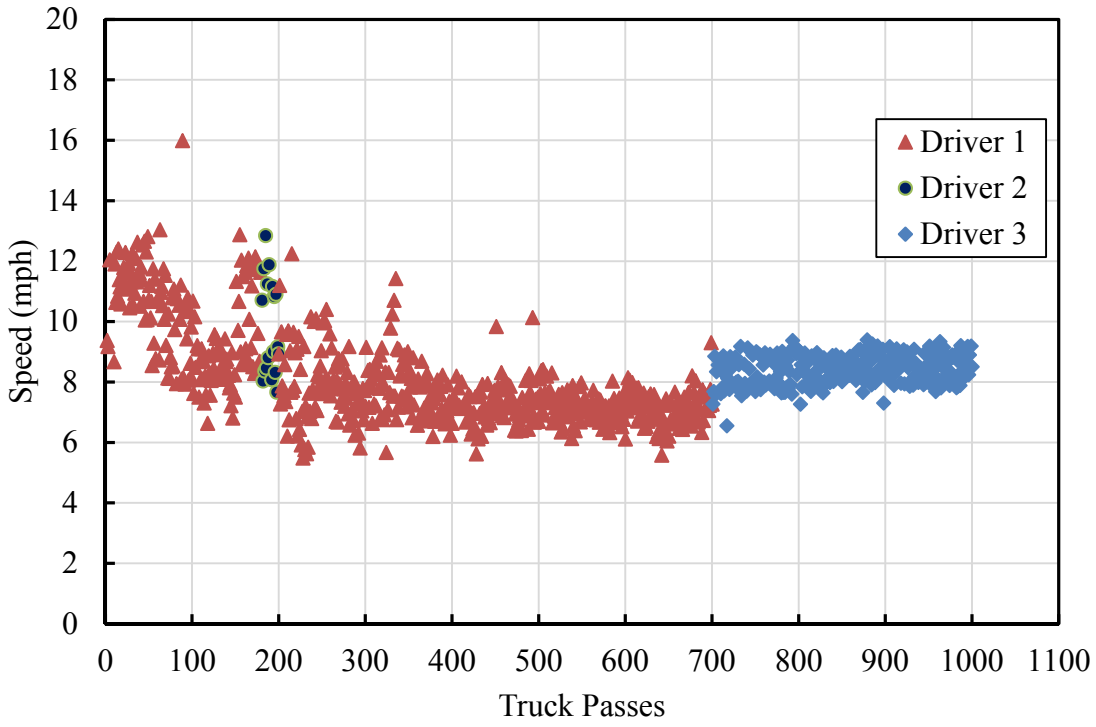

Figure 7-1. Truck speed

7.3 Field Observations

The deformation performance of the test sections was investigated under channelized traffic loading. The traffic loading was induced by a fully loaded dump truck, as explain in Chapter 3. The 1000 truck passes were started on June 11th, 2014 and completed by July 1st. In order to guide the drivers to drive over the pressure cells (EPCs) and channelize the traffic, traffic cones were placed along the sides of the test pad, as shown in Figure 7-2. At different times during the testing, Lidar scan surveys were carried out to monitor and record the permanent deformation of each section. This section presents visual observations that were noted while conducting the full-scale load test.

Figure 7-2. Traffic cones for channelizing the traffic.

7.3.1 Select fill test section

As previously described, section 1 was stabilized by replacing the soft subgrade with select fill material type II. Figure 7-3 shows test section 1 after 100 passes. It can be seen that no significant rut depth was yet developed, however select material started to displace laterally and accumulate on the outer and inner edges of each wheel path. Figure 7-4 shows section 1 after 300 traffic passes where signs of rutting can be seen more clearly. The condition of the test section 1 after 1000 passes is shown in Figure 7-5. Although the cumulative rut depth in section 1 at the end of traffic loading was greater than the geosynthetics-reinforced sections, it was still serviceable and the rutting was less than the NCDOT acceptance criteria of 75 mm.

Figure 7-3. Test section 1, after 100 traffic passes.

Figure 7-4. Test section 1, after 300 traffic passes.

Figure 7-5. Test section 1, after 1000 traffic passes.

7.3.2 Geosynthetics-reinforced sections

Sections 2 and 3 were reinforced by geogrid and geotextile, respectively. Both geosynthetic-reinforced sections showed similar performance under traffic load. The observed cumulative rut depths in these sections was significantly less than section 1. Figures 7-6 and 7-7 show sections 2 and 3 after 1000 traffic passes, respectively. It can be seen that the cumulative rut depth in both sections 2 and 3 were less than 1 inch. Neither geosynthetic-reinforced section required maintenance or repair. It is worth noting that no tension cracks were observed in the reinforced sections.

Figure 7-6. Test section 2, Geogrid reinforced, after 1000 traffic passes.

Figure 7-7. Test section 3, Geotextile reinforced, after 1000 traffic passes.

7.2.3 Lime stabilized section

Section 4 was treated by lime stabilization. A significant amount of cumulative rut depth was noticed in the outer wheel path after only a few truck passes, as shown in Figure 7-8. With continued traffic, the cumulative lateral and vertical deformation in section 4 increased, until 100 after passes the under carriage of the test vehicle had begun scrubbing the mound of heaved soil that ran in between the outer and inner wheel path, as shown in Figure 7-9. At this point the test was paused for few weeks, to evaluate possible alternatives. After consulting with the NCDOT and contractor, it was decided to abandon section 4 and the field test continued with the three other sections. The NCDOT investigation identified that contractor had incorrectly used agriculture lime with low calcium carbonate content, which was not suitable for subgrade treatment.

Figure 7-8. Test section 4, lime stabilized, after 10 traffic passes.

Figure 7-9. Test section 4, lime stabilized, after 100 traffic passes.

7.4 LiDAR Data Analysis

Lidar scan data were transferred into MicroStation® software for further processing and deleting extra points and then they were exported into the *.DXF format file. Figure 7-10 shows an example of scanned points. In order to call and open these data in Matlab, the free version of DXF2XYZ software was used to convert *.DXF file into *.TXT format. A Matlab code was developed to call the *.TXT files and open them in Matlab. Since the spacing resolution of scanned points was 0.5", grids in both vertical and horizontal direction were generated in Matlab, with 1" node spacing by using the coordinates of corners of the test pads, as shown in Figure 7-11. By generating these grids, measured elevations of the nearest scanned point to the intersection of horizontal and vertical grid lines was assigned to the intersection point. By using the code and calling scanned data, the changes in elevation were calculated for each time step, corresponding to a number of truck load cycles.

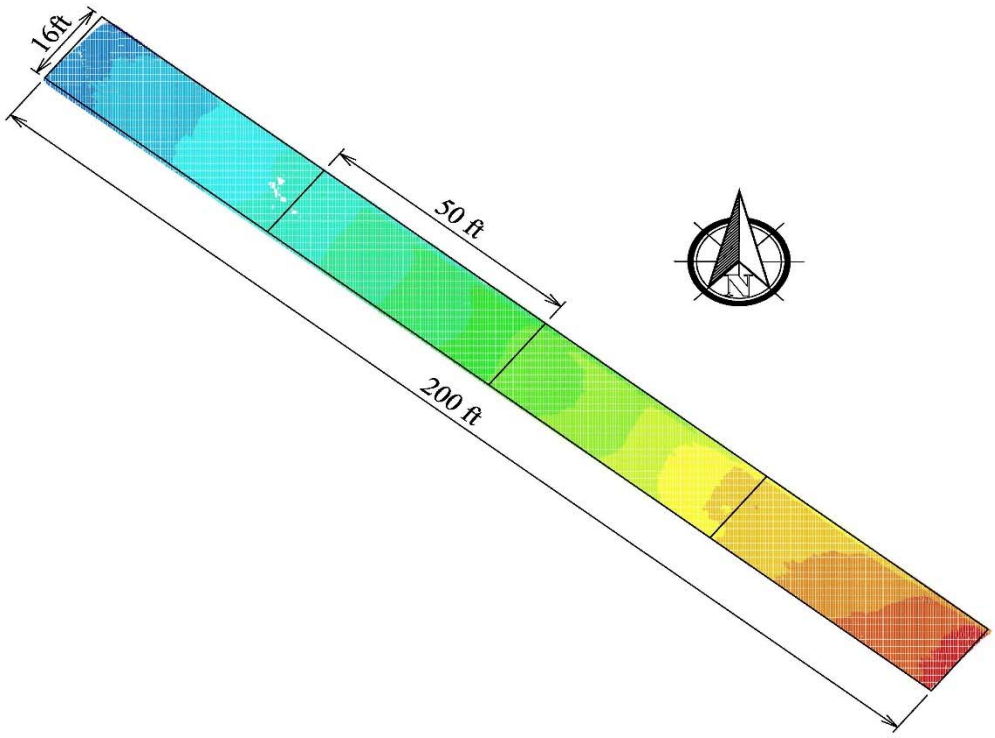

Figure 7-10. Example of Lidar scanned points.

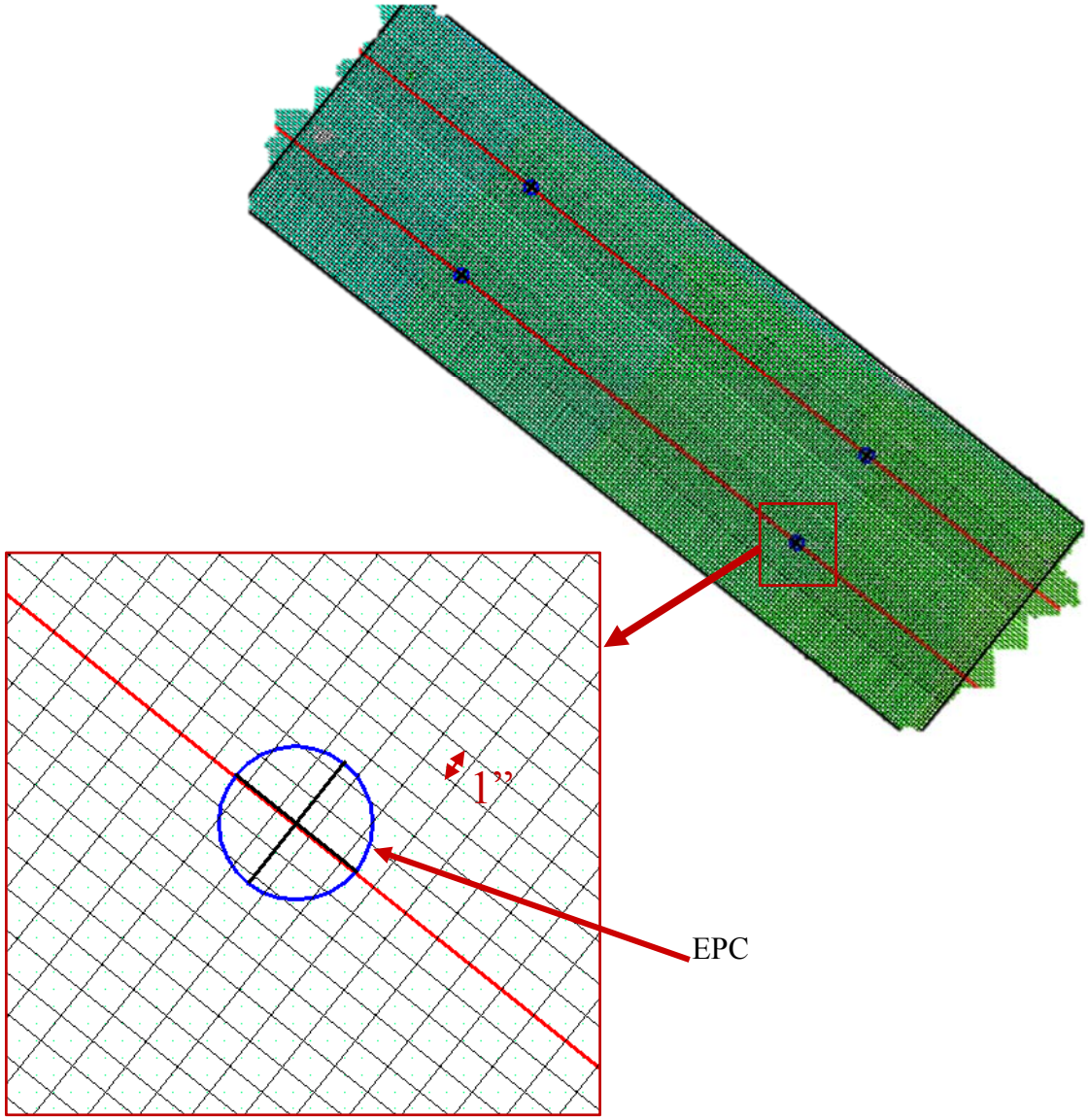

Figure 7-11. Generated grids in Matlab.

7.4.1 Excavation and backfill depth

GPS coordinates of the Earth Pressure Cell (EPC) locations were documented at their installation. These coordinates were used to calculate depth of excavation and backfill at the location of each pressure cell to determine thickness of the select fill material and ABC layer. As mentioned in a previous section, the diameter of each EPC was 9”. Hence for better estimation of the depth of excavation and backfill, instead of using elevation change of only one point, an

average of elevation change of all points located above the top of each pressure cell was computed. The depth of the excavation and backfill, corresponding to each EPC, is summarized in Tables 7-1 and 7-2, respectively. It can be seen that because of the ground slope to the side, the excavation depth at one side, C31 and C32 at the OWP, was higher that the required excavation at the other side, C33 and C34 at the IWP.

It can be seen that section 1 was excavated between 29” to 31” and backfilled with 29” to 33” of fill material class II. However, the excavation/backfill depth was 31” in first place. Based on the Lidar scan data analysis, it was realized that sections 2 and 3 were excavated between 6”-8” and 5”-9”, respectively. After installing geogrid in section 2 and geotextile in section 3, aggregate base course with 7.4”-12” and 10”-11.6” thickness was compacted in sections 2, and 3, respectively. These variations in the thickness of ABC layer are utilized later during the discussion on deformation behavior and measured pressures.

Table 7-1. Excavation depth

Section No.	Section 1: Select Fill				Section 2: 9" ABC over GG				Section 3: 9" ABC over GT			
EPC No.	C11	C12	C13	C14	C21	C22	C23	C24	C31	C32	C33	C34
Excavation Depth (in)	29.5	31.2	28.7	30.2	7.14	5.90	6.96	8.39	8.6	8.9	5.3	7.6

Table 7-2. Backfill depth

Section No.	Section 1: Select Fill				Section 2: 9" ABC over GG				Section 3: 9" ABC over GT			
EPC No.	C11	C12	C13	C14	C21	C22	C23	C24	C31	C32	C33	C34
Backfill Depth (in)	29.1	32.0	31.4	32.8	7.41	8.21	9.82	11.2	11.6	9.8	11.5	11.6

7.4.2 Rut depth test results

As noted, a virtual horizontal and vertical grid system was generated over the three test sections and the coordinates of each scanned point were assigned to the nearest grid point. The elevation change for different time steps was calculated with respect to the initial elevation before subjected to the traffic load, and plotted for the entire test site. These data were used to discern the location of the wheel paths. As shown in Figure 7-12, cold colors indicate settlement and wheel paths and hot colors indicate pumping (elevation rise) after 1000 track passes.

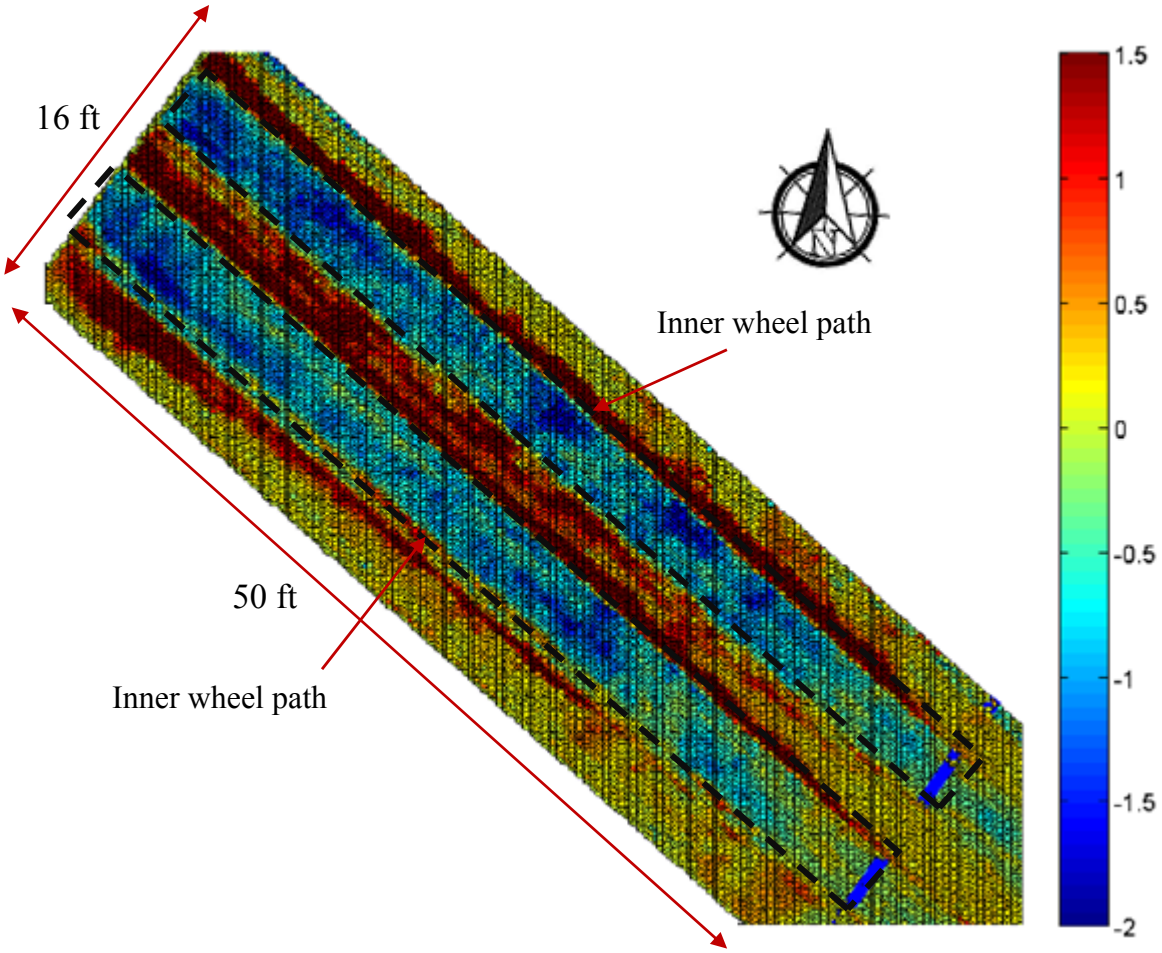

Figure 7-12. Pumping and rutting over test section 1, after 1000 passes (legend in inches)

The results of these analyses indicated a 46-inch width of wheel path, based on the area of the cold colors, shown in Figure 7-12. The area of outer and inner wheel path was extracted for clarity of presentation. Figures 7-13 to 7-18 show the contours of elevation change under inner and outer wheel paths in sections 1, 2 and 3, respectively. It can be seen that the location of the pressure cells were on the center line of each wheel path. The significant rut depth at the interface of sections 3 and 4 can clearly be seen in Figures 7-17 and 7-18, however as it did not reach to the EPC 34 location, it did not have any effect on the deformation analysis.

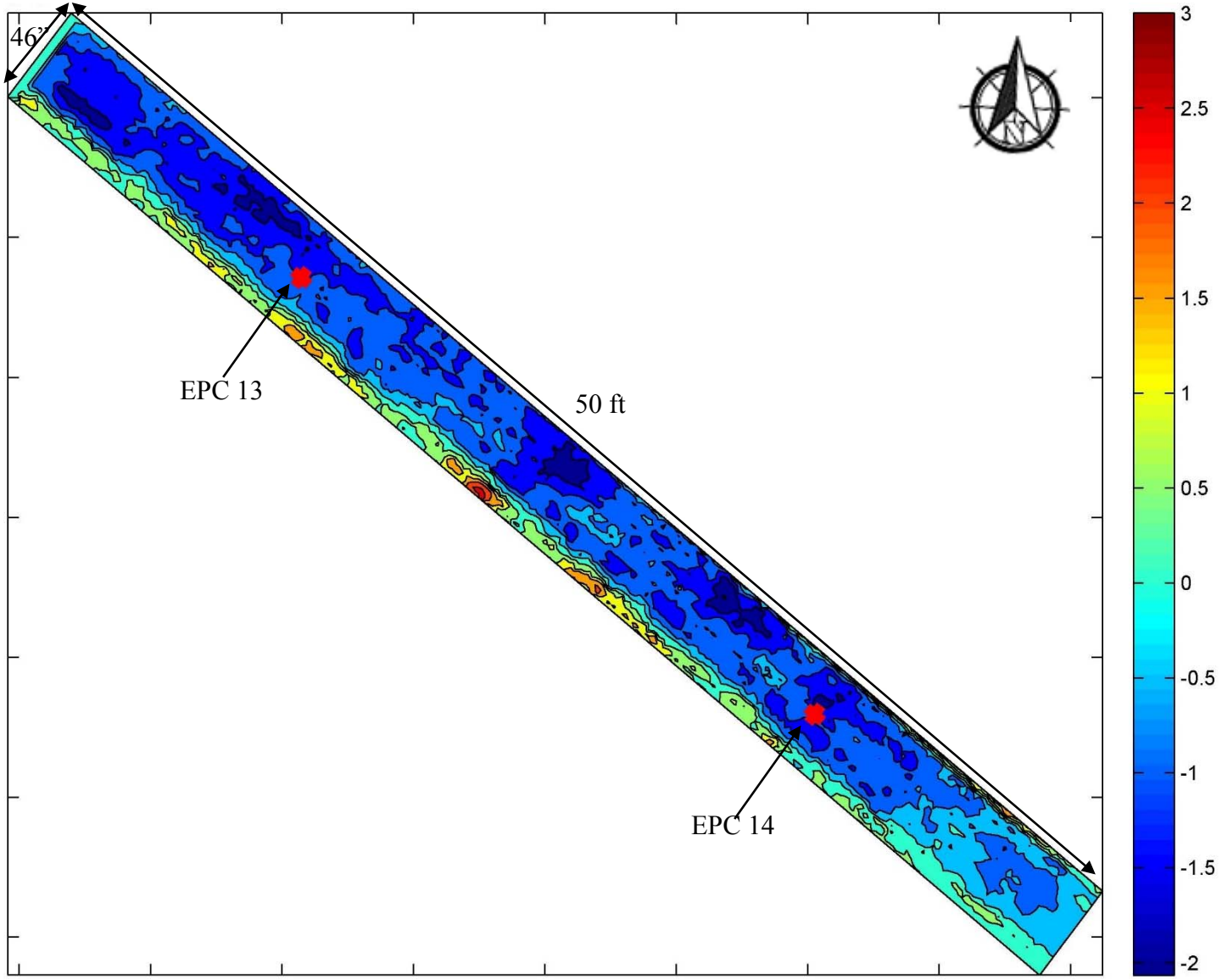

Figure 7-13. Elevation change contours after 1000 passes, inner wheel path section 1(legend in inches)

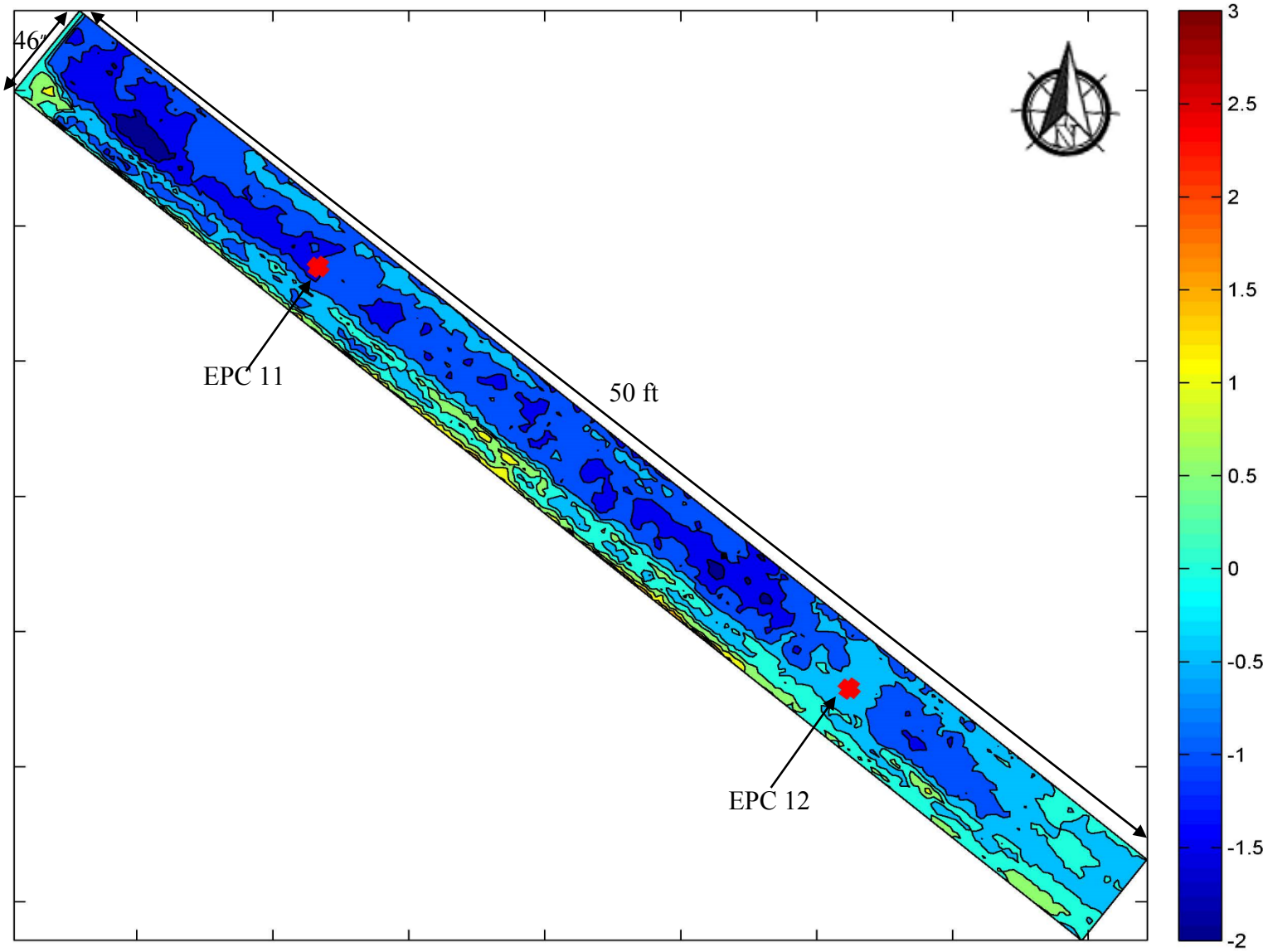

Figure 7-14. Elevation change contours after 1000 passes, outer wheel path section 1(legend in inches)

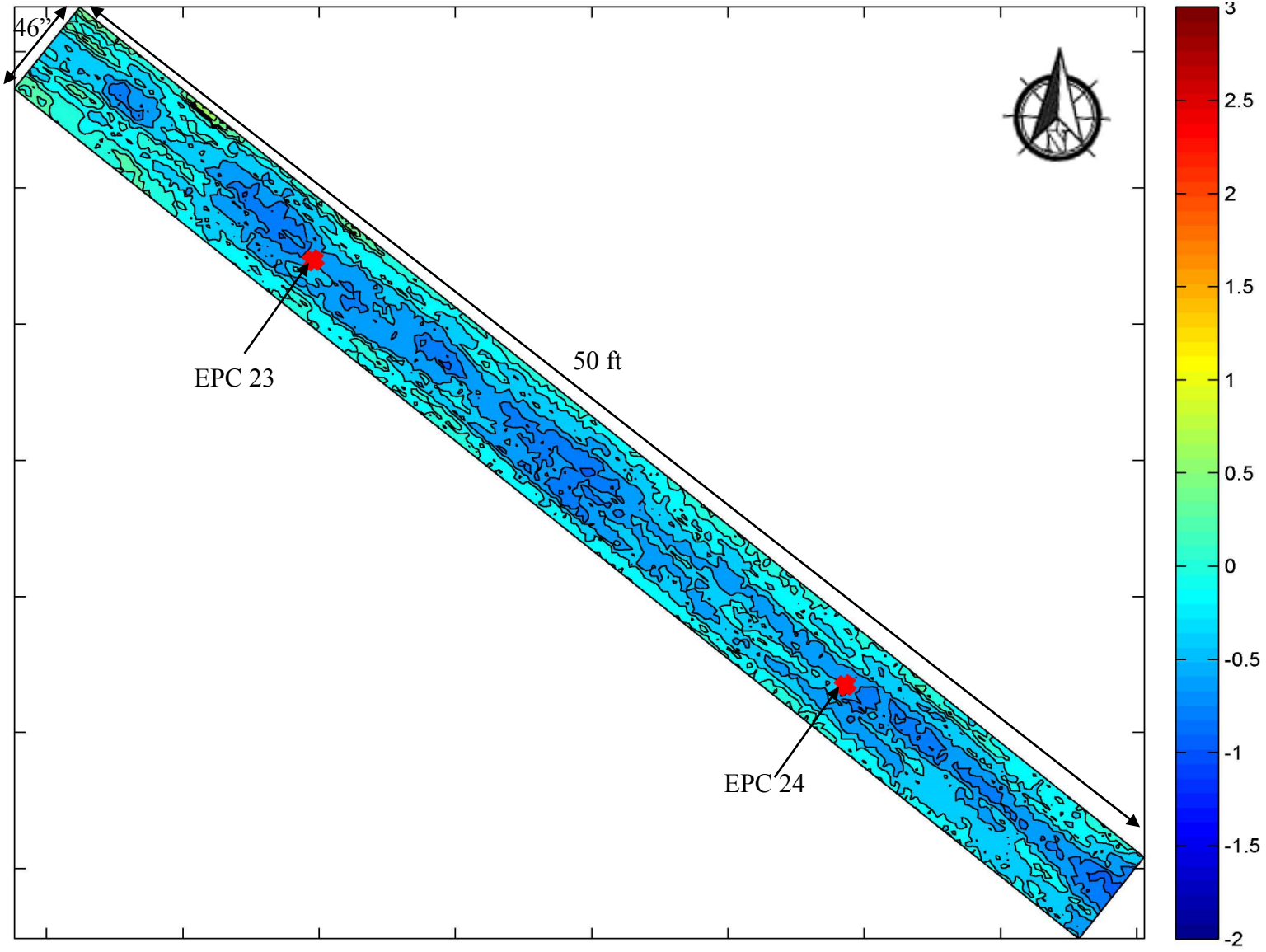

Figure 7-15. Elevation change contours after 1000 passes, inner wheel path section 2(legend in inches)

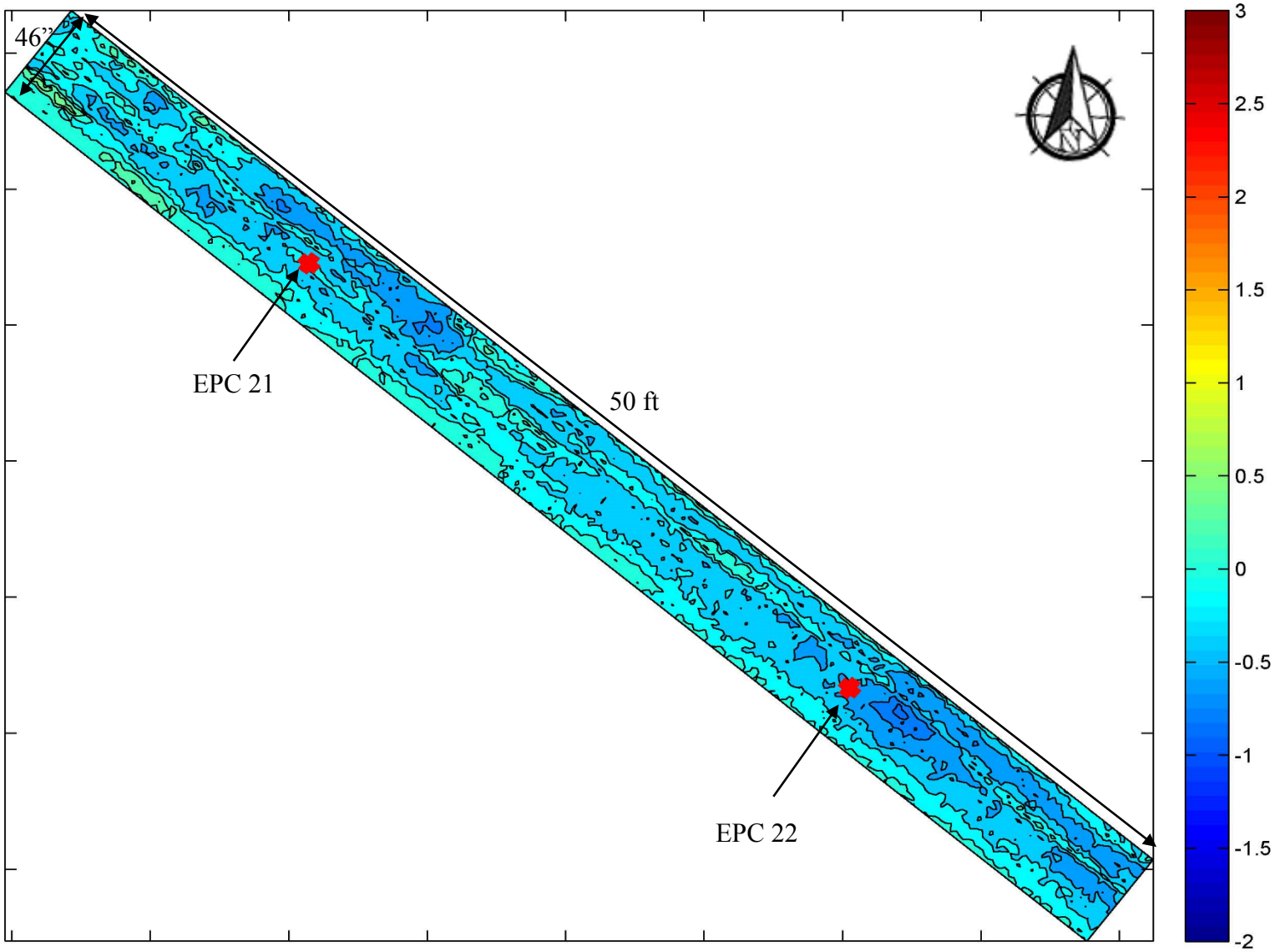

Figure 7-16. Elevation change contours after 1000 passes, outer wheel path section 2(legend in inches)

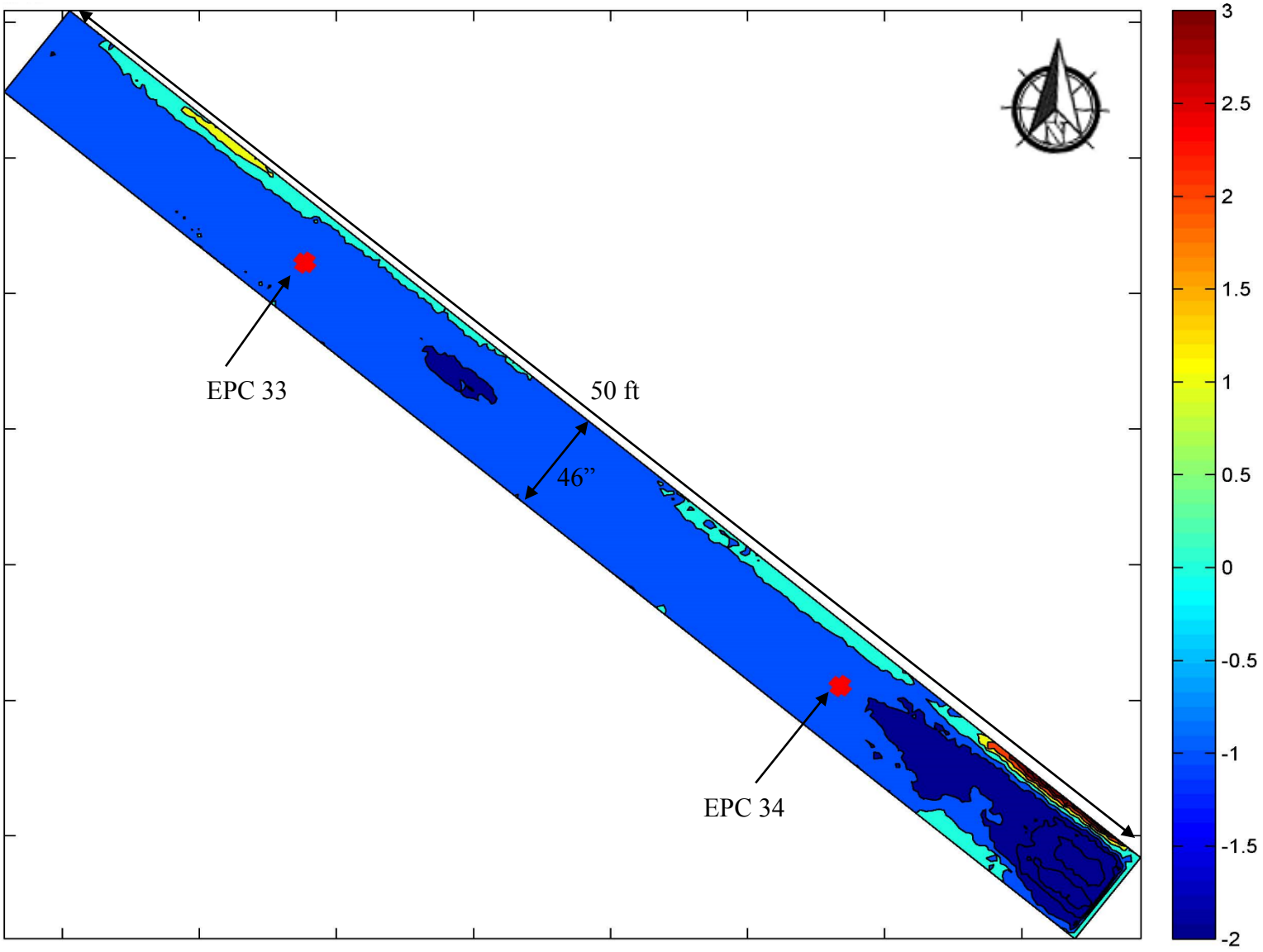

Figure 7-17. Elevation change contours after 1000 passes, inner wheel path section 3(legend in inches)

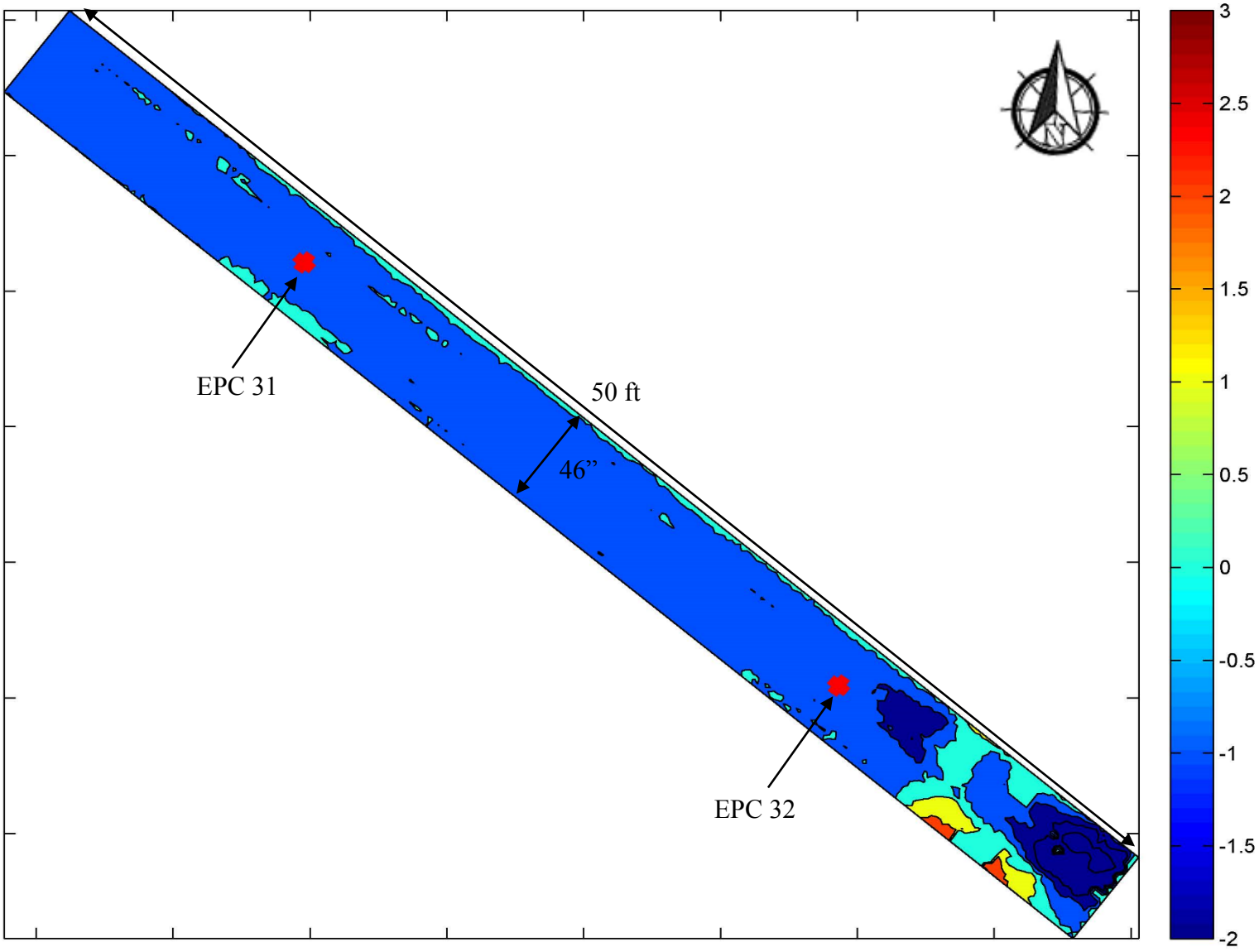

Figure 7-18. Elevation change contours after 1000 passes, outer wheel path section 3(legend in inches)

Since the overlapping test sections would not accurately represent their respective stabilization measure (Cowell et al. 2012), the portion of wheel path within each test section that ran outside the two EPCs was excluded from further deformation analysis.

As shown in Figures 7-13 to 7-18, the maximum cumulative rut depth did not occurred right on the centerline of each wheel path. Therefore, and to be able to capture the maximum elevation change at each cross section, the grid lines in Figure 7-19 are used. The maximum rut depth on each horizontal grid was found and used to develop the longitudinal surface deformation of each wheel path. Maximum elevation change along inner and outer wheel paths between two pressure cells after 1, 10, 100, 500 and 1000 passes, were plotted for sections 1, 2 and 3 and are shown in Figures 3-20 to 3-22. The north edge of section 1 is considered as the starting point.

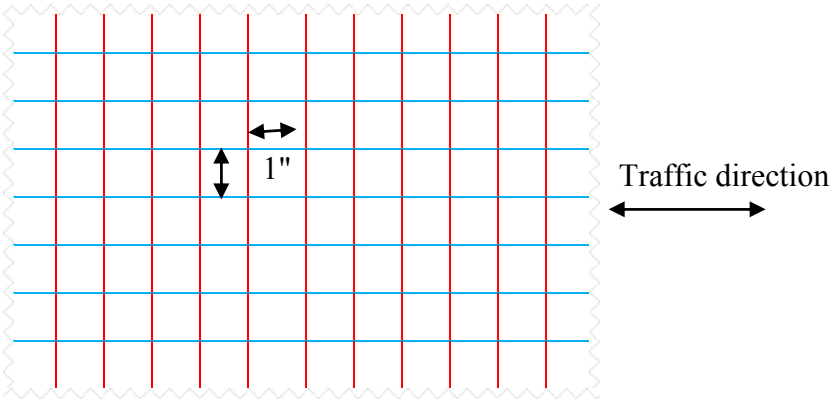

Figure 7-19. Demonstrating capturing maximum elevation change

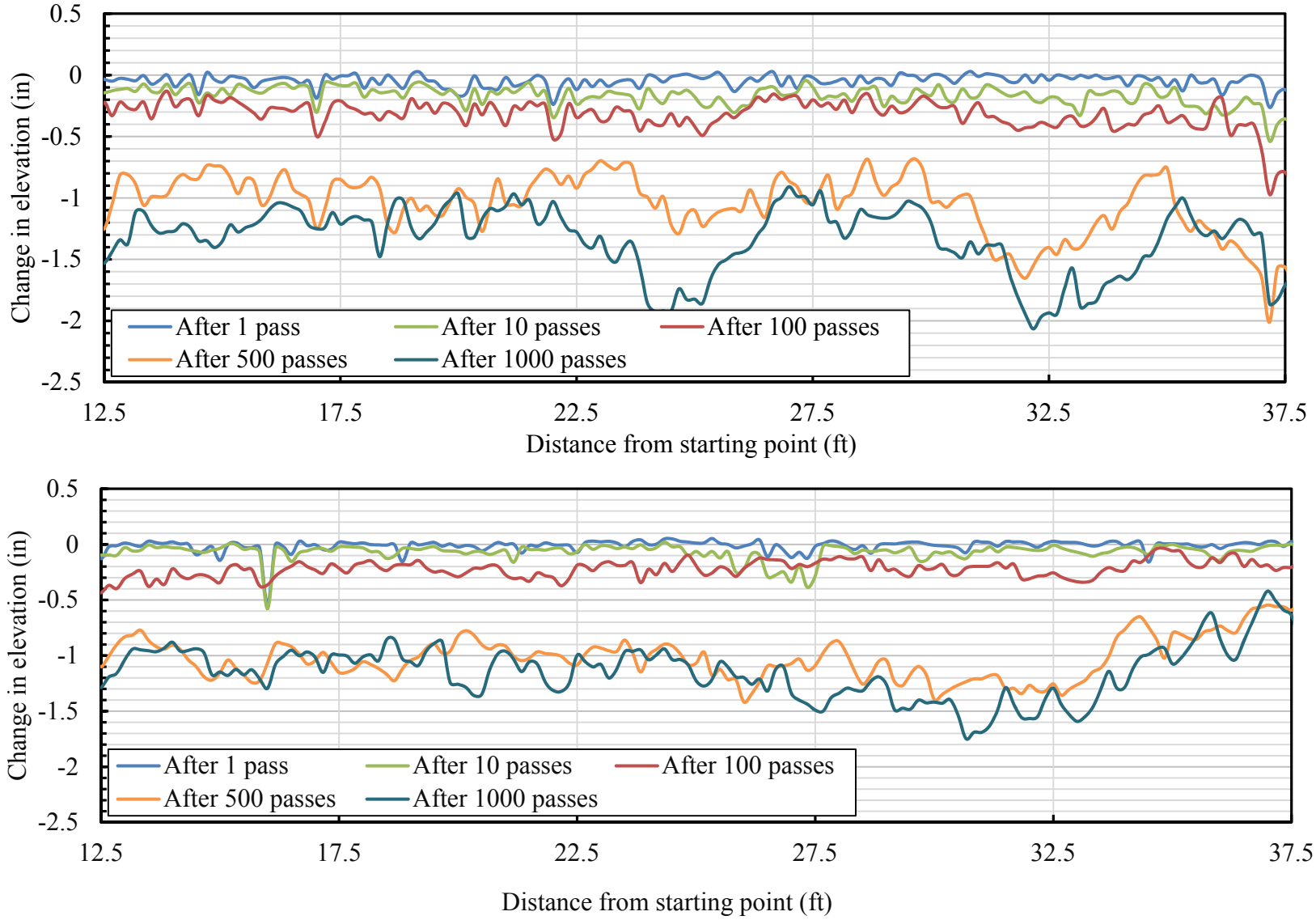

Figure 7-20. Longitudinal profile of inner (top) and outer (bottom) wheel path in section 1

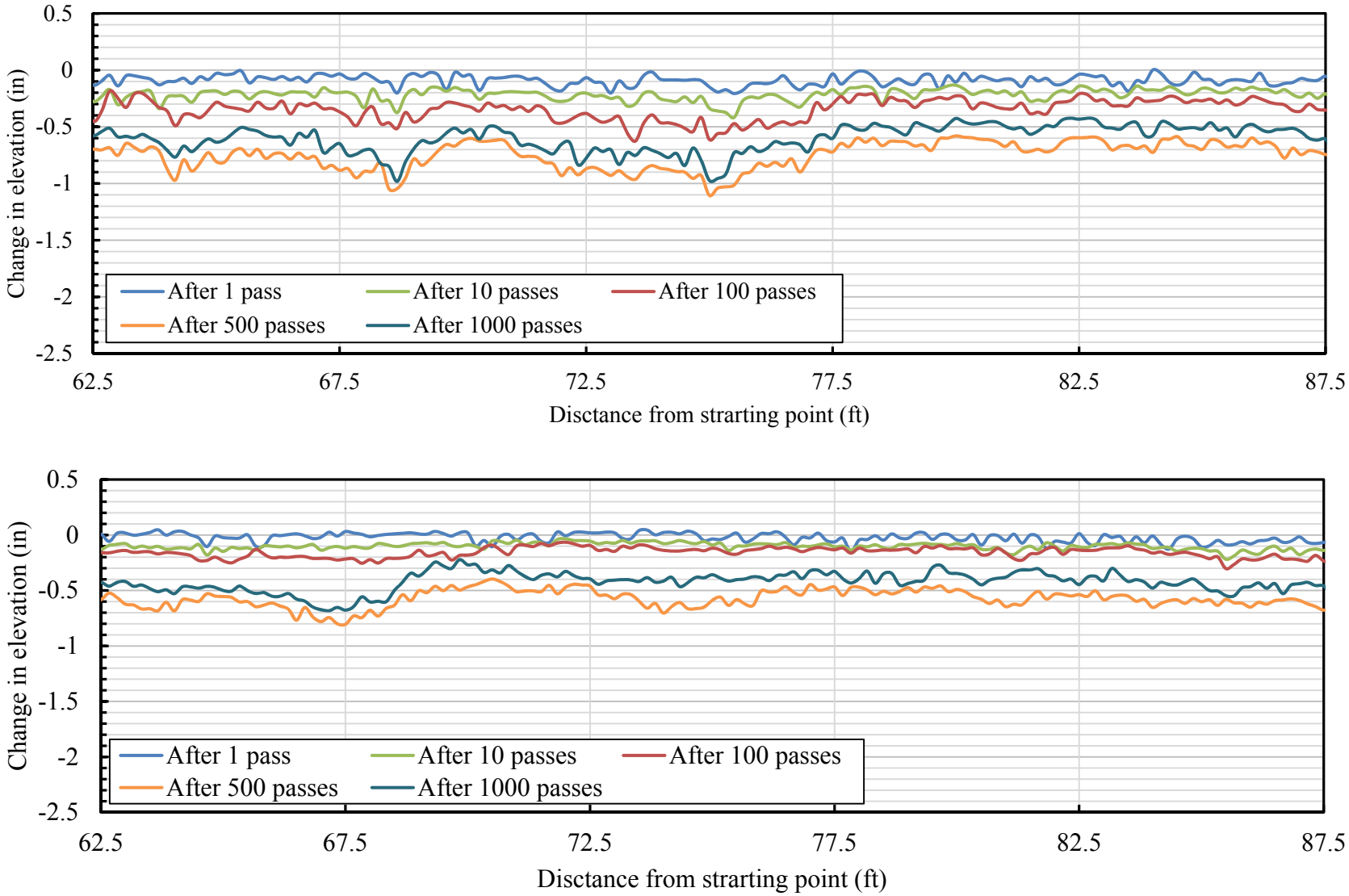

Figure 7-21. Longitudinal profile of inner (top) and outer (bottom) wheel path in section 2

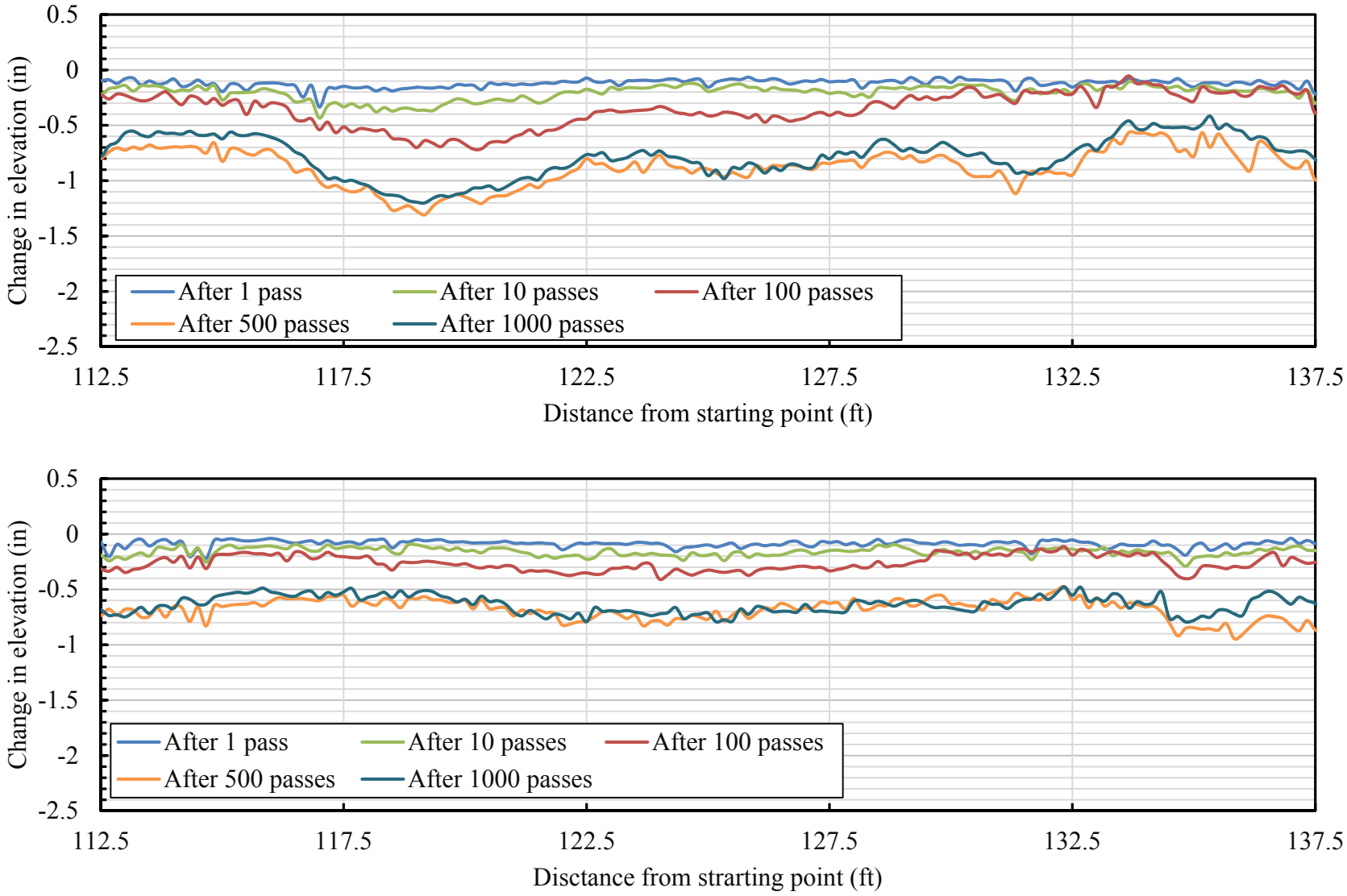

Figure 7-22. Longitudinal profile of inner (top) and outer (bottom) wheel path in section 3

To track the trend of permanent deformation development under the applied truck load, the deformation calculations under the wheel paths in each test section were focused on two zones; north and south. The north-west (called north) and south-east (called south) zones are 6 ft long and cover the area 3 ft north-west and 3 ft south-east of each pressure cell, as shown in Figure 7-23. The average elevation change along the longitudinal direction in each of the zones were calculated after 1, 10, 50, 100, 200, 300, 500, 700, 800, 900 and 1000 truck passes for the both inner and outer wheel paths in each test section.

Figures 7-24 and 7-25 show the cumulative deformation of section 1, stabilized by select fill materials. It can be seen that the rut depth reached a relatively constant value after 700 and 500 passes in the north and south sections, respectively. As shown in Figures 7-26 to 7-29, for sections with geotextile and geogrid reinforcement, the cumulative rut depth is significantly less than the permanent deformation in section 1, and reached a relatively constant value after 500 traffic passes. It can be seen in Figures 7-26 to 7-29 that the cumulative vertical deformation reduced slightly at pass No. 700 where the drivers switched. As explained later in this chapter, by switching the driver at this pass number, the wheel paths moved slightly (because of the driver's habit), thus the induced lateral displacement produced by the new established wheel path, the cumulative vertical deformation under the wheel paths, located directly over the EPC, reduced.

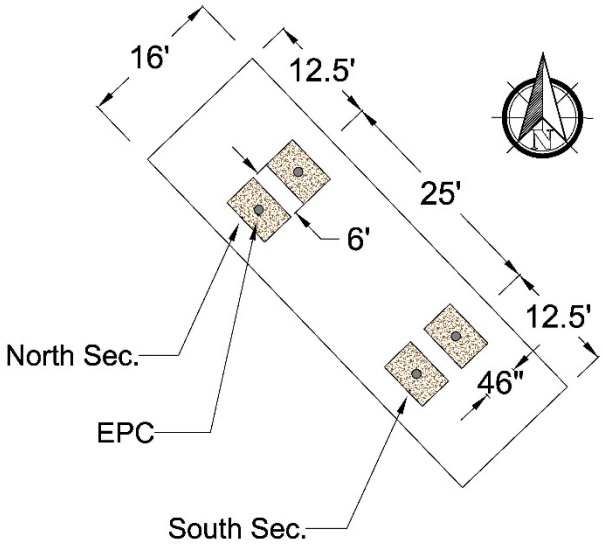

Figure 7-23. Considered area for surface deformation analysis

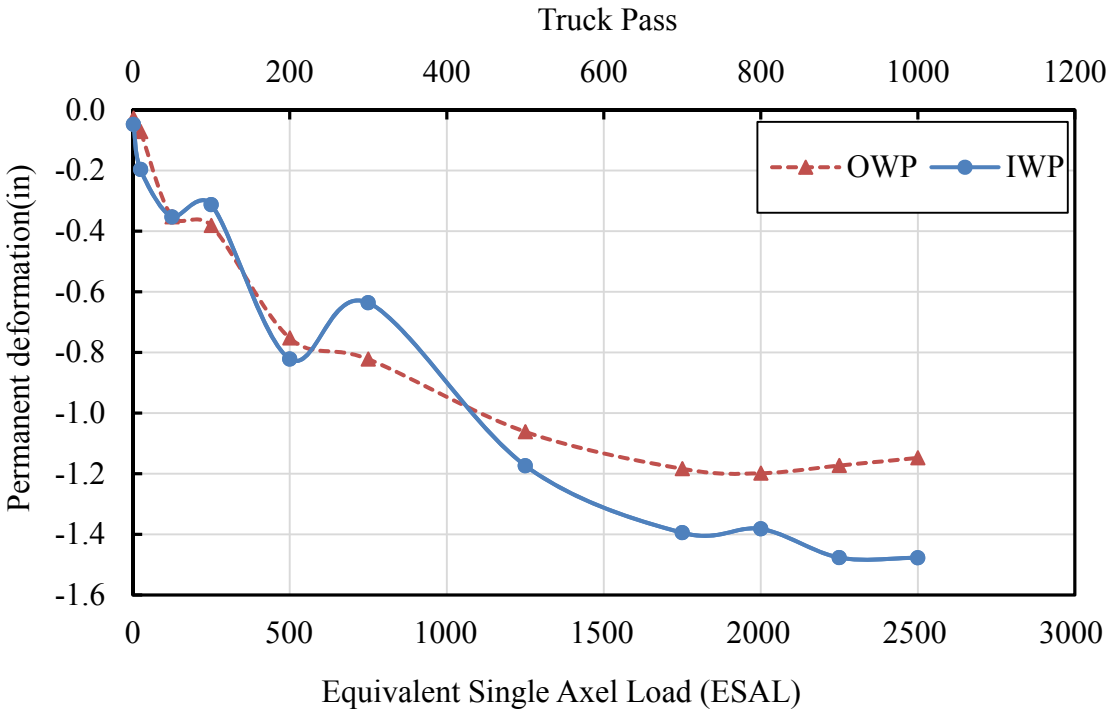

Figure 7-24. Cumulative permanent deformation for test section 1, North sections

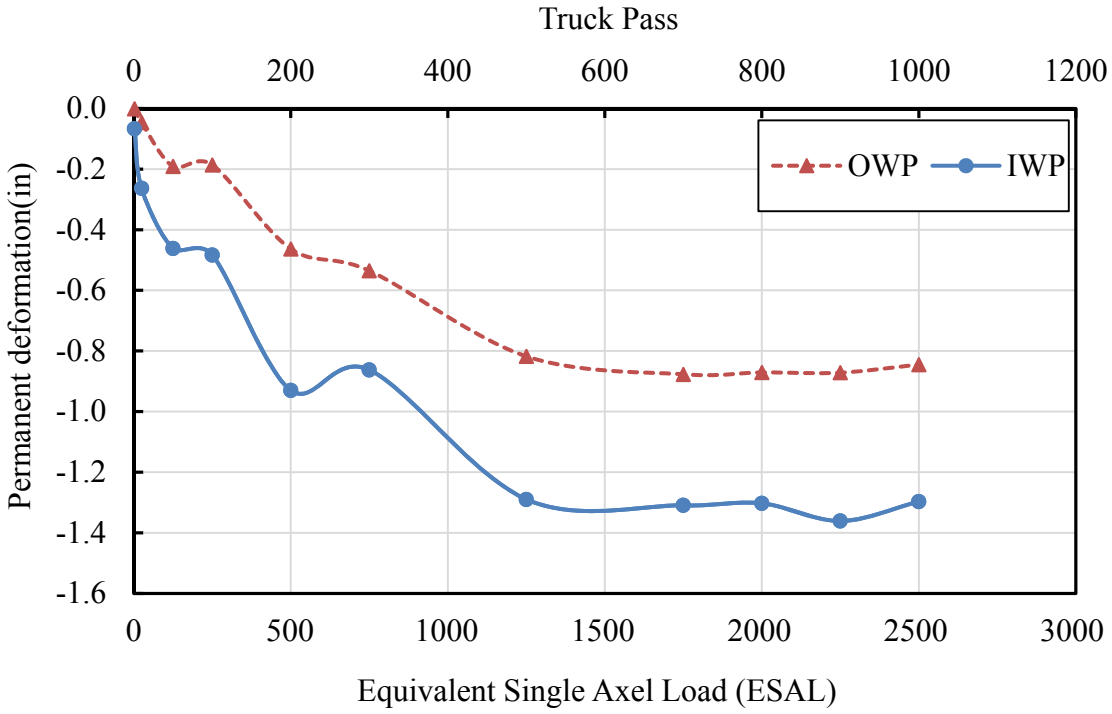

Figure 7-25. Cumulative permanent deformation for test section 1, South sections

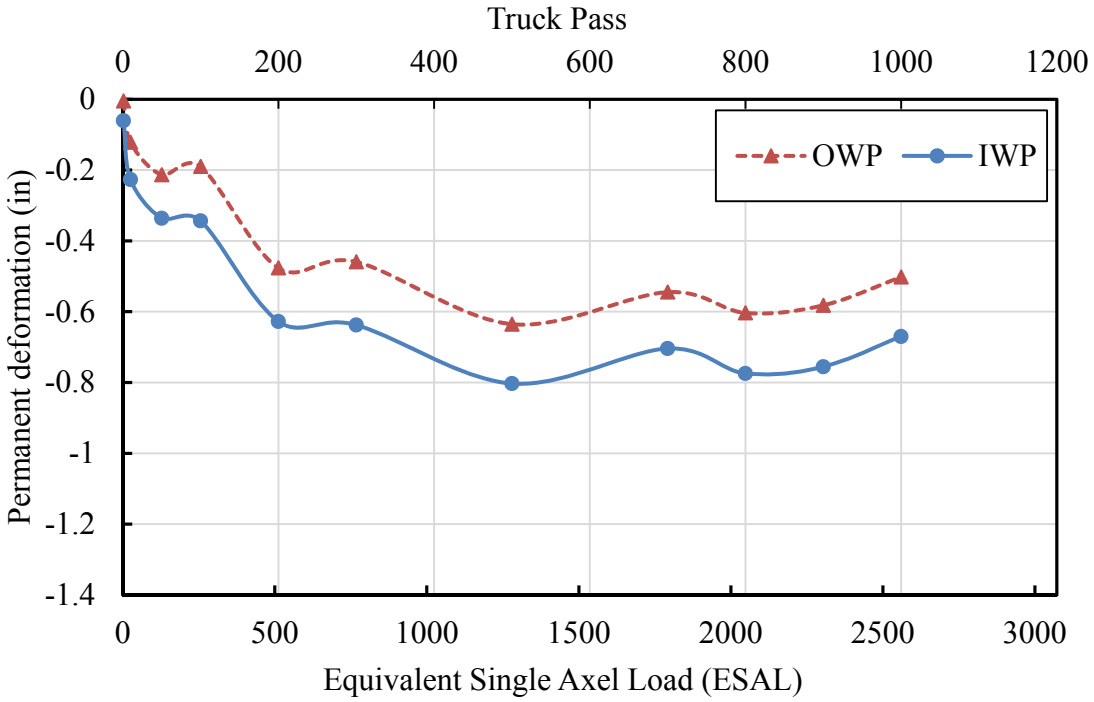

Figure 7-26. Cumulative permanent deformation for test section 2, North sections

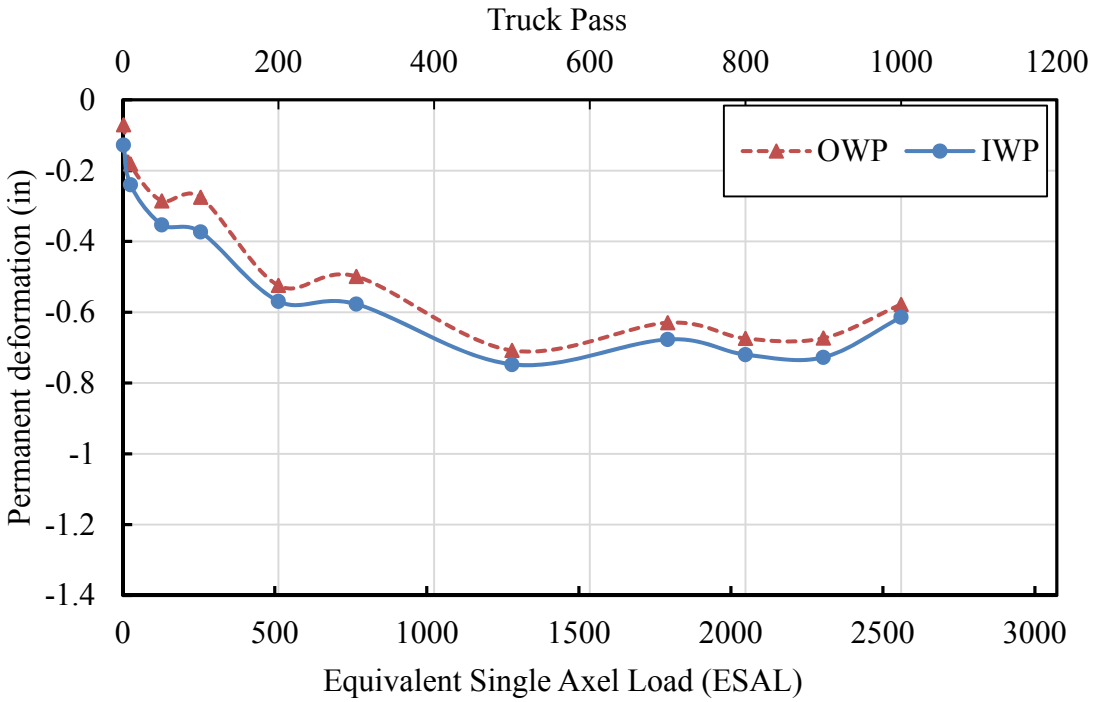

Figure 7-27. Cumulative permanent deformation for test section 2, South sections

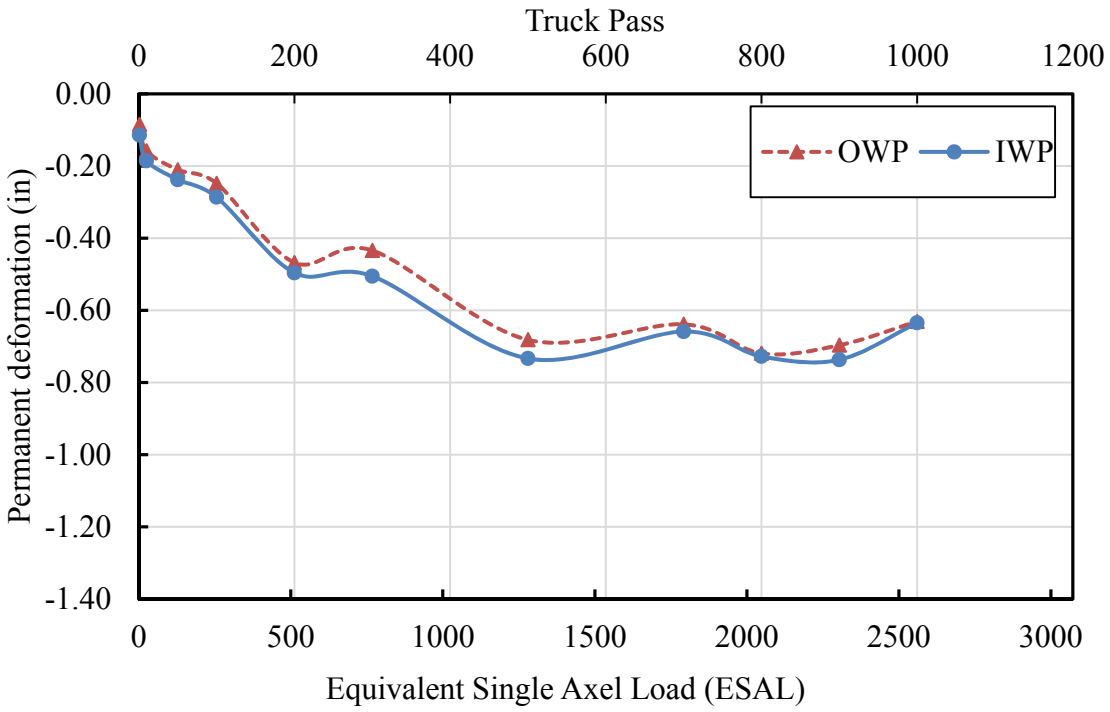

Figure 7-28. Cumulative permanent deformation for test section 3, North sections

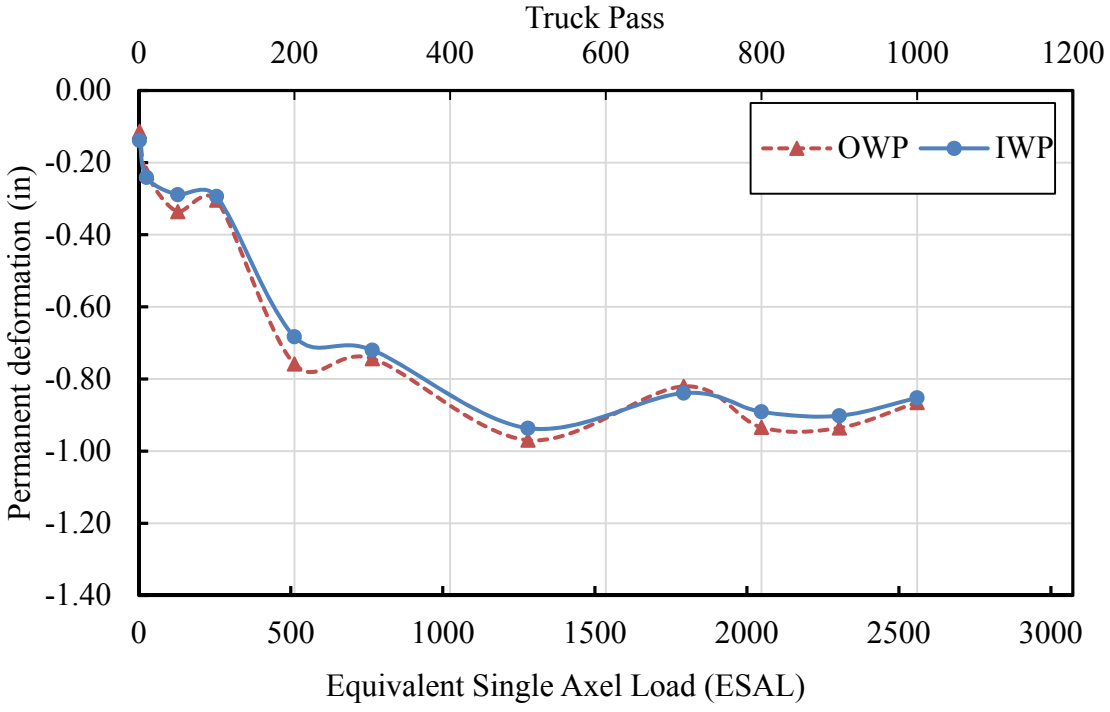

Figure 7-29. Cumulative permanent deformation for test section 3, South sections

7.5 Stress Distribution

Four Earth Pressure Cells (EPCs) were installed 3 inches below the interface of the subgrade and treated zone, in each test section (two in each wheel path). For each traffic pass, measured pressures by EPCs were saved into one TXT file with 12 columns with each column corresponding to one EPC. A Matlab code was developed to call all *.TXT files, one by one, and finds the peak value recorded by each pressure cell, during each traffic pass, as shown in Figure 7-30.

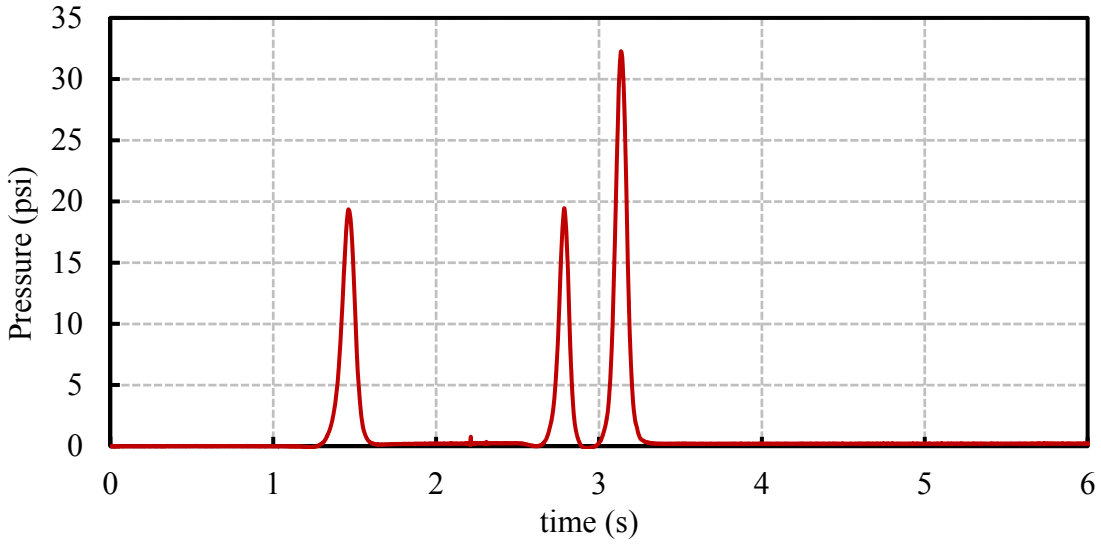

Figure 7-30. Example of recorded pressure by EPC.

Figures 7-31 to 7-33 show the measured pressure by EPCs in sections 1, 2 and 3, respectively. The analysis indicates a range of measured pressure values, which could be caused by direction of traffic and drivers habits. To illustrate effect of traffic direction, the recorded data were separated into two categories, South to North and North to South directions. It was seen that for each pressure cell, the range of pressure measured narrowed significantly. As shown in Figure 7-34(a-c), the variation of applied stress reduced from 2 psi to 1 psi, 10 psi to 5 psi and 8 psi to 4 psi for EPCs 11, 21 and 32, respectively, after separating the recorded applied stress by travel direction. The separated measured stresses for all pressure cell are presented in Appendix E.

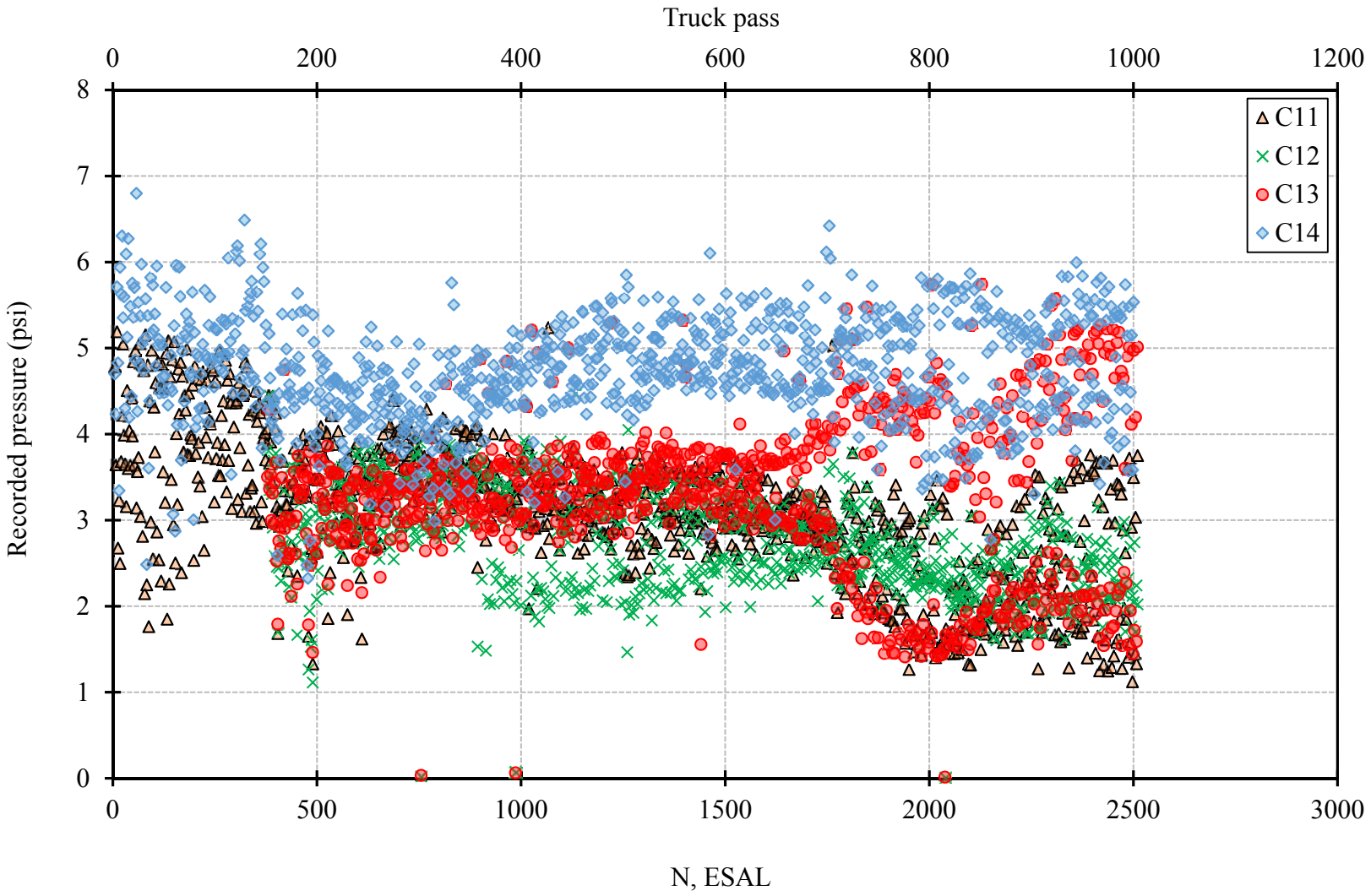

Figure. 7-31. Measured pressure in section 1

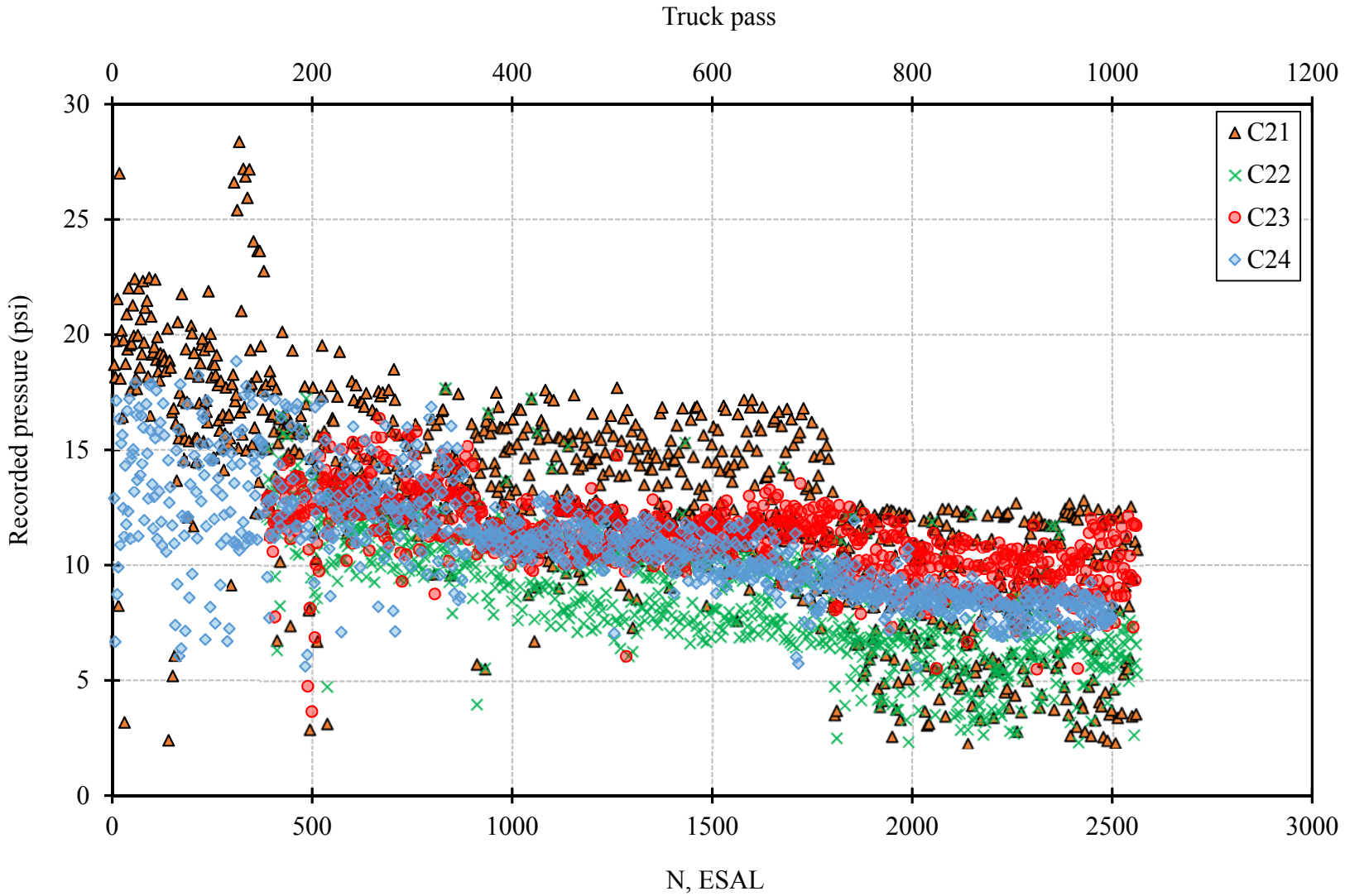

Figure 7-32. Measured pressured in Section 2

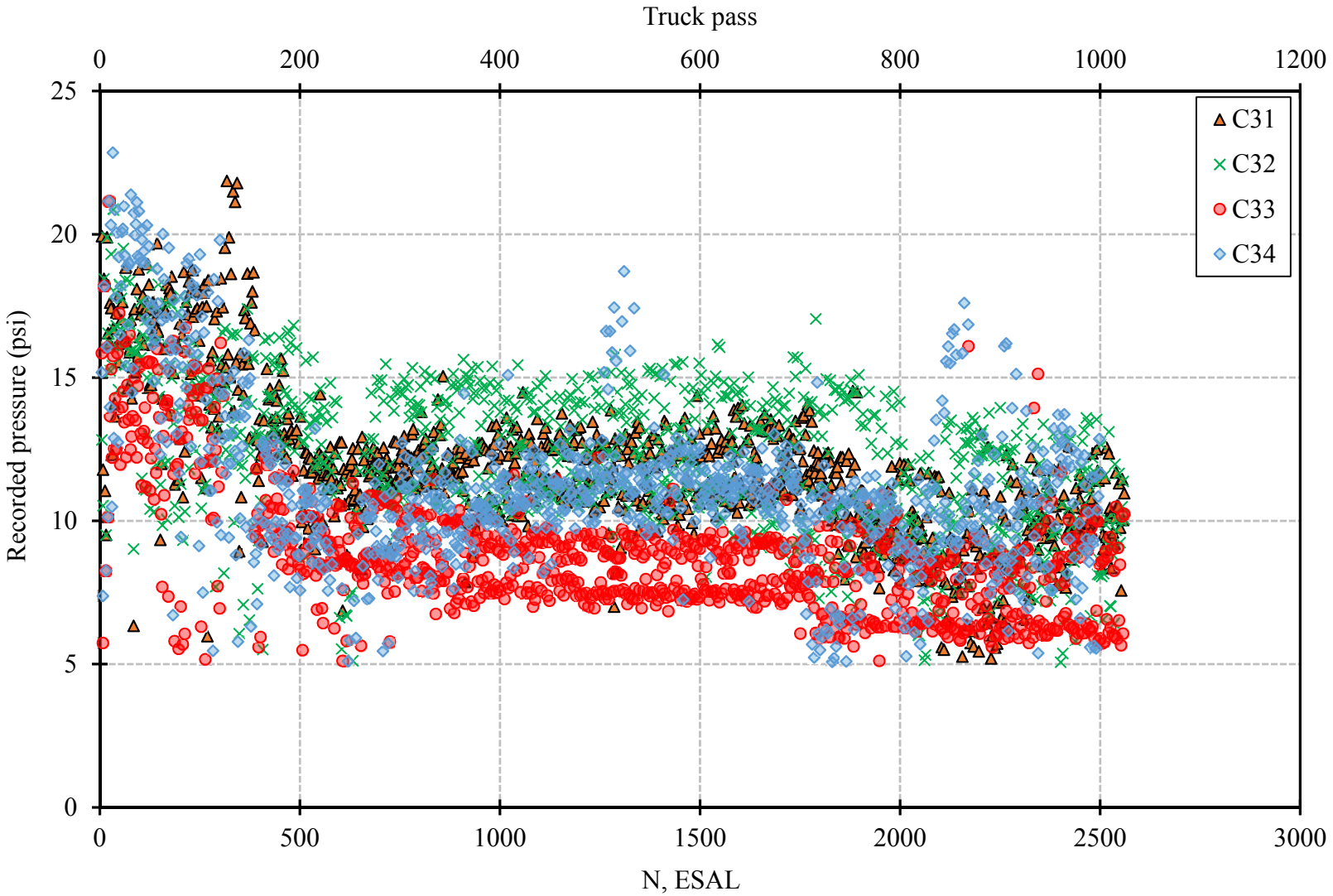

Figure 7-33. Measured pressure in section 3

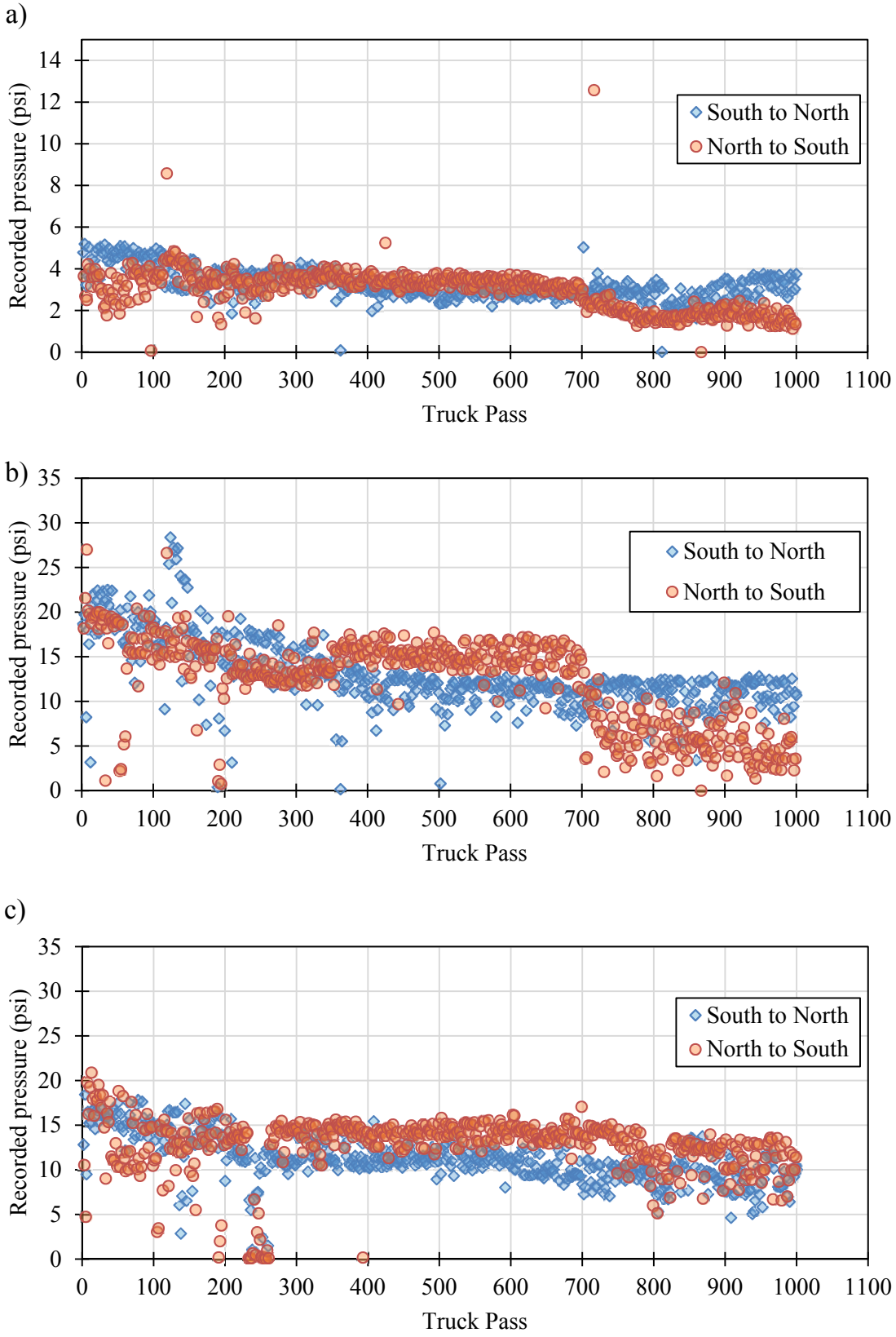

Figure 7-34. Measured pressure by traffic direction a) EPC11, b) EPC21, c) EPC32

Drivers' preference can be another reason for induced variability in data. Therefore, the recorded data were broken into three portions as shown in Figure 7-35, with each data set corresponding to a particular driver. It was concluded that, the second driver frequently missed the EPCs' locations (green dots).

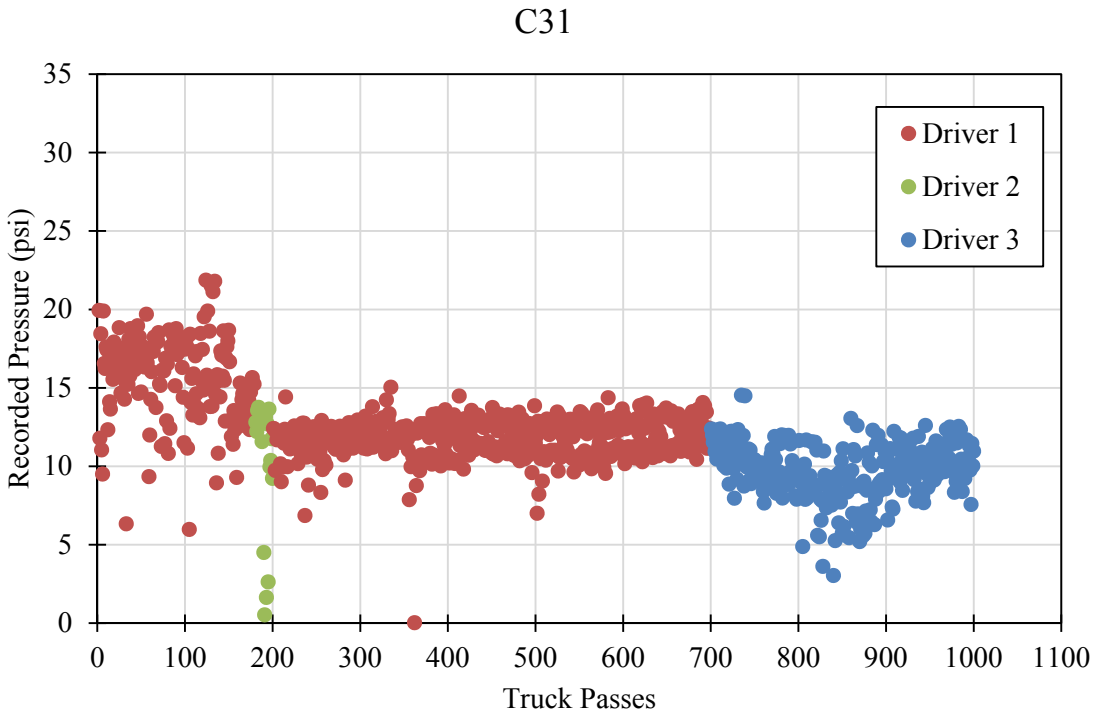

Figure 7-35. Distinguished measured pressure by drivers

Figures 7-36 and 7-37 show the surface deformation contours under the outer wheel path in section 2 that occurred during passes number 500 to 700 that were produced by driver No. 1 and passes number 700 to 800 that were produced by driver No.2, respectively. It can be seen that during passes 500 to 700, the earth pressure cells C21 and C22 were located right beneath the wheel path, and driver 1 was driving over the location of the EPC as intended. However, as shown in Figure 7-37, driver 2 was driving the truck in such a way that the location of outer wheel path was somewhat moved to the right and EPC C21 and C22 were located at the edge of the wheel path.

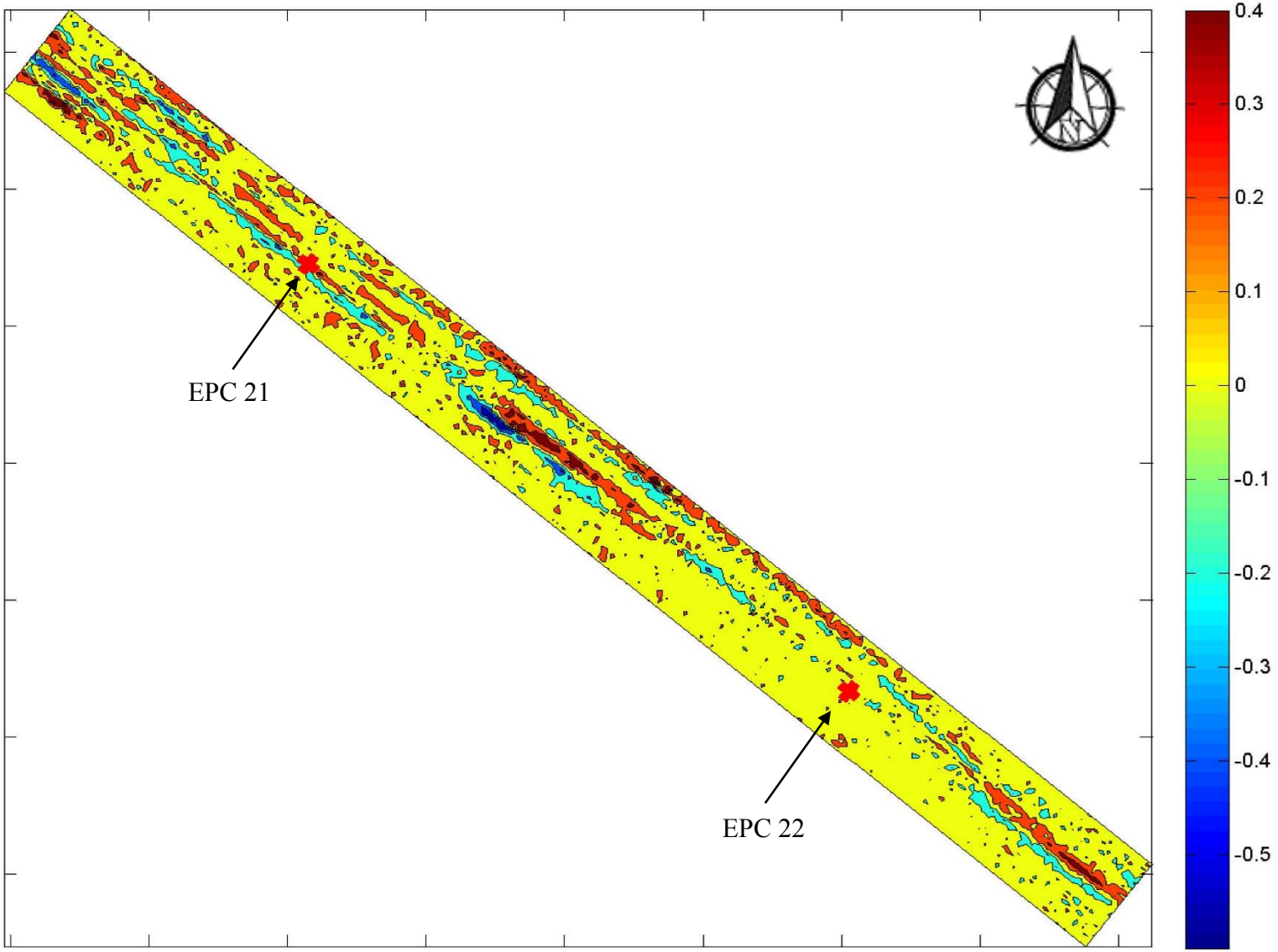

Figure 7-36. Surface deformation contours of OWP between passes No. 500-700, section 2-Driver 1

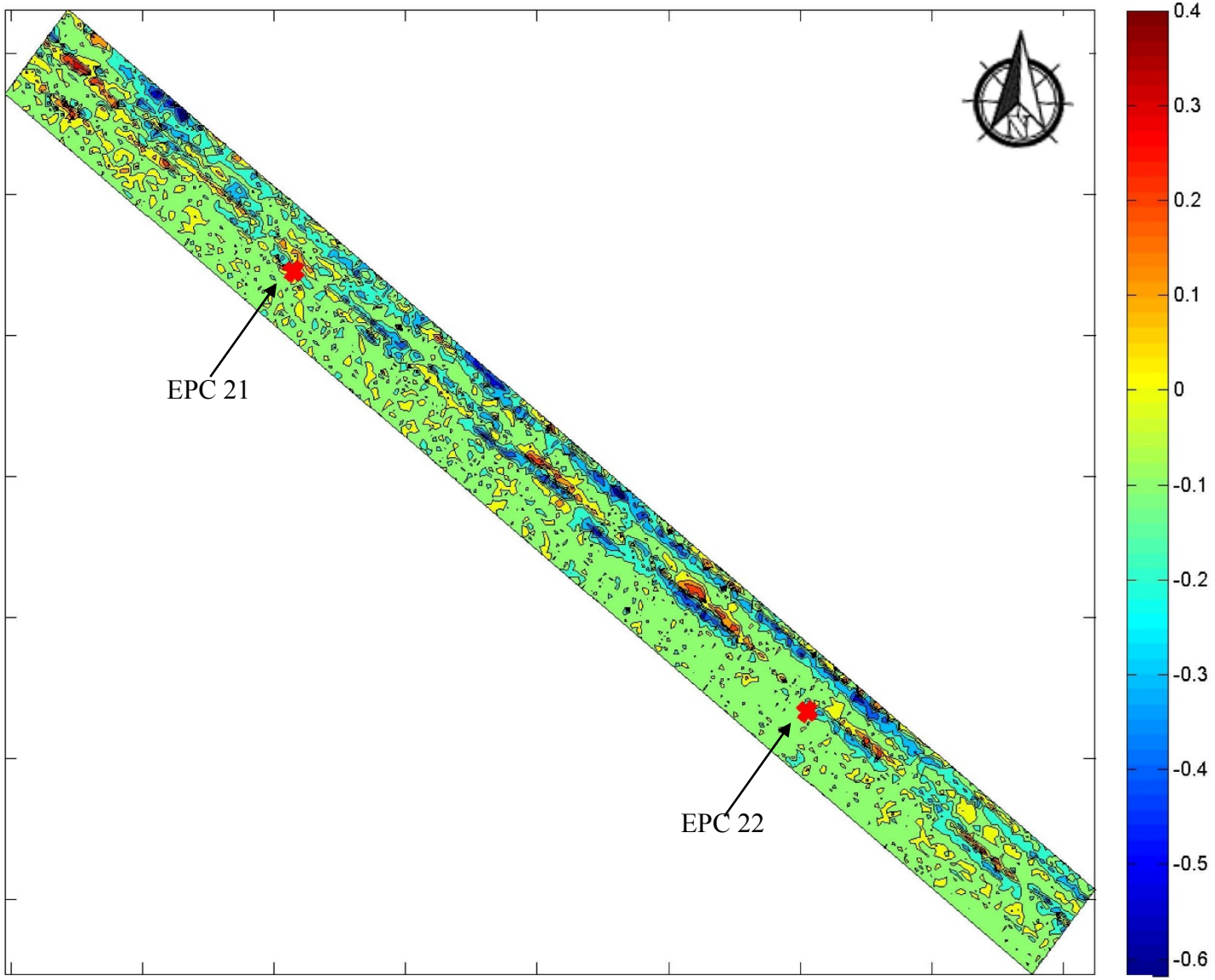

Figure 7-37. Surface deformation contours of OWP between passes No. 700-800, section 2-Driver 2

As shown in Figure 7-37, the truck wheels did not pass consistently over the location of the EPCs. Schematic diagrams in Figure 7-38 conceptualize different scenarios of EPC locations with respect to the truck configuration, and tire location. This is based on a tire contact area that is rectangular in shape and has dimension of 8" x 54". Figure 7-38(a) shows that if a driver tries to hit the EPC location on his side, the other EPCs would be off by 2" to 5" from the center of the tire contact area. Figure 7-38(b) indicates that the EPCs could be between 3 to 10 inches off of the loaded area if a driver completely misses the EPC on his side. Figure 7-38(c) demonstrates that if one of the EPCs is located exactly beneath center of the dual tires, the EPC on the other side would be under the outer wheel of the dual tires. This also may explain the difference of recorded pressure for the two traffic directions, north to south and south to north. Figure 7-38(d) shows a worst case scenario where the dual tires were at the edge of one EPC, (15" offset) and the EPC located on the other side is off by 9".

Ahlvin and Ulery (1962) presented a detailed tabulation for calculation of vertical stress below a uniformly loaded flexible area at any desired point. The vertical stress at any point located at depth z and distance r from the center of loaded area can be calculated by Eq. 7-1:

$$\Delta\sigma_z = q(A' + B') \qquad \text{Eq. (7-1)}$$

Where A' and B' are functions of z/a and r/a (and a= radius of loaded area)

Stress distribution with depth under a loaded area for the stated scenarios were calculated for a given rear axle load and tire pressure of 85 psi. As shown in Figure 7-39, the applied pressure with depth changes when the location of the loaded area moves laterally only a few inches. This is more pronounced for the shallow depths. It can be seen that for sections 2 and 3, where the EPC were located at 3" below the subgrade (~11" below the ground surface) the pressure has the potential to vary between 2 and 20 psi; and in section 1, with the EPC located 35" below the ground surface, the measured pressure might vary by 2 to 5 psi, which is consistent with measured values.

It is worth noting, that although the Ahlvin and Ulery (1962) table is for calculating stress distribution with depth in single layer elastic subgrade under static loading, it still presented results useful to explain the effect of the lateral-wheel wander on the measured pressure near the interface of the subgrade and stabilized layer.

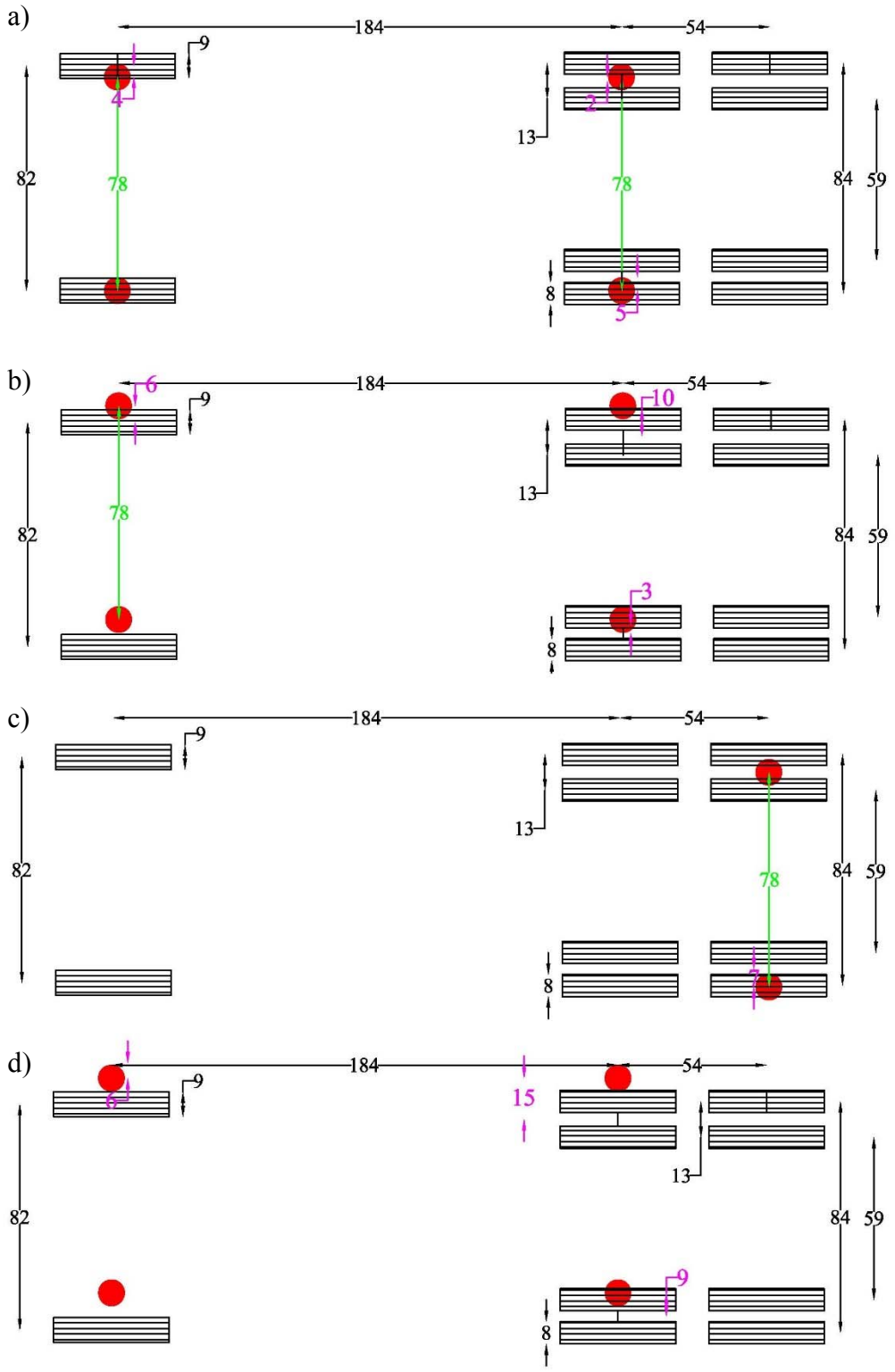

Figure 7-38. Tire locations relative to the EPCs used to perform stress analysis

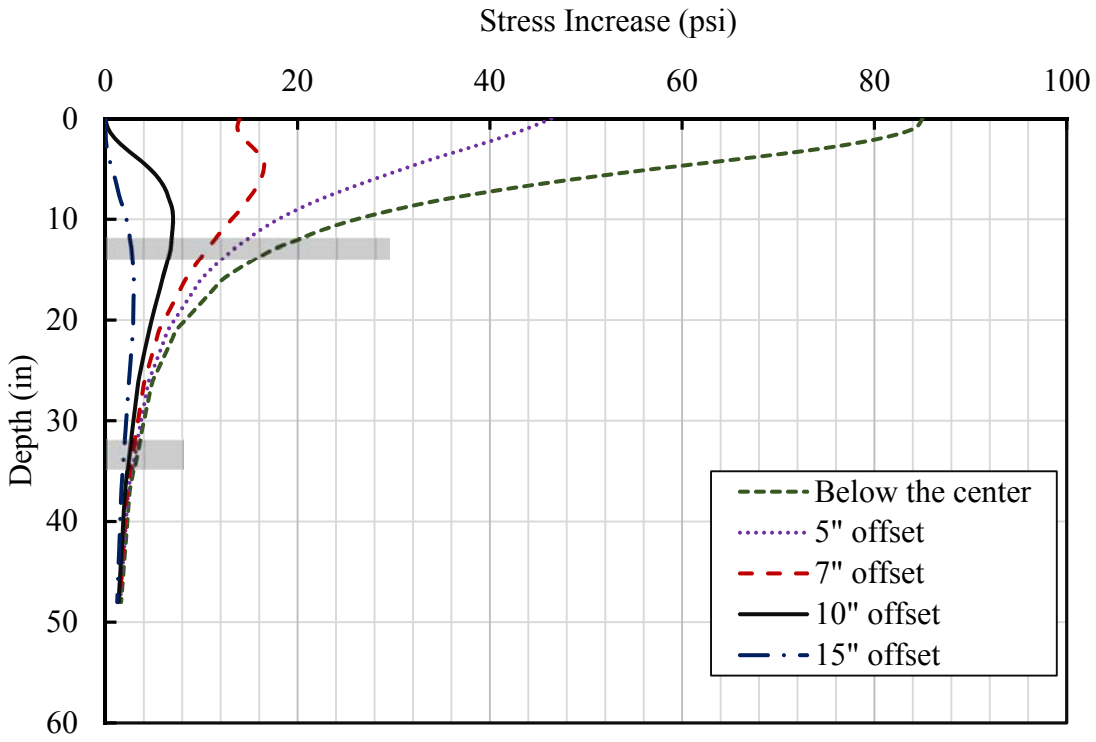

Figure 7-39. Estimate of the stress distribution at the EPC for different tire

7.6 Moisture and Suction Measurements

The moisture and suction of the subgrade layers were monitored and recorded by 10HS Decagon® moisture sensors and MPS-2 Decagon® suction sensors, respectively. As shown in Figure 7-40(a), in all test sections the volumetric moisture content changed by 1-2% during testing. It can be seen from Figure 7-40(b) that the matric suction was decreasing during the first week after installation, and started to increase slightly during the duration of the full scale testing.

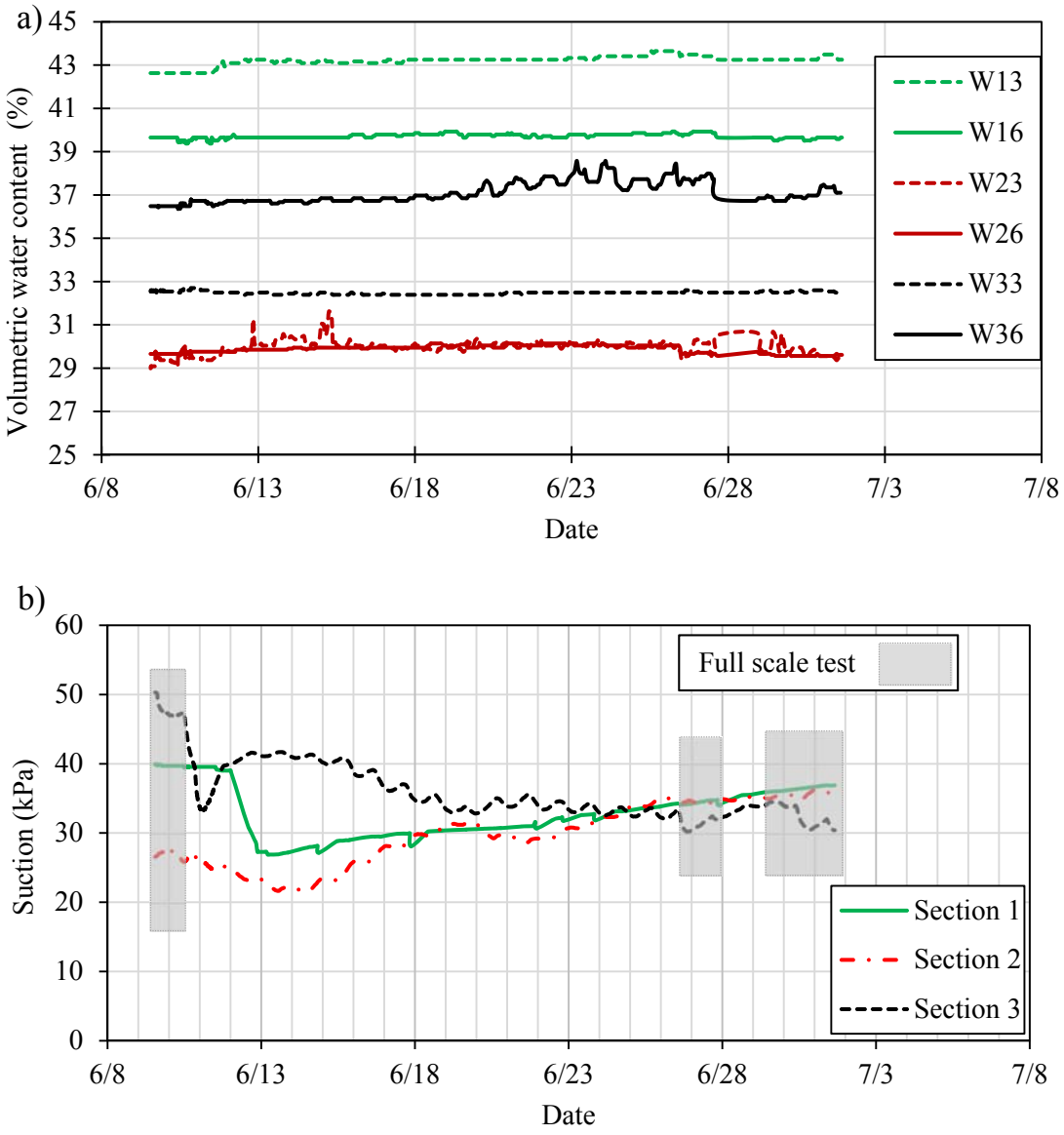

Figure 7-40. a) Recorded volumetric water content (top) b) matric suction (bottom)

7.7 Summary

In summary, the measured vertical stress near the interface of the subgrade for the geosynthetics-reinforced sections was decreased with the number of truck loading from 20 psi to 10 on section 2, and from 16 psi to 8 psi on section 3. This is attributed to the densification of the aggregate base course as well as the increasing the matric suction level of the base layer, from 25 kPa to 35 kPa, as a result of the hot weather during the summer. The geosynthetics-reinforced sections

experienced 0.5” and 0.7” of surface deformation for the geogrid- and geotextile-reinforced sections, respectively, while the select fill-stabilized section showed a 1.2” vertical deformation after 1000 traffic passes. The rut depth increased with traffic passes and reached a relatively constant value within the 1000 truck passes. In this case, in both geotextile and geogrid sections, the rut depth increased until 500 truck passes while in section 1, the rut depth reached its limit after 700 passes.

CHAPTER 8: NUMERICAL ANALYSIS

An extensive set of finite element analyses have been performed in PLAXIS 2D and 3D to simulate behavior of the field test sections under construction loading. The deformation behavior of the subgrade soil and aggregate base course layer was investigated in the context of Mohr-Coulomb, Hardening Soil (HS), and Hardening Soil Small Strain (HS small) constitutive models. A summary of the FEM analyses is presented in this chapter.

8.1. Model Parameters

As previously described, the constitutive models require as an input stiffness and shear strength parameters. In order to assign appropriate parameters to the subgrade and ABC layers, the results from the laboratory tests on the undisturbed specimens were used. The parameters utilized herein are from the resilient modulus, monotonic triaxial compression and bender element tests.

8.1.1 Aggregate base course

As stated in Chapter 3, aggregate base course class IV was used in test sections 2 and 3, which were reinforced with geogrids and geotextiles, respectively. The grain size distribution of the ABC used in this study is presented in Figure 8-1. In order to select appropriate stiffness parameters (E_{50}, E_{oed}, E_{ur}, G_0 and $\gamma_{0.7}$) for the analyses, reported results from the literature on the ABC material were used. Cowell et al. (2012) performed a series of resilient modulus tests on the ABC class IV used in their study. They found the resilient modulus of the ABC with relative compaction of 95%, can be described by Eq. 8-1 (M_r expressed as a function of the bulk stress):

$$M_r = 4.1046\theta^{0.6085} \qquad \text{Eq. (8-1)}$$

As shown in Figure 8-1, the grain size distribution of the ABC used in Cowell et al. (2012) study is comparable to the ABC used in this study; hence their results are utilized herein. In order to select the appropriate bulk stress level, a series of trials were performed in PLAXIS, by changing the resilient modulus and evaluating the resulting vertical and lateral pressures. The E_{50} and E_{oed} are selected as equal to 1/3 of E_{ur}.

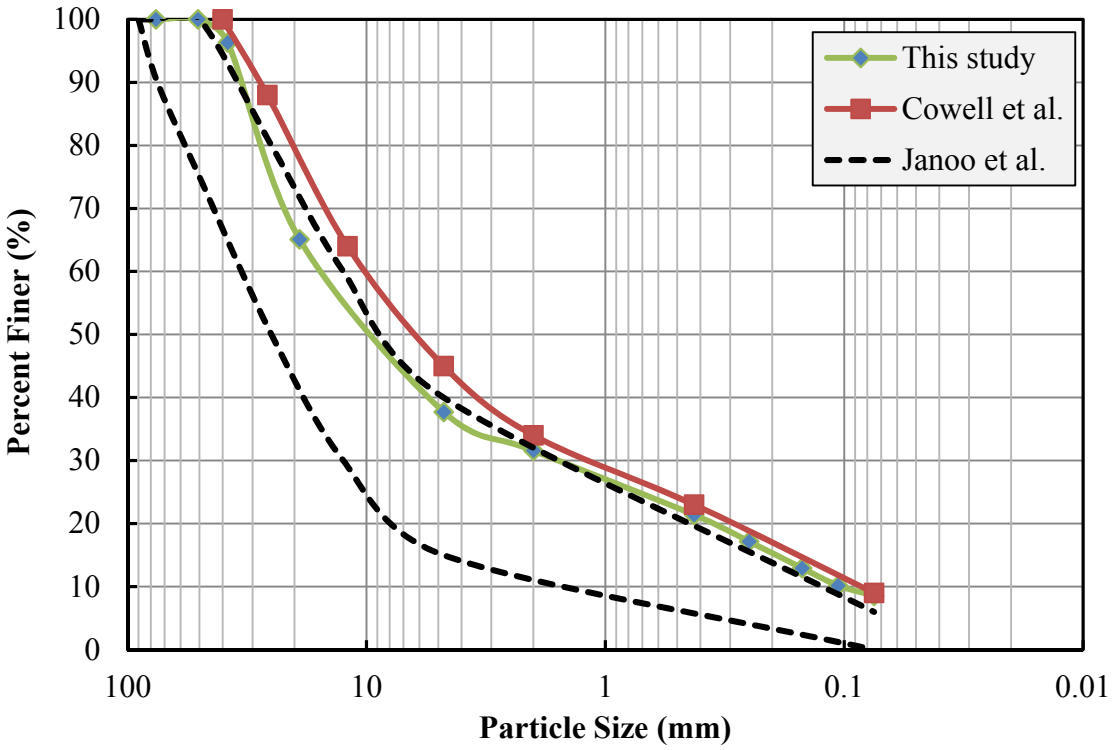

Figure 8-1. Grain size distributions of ABC

Janoo et al. (2004) reported the results of laboratory monotonic triaxial compression tests on ABC materials with grain size distributions shown is Figure 8-1. Since the grain size distribution of the ABC material used in this study falls toward the finer range of their study materials, their results are used to estimate a friction angle of 43degrees and cohesion of 8 psi. these are used as input parameters for the numerical analyses performed herein..

Ayithi and Hiltunen (2013) performed fixed-free resonant column testing on compacted ABC specimens to investigate the effect of the matric suction, confining pressure and void ratio on the small strain shear modulus (G_0). As shown in Figure 8-2, the grain size distribution of the Georgia Granit ABC used in their study is comparable to the ABC used in this study, and both material are classified as GW-GM, according to the USCS System. The reported G_{max} results by Ayithi and Hiltunen (2013), at the reference pressure, is used herein for numerical analyses.

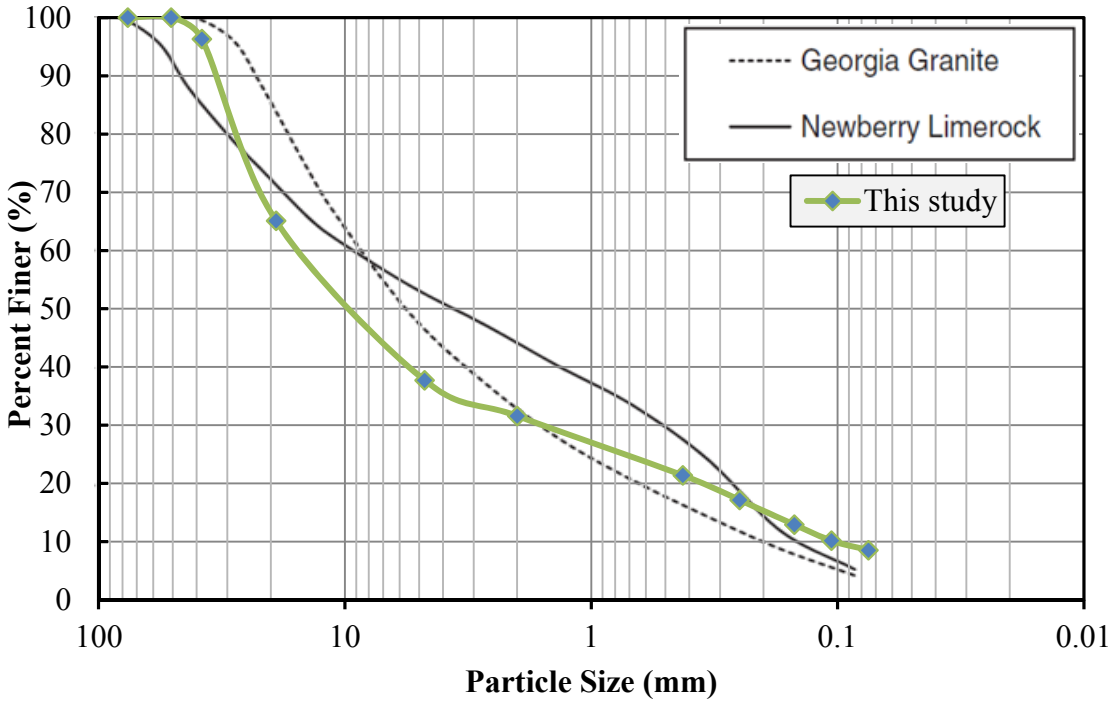

Figure 8-2. Grain size distribution curves of ABC from this study and that tested by Ayithi and Hiltunen (2013)

The stiffness and shear strength properties of the ABC material used for the numerical analyses are summarized in Table 8-1.

Table 8-1. ABC material properties used in numerical analyses.

CM[1]	H (in)	γ_{moist} (pcf)	e_0	E_{50}^{ref} (ksi)	E_{oed}^{ref} (ksi)	E_{ur}^{ref} [2] (ksi)	m	ν_{ur}	G_0^{ref} (ksi)	$\gamma_{0.7}$ (%)	φ'	c'(psi)	R_f
HS Small Strain	8	144	0.4	24	24	48	0.64	0.2	35	0.005	43	8	0.9
HS	8	144	0.4	24	24	48	0.64	0.2	NA	NA	43	8	0.9
MC	8	144	0.4	NA	NA	35	NA	0.2	NA	NA	43	8	NA

[1] Constitutive model

[2] E @ $\sigma_3 = 3.47$ and $\sigma_1 = 27.2$ *psi*, for MC model

8.1.2 Subgrade soils

Based on the index properties and construction history at the test site, it was concluded that the upper 32 inches of the site soil was a compacted fill classified as A-4 (SM); underlain by a natural high plasticity Silt, A-7-5 (MH). A series of laboratory tests, including the resilient modulus, monotonic triaxial compression, and bender element tests were carried out in order to obtain parameters for the numerical analyses constitutive model. The E_{50}^{ref} values were computed from monotonic triaxial test performed at the reference confining pressure (14.5 psi). The E_{ur}^{ref} values were obtained by extrapolating the resilient modulus test results to obtain the M_r at the reference confining pressure and vertical stress of 8 psi. The E_{ur}^{ref} was directly obtained from the resilient modulus test, at $\sigma_3 = 2$ and $\sigma_1 = 8\ psi$. The G_0^{ref} was measured by bender element test at the reference confining pressure. The $\gamma_{0.7}$ was selected from reported Resonant Column test results by Borden et al. (1996) on the Piedmont soils. For the A-7-5 (MH) subgrade soil, the undrained shear strength parameters were computed from the in situ field testing. These parameters are summarized in Table 8-2 and 8-3 for the A-4 and the A-7-5 soils, respetively.

Table 8-2. A-4 soils properties used in numerical analyses.

CM[1]	H (in)	γ_{moist} (pcf)	e_0	E_{50}^{ref} (ksi)	E_{oed}^{ref} (ksi)	E_{ur}^{ref} [2] (ksi)	m	ν_{ur}	G_0^{ref} (ksi)	$\gamma_{0.7}$ (%)	φ'	c'(psi)	R_f
HS Small Strain	24	123	0.57	3	3	14.5	0.5	0.2	21	0.01	25	2	1
HS	24	123	0.57	3	3	14.5	0.5	0.2	NA	NA	25	2	1
MC	24	123	0.57	NA	NA	5	NA	0.2	NA	NA	25	2	NA

[1] Constitutive model

[2] E @ $\sigma_3 = 2$ and $\sigma_1 = 8\ psi$, for MC model

Table 8-3. A-7-5 soils properties used in numerical analyses.

CM	H (in)	γ_{moist} (pcf)	e_0	E_{50}^{ref} (ksi)	E_{oed}^{ref} (ksi)	E_{ur}^{ref} (ksi)	m	ν_{ur}	G_0^{ref} (ksi)	$\gamma_{0.7}$ (%)	Su (psi)	R_f
HS Small Strain	148	120	0.84	7	3.5	21	1	0.2	80	0.0038	20	1
HS	148	120	0.84	7	3.5	21	1	0.2	NA	NA	20	1
MC	148	120	0.84	NA	NA	15	NA	0.2	NA	NA	20	NA

8.1.3 SWCC and matric suction state

The soil water characteristic curves for the ABC, A-4, and A-7-5 soils were developed from the data collected in this study as well as proposed correlations in the literature. These were also verified by laboratory-measured suctions using a miniature tensiometer.

8.1.3.1 ABC SWCC

The SWCC of ABC materials was estimated from the data presented by Ba et al. (2013). Figure 8-3, shows grain size distribution for the Bakel Black Quartzite ABC. This grain size distribution is the closest to the ABC material used in this study that the authors can find in literature. Therefore, the reported SWCC parameters for Bakel Black Quartzite ABC are used for numerical analysis.

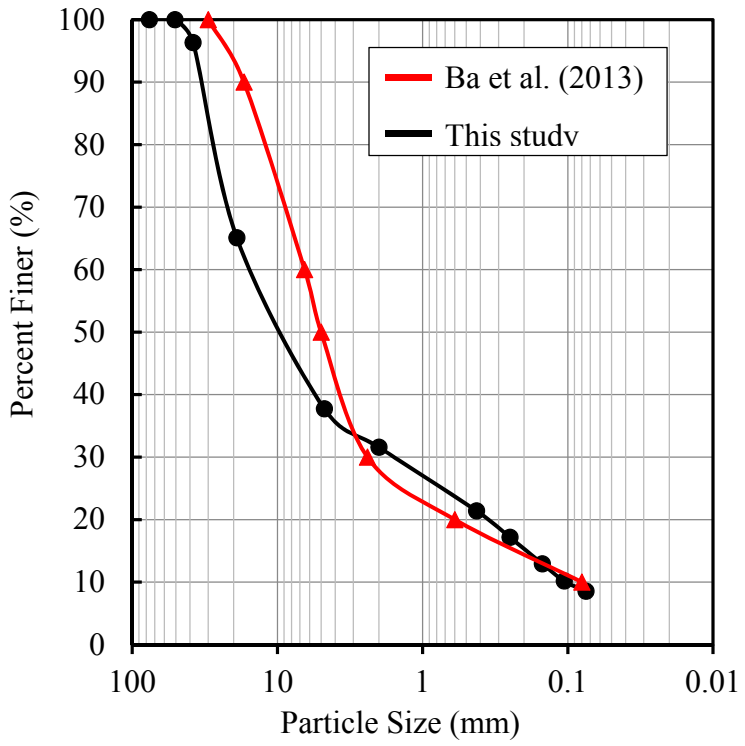

Figure 8-3. Bakel Black Quartzite ABC grain size distribution, Ba et al. 2013

Figure 8-4 shows the developed ABC SWCC curve based on the Fredlund and Xing (1994) model. The SWCC parameters are presented in Table 8-4 for the two subgrade soil types and the ABC layer.

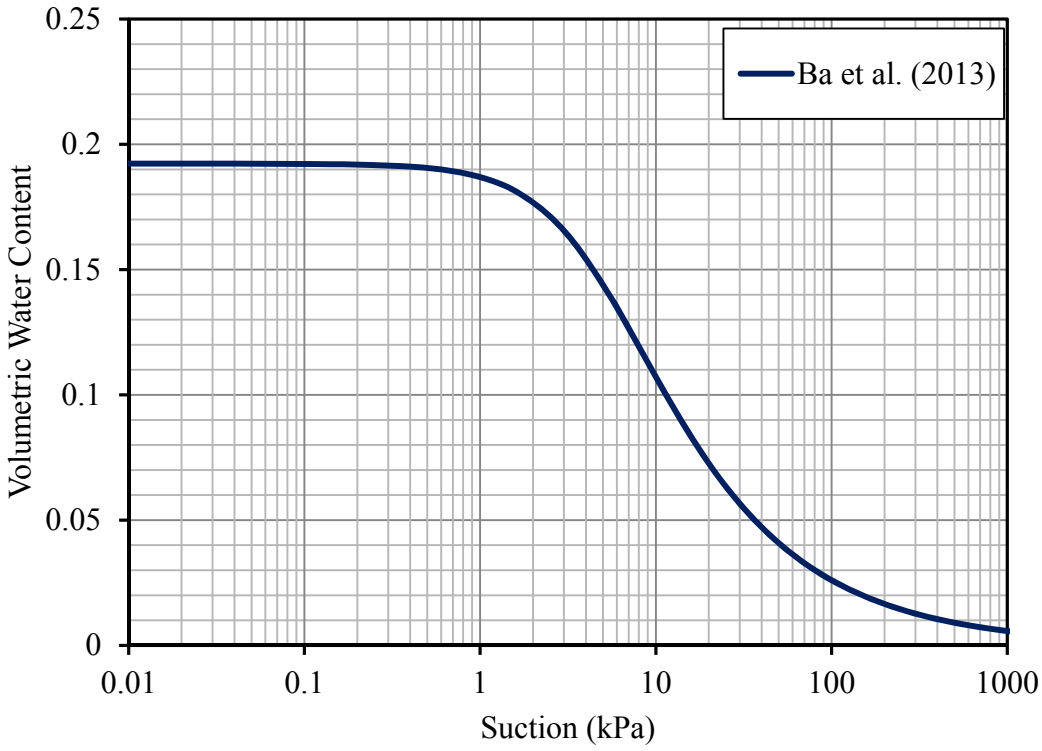

Figure 8-4. Aggregate base course SWCC, Ba et al. (2013).

Table 8-4. Fredlund and Xing (1994) SWCC model parameters.

	θ_s	θ_r	a	n	M
A-4 (SM)	0.36	0.09	0.13	2.6	0.6154
A-7-5 (MH)	0.54	0.03	0.1365	1.1487	0.1295
ABC	0.1923	0.00001	0.20	1.6577	0.3967

8.1.3.2 A-4 (SM) soil SWCC

The SWCC for the A-4 soil was developed based on the proposed model by Zapata et al. (2000) for soil with PI=0. Figure 8-5 shows the developed SWCC and laboratory measured suction values obtained within the Shelby tube samples. It can be seen that the laboratory-measured suction values are in good agreement with the SWCC estimated from the soil-properties.

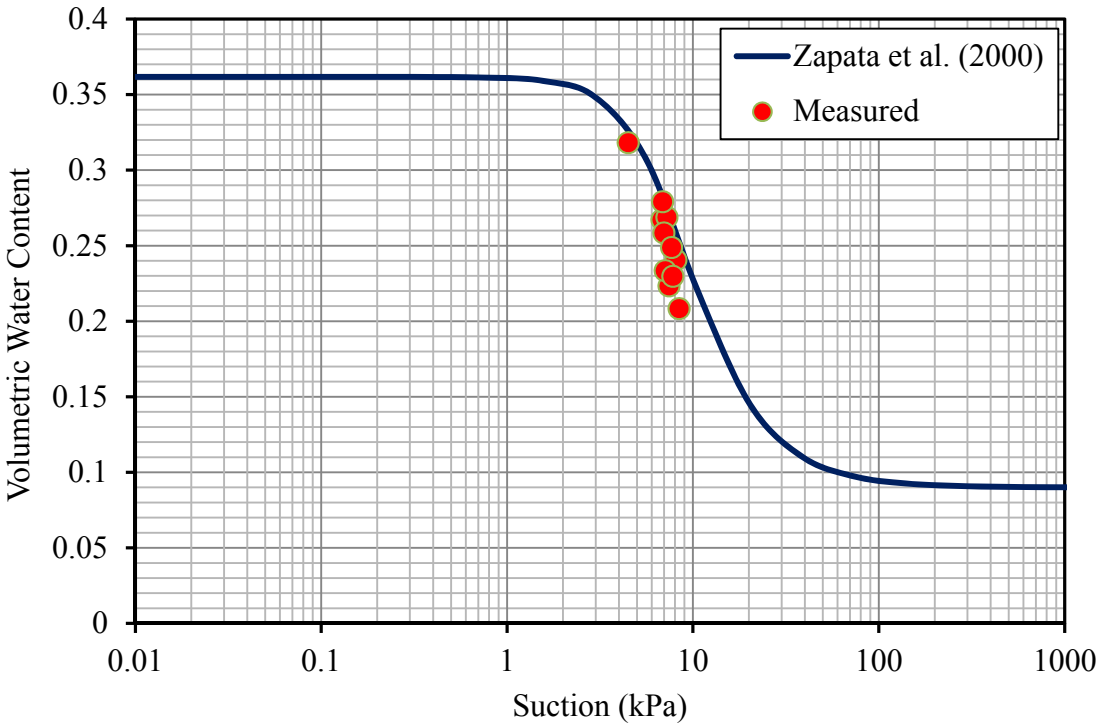

Figure 8-5. Developed A-4 (SM) soil SWCC, from Zapata et al (2000)

8.1.3.3 A-7-5 (MH) soil SWCC

Wang (2014) performed extensive laboratory SWCC testing on Piedmont residual soils from Greensboro, North Carolina. The tested materials included a wide range of the low to high plasticity soils. The grain size distribution and laboratory measured suction values of the A-7-5 soil specimens were compared to those tested by Wang (2014). Figure 8-6 shows the developed SWCC for the A-7-5 soil by Wang (2014), as well as tensiometer-measured suctions from Shelby tubes samples obtained in this study. It can be seen that developed SWCC by Wang (2014) is compatible with the laboratory-measured suction levels in this study. The SWCC properties of the A-7-5 soil are presented in Table 8-4.

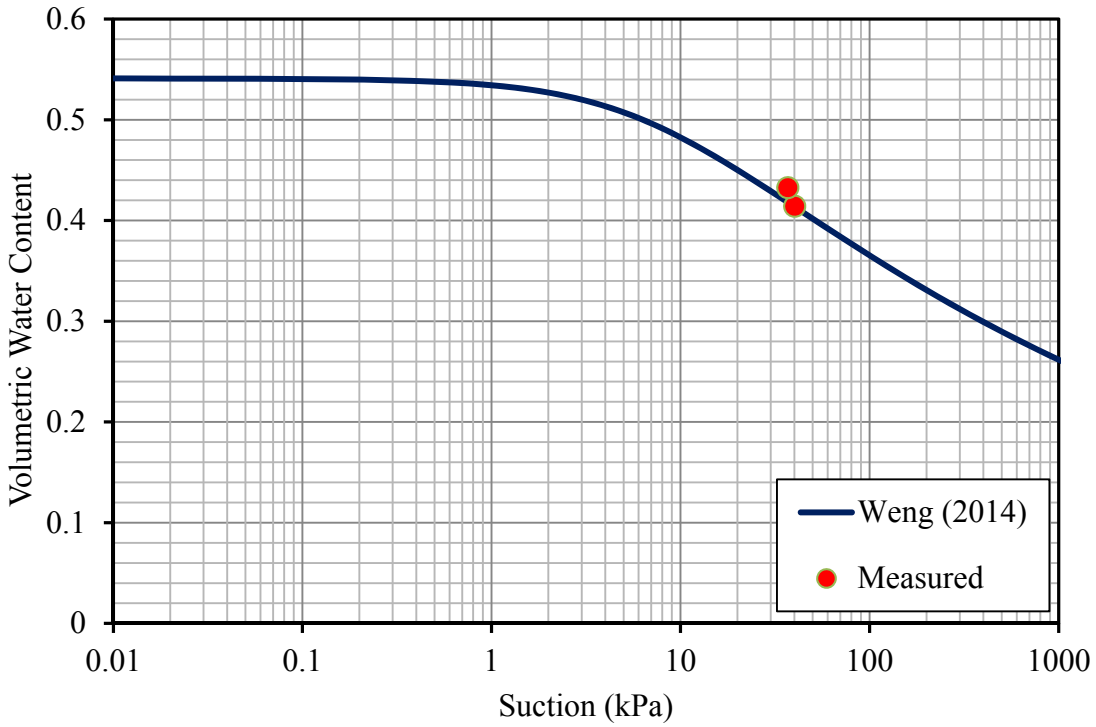

Figure 8-6. Developed SWCC for A-7-5 soil, Wang (2014)

8.1.4 Geosynthetics and Interface

The geosynthetic reinforcement was modeled in FEA analyses as a linear elastic material. The only needed parameter for geosynthetic materials is an elastic normal stiffness, EA, which is given by Eq. 8-2:

$$EA = \frac{T_{@\varepsilon\%}}{\varepsilon} \qquad \text{Eq. (8-2)}$$

Where $T_{@\varepsilon\%}$ is the axial strength at a given magnitude of strain, $\varepsilon\%$. The EA values of 16200, and 48000 (lb/ft) were calculated for the geogrid and geotextile used in the full scale testing, respectively, at a strain level of 5%. The interface layers are defined on both side of the geogrid. A reduction factor of 1 (meaning no reduction in the interface strength, or 100% efficiency of the geosynthetic materials) was assigned to the interface of geogrid and ABC, and geogrid and subgrade soil.

8.2 Selection of Appropriate Constitutive Model

A series of 2D axisymmetric Finite Element Analyses (FEA) were performed in PLAXIS. The geogrid-reinforced test section (section 2) was modeled by assigning the stiffness and shear strength properties, as described in the previous section, to the base and subgrade layers. The deformation behavior of the test section was investigated under cyclic loading within the context of the three soil constitutive models.

8.2.1 Model geometry

The geometry of the geogrid reinforced section was evaluated under cyclic traffic loading. From Lidar Scan data, the initial thickness of ABC is esimtated as 8 inches. From the Shelby tube, the initial thickness of the A-4 soil was estimated as 32 inches. This soil was underlain by the stiff A-7-5 soil. Therefore, in the numerical analyses, 8 inches of ABC is considered overlying 24 inches of soft A-4 soil, which is underlain by a stiff A-7-5 soil. The geometry was modeled in axisymmetric mode, with 15-node triangle elements in a 180 by 120 inches domain (after Howard and Warren, 2009), as shown in Figure 8-7. The generated mesh is very fine under the loaded area, and slightly coarsened with distance away from the center of the loaded area.

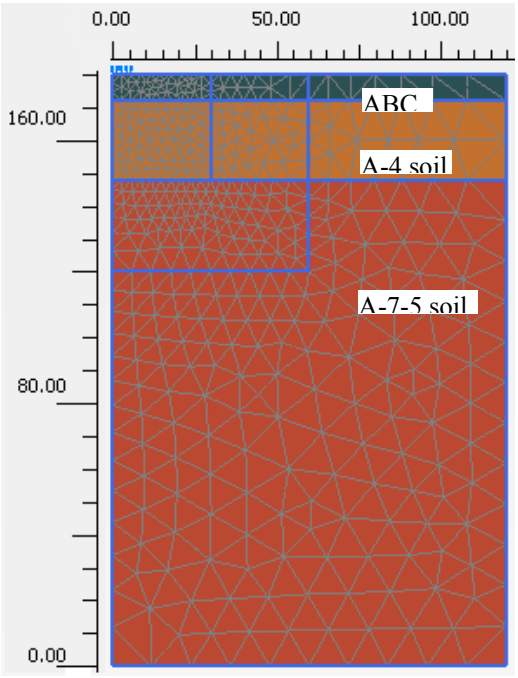

Figure 8-7. FEM domain

8.2.2 Cyclic loading

Analyses were performed to investigate the deformation behavior of unreinforced section under cyclic loading. The shape of the cyclic load was captured from the EPC recorded data, as shown in Figure 8-8. As previously described, a tire pressure of 85 psi was measured in the field and a rear axle load of 9000 lbs was estimated from the measured truck weight. Therefore, the radius of the loaded area was computed as 5.8 inches. Absorbent boundaries were assigned into the model to absorb stress waves without rebounding into the loaded area.

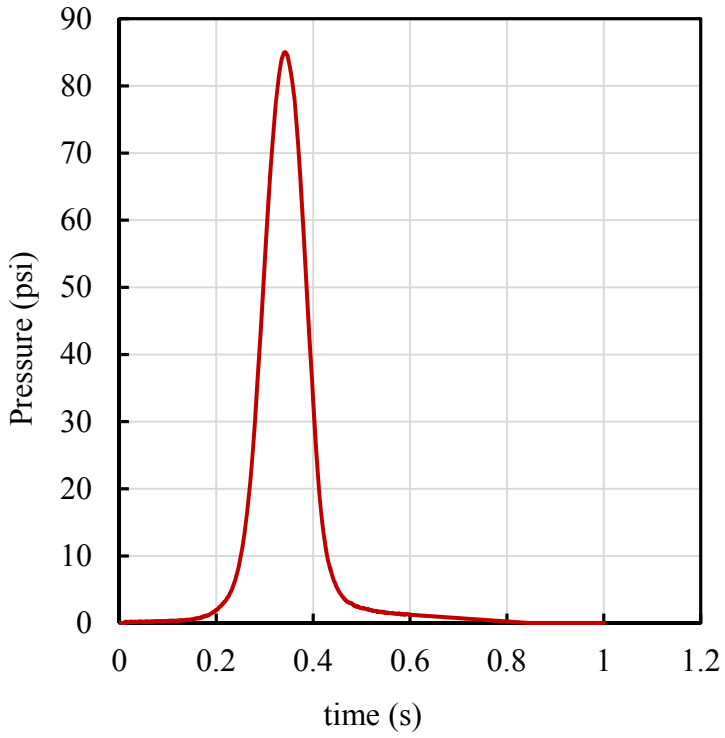

Figure 8-8. One applied load cycle.

8.2.3 Appropriate constitutive model

Figure 8-9 shows the vertical deformation of the unreinforced section under cyclic loading with the use of the Mohr-Coulomb constitutive model. It can be seen that after 20 load cycles, the cumulative deformation approaches a constant value and does not change thereafter. As shown in Figure 8-10, the computed applied stress at the top of the subgrade also does not change after 20 load cycles; which is not in agreement with the field observation.

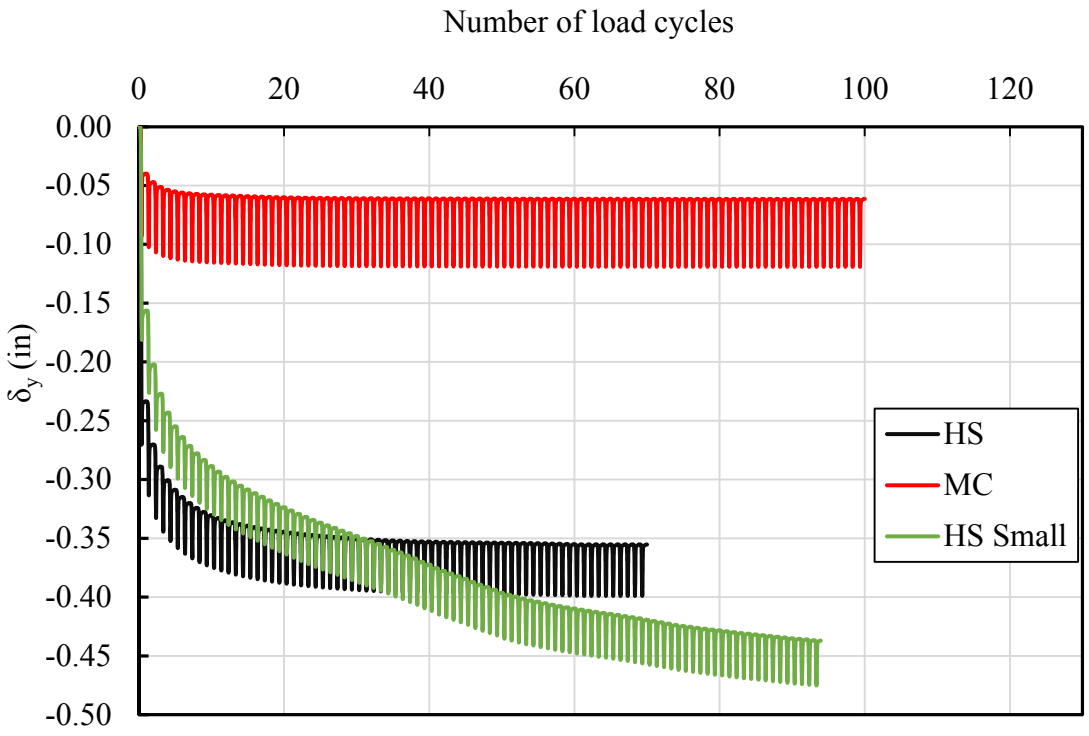

Figure 8-9. Vertical deformation at the surface under cyclic load

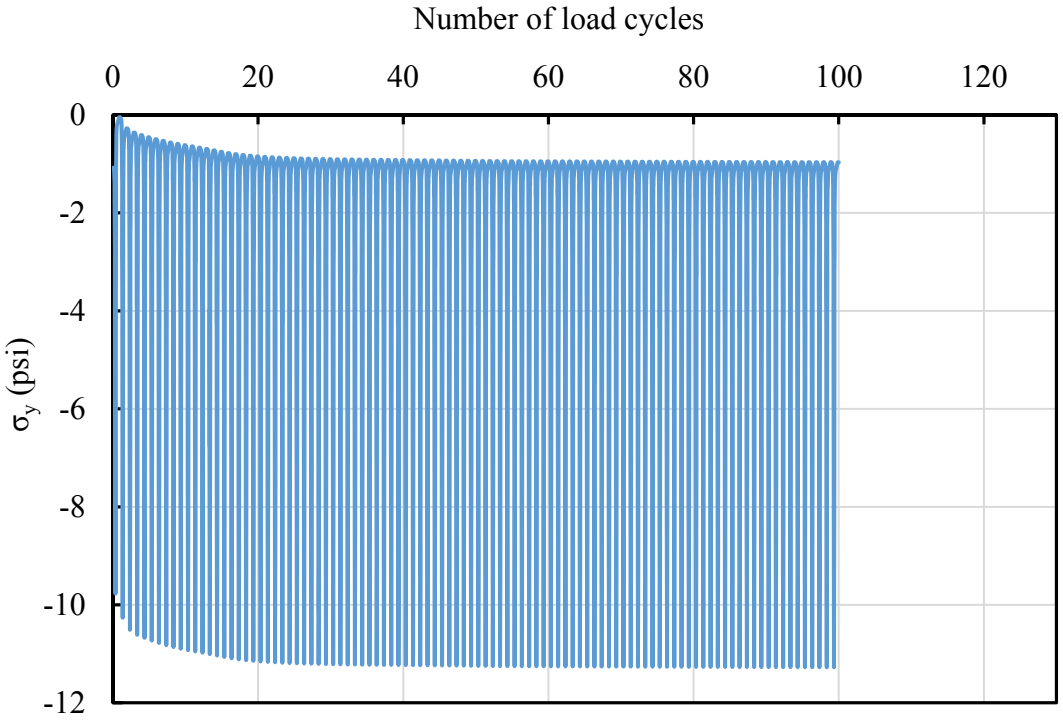

Figure 8-10. Vertical stress at the top of the subgrade (MC)

The computed surface vertical deformation from the HS model, under cyclic load, is shown in Figure 8-9. In contrast to the MC model, it can be seen that the cumulative vertical deformation increases until load cycles No. 60, and it is significantly greater than the values obtained from the MC analyses. Figure 8-11 shows the computed vertical stress at the top of the subgrade, which is seen to increase slightly with number of load cycles unit it reaches a constant value at load cycle No. 60. Compared to the results from MC model, the computed vertical stress from HS model is greater by a factor of three.

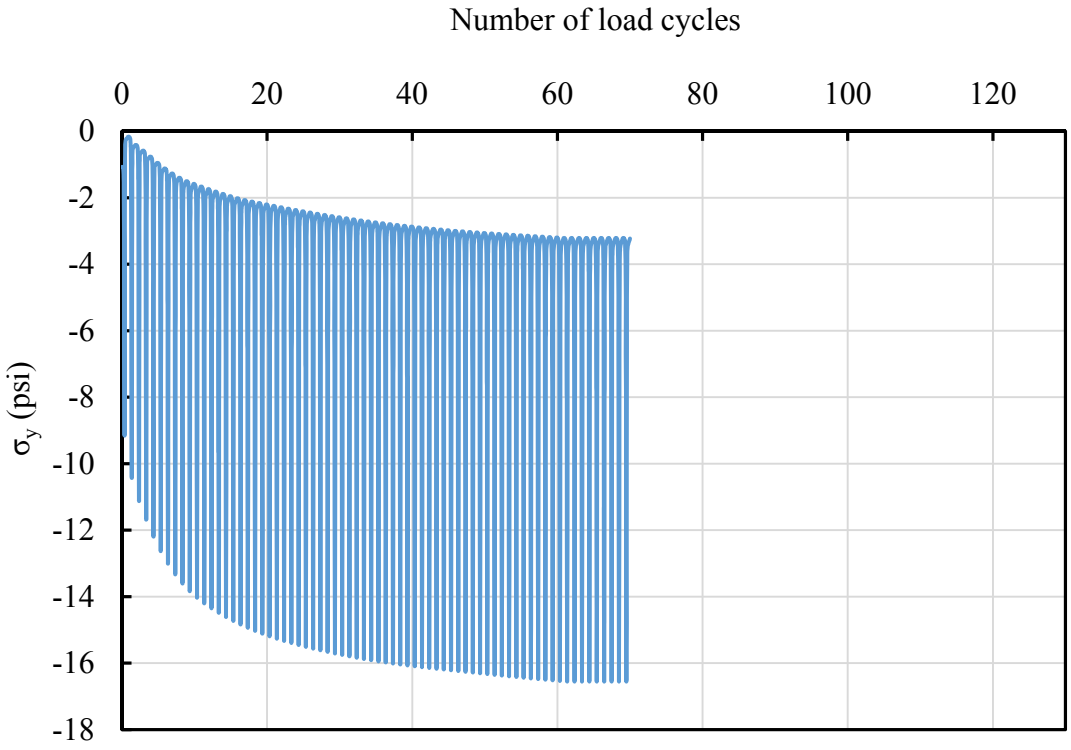

Figure 8-11. Vertical stress at the top of the subgrade (HS)

The third soil model investigated is the HS Small Strain, with the computed vertical deformation under cyclic loading plotted in Figure 8-9. For this case, it can be seen that the cumulative vertical deformation is still increasing after 90 load cycles, which is consistent with field observations. From these results, it is concluded that the HS Small Strain model is the more suitable soil constitutive model, as it is capable of capturing the incremental cumulative deformation of base/subgrade layers under cyclic loading. In contrast to the HS model, the HS Small Strain model will show hysteretic behavior of soils under cyclic loading, as shown in

Figure 8-12. After load reversal is detected, the stiffness is reset at G_0, and reduces again during unloading until the next load reversal. Therefore HS small model "memorizes" strain history and uses a generalized shear strain parameter to determine corresponding shear modulus. The strain history used in HS small model is given by Eq. 8-3 (Equations to follow are from PLAXIS Manual):

$$\gamma_{hist} = \sqrt{3}\frac{\left\|\underline{\underline{H}}\,\Delta\underline{e}\right\|}{\left\|\Delta\underline{e}\right\|} \qquad \text{Eq. (8-3)}$$

Where $\underline{\underline{H}}$ is a symmetric tensor that represents the deviatoric strain history of the material, while $\Delta\underline{e}$ is the actual deviatoric strain increment. Once the direction of the strain is reversed, the tensor $\underline{\underline{H}}$ is partially or fully reset and then the actual deviatoric strain tensor is applied into the equation. In order to take the strain history into account, Eq. 2-18 is modified in HS small model to Eq. 8-4:

$$\frac{G_s}{G_0} = \frac{1}{1+0.385\left|\frac{\gamma_{hist}}{\gamma_{0.7}}\right|} \qquad \text{Eq. (8-4)}$$

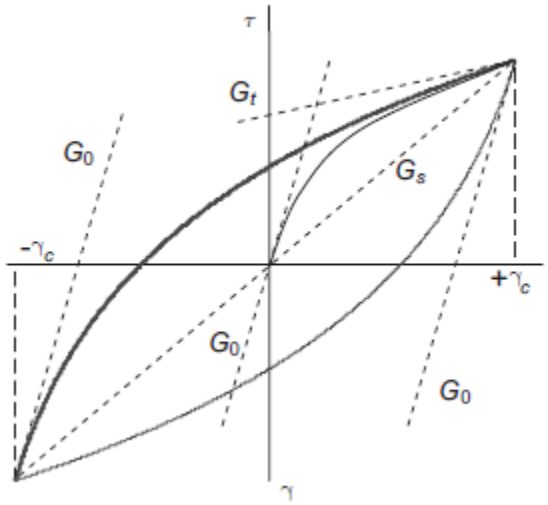

Figure 8-12. Hysteretic behavior in HS small

Although both HS and HS small models take into account the softening and hardening behavior of soils with increasing confining pressure and strain levels, the HS model does not account for higher soil stiffness values related to very small strain levels (i.e. $\epsilon = 10^{-5}$-10^{-4}), hence as shown in the Figure 8-9, the computed vertical deformations from HS model are greater than those from HS Small model, for the first 30 load cycles.

8.2.4 Reinforced behavior: the issue with PLAXIS 2D

Permanent deformation behavior of the reinforced section was simulated in the axisymmetric mode in PLAXIS 2D. Interface layers were used between the geogrid reinforcement and the ABC layer as well as between the geogrid and subgrade. After comprehensive analyses it was realized that the PLAXIS 2D axisymmetric mode is not able to capture the deformation behavior of the geosynthetic reinforced sections using interface layers. As shown in Figures 8-13(a-b), a significant gap develops between the geogrid and the soil mass underneath.

It was realized under cyclic load, the gap starts to occur during the unloading phase and it is scaled by the number of load cycles. After communicating with PLAXIS engineers, their response was that *"The gap observed is due to low stiffness of the structure part connected at the left boundary, the scientific background is as mentioned earlier that, in axisymmetry mode, material stiffness is calculated based on how far away the stress point is from the axis-of-symmetry, therefore when you connect interface/ geogrid to the axis, you have ultra-low material stiffness for the stress point lying in the axis, that triggers the phenomenon".*

Therefore, it was decided to use PLAXIS 3D in order to model the reinforced sections with interface under cyclic load.

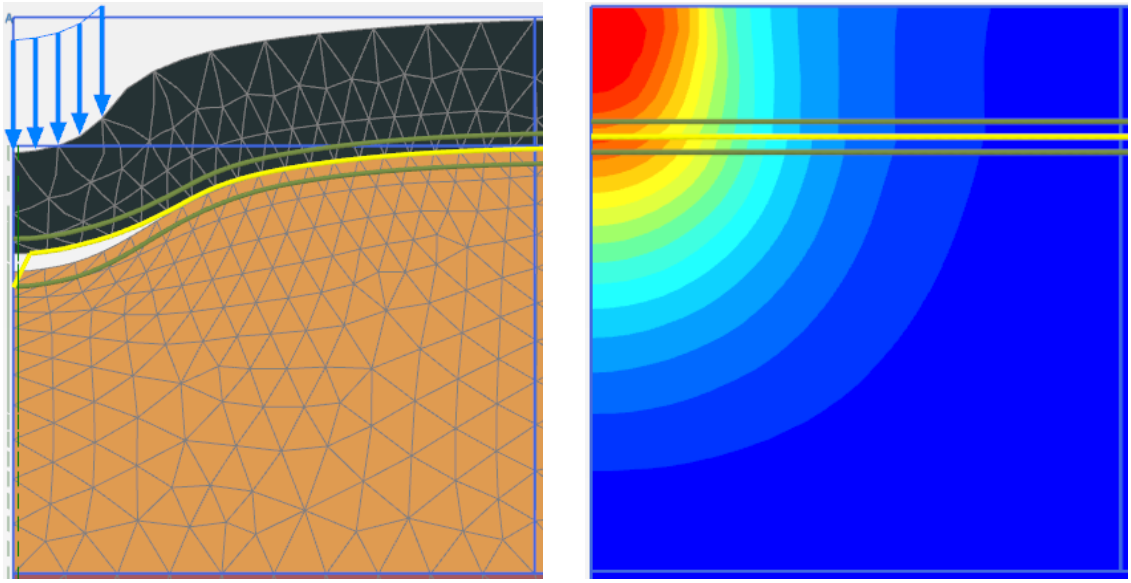

Figure 8-13. a) The generated gap under cyclic load (zoomed interested area), b) deformation contours

8.3 Unsaturated Subgrade under Cyclic Loading: 3D Model

From the 2D analyses of unreinforced section behavior under cyclic load, it was concluded that in order to capture realistic deformation behavior of base and subgrade layers, the stiffness reduction by number of load cycles, needs to be modeled. Hence the Small Strain Hardening Soil constitutive model was implemented in this analysis.

8.3.1 Model geometry specifications

The performance of the geogrid reinforced section was investigated under cyclic load, by modeling a quarter of the loaded area in PLAXIS 3D, as shown in Figure 8-14. As previously stated, the radius of loaded area was calculated as 5.8 inches. The model domain extended 120 inches in both X and Y direction and 180 inches in Z direction, in order to minimize boundary effects and rebounding of the reflected wave into the loaded zone of interest. The absorbent boundaries were also considered for X_{max}, Y_{max}, and Z_{min} plane. A set of the general fixities were imposed to the boundaries of the geometry model, as summarized in Table 8-5:

Table 8-5. Geometry boundary conditions.

Plane	Deformation fixities	Deformation
X min	Normally fixed	Ux=0
X max	Normally fixed	Ux=0
Y min	Normally fixed	Uy=0
Y max	Normally fixed	Uy=0
Z min (bottom)	Fully fixed	Ux=Uy=Uz=0
Z max (surface)	Free	free

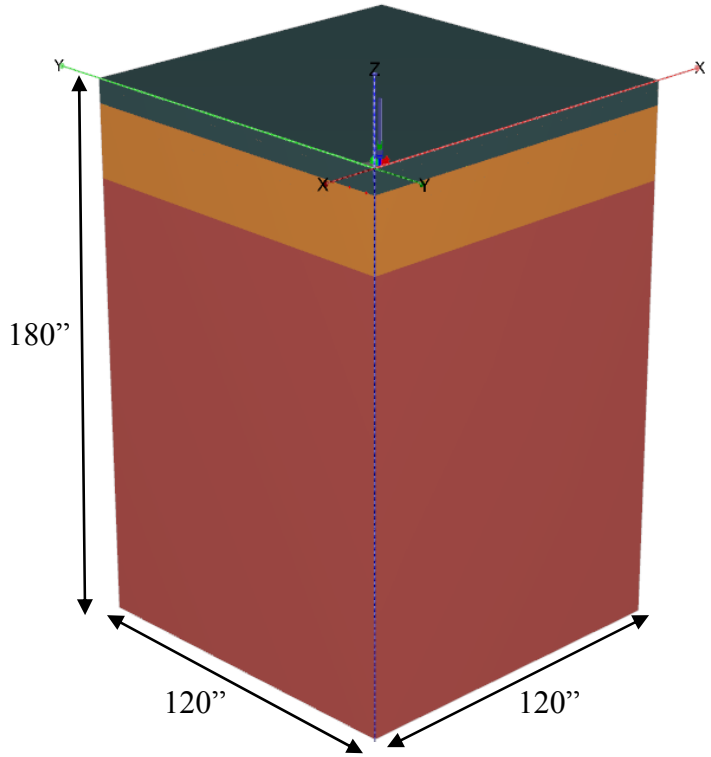

Figure 8-14. Model geometry.

8.3.2 Mesh sensitivity

In order to eliminate the effect of the size of the generated mesh on the results, the ABC and soft A-4 subgrade soil were divided into 3 volumes, as shown in Figure 8-15. Different combinations of coarseness factors were assigned to the soil volumes, until no change in surface deformation under static load was obtained. Figure 8-16 shows the number of elements in ABC and A-4 subgrade soil volumes 1 and 2 vs vertical deformation. It can be seen that adding more elements beyond 1000 does not further change the calculated deformation.

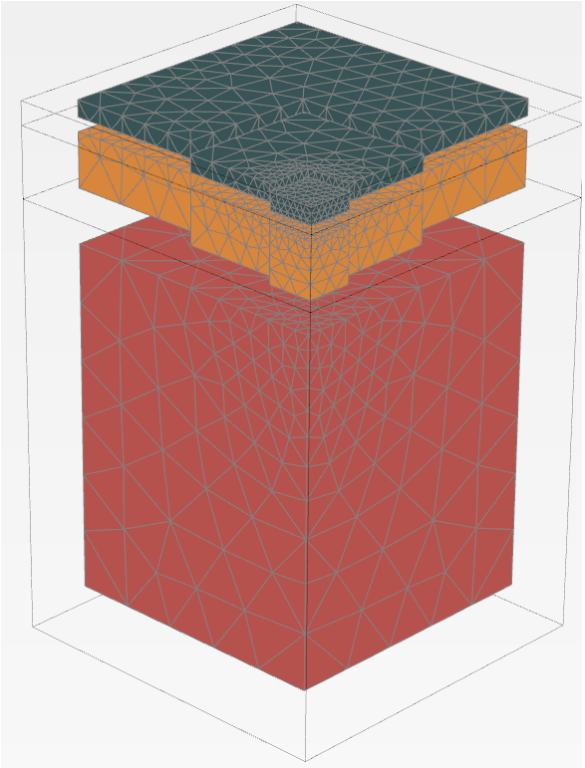

Figure 8-15. Soil volumes and generated mesh

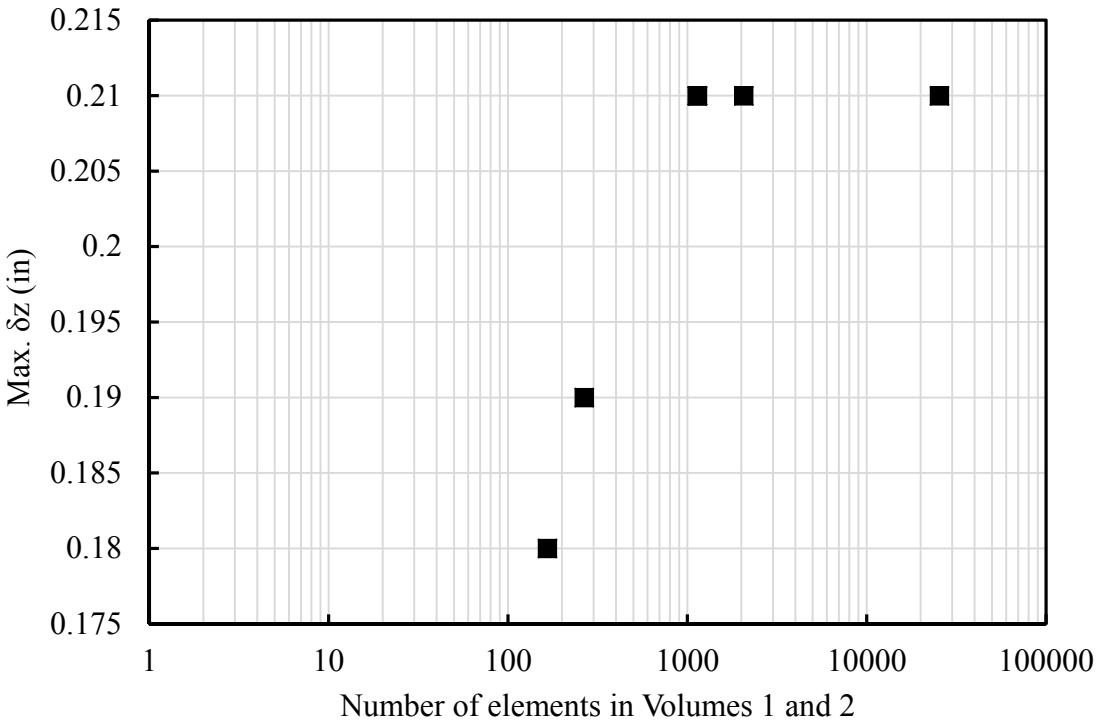

Figure 8-16. Mesh sensitivity results.

8.3.3 Model calibration

Figure 8-17 shows the vertical deformation contours after 100 load cycles. It was observed that no gap was generated at the interface of the geogrid and base/subgrade layers. Accordingly the analyses are robust, and the results seem to conform to logic.

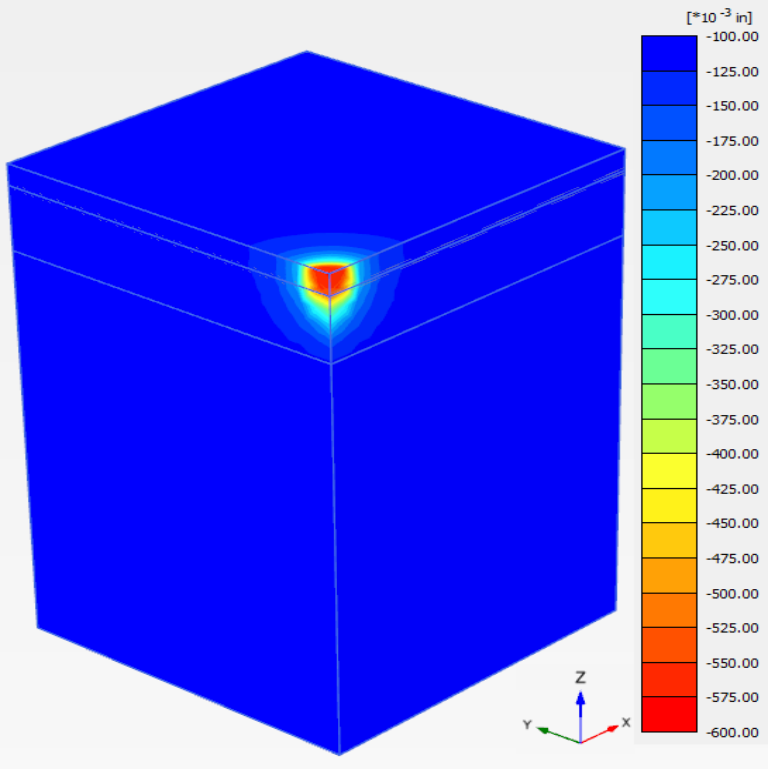

Figure 8-17. Deformation contour after 100 load cycles.

Figure 8-18 shows the calculated permanent deformation under cyclic loading. It can be seen that the computed vertical deformation was significantly higher than the measured permanent deformation in the field at the southern part of the outer wheel path in section 2.

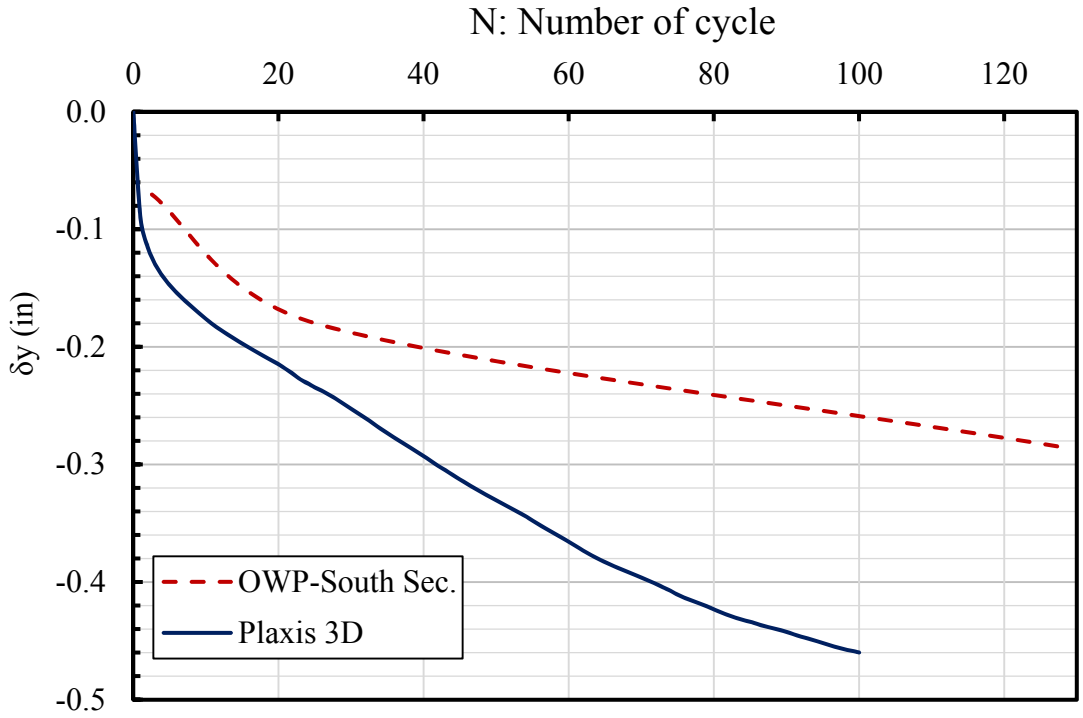

Figure 8-18. Computed vs measured vertical deformation

As stated in the previous section, primary deformation analysis indicated significant difference between measured surface deformation in the field and numerical analysis results, hence the stiffness properties of A-4 materials, E50 and E_{ode}, were modified to calibrate the numerical result with field measurements. Final properties of the soil layers, as well as assigned matric suction values for each layer are summarized in Table 8-6.

Table 8-6. Modified soils properties used in numerical analyses.

Soil	H (in)	γ_{moist} (pcf)	e_0	E_{50}^{ref} (ksi)	E_{oed}^{ref} (ksi)	E_{ur}^{ref} 2 (ksi)	m	ν_{ur}	G_0^{ref} (ksi)	$\gamma_{0.7}$ (%)	φ'	c'/Su(psi)	R_f	ψ (psi)
ABC	8	144	0.34	24	24	48	0.64	0.2	35	0.005	43	8	0.9	6
A-4	24	123	0.57	4.5	4.5	14.5	0.5	0.2	21	0.01	25	2	0.9	6
A-7-5	148	120	0.84	7	3.5	21	1	0.2	80	0.03	NA	28	0.9	6

Figure 8-19, shows the surface deformation of the reinforced section, under 300 load cycles. It can be seen that the results obtained from PLAXIS 3D provide a closer match with the measured field surface deformation when the input parameters are calibrated. It can be seen that after 200 load cycles the rate of cumulative deformation is decreasing as well, following the trend of the measured data.

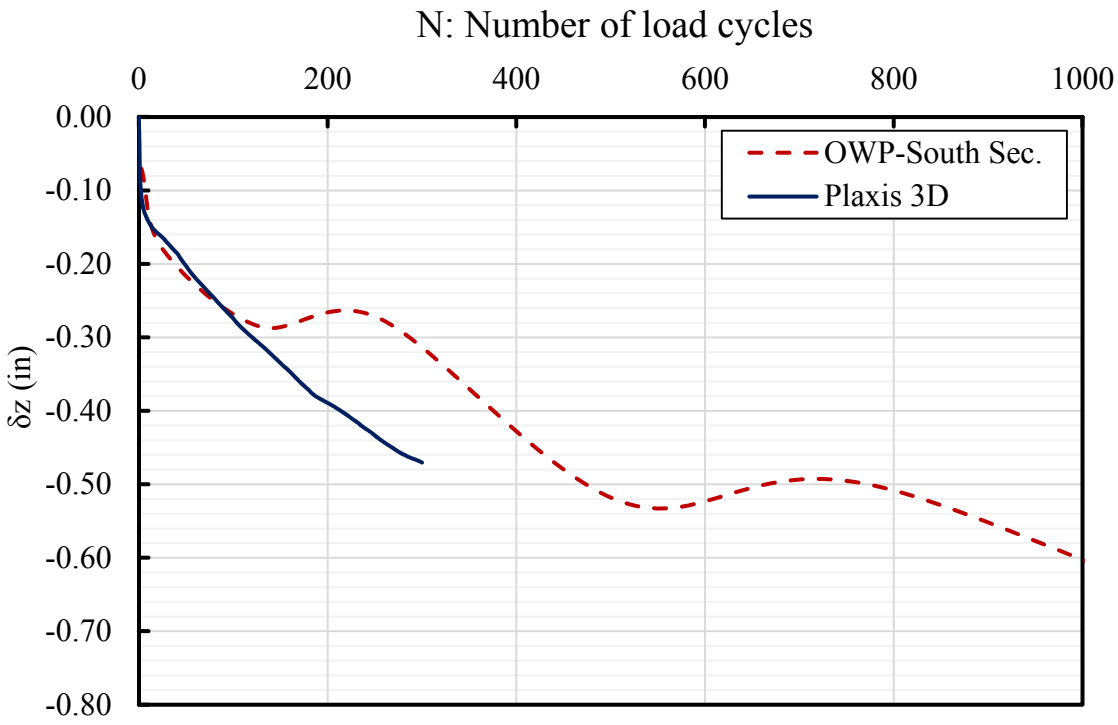

Figure 8-19. Surface deformation under cyclic loading, after adjusting parameters.

8.3.5 Stress distribution analysis

Field-measured pressures from EPC C22 and the average of the computed stresses of two stress points from PLAXIS 3D at a depth of 3 inches below the interface of the subgrade and ABC layer (depth of the installed pressure cells in the field) vs number of load cycles are plotted in Figure 8-20. It is observed that both measured and computed pressures follow a similar trend, and the measured pressure at the top of the subgrade is seen to increase gradually for the first 60 cycles and then decrease as the number of load cycle increase beyond 60. The same trend was reported by Quin et al. (2013), Tingle et al. (2009) and Thakur et al. (2012). This reduction in stress at the top of the subgrade can be explained by mobilization of the tensile strength of the

geogrid (as nearly 0.25 inch of vertical deformation occurred after 60 load cycles), which produces up-lift attenuate the applied stresses transferred into the subgrade layer (Quin et al., 2013).

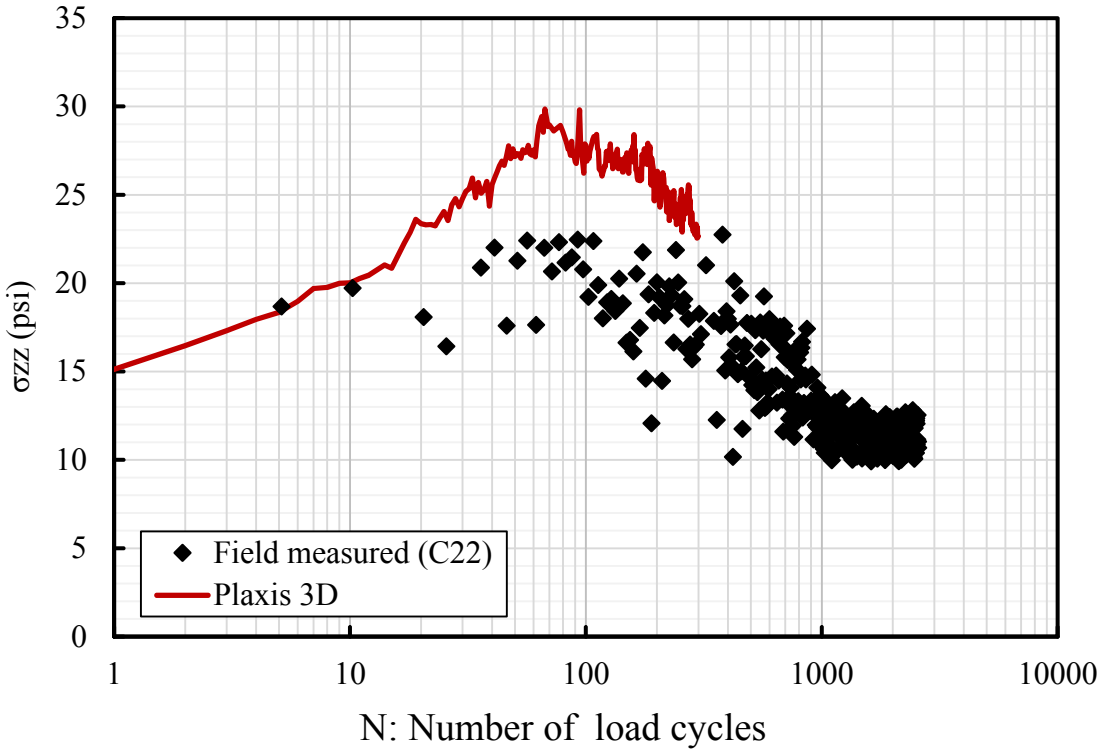

Figure 8-20. Applied pressure at the top of the subgrade

In addition to the geogrid mobilization, the ratio of the ABC modulus to the subgrade modulus also influences the magnitude of the stress transferred into the subgrade layer. An increase in modulus ratio leads to a reduction in transferred stress, as was observed by Leng and Gabr (2002). Figure 8-21 shows the ratio of the secant modulus of the ABC to subgrade layer, computed from PLAXIS model results. It can be seen that the secant modulus ratio decreases during initial cycles of loading, therefore more stress is transferred into the subgrade; however, as the modulus ratio starts increasing after about 70 load cycles, a reduction in applied pressure on the top of the subgrade soil layer is computed. Such a reduction is estimated as long as the ratio of the ABC modulus to the subgrade modulus continues to increase.

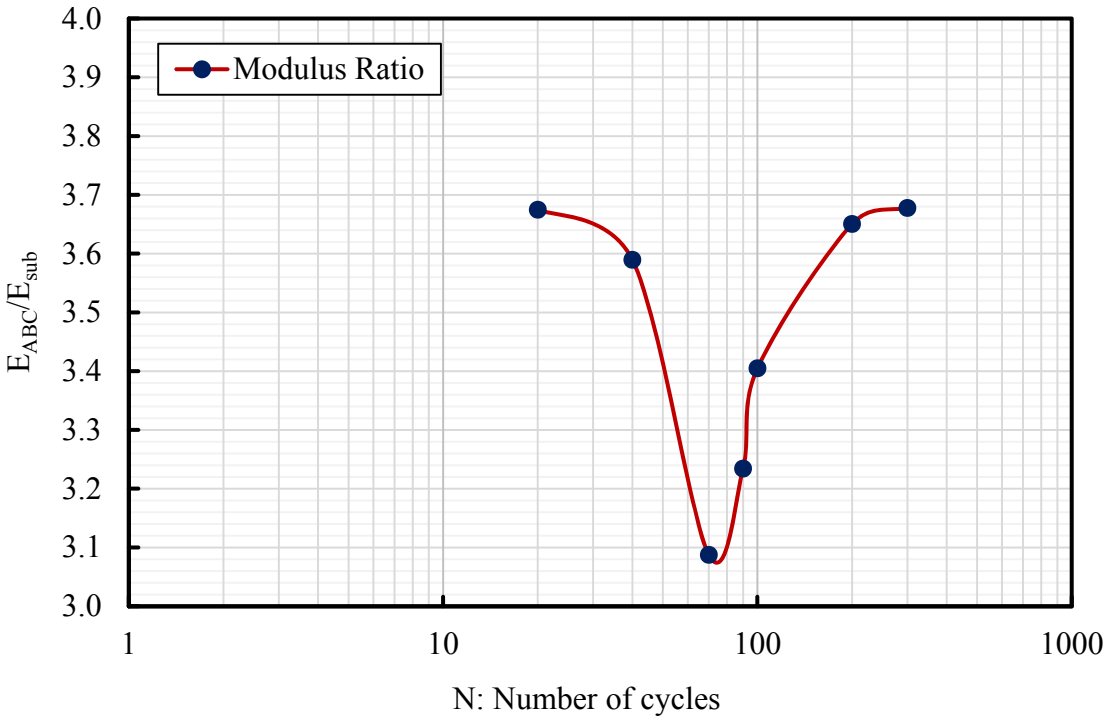

Figure 8-21. Secant modulus ratio, (E_{ABC}/E_{sub})

From these results, it was concluded that the transferred pressure onto the subgrade layer is a function of both mobilization of the tensile strength reinforced layer, and modulus ratio of the ABC to subgrade soil layers (bearing in mind that the modulus value is also a function of the matric suction level). Figure 8-21 shows the computed stress at the top of the subgrade as a function of distance from the centerline of the loaded area, for load cycles 30, 150 and 300. It can be seen that with increasing cycles of loading, not only the magnitude of the transferred stress decreases, but also the applied pressure distributes more uniformly over the subgrade, and the stress transferred onto the subgrade beyond the loaded area ($x > 5.8$”) increases.

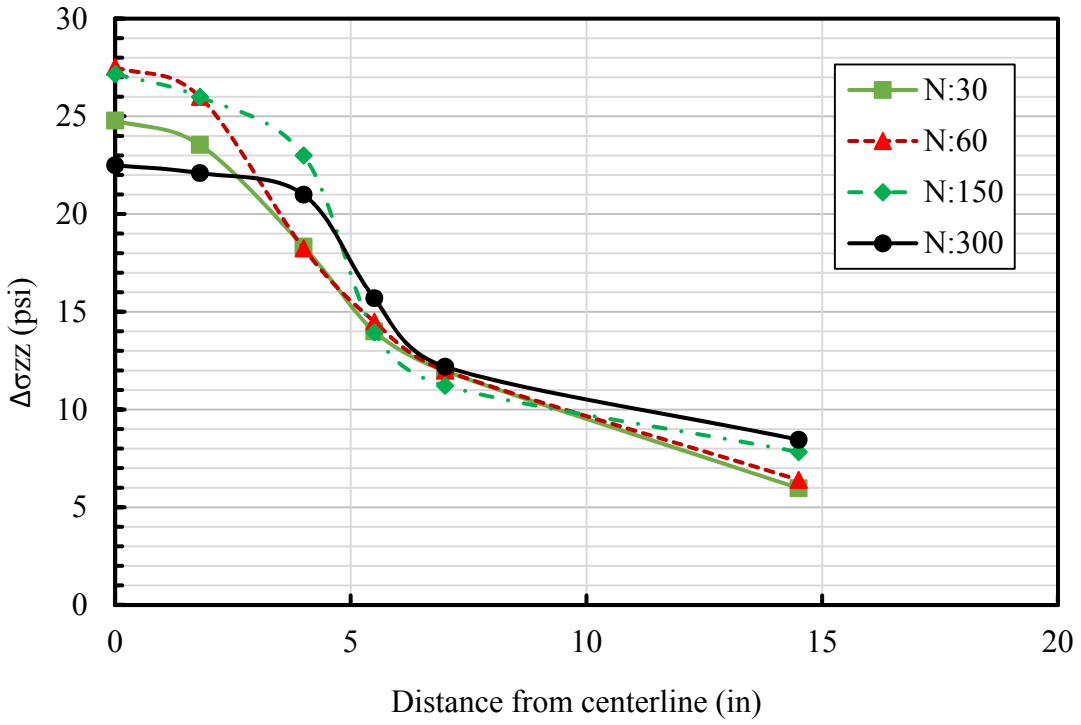

Figure 8-21. Distribution of the applied pressure at the top of the subgrade.

8.3.6 Matric suction effect

The effect of the matric suction state of the aggregate base course layer on the deformation behavior of the reinforced section was investigated using PLAXIS 3D. The surface deformation under 200 load cycles was computed using ABC matric suctions of 6, 11.6, and 17.5 psi (40, 80 and 120 kPa), with the results plotted in Figure 8-23. It is seen that an increase in ABC matric suction can slightly reduce the cumulative deformation, with such an effect becoming more pronounced with increasing number of load cycles. As discussed previously, the HS Small strain constitutive model records and keeps a strain history tensor, which is used to calculate the tangent shear modulus and strain values for the current step. Therefore the effect of the matric suction on reducing the deformation is accumulating under cyclic loading and becomes more conspicuous with increasing number of load cycles.

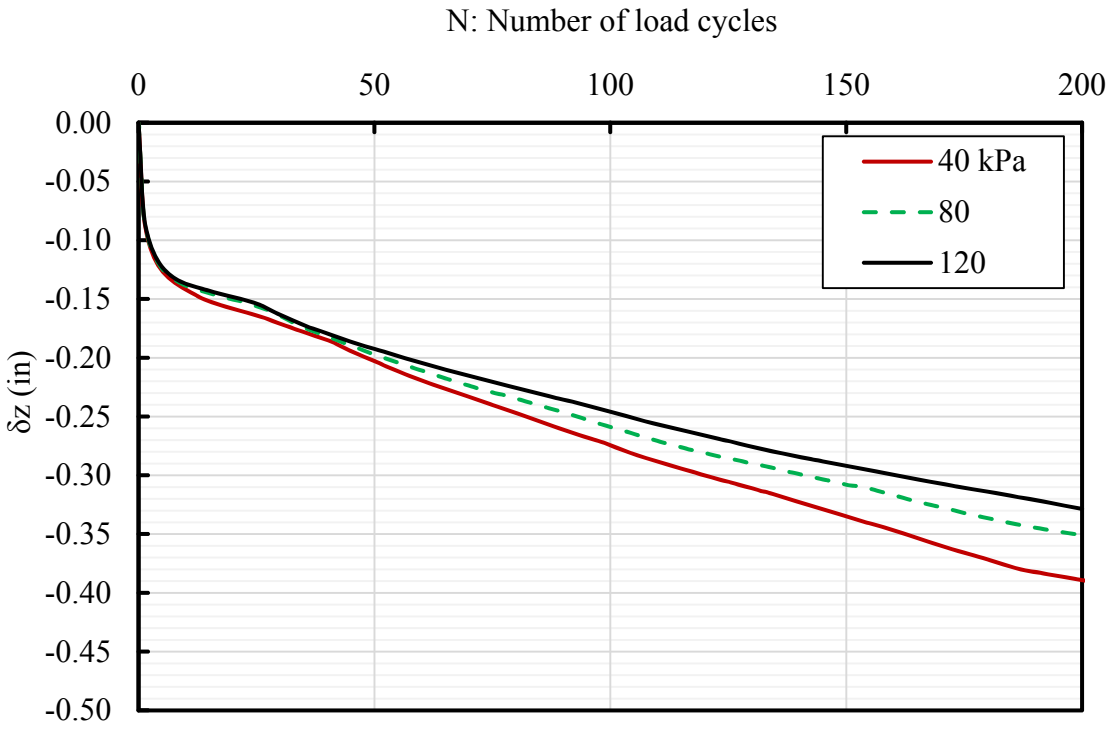

Figure 8-23. Effect of the ABC matric suction state on cumulative deformation.

8.4 Modeling Proof Rolling Test

Proof roll testing is performed to evaluate subgrade stability. A proof roller is a loaded single axle, four wheels trailer, as shown in Figure 8-24. Based on the NCDOT specification (NCDOT, 2012, section 260), the maximum center-to-center spacing between adjacent wheels is 32 inches, with tire pressures between 68 and 72 psi. The load capacity of the trailer is from 48 to 50 tons. For the numerical analysis, the gross weight of the trailer was assumed to be 50 ton, equally distributed between four wheels with a tire pressure of 70 psi and center-to center-spacing between adjacent wheels of 32 inches. Therefore, the radius of the contact area is calculated to be 10.6 inches. Figure 8-25 shows the configuration of the proof roll trailer. The deformation behavior of the subgrade soils under 2 passes of the proof roll trailer load was investigated by modeling the loaded area ain the Plane Strain mode in PLAXIS 2D, and as four circular loaded areas, as shown in Figure 8-25, in PLAXIS 3D.

Figure 8-24. Proof roll trailer (courtesy M. Valiquette, NCDOT, Borden et al., 2010)

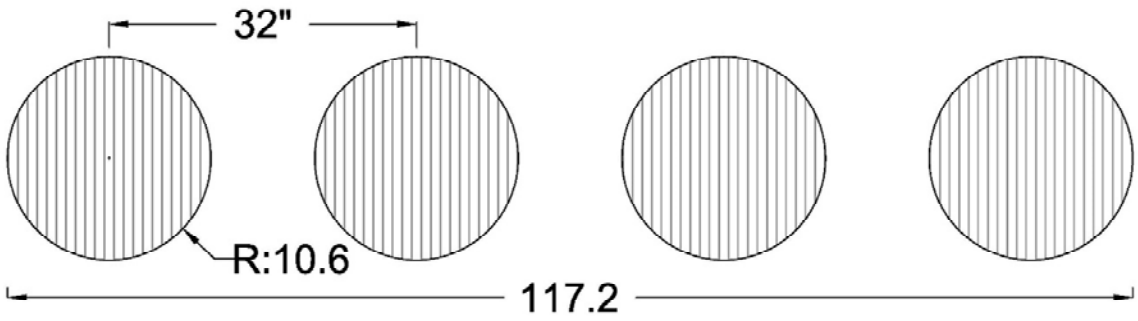

Figure 8-25. 50 ton proof roll trailer configuration, (tire pressure 70 psi).

8.4.1 Materials properties

The deformation behavior of the subgrade soil in test section 2 was evaluated both before and after stabilization by geogrid reinforcement and ABC layer. The validated properties, in PLAXIS 3D model, of the subgrade soils, ABC from previous section (summarized in Table 8-7) were used. The same matric suction state was considered as used in the previous analyses.

In order to extend the numerical analyses results for practical use, the deformation performance of the saturated subgrade before and after stabilization with ABC Class IV, with the properties developed in this study, was investigated under proof roller load in Plane strain and PLAXIS 3D models.

As previously stated, the ABC material properties were assumed to be similar to the ABC class IV, as presented in Table 8-7, without considering matric suction. The analyses were performed for a saturated subgrade layer assumed to have a DCPI between 10 and 100, the range of DCPI values which were measured during this study. The following equations are used to find the properties for the analyses:

Coonse's model (residual soil):

$$Log(CBR) = 2.53 - 1.14 \times \log(DCPI) \qquad \text{Eq. (8-5)}$$

Undrained shear strength

Danistan and Vipulanandan (2009)

$$Su_{subgrade\ soil} = -0.282 \times (CBR)^2 + 14.97 \times (CBR) \qquad \text{Eq. (8-6)}$$

Stiffness properties of the subgrade soils were estimated by using the DCPI values in conjunction with the proposed resilient modulus prediction model from DCPI presented in Chapter 5. The Eur is assumed equal to Mr, and $E_{50} = E_{ode} = E_{ur}/3$.

The maximum shear modulus is calculated using Eq. 8-7 (NCHRP 2008), and assuming v of 0.2 under cyclic loading.

$$G_{\max} = \frac{M_r}{2(1+\nu)} \qquad \text{Eq. (8-7)}$$

Estimated subgrade properties for these analyses are summarized in Table 8-8.

Table 8-8. Estimated subgrade properties.

DCPI (mm/blow)	100	90	60	50	40	30	20	10
CBR	2	2	3	4	5	7	11	25
s_u (psi)	3.7	4.2	6.5	7.9	9.9	13.2	19.1	28.7
Mr (psi)	4605	4798	5425	5652	5889	6134	6377	6568
E_{50}	1439	1499	1695	1766	1840	1917	1993	2052
Eode	1439	1499	1695	1766	1840	1917	1993	2052
Gmax	1919	1999	2260	2355	2454	2556	2657	2736

8.4.2 Cyclic loading

A tire pressure of 70 psi is assumed for cyclic loading analysis. The two load cycles, which represent two proof roller passes are considered as shown in Figure 8-26.

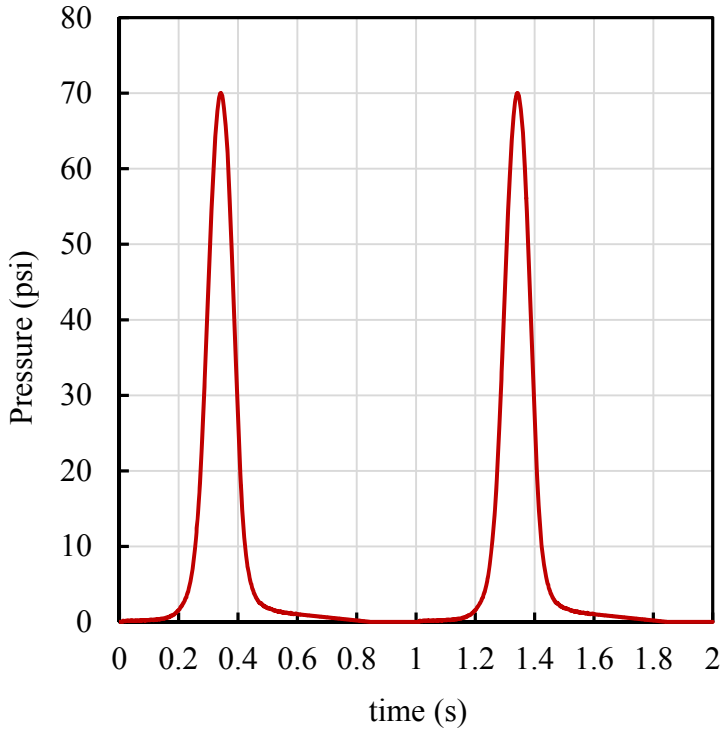

Figure 8-26. Proof roller load cycles.

8.4.3 Plane strain geometry

The deformation performance of the subgrade soils under cyclic proof roller loading was evaluated in Plane Strain mode in PLAXIS 2D (in addition to the PLAXIS 3D analyses), by implementing 15 node elements. The geometry of the model domain is shown in Figure 8-27. The boundaries are located at 300 inches both side of the centerline, and 200 inches in Z direction. The finest mesh was imposed for the zone close to the loaded area, which gradually become coarser with distance from loaded region. Absorbent boundaries were also implemented in order to prevent wave reflection into the soil body.

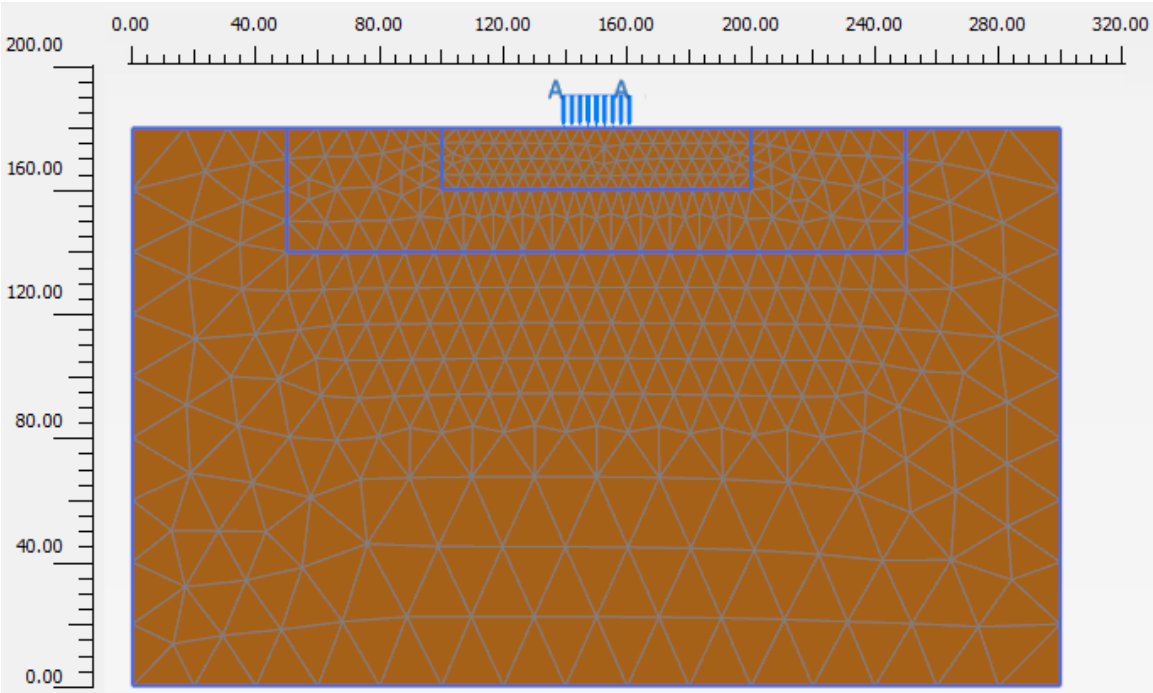

Figure 8-27. Plane strain geometry and mesh distribution.

8.4.4 PLAXIS 3D geometry

The surface deformation after two proof roller passes was also computed for subgrade with DCPI ranging between 10 and 100 in PLAXIS 3D using 10-node tetrahedral elements. Four wheel loads were considered, as shown in Figure 8-28, with a radius of 10.6 inches and center to center spacing of 32 inches. The boundaries were extended 220 inches in the X direction, 240" in both Y directions and 180 inches in the Z direction. Absorbent boundaries were also imposed on the

Xmax, Ymax, Ymin, and Zmin planes. The ground water table was assumed to be on the top of the subgrade.

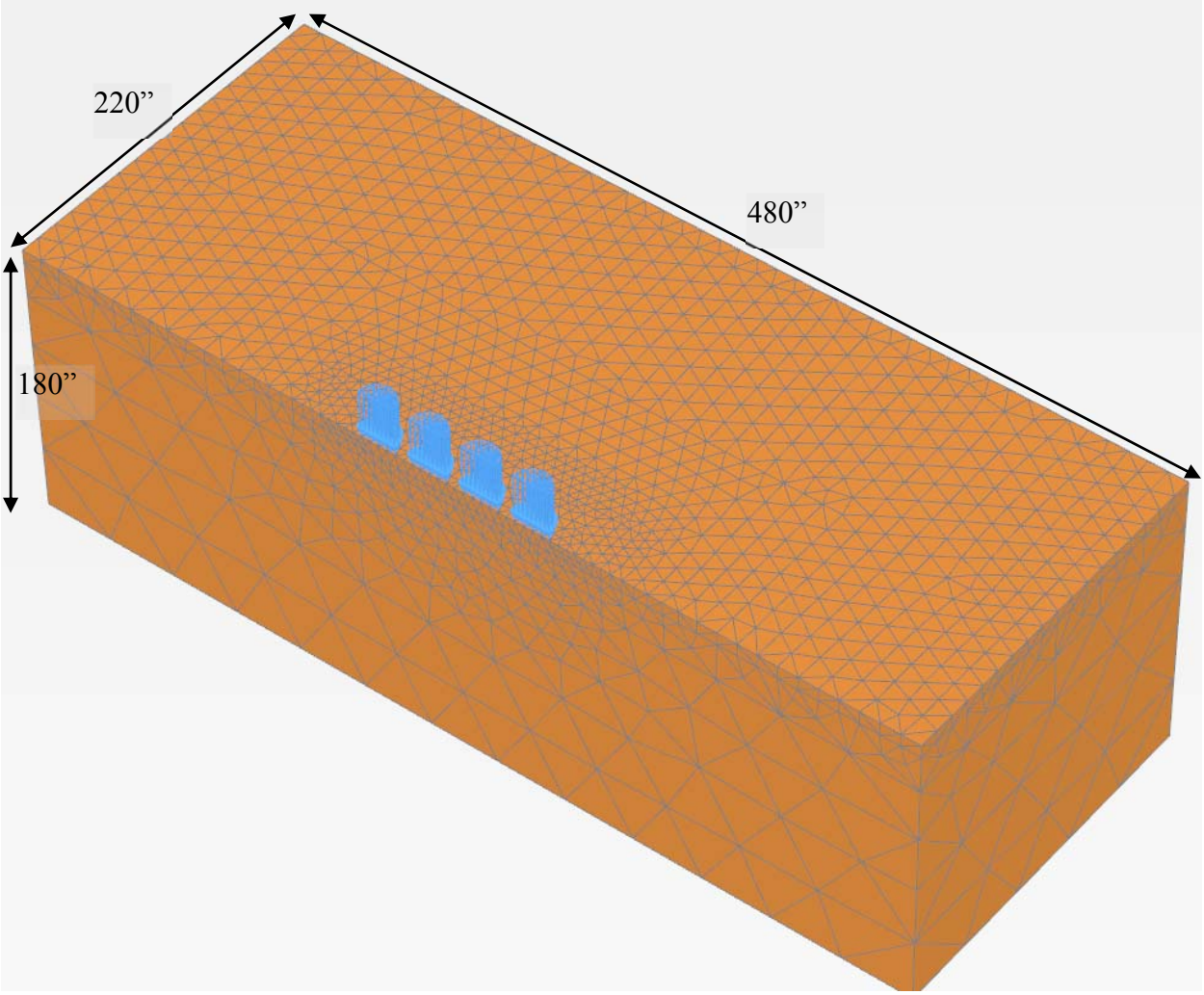

Figure 8-28. Proof roller test model geometry. PLAXIS 3D

8.4.5 Numerical analysis: Proof rolling

The deformation performance of the test site two subgrade soil layers system, 32 inches compacted A-4 soil on the top of the natural A-7-5 residual soil, with their calibrated in situ parameters, as presented in Table 8-7, and geogrid reinforcement under the proof roller test loading was investigated in PLAXIS 3D. Table 8-9 shows the computed maximum deformation. It can be seen that even without any stabilization, the subgrade soil would pass the deformation criterion of the proof roller test (less than 1 inch), which is consistent with both the NCDOT and

Borden et al. (2010) undercut criteria results. In the field, the subgrade was judged to have performed acceptably in some stations prior to stabilization.

Table 8-9. Computed deformation before and after stabilization under proof roller

Site condition	Maximum deformation (in)
Natural unsaturated subgrade soil	0.40
GG reinforced subgrade+ 8" ABC	0.22

Figure 8-29 shows the cumulative surface deformation of the subgrade after two proof roller passes from plane strain analysis and from half of the domain analysis in PLAXIS 3D. It can be seen that the plane strain deformations are significantly greater than those from the 3D analysis, and provide an unrealistic evaluation of the subgrade stability. As shown in Figure 8-29, 3D analyses for DCPI greater than 48 mm/blow show a computed deformation greater than 1 inch, which is outside the indicated green area, suggesting soil stabilization would be required. This result is occurring at a modestly higher DCPI than the NCDOT undercut criteria of 38 mm/blow (which shows ¾ inch corresponding computed deformation). Since the judgment of the adequacy of the proof rolling test results is subjective, and it is perhaps difficult to discern ¾ of an inch versus 1 inch, it is proposed that the NCDOT criterion of 38 mm/blow is still reasonable for the Piedmont soil at the test site.

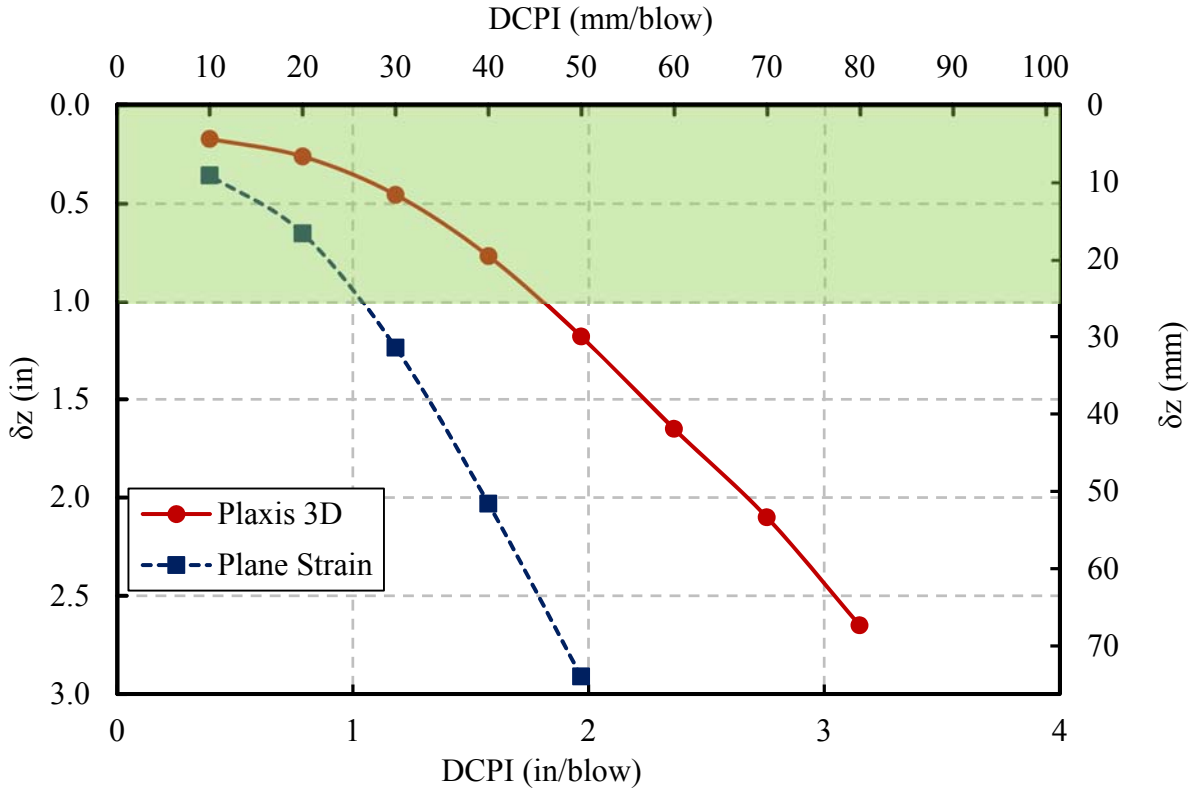

Figure 8-29. Surface deformation after two proof roller passes.

Figures 8-30 and 8-31 show the PLAXIS 3D-computed surface deformation of the aggregate base layer surface after two proof roller passes. As shown in Figure 8-30, the effect of the subgrade strength and stiffness properties on the surface deformation decreases with increasing thickness of the aggregate base layer. In addition, it can be seen that the effect of the ABC layer in reducing the surface deformation becomes more pronounced with increasing DCPI value. It is however the case that a minimum of 4-6 inches of ABC thickness should be used for constructability and in order to minimize damage to the geosynthetic reinforcement during construction.

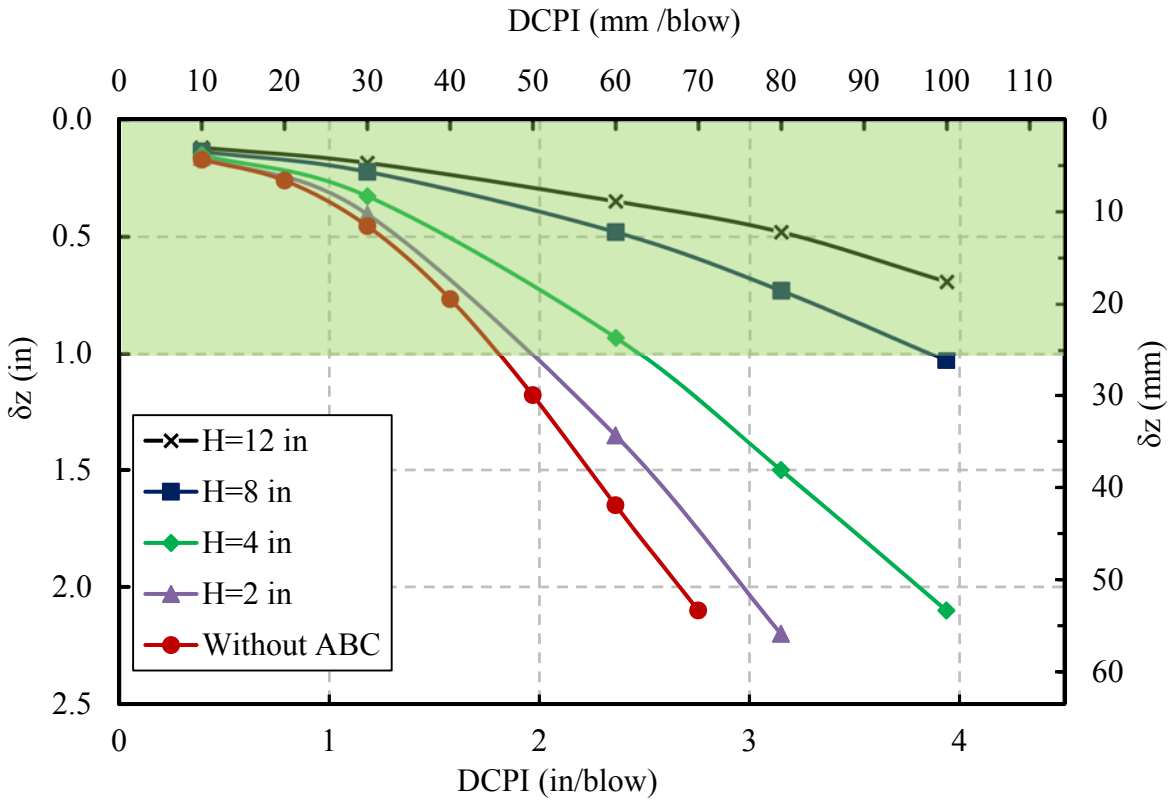

Figure 8-30. Computed Surface deformation for different thickness of ABC

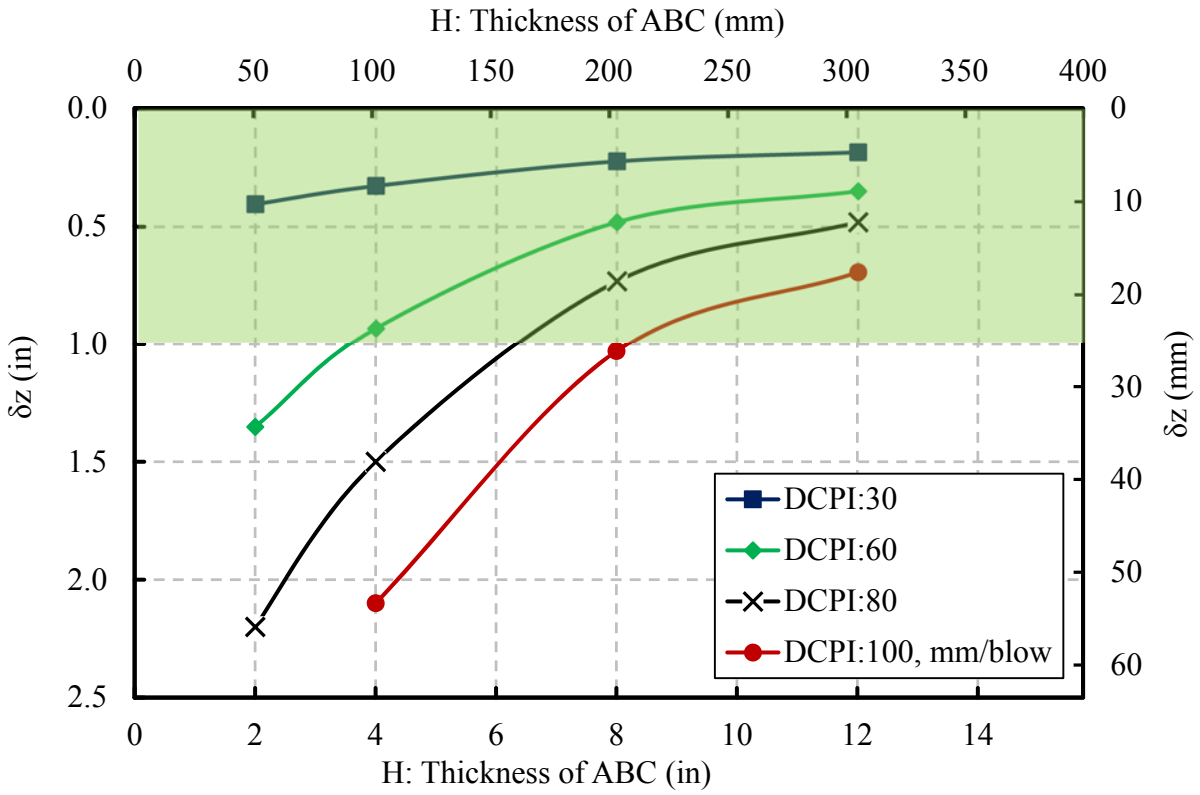

Figure 8-31. Computed surface deformation vs thickness of ABC

8.5 Summary

From extensive numerical analyses of unreinforced unsaturated subgrades under repeated cyclic loading in PLAXIS 2D and 3D, the following conclusions can be advanced:

- A design chart was developed from numerical analysis performed in PLAXIS 3D to enable the selection of an appropriate thickness of ABC based on measured DCPI subgrade soil values.
- The matric suction state of the ABC layer has a notable effect on the surface deformation of a reinforced subgrade under cyclic loading. An increase of matric suction in the ABC layer is associated with a decrease in the surface deformation of the reinforced subgrade under cyclic loading.

- Based on numerical analyses of the subgrade soil under simulated proof roller loading, the computed deformation from a plane strain mode is shown to be significantly higher than that computed under four loaded areas in PLAXIS 3D.
- Analyses demonstrate that an appropriate constitutive model should be utilized in order to accurately model the deformation behavior of the base and subgrade layers under cyclic loading. For this purpose, the constitutive model which is capable of modeling soil stiffness reduction with increasing the strain level needs to be used. Hence the HS small constitutive model was utilized in this study.
- The effect of the subgrade strength and stiffness on surface deformation decreases with increasing thickness of aggregate base layer.
- The effect of the ABC layer in reducing the surface deformation become more pronounced with increasing DCPI value.

CHAPTER 9: SUMMARY AND CONCLUSIONS

The overarching objective of this research project was to evaluate the applicability of the undercut criteria, previousely developed in an earlier research phase, at a test site within the Piedmont geologic area of North Carolina. The site is located at the intersection of NC 65 East and U.S. Route 220 South, approximately 20 miles NNW of Greensboro (coordinates: 36.268082 -79.93053.) The results presented herein included collection of data from Light Weight Deflectometer (LWD) and Dynamic Cone Penetrometer (DCP) to assess subgrade properties. Three test pads were constructed on comparable subgrade conditions with different stabilization measures, and subjected to 1000 passes of a loaded construction truck. Four Earth Pressure Cells (EPC) were embedded within the wheel path (two in each wheel path) for each test section to monitor stress variations with traffic loading. A surface profiler (Lidar-based surveying) was used at periodic intervals to monitor plastic deformation and wheel path rutting with loading cycles. Moisture and suction sensors were embedded in the subgrade to monitor moisture and suction variation. The results from the field testing were used to assess the extent to which the use of each stabilization measure is effective in rendering the soft soil layer as meeting the criteria for a stable subgrade.

The collected field data, including LIDAR measured surface displacements (plastic deformation), laboratory and field measured shear strength and modulus properties, were implemented into the proposed undercut criteria from the Phase I study, which is documented in Borden et al. (2010). Numerical analyses were performed using Plaxis 2D and 3D software, in order to study the deformation performance and stress distribution in reinforced unsaturated subgrade soil under cyclic traffic loading. The deformation performance of the subgrade soils under proof roller loading was studied in plain strain 2D and Plaxis 3D models. Guidelines regarding thickness of ABC under various subgrade strength values were proposed based on the results of the numerical analyses. Based on the work conducted in this study, the following observations and conclusions are advanced:

Full scale testing

- The measured vertical stress near the interface of the subgrade for the geosynthetics-reinforced sections was seen to decrease with increasing number of truck passes from 20 psi to 10 psi in section 2, and from 16 psi to 8 psi in section 3, while the recorded pressure in section 1 was almost constant, 4+/-2 during traffic. This decrease of measured stress in geosynthetics reinforced sections is attributed to progressive densification of the aggregate base course, mobilization of reinforced layer tensile strength as well as increasing matric suction in the subgrade layer, from 25 kPa to 35 kPa, as a result of the "hot" summer weather during which the project was conducted.
- Since each driver intended to drive over the EPCs on his side, the EPCs on the other side were off between 5 to 15 inches of the truck tires (loaded area). It was observed that lateral wander of the truck tires has a more significant effect on the measured stress in the shallow depth in subgrade layer (section 2 and 3). Hence monitored pressure was categorized by traffic direction, north to south and south to north. The variation of recorded pressure was reduced from 2 psi to 1 psi, 10 psi to 5 psi and 8 psi to 4 psi in section 1, 2, and 3, respectively. It was observed that the
- The geosynthetics-reinforced sections experienced 0.5" and 0.7" of surface deformation for the geogrid- and geotextile-reinforced sections, respectively. The select fill-stabilized section showed a 1.2" of deformation after 1000 truck passes.
- The rut depth (defined as vertical displacement from the original ground surface) increased with truck passes until reaching a relatively constant value within the 1000 truck passes. In this study, the rut depth increased until 500 truck passes in both geotextile and geogrid sections. In section 1 (select fill section), the rut depth reached a limiting value after 700 passes.

Undercut criteria evaluation

- The applicability of the previously developed and reported undercut criteria using soil properties estimated from laboratory testing (i.e. triaxial and resilient modulus) and/or DCP testing was validated for the Piedmont residual subgrade soils at the test site.
- It was demonstrated that the proposed undercut criteria can be used to assess deformation response under traffic loading on the basis of 1-inch limit, and performance capacity factor of 1.5 or higher for stabilized section. The 1-inch limit addresses issues related to deep layers "pumping" while the performance capacity factor addresses issues related to localized bearing failure.

Resilient modulus prediction models

- The evaluation of models reported in literature which directly estimate the Mr of soils from the DCP and LWD measurements showed that they overestimated measured Mr values. In addition, these models are only valid at one stress level which limits their applicability to one particular configuration of pavement section layers.
- Good agreement was obtained between calculated Mr values from proposed DCP-Mr and LWD-Mr models and the laboratory-measured resilient modulus data.
- Examination of the performance of the proposed LWD and DCP-Mr models with a quarter of the data set, which was not included in the statistical analyses, indicated that on average the proposed LWD and DCP models underestimated the Mr by 7 and 4%, respectively.
- Predicted Mr values by the proposed LWD and DCP models were seen to be in reasonably good agreement with the laboratory-measured Mr presented in the literature. The results indicated generally 11 and 8% underestimation, with coefficients of determination of 0.96 and 0.53, respectively.
- The proposed LWD and DCP models are capable of predicting the resilient modulus of low plasticity soils SM, ML, and SC (A-4a and A-4), with PI<5, and 40%<P_{200}<55%; at any stress state. Such values can be used along with the subgrade's shear strength to discern the need for undercutting during the design phase based on the criteria presented in Borden et al 2010.

Numerical analyses

- The matric suction state of the ABC layer was shown to have a notable effect on the surface deformation of a reinforced subgrade under cyclic loading. An 80 kPa increase in matric suction in the ABC layer (from 40 kPa to 120 kPa) was associated with a 25 % decrease in the surface deformation (from 0.40" to 0.30") of the reinforced subgrade under cyclic loading.
- Based on numerical analyses of the subgrade soil under simulated proof roller loading, the computed deformation from a plain strain mode is shown to be significantly higher than that computed under four loaded areas in Plaxis 3D. This is a limitation of using plain strain model approach in characterizing behavior during the design phase. In addition, analyses demonstrate that an appropriate constitutive model should be utilized in order to accurately model the deformation behavior of the base and subgrade layers under cyclic loading. For this purpose, the constitutive model which is capable of modeling degradation of soil stiffness with increasing the strain level needs to be used.
- The effect of the subgrade strength and stiffness on surface deformation decreases with increasing thickness of aggregate base layer. This is due to the larger attenuation of the applied stress increase with the increasing thickness of the ABC layer.
- A design chart was developed from numerical analysis performed in Plaxis 3D to enable the selection of an appropriate thickness of ABC based on the measured DCPI of the subgrade soil. The proposed recommendations were based on limiting the surface deformation to a prescribed value as a function of number of EASLs.

The results presented herein are intended to assist NCDOT and their contractors with a tool for decision making to systematically determine whether undercutting and stabilization measures are needed. It was demonstrated that the proposed undercut criteria can be used to assess the adequacy of the subgrade soils to support traffic loading on the criteria basis of 1-inch deformation limit, and performance capacity factor of 1.5 or higher. In this case, the 1-inch limit addresses issues related to deep layers "pumping" while the performance capacity factor addresses issues related to localized bearing failure. Implementation of the research project is recommended along the following tracks:

i. Use of the data and approach presented in this report to discern whether undercutting of the perceived soft soils is necessary for the construction of the roadway. The results from field testing indicated that the criteria proposed by Borden et al 2010 in terms of the strength and stiffness of the subgrade soils is valid for defining situations in which undercut is needed based on quantifiable criteria presented.

ii. Use the recommended approach utilizing data from DCP, LWD, resilient modulus testing, and conventional geotechnical testing to make a determination regarding the need for undercut during the design phase. In addition, the results indicated that the NCDOT criterion using the DCP Index of 38mm/blow is valid and can be used if expedient determination is needed during the construction phase.

iii. Estimate the depth of undercut and the corresponding thickness of the select fill or ABC layer, depending on the stabilization measure to be implemented. It should be mentioned that these layers (select fill or ABC) are a part of the subgrade stabilization measure and should not be included during the design as a part of the pavement section layers (base, subbase, and asphalt)

iv. Provide information on the stabilized section properties that will inform the design process of the pavement section.

v. Determining the depth of undercut required in the case where no other additional means of stabilization is to be used. The depth of undercut should be established based on strength and modulus properties as assessed from the DCP data or conventional engineering properties of soils determined from laboratory testing.

REFERENCES

AASHTO. (1993). Guide for Design of Pavement Structures. American Association of State Highway and Transportation Officials.

AASHTO, (2003): Standard method of test for determining the resilient modulus of soils and aggregate materials, AASHTO T307-99, Washington, D.C.

Abu-Farsakh, M.Y., Alshibli, K., Nazzal, M., and Seyman, E., (2004), "Assessment of In-situ Test Technology for Construction Control of Base Courses and Embankments". Louisiana Transportation Research Center (LRTC) Project No. 02-1GT, Louisiana Department of Transportation and Development, May 2004, 143 Pages.

Ahlvin, R. G., & Ulery, H. H. (1962). Tabulated values for determining the complete pattern of stresses, strains, and deflections beneath a uniform load on a homogeneous half space. Highway Research Board, Bulletin 342, 1-13.

Allbright, R. L. (2002). Evaluation of the Dynamic Cone Penetrometer and its Correlations with Other Field Instruments. M.S. Thesis, Department of Civil and Environmental Engineering, University of Wisconsin-Madison, WI.

Asphalt Institute, (1989), "The Asphalt Handbook. Manual". Series No. 4 (MS-4), 1989, pp. 435-437.

ASTM D1557-09, (2009), Standard Test Methods for Laboratory Compaction Characteristics of Soil Using Modified Effort, Annual Book of ASTM Standards, ASTM International, West Conshohocken, PA.

ASTM D2216, (2010), Standard Test Methods for Laboratory Determination of Water (Moisture) Content of Soil and Rock by Mass.

ASTM D422-63, (2007), Standard Test Method for Particle-Size Analysis of Soils.

ASTM D4318-10, (2010). Standard Test Methods for Liquid Limit, Plastic Limit, and Plasticity Index of Soils.

ASTM D6913, (2009), Standard Test Methods for Particle-Size Distribution (Gradation) of Soils Using Sieve Analysis.

ASTM D6951-09, (2009), Standard Test Method for Use of the Dynamic Cone Penetrometer in Shallow Pavement Applications, Annual Book of ASTM Standards, ASTM International, West Conshohocken, PA.

ASTM D854. (2010), Standard Test Methods for Specific Gravity of Soil Solids by Water Pycnometer.

ASTM E2583-07. (2011), Standard Test Method for Measuring Deflections with a Light Weight Deflectometer (LWD). ASTM Standards, ASTM International, West Conshohocken, PA.

ASTM D 4767-04, (2004), Standard Test Method for Consolidated Undrained Triaxial Compression Test for Cohesive Soils. West Conshohocken: American Society for Testing and Materials

ASTM D6938-10, (2010), Standard Test Method for In-Place Density and Water Content of Soil and Soil-Aggregate by Nuclear Methods (Shallow Depth). West Conshohocken: ASTM International.

Atkinson, J. H., Sallfors, G., (1991), "Experimental determination of soil properties", In Proc., 10th ECSMFE, 3, 915-956

Austin, D. N., & Coleman, D. M. (1993). "A Field Evaluation of Geosynthetic Reinforced Haul Roads over Soft Foundation Soils". Conference Proceedings, Geosynthetics '93. Vancouver, Canada.

Ayithi, A., Hiltunen, D. R., (2013), "Characterization of Moisture-Dependent Changes in Stiffness of Unbound Aggregate Base Materials in Florida", Transportation Research Record: Journal of the Transportation Research Board, No. 2349, Transportation Research Board of the National Academies, Washington, D.C., pp. 25–31.

Ayres, M. (1997). "Development of a Rational Probabilistic Approach for Flexible Pavement Analysis." D.Phil. dissertation, University of Maryland, College Park, MD.

Ba, M., Nokkaew, K., Fall, M., Tinjum, J. M., (2013), "Effect of Matric Suction on Resilient Modulus of Compacted Aggregate Base Courses", Geotech Geol Eng, 31:1497–1510

Barksdale, R. D., Brown, S. F., and Chan, F., (1989). "Potential benefits of geosynthetics in flexible pavement systems", National Cooperative Highway Research Program Report No. 315, Transportation Research Board, National Research Council, Washington, DC, USA, 56 p.

Benz, T. (2006), "Small-strain stiffness of soils and its numerical consequences", Ph.D thesis, university of Stuttgard.

Benz, T., Vermeer, P.A., and Schwab, R., (2008), "A Small-strain Overlay Model", International journal for numerical and analytical methods in geomechanics, Int. J. Numer. Anal,. Meth. Geomech., 33:25-44.

Bishop, A. W., and D. W. Hight, (1977), "The value of Poisson's ratio in saturated soils and rocks stressed under undrained conditions". Geotechnique 27, No. 3, pp 369-384.

Borden, R. H., Cote, B. M., Gabr, M. A., Park, Y., Pyo, S., & Robinson, B. R. (2010). Establishment of Subgrade Undercut Criteria and Performance of Alternative Stabilization Measures. Raleigh: NCDOT.

Borden, R. H., Shao, L., and Gupta, A., (1996), "Dynamic Properties of Piedmont Residual Soils", Journal of Geotechnical Engineering, Vol. 122, No. 10.

Brinkgreve, R.B.J, (2010), "Plaxis Materials Models Manual".

Brinkgreve, R.B.J., Kappert, M.H., and Bonnier, P.G., (2007), "Hysteretic damping in a small-train stiffness model", Numerical Models in Geomechanics – NUMOGX, Rhodes, 737-742.

Carmichael, R.F. and Stuart, E., (1985), "Predicting Resilient Modulus: A Study to Determine the Mechanical Properties of Subgrade Soils". In Transportation Research Record: Journal of the Transportation Research Board, No. 1043, Transportation Research Board, National Research Council, Washington, D.C., pp. 145–148.

Chaddock, B. C. (1988). “Deformation of Road Foundations with Geogrid Reinforcement”. Research Report 140. Transportation and Road Research Laboratory, Berkshire, U.K.

Chai, G., and Roslie, N., (1998), “The Structural Response and Behavior Prediction of Subgrade Soils using Falling Weight Deflectometer in Pavement Construction”. Third International Conference on Road and Airfield Pavement Technology, April 1998.

Chen, D-H., Lin, D-F., Liau, P-H., and Bilyeu, J., (2005), “A Correlation Between Dynamic Cone Penetrometer Values and Pavement Layer Moduli.” Geotechnical Testing Journal, Vol. 28, No. 1, Pages 42-49.

Cote, B. M. (2009). “Performance Comparison of Mechanical and Chemical Stabilization of Undercut Subgrades”. Raleigh, NC: North Carolina State University: Masters Thesis.

Cowell, T. D., Pyo, S. C., Gabr, M. A. and Borden, R. H., (2012), “Field Verification of Undercut Criteria and Alternatives for Subgrade Stabilization – Coastal Plain”, Publication FHWA/NC/2008-13, FHWA, U.S. Department of Transportation.

Danistan, J., & Vipulanandan, C. (2009). “Relationship between CBR values (un-soaked) and undrained shear strength of artificial CH soils. Proceedings of CIGMAT-2009 Conference & Exhibition. Houston, TX: University of Houston.

De Gardiel, R., & Javor, E. (1986). “Mechanical Reinforcement of Low-Volume Roads by Geotextiles”. Proceedings, Third International Conference on Geotextiles, (pp. 1021- 1026). Vienna, Austria.

Decagon Devices, Inc. (2010). 10HS Soil Moisture Sensor Operator's Manual: Version 3. Pullman: Decagon Devices, Inc.

Decagon Devices, Inc. (2012, February 14). 10HS Soil Moisture, large area of influence.

Dondi, G., (1994). “Three-dimensional finite element analysis of a reinforced paved road.” Proceedings of the Fifth International Conference on Geotextiles, Geomembrane and Related Products, Singapore, pp. 95-100.

Drumm, E.C., Boateng-Poku, Y. and Johnson, P. T., (1990), "Estimation of Subgrade Resilient Modulus from Standard Tests", Journal of Geotechnical Engineering, Vol. 116, No. 5, pp. 774–789.

Duncan, J.M., Chang, C.Y., (1970), "Nonlinear analysis of stress and strain in soil", ASCE J. of the soil Mech. and Found. Div., 96, 1629-1653

Dunlap, W.S., (1963), "A Report on a Mathematical Model Describing the Deformation Characteristics of Granular Materials". Technical Report 1, Project 2-8-62-27, Texas Transportation Institute, Texas A&M University, College Station.

Elias, M. B. and Titi, H. H., (2006), "Evaluation of Resilient Modulus Model Parameters for Mechanistic–Empirical Pavement Design', Transportation Research Record: Journal of the Transportation Research Board, No. 1967, Transportation Research Board of the National Academies, Washington, D.C., pp. 89–100.

Elliot, R.P., S.I. Thorton, K.Y. Foo, K.W. Siew, and R. Woodbridge, (1988), "Resilient Properties of Arkansas Subgrades". Final Report, TRC-94, Arkansas Highway and Transportation Research Center, University of Arkansas, Fayetteville.

Eun, J. and J. Lee., (2012), "Effect of Soil Parameters on Elastic Characteristics of Subgrade Materials". Journal of Materials in Civil Engineering, Vol. 24, No. 4, pp 409-417.

Fannin, R. J., & Sigurdsson, O. (1996). "Field Observations on Stabilization of Unpaved Roads with Geosynthetics". Journal of Geotechnical Engineering, 544-553.

Farrar, M.J. and J.P. Turner, (1991), "Resilient Modulus of Wyoming Subgrade Soils". MPC Report No. 91-1, Mountain Plains Consortium, Fargo, N.D.

FHWA. (2008). Ground-Based LiDAR: Rock Slope Mapping and Assessment. Lakewood: FHWA: Central Federal Lands Highway Division.

Fleming, P. R., M. W. Frost, and J. P. Lambert, (2007), "Review of Lightweight Deflectometer for Routine in Situ Assessment of Pavement Material Stiffness". In Transportation Research

Record: Journal of the Transportation Research Board, No. 2004, Transportation Research Board of the National Academies, Washington, D.C., pp. 80–87.

Fredlund, D. G., and Xing, A. (1994). "Equations for the soil-water characteristic curve." Canadian Geotechnical Journal, 31(4), 521-532.

Gabr, M.A., Coonse, J., and Lambe, P.C., (2001), "A Potential Model for Compaction Evaluation of Piedmont Soils Using Dynamic Cone Penetrometer (DCP)." Geotechnical Testing Journal, Vol. 24, No. 3, September 2001, Pages 308-313.

Gabr, M.A., Hopkins, K., Coonse, J., and Hearne, T., (2000), "DCP Criteria for Performance Evaluation of Pavement Layers." Journal of Performance and Constructed Facilities, ASCE, Vol. 14, No. 4, November 2000, Pages 141-148.

Geokon, I. (2007). Instruction Manual: Model 3500, 3510, 3515, 3600. Lebanon.

George, K. P., and Uddin, W., (2000), "Subgrade Characterization for Highway Pavement Design," Final Report MS-DOT-RD-00-131, Mississippi Department of Transportation.

Hasan, A., (1996), "The Effect of Material Parameters on Dynamic Cone Penetrometer Results for Fine-grained Soils and Granular Base Materials," Ph.D., Dissertation, Oklahoma State University, Stillwater.

Herath, A., Mohammad, L. N., Gaspard, K., Gudishala, R. and Abu-Farsakh, M. Y., (2005), "The use of Dynamic Cone Penetrometer to Predict Resilient Modulus of Subgrade Soils", Geotechnical Special Publication No. 130: Advances in Pavement Engineering, Geo-Frontiers, pp. 17-32.

Hossain, M. S.. Characterization of Unbound Pavement Materials from Virginia Sources for Use in the New Mechanistic-Empirical Pavement Design Procedure. FHWA/VTRC 11-R6.

Hudson, J.M., Drumm, E.C. and Madgett, M., (1994), "Design Handbook for the Estimation of Resilient Response of Fine-Grained Subgrades", Proceedings of the 4th International Conference on the Bearing Capacity of Roads and Airfields, University of Minnesota, Minneapolis, Vol. 2, pp. 917–931.

Hufenus, R., Rueegger, R., Banjac, R., Mayor, P., Springman, S. M., & Bronnimann, R. (2006). "Full-scale field test on geosynthetic reinforced unpaved roads on soft subgrades". Geotextiles and Geomembranes, 24, 21-37.

Janoo, V., Bayer, J. J., Benda, C.C., (2004), "Effect of Aggregate Angularity on Base Material Properties", Journal of Materials in Civil Engineering, Vol. 16, No. 6, pp. 614-622.

Kondner, R.L., (1963), "A hyperbolic stress strain formulation for sand", 2. Pan. Am. ICOSFE Brazil, 1, 289-324.

Leng, J., Gabr, M. A., (2005), "Numerical Analysis of Stress-deformation Response in Reinforced Unpaved Road Sections", Geosynthetics International, Vol.12, No.2, pp.111-119.

Li, D. and E. T. Selig, (1994), "Resilient Modulus for Fine-Grained Subgrade Soils". Journal of Geotechnical Engineering, Vol. 120, No. 6, pp 939-957.

Miura, N., Sakai, A., Taesiri, Y., Yamanouchi, T. and Yasuhara, K., (1990). "Polymer grid reinforced pavement on soft clay grounds", geotextiles and geomembranes, Vol. 9, No. 1, pp. 99-23.

Mohammad, L. N., Herath, A., Gudishala, R., Nazzal, M. D., Abu-Farsakh, M. Y. and Alshibli, K., (2008), "Development of Models to Estimate the Subgrade and Subbase Layers' Resilient Modulus from In situ Devices Test Results for Construction Control", Publication FHW-LA-406. FHWA, U.S. Department of Transportation.

Mooney M. A., and P. K. Miller, (2009), "Analysis of Lightweight Deflectometer Test Based on In Situ Stress and Strain Response". Journal of Geotechnical and Geoenvironmental Engineering, Vol. 135, No. 2, pp 199-208.

National Cooperative Highway Research Program (NCHRP), (2003), "Harmonized test methods for laboratory determination of resilient modulus for flexible pavement design", Final Rep. NCHR Project No. 1-28 A, National Cooperative Highway Research Program (NCHRP), Washington, D.C.

National Cooperative Highway Research Program (NCHRP), (2004), "Guide for Mechanistic-Empirical Design of New and Rehabilitated Pavement Structures", Part 2, Design Inputs, NCHRP 1-37A, Final Report.

Nazzal, M. D., Abu-Farsakh, M. Y. and Mohammad, L. N., (2010). "Implementation of a critical state two-surface model to evaluate the response of geosynthetic reinforced pavements." International Journal of Geomechanics, Vol. 10, No. 5, p202-212.

Nazzal, M. D., and Mohammad, L. N., (2010), "Estimation of Resilient Modulus of Subgrade Soils for Design of Pavement Structures", Journal of Materials in Civil Engineering, Vol. 22, No. 7. Pavement Condition Survey Manual, 1998,

NCDOT. (2012). Standard Specifications for Roads and Structures. Raleigh: North Carolina Department of Transportation.

NCHRP, (2008), "Estimating stiffness of subgrade and unbound materials for pavement design". Transportation Research Board of the National Academies, Washington, D.C.

NCHRP, (2003), "Harmonized test methods for laboratory determination of resilient modulus for flexible pavement design". Final Rep. NCHR Project No. 1-28 A, National Cooperative Highway Research Program (NCHRP), Washington, D.C.

Pezo, R. F., (1993), "A General Method of Reporting Resilient Modulus Tests of Soils: A Pavement Engineer's Point of View", Presented at the 72nd Annual Meeting of the Transportation Research Board, Washington, D.C.

Picornell, M., and Nazarian, S. (1998), "Effect of Soil Suction on The Low Strain Shear Modulus of Soils", Proceeding of 2nd international conference on unsaturated soils: UNSAT 98, Beijing, China, 102-107.

Powell, W. D., Potter, J. F., Mayhew, H. C., and Nunn, M. E., (1984), "The Structural Design of Bituminous Roads", Transport and Road Research Laboratory (TRRL), Report LR 1132, Berkshire, United Kingdom.

Qian, Y., Han, J., Pokharel, S. K., Parsons, R. L., (2013), "Performance of Triangular Aperture Geogrid-Reinforced Base Courses over Weak Subgrade under Cyclic Loading", J. Mater. Civ. Eng. 2013.25:1013-1021.

Quin, X., Gray, D.H., and Richard, W. (1993), "Voids and Granulomerty: Effects on Shear Modulus of Unsaturated Sands", Journal of Geotechnical engineering, 119 (2), 295-314.

Rahim, A. M., and George, K. P., (2004), "Subgrade Soil Index Properties to Estimate Resilient Modulus", Transportation Research Board of the National Academies, Washington, D.C.

Retrieved from Decagon Devices: http://www.decagon.com/products/sensors/soilmoisture-sensors/10hs-soil-moisture-large-area-of-influence/

Seed, H. B., Mitry, F. G., Monismith, C. L. and Chan, C. K., (1697), "NCHRP Report 35: Prediction of Flexible Pavement Deflections from Laboratory Repeated-Load Tests", Highway Research Board, National Research Council, Washington, D.C.

Terzaghi, K., and R. B. Peck., (1967), "Soil mechanics in engineering practice". 2nd Ed., John Wiley & Sons, Inc., New York.

Thakur, J. K., Han, J., Pokharel, S. K., Parsons, R. L., (2012), "Performance of geocell-reinforced recycled asphalt pavement (RAP) bases over weak subgrade under cyclic plate loading", Geotextiles and Geomembranes 3, 14-24.

Tingle, J. S., & Jersey, S. R. (2009). "Full-Scale Evaluation of Geosynthetic-Reinforced Aggregate Roads". Transportation Research Record: Journal of Transportation Research Board, No. 2116, 96-107.

Tingle, J. S., & Webster, S. L. (2003). "Corps of Engineers Design of Geosynthetic-Reinforced Unpaved Roads". Transportation Research Record: Journal of Transportation Research Board, No. 1849, 193-201.

Tingle, J. S., Jersey, S. R., (2005), "Cyclic Plate Load Testing of Geosynthetic-Reinforced Unbound Aggregate Roads", Transportation Research Record: Journal of the Transportation

Research Board, No. 1936, Transportation Research Board of the National Academies, Washington, D.C., 2005, pp. 60–69.

Toros, U. (2008), “Effects of Moisture and Time on Stiffness of Unbound Aggregate Base Course Materials”, Ph.D Dissertation, University of Florida, May 2008.

Van Genuchten, M. T. (1980). "A closed-form equation for predicting the hydraulic conductivity of unsaturated soils." Soil Sci.Soc.Am.J., 44(5), 892-898.

Vanapalli, S. K. and Han, Z., (2010), “Prediction of the Resilient Modulus of Unsaturated Fine-Grained Soils”, Proc. of Int. Conf. on Advances in Civil Engineering, AETACE.

Vennapusa, P. K. R., (2008), “Investigation of roller-integrated compaction monitoring and in-situ testing technologies for characterization of pavement foundation layers”. Graduate Theses and Dissertations.

Wang, C., (2014), “Soil Suction Characterization and New Model for Predicting Suction in Residual Soils”, Ph.D dissertation, North Carolina State University, Raleigh, NC.

Wathugala, G. W., Huang, B., and Pal, S., (1996). “Numerical simulation of geosynthetic reinforced flexible pavement”, Transportation Research Record 1534, Transportation Research Board, national Research Council, Washington, DC, USA, pp.58-65.

Webster, S. L., & Alford, S. J. (1978). “Investigation of Construction Concepts for Pavements Across Soft Ground”. Vicksburg, Miss.: Technical Report S-78-6. U.S. Army Corps of Engineers Waterways Experiment Station.

Webster, S. L., & Watkins, J. E. (1977). “Investigation of Construction Techniques for Tactical Bridge Approach Roads across Soft Ground.” Vicksburg, Miss.: Technical Report S-77-1.

Webster, S. L., Brownand, R.W. and Porter, J. R., (1994), “Force Projection Site Evaluation Using the Electric Cone Penetrometer and the Dynamic Cone Penetrometer”, Report GL-94-17, U.S. Waterways Experimental Station.

White, D., M. Thompson, and P. Vennapusa, (2007), “Field Validation of Intelligent Compaction Monitoring Technology for Unbound Materials”. Report No. MN/RC-2007-10.

Witczak, M.W. and J. Uzan., (1988), “The Universal Airport Pavement Design System”. Report 1 of 4, Granular Material Characterization, University of Maryland, College Park.

Yau, A. and Von Quintus, H., (2002), “Study of laboratory resilient modulus test data and response characteristics”, Rep. No. FHWA-RD-02-051, FHWA, U.S. Department of Transportation, Washington, D.C.

Zapata, C. E., Houston, W. N., Houston, S. L., and Walsh, K. D. (2000). "Soil-water characteristic curve variability." Geotech Spec Publ, (99), 84-12

APPENDIX

Appendix A: MPS-2 Suction sensor Calibration

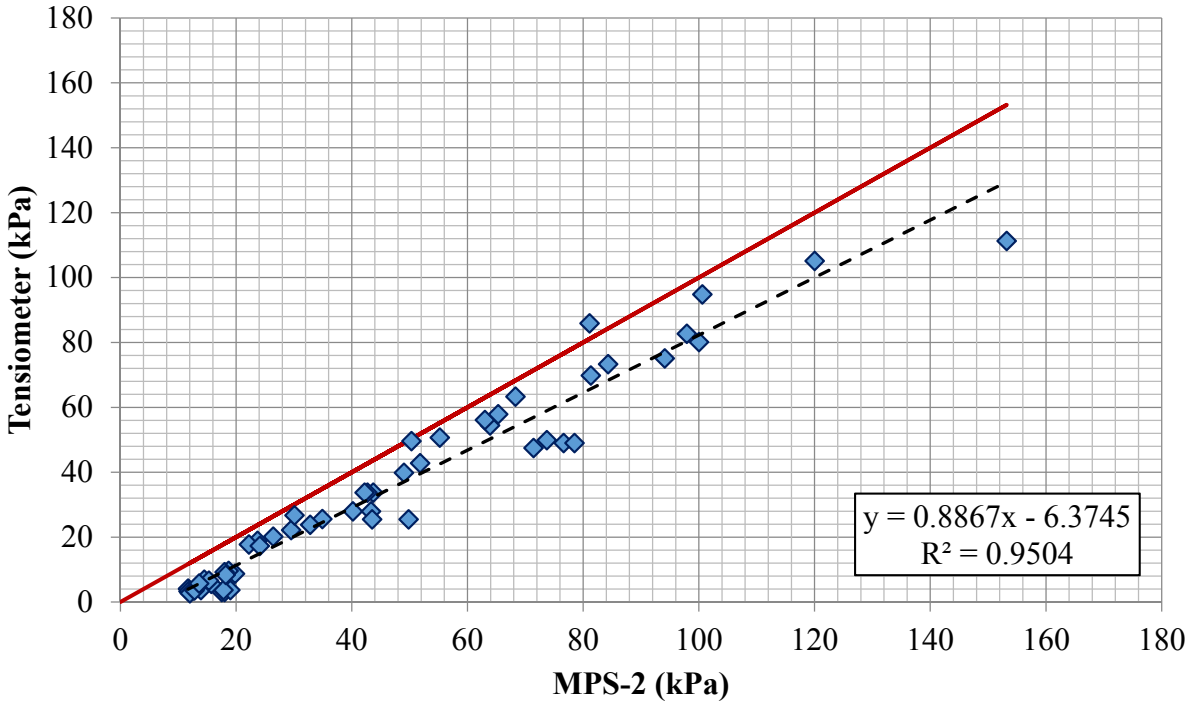

Figure A-1. MPS-2 Suction sensor Calibration

Appendix B: EPC Calibration

The first attempt to calibrate the Geokon pressure cells involved the use of an MTS hydraulic press at the Constructed Facilities Laboratory at NCSU. Two rubber plates were created to transfer the applied load from the MTS hydraulic press to the pressure cells, as illustrated in Figure 1, below.

Figure B-1. MTS hydraulic press applying load to Geokon Pressure Cell

The MTS hydraulic press was set to the displacement mode setting and was allowed to slowly increase from zero loading to the desired maximum load for each test. The applied pressure was calculated as the applied load divided by the area of the circular rubber plate that was contacting the pressure cell. The desired maximum applied pressure was decided to be 50 kPa lower than the pressure rating of each respective pressure cell. For a set number of load magnitudes, the corresponding readout (in mA) from the pressure cell was recorded by way of the Vishay system and Micromeasurements Strainsmart software, described in section x.x of this report.. After completing the calibration of the pressure cells using the MTS hydraulic press, the mA readouts from the pressure cell were converted to kPa readouts using the data reduction method listed in section x.x of this report. It was determined that the pressures reported by pressure cells were not consistent with the loading applied by the MTS hydraulic press. It was then decided that the use

of the MTS hydraulic press was not appropriate in our case due to the non-uniform distribution of stress which is a function of the aspect ratio of the pressure cell, the stiffness of the pressure cell, and the size of the rubber contact plates.

In order to more accurately calibrate the pressure cells, a Hydrostatic testing chamber was constructed which would allow the pressure plate to rest inside a rigid tank that would then be pressurized with air. The hydrostatic chamber, which was constructed by the staff at the Constructed Facilities Laboratory at NCSU, is shown in Figure 2, below.

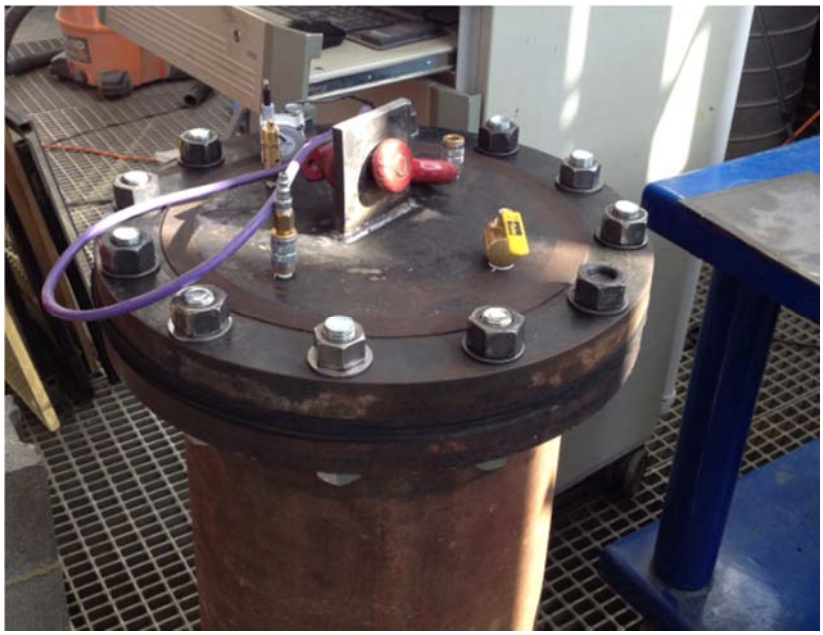

Figure B-2. Hydrostatic Testing Chamber

In this method, the user was able to manually add or reduce air pressure inside the tank (using the CFL air compressor) to obtain the desired pressure magnitude. The known, or applied, pressure was determined by reading the external pressure gauge. Two pressure gauges with different ranges of pressure readout were used to minimize human error. Simultaneously, the user recorded the pressure cell readout (in mA) by way of the Vishay software. After collecting the data pairs described above, over the range of 0 psi to the maximum desired pressure for each pressure cell, the known pressure was converted from psi to kPa and the pressure cell readout was converted from the mA reading to kPa reading according to the provided Geokon calibration data for each pressure cell. The results of the hydrostatic chamber tests are included in section x.x of this report.

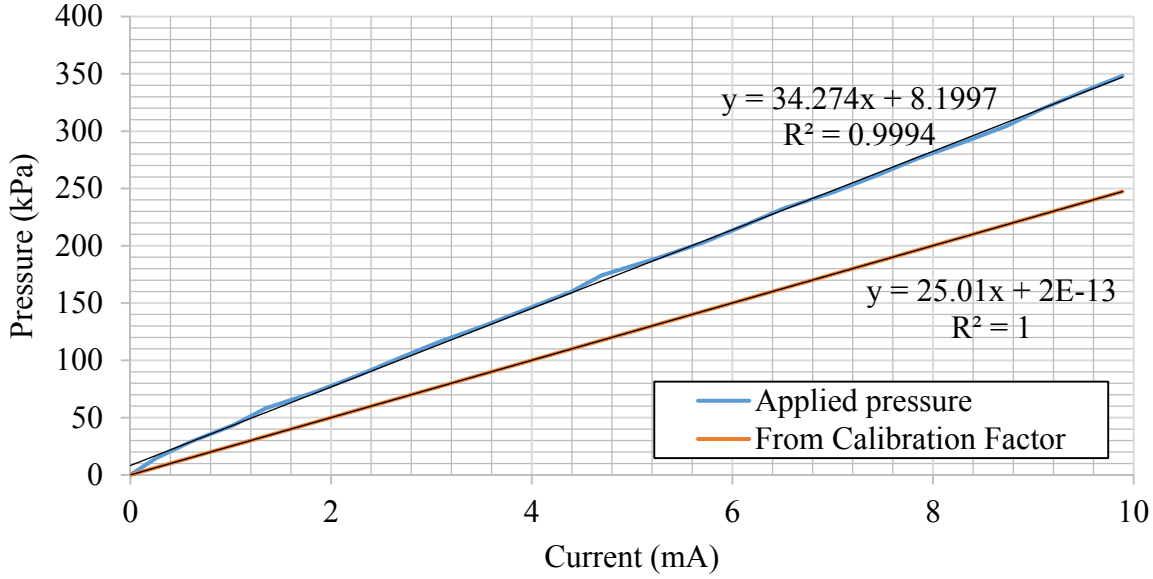

Figure B-3. Calibration of Earth pressure cell by MTS

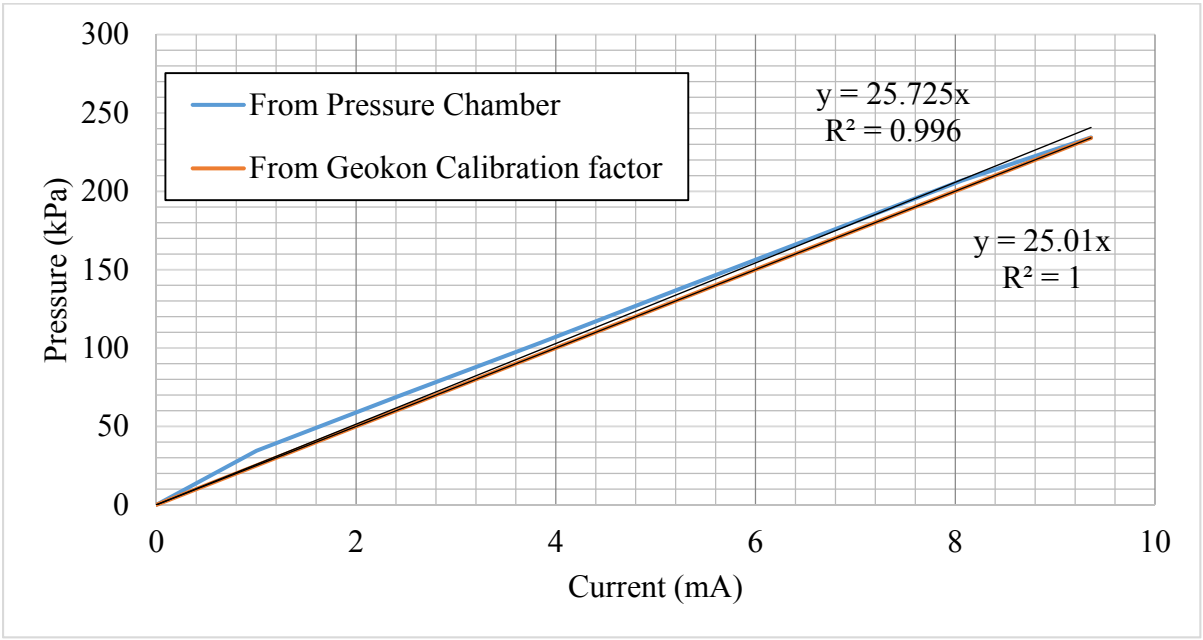

Figure B-4. Calibration of Earth pressure cell by air pressure chamber

Appendix C: CU Triaxial test results

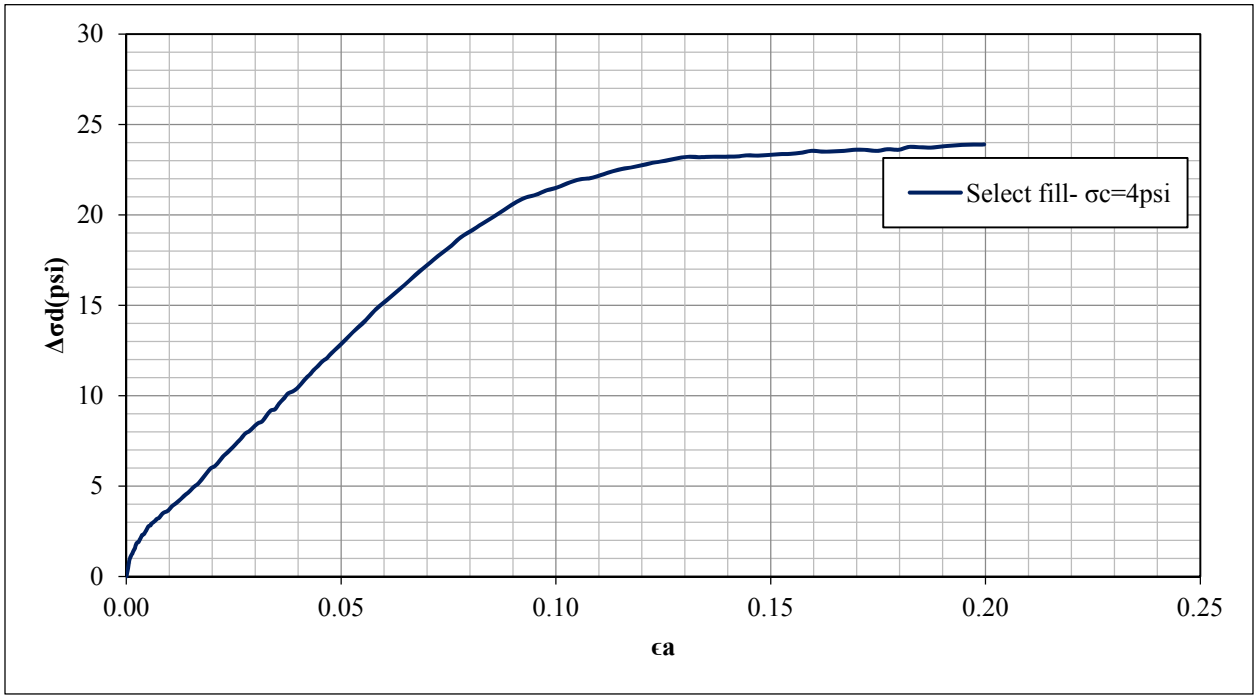

Figure C-1. Stress-strain curve of select fill material, Dr:95%, σ'_c:4 (psi)

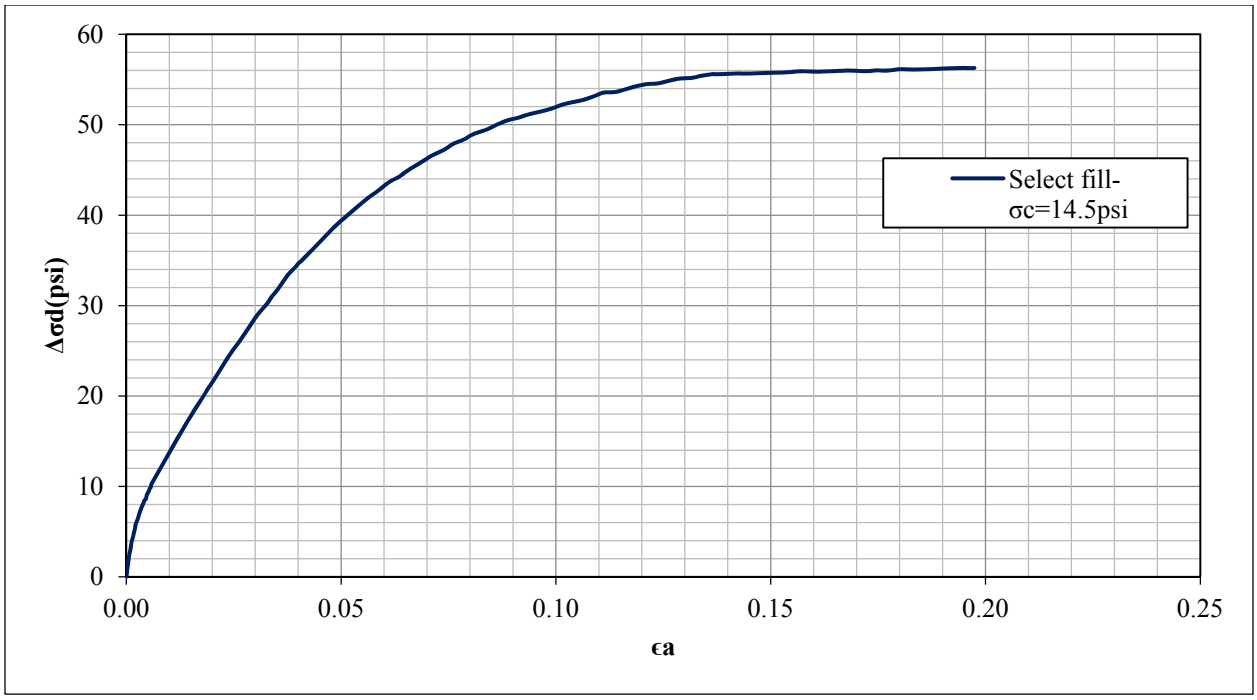

Figure C-2. Stress-strain curve of select fill material, Dr:95%, σ'c:14.5 (psi)

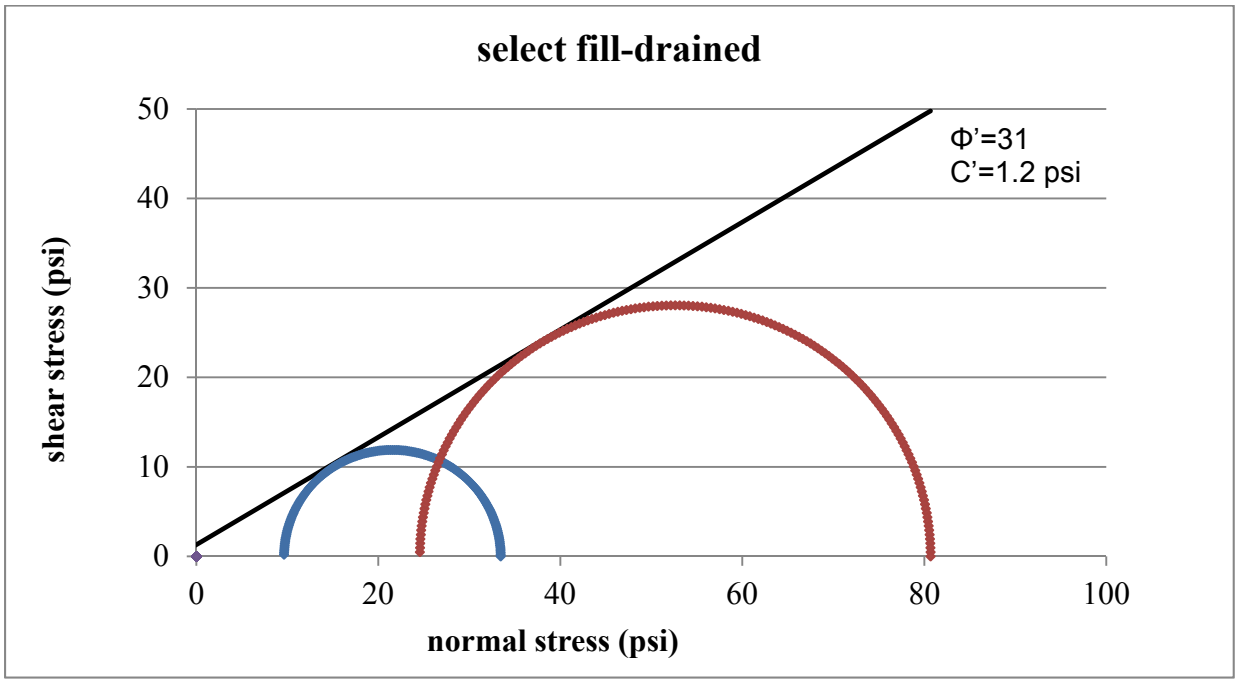

Figure C-3. Mohr circles in terms of effective stress (select fill, Dr: 95%)

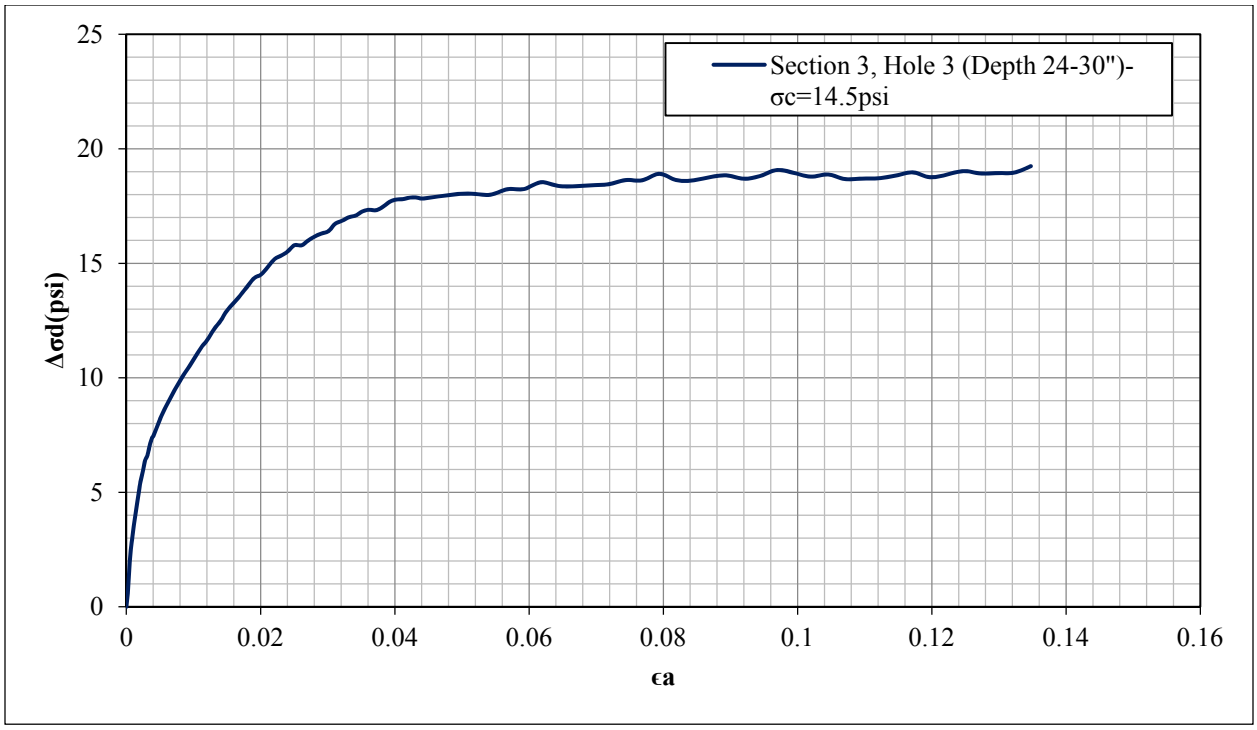

Figure C-4. Stress-strain curve of A-4 soil, specimen H33, σ'_c: 14.5 (psi)

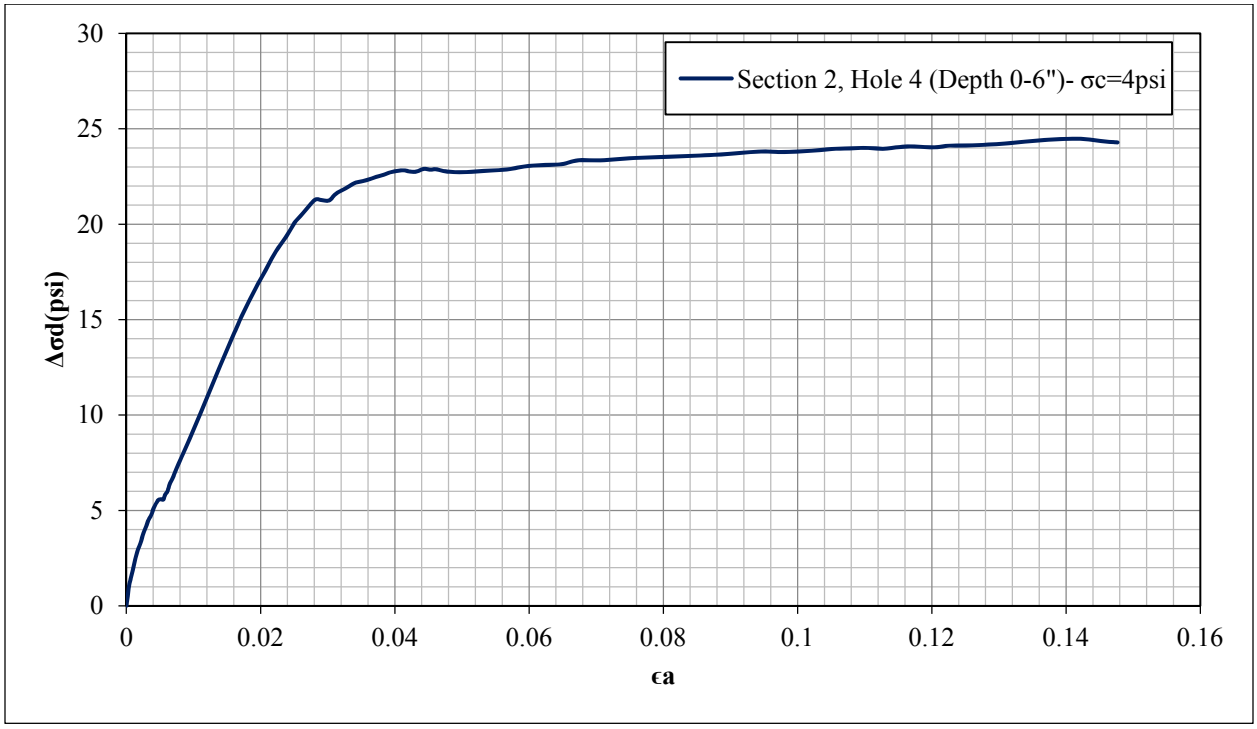

Figure C-5. Stress-strain curve of A-4 soil, specimen H41, σ'_c: 4 (psi)

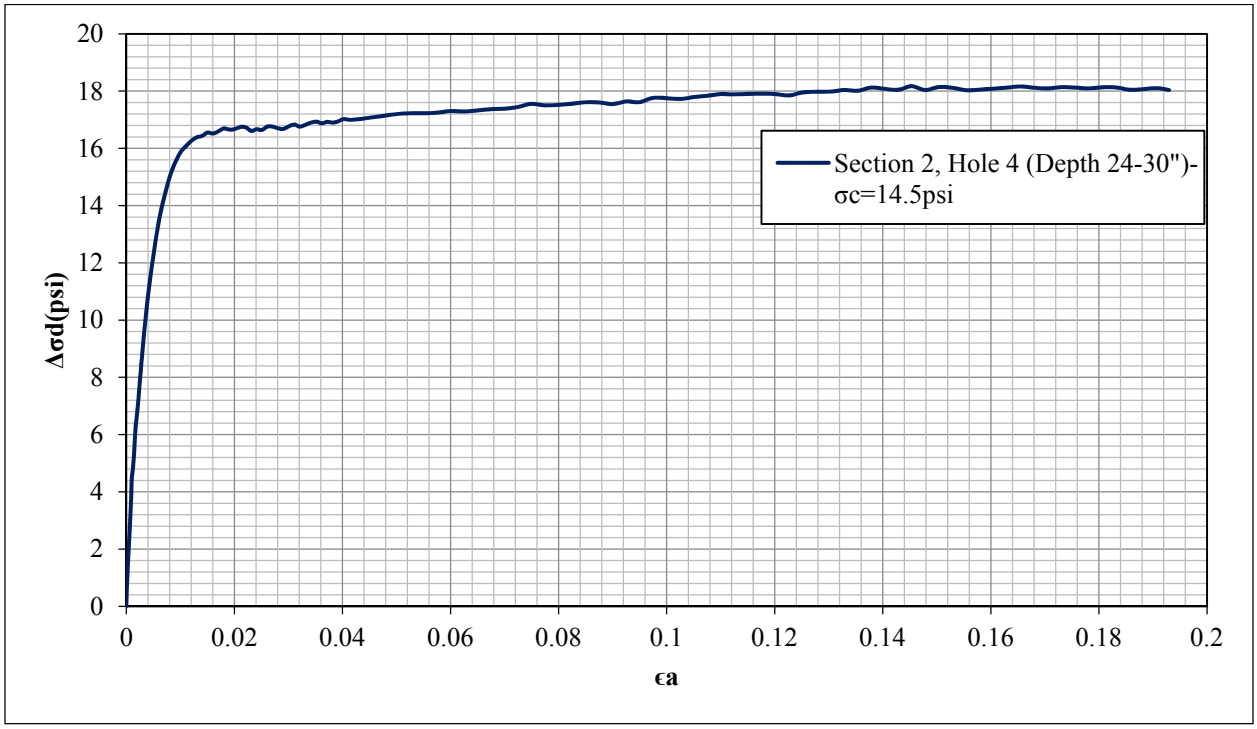

Figure C-6. Stress-strain curve of A-4 soil, specimen H43, σ'_c: 14.5(psi)

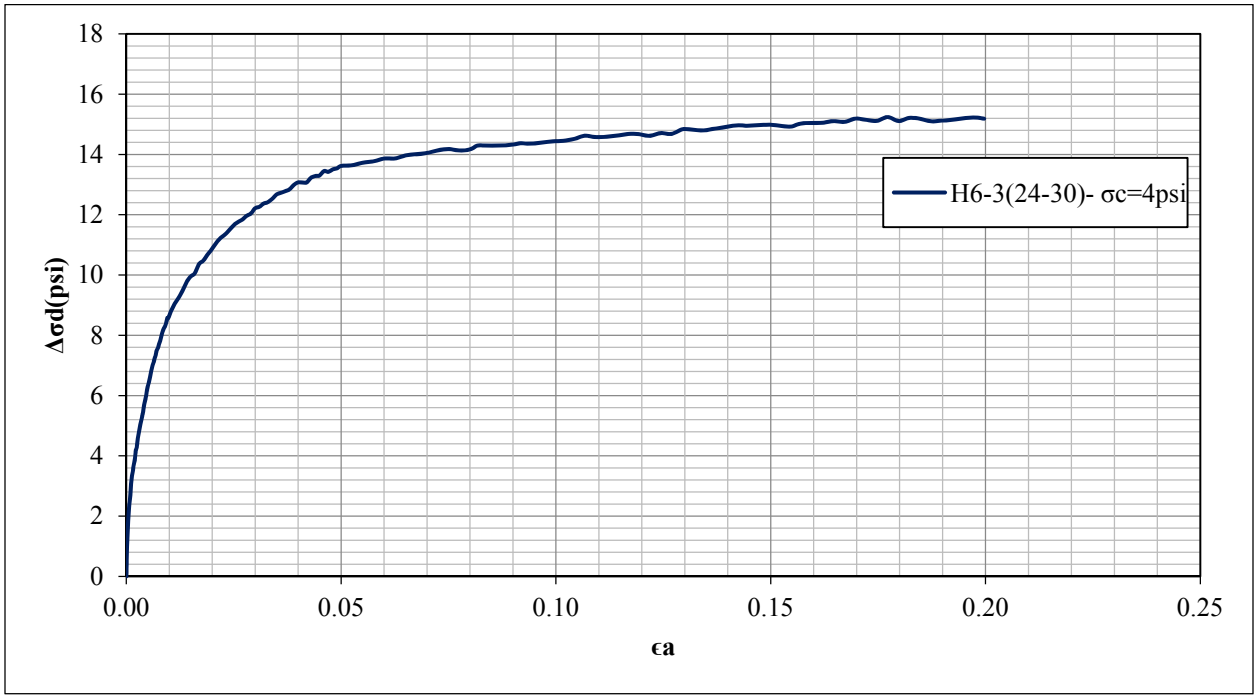

Figure C-7. Stress-strain curve of A-4 soil, specimen H63, σ'c: 4.5(psi)

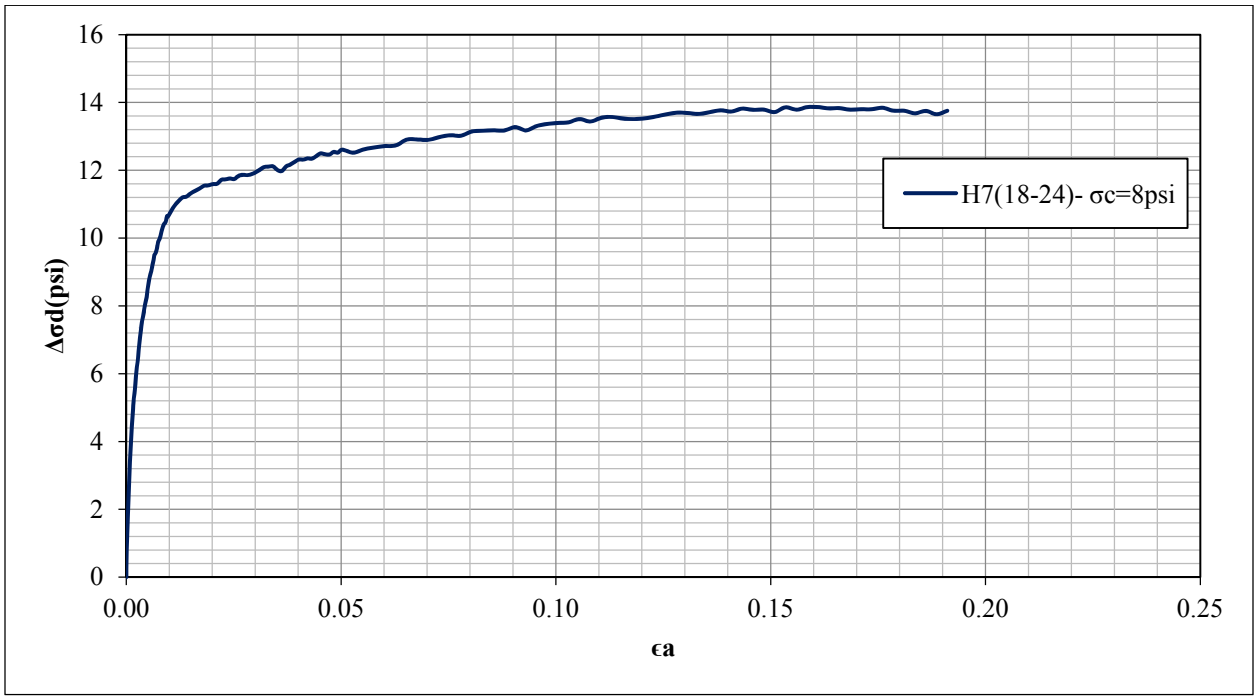

Figure C-8. Stress-strain curve of A-4 soil, specimen H81, σ'c: 8(psi)

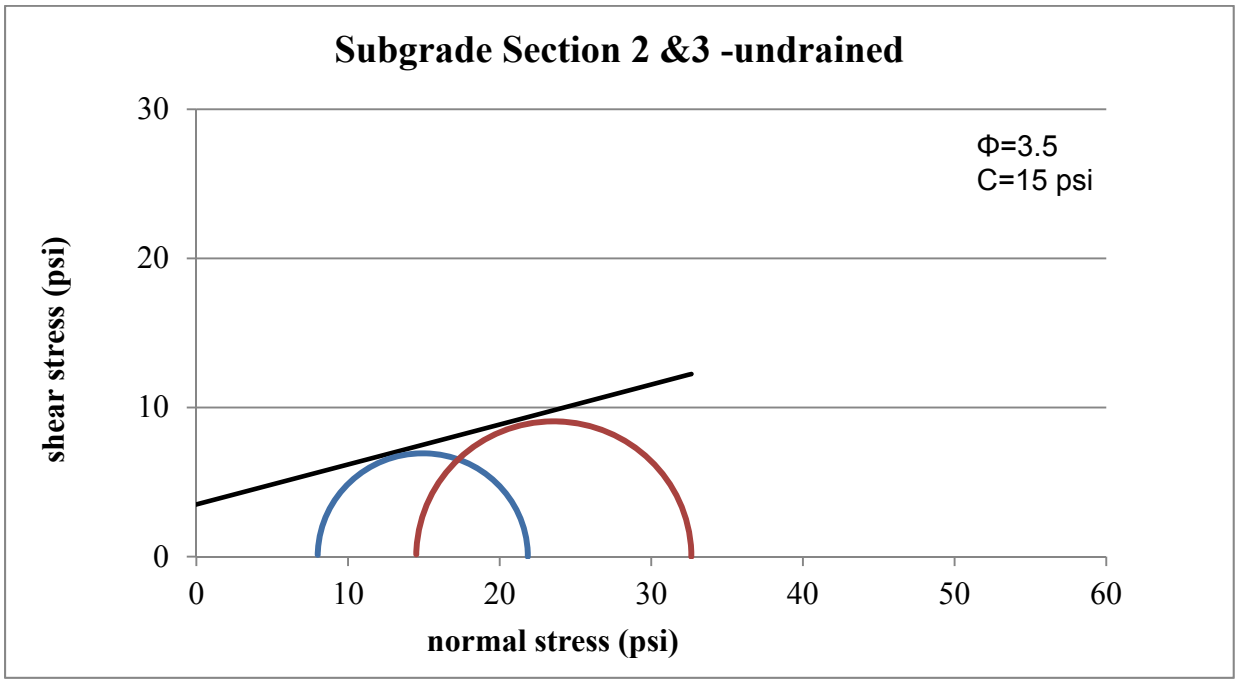

Figure C-9. Mohr circles in terms of total stress (A-4 soil)

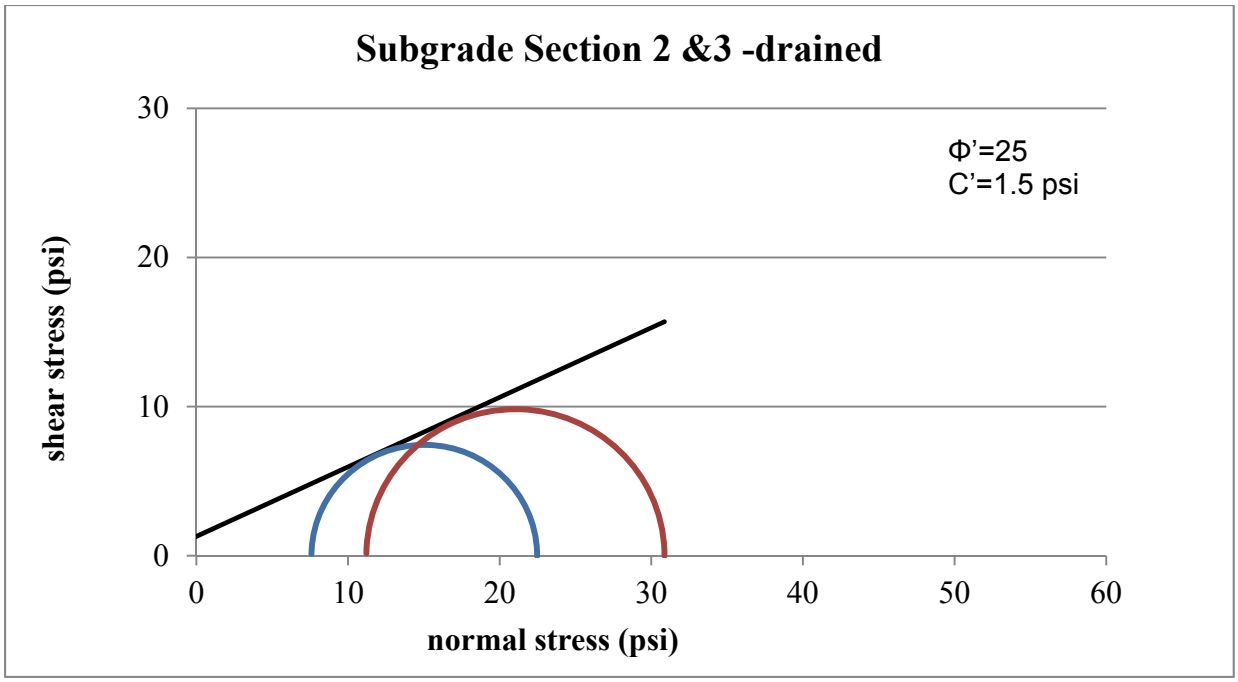

Figure C-10. Mohr circles in terms of effective stress (A-4 soil)

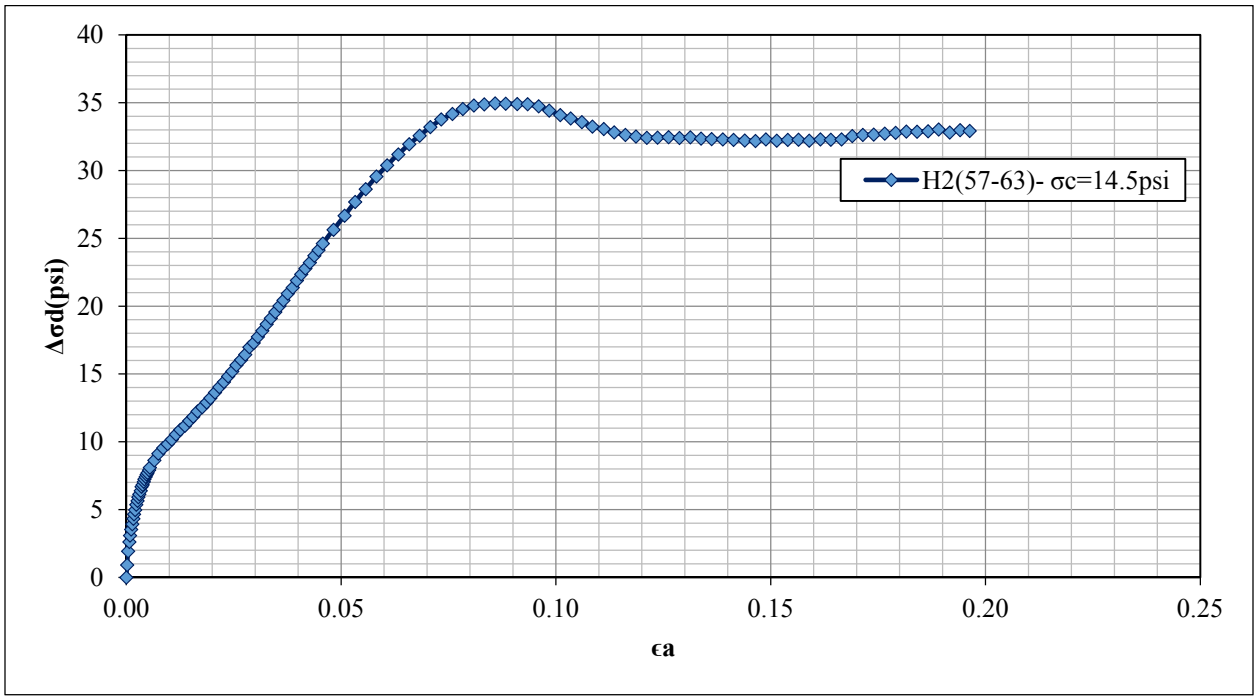

Figure C-11. Stress-strain curve of A-7-5 soil, specimen H21, σ'_c: 14.5(psi)

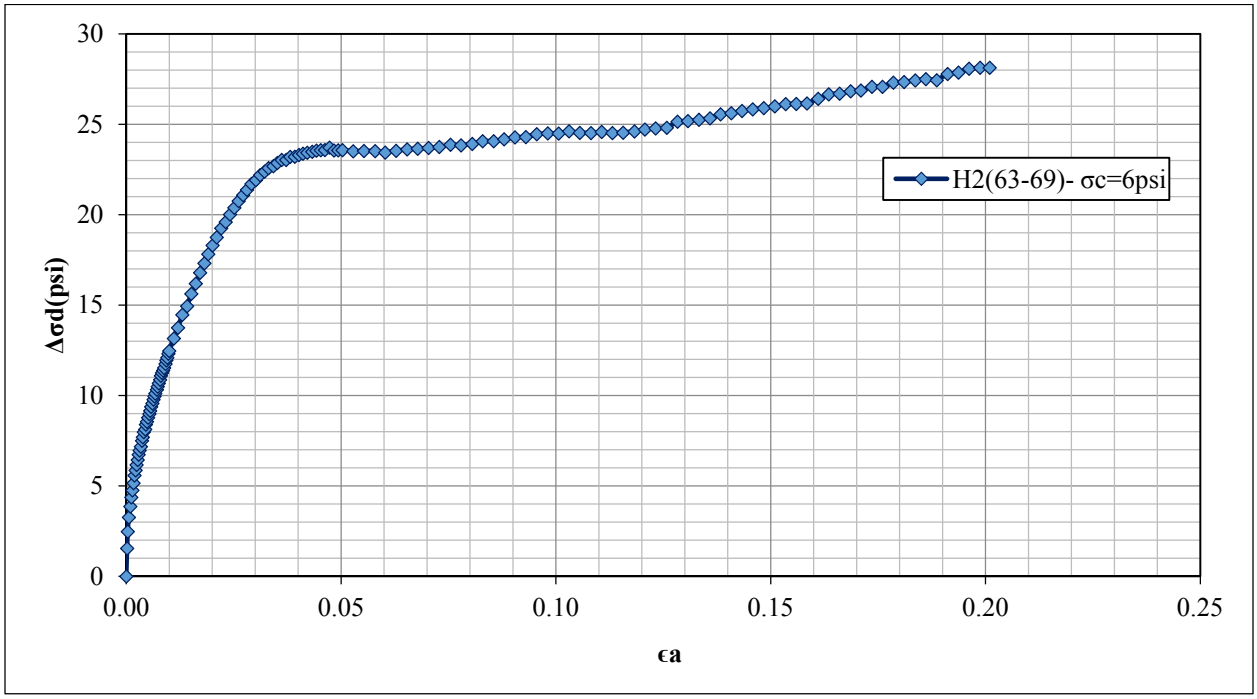

Figure C-12. Stress-strain curve of A-7-5 soil, specimen H22, σ'c: 6(psi)

Appendix D: Resilient modulus laboratory tests

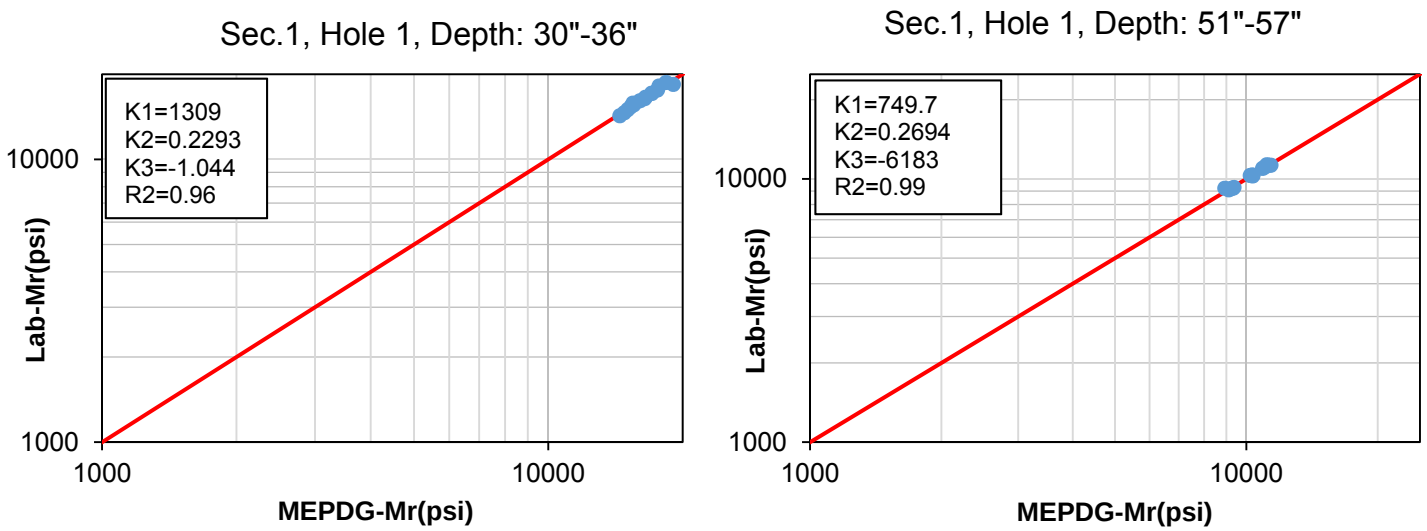

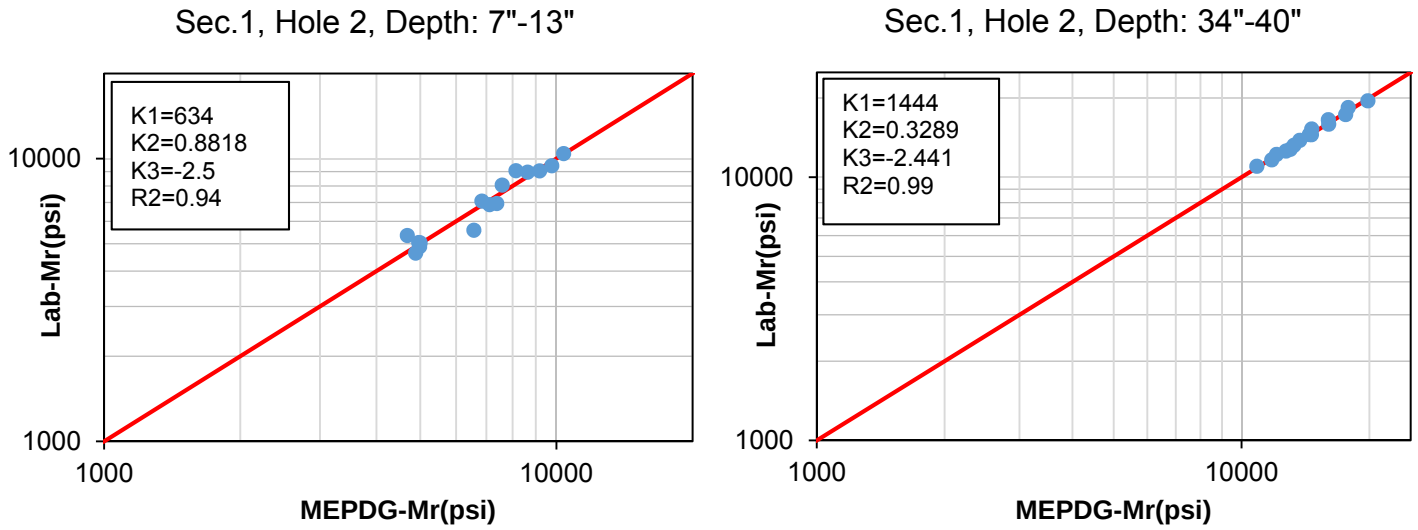

Figure D-1. Laboratory resilient modulus test results, specimens from section 1

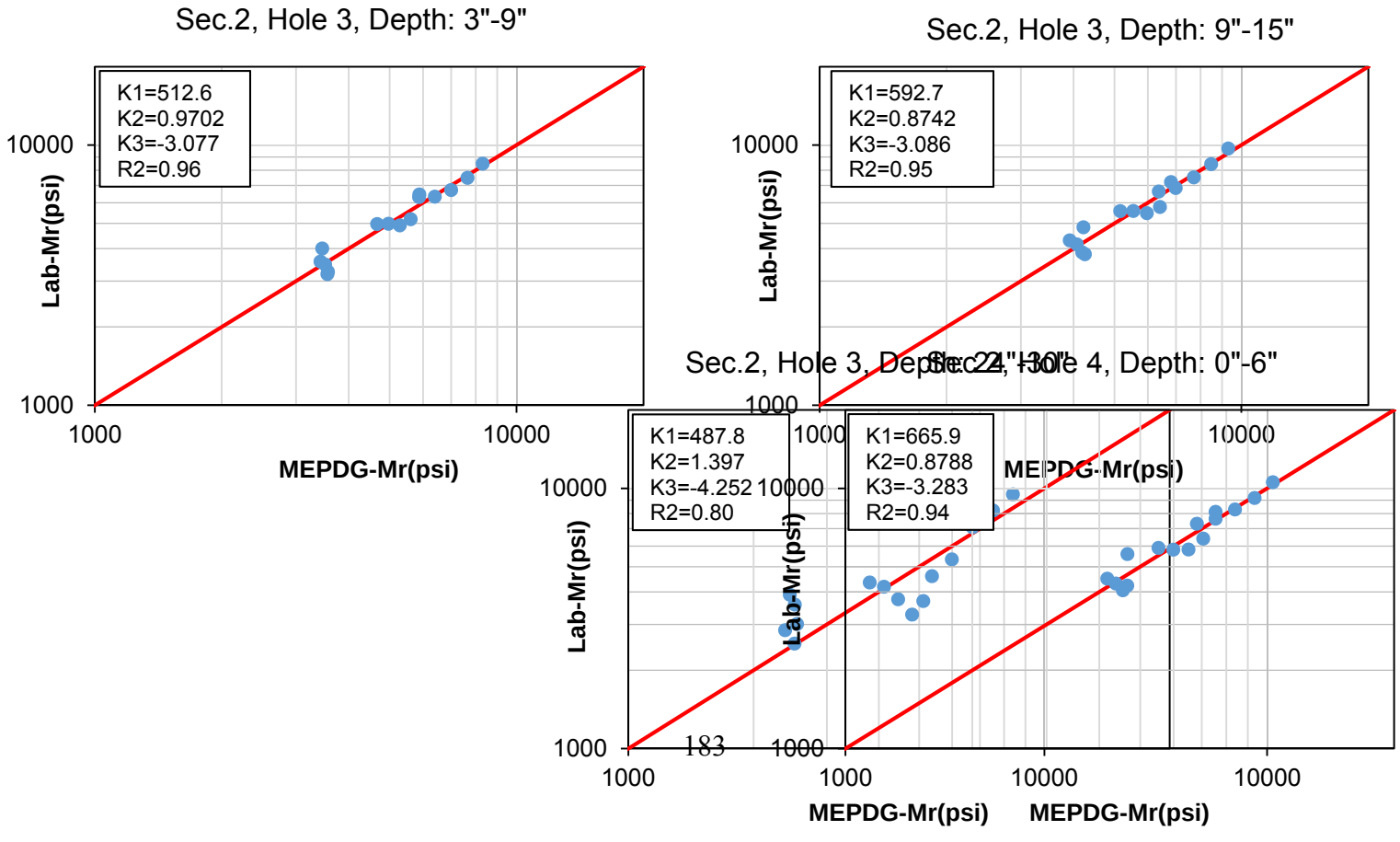

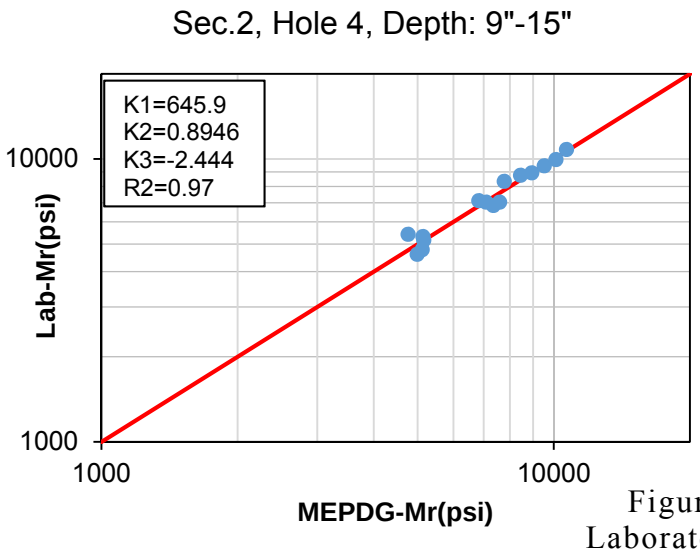

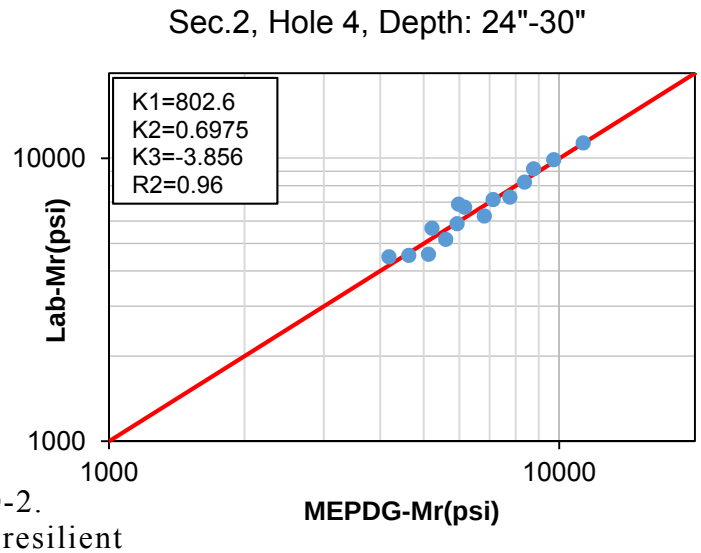

Figure D-2. Laboratory resilient modulus test results, specimens from section 2

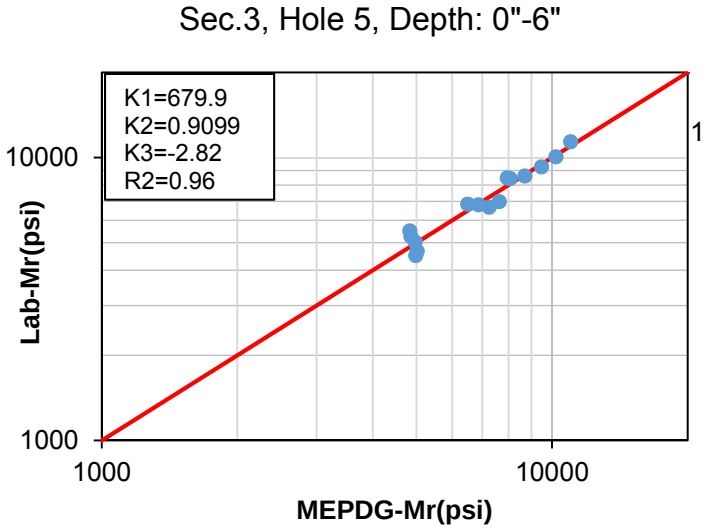

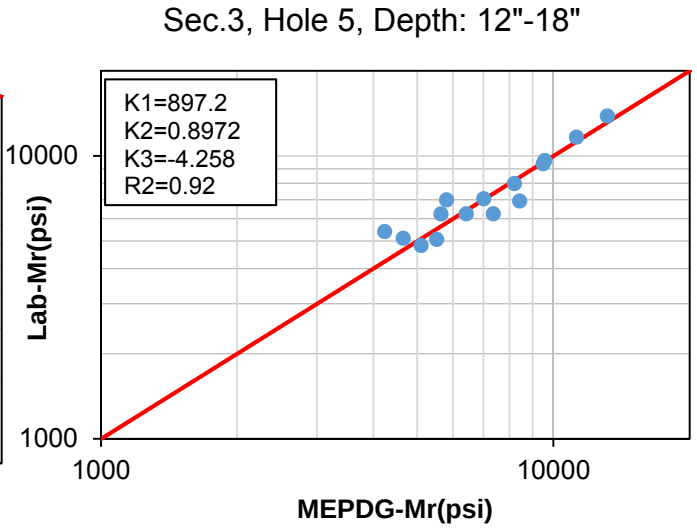

Figure D-3. Laboratory resilient modulus test results, specimens from section 3

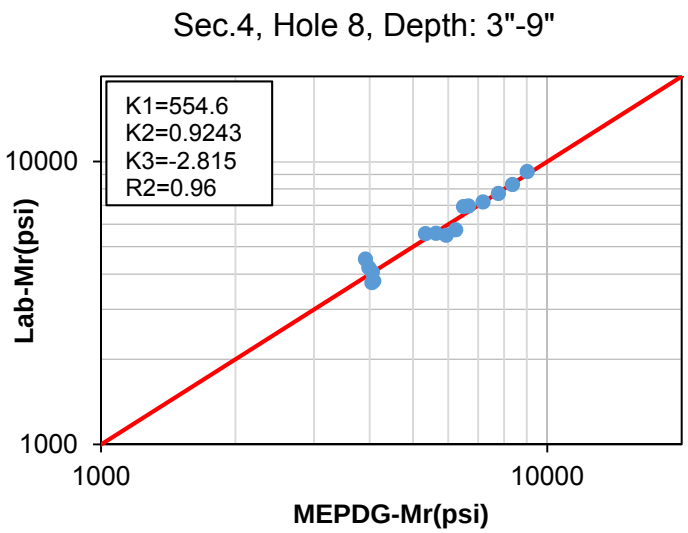

Figure D-4. Laboratory resilient modulus test results, specimens from section 4

Appendix E: Earth Pressure Cells measurement

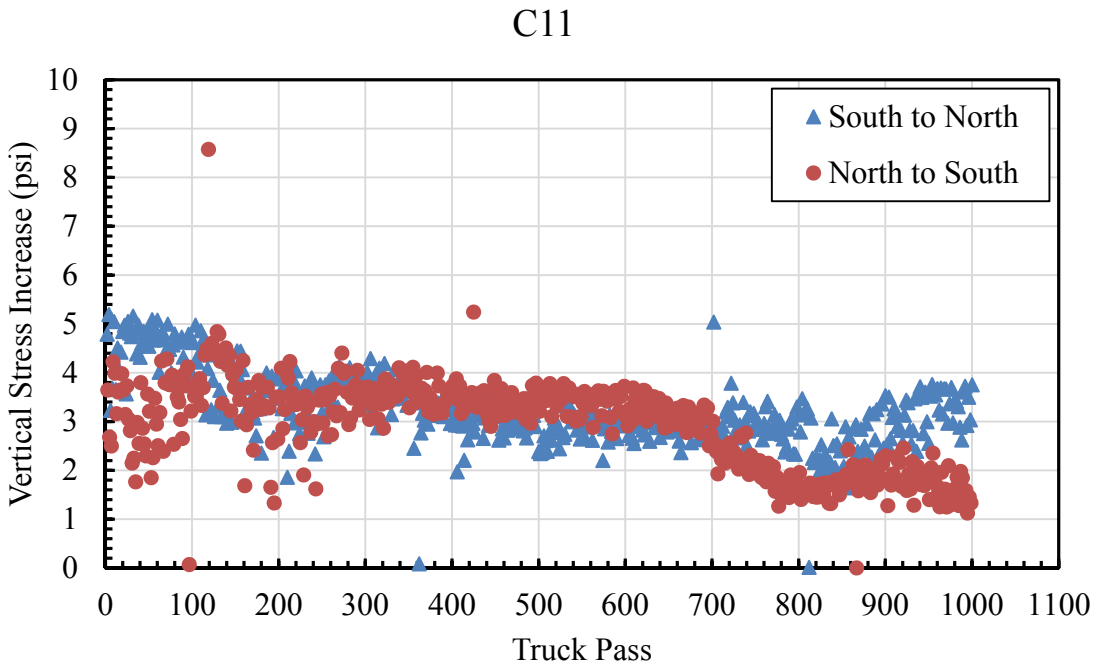

Figure E-1. Measured pressure by EPC C11

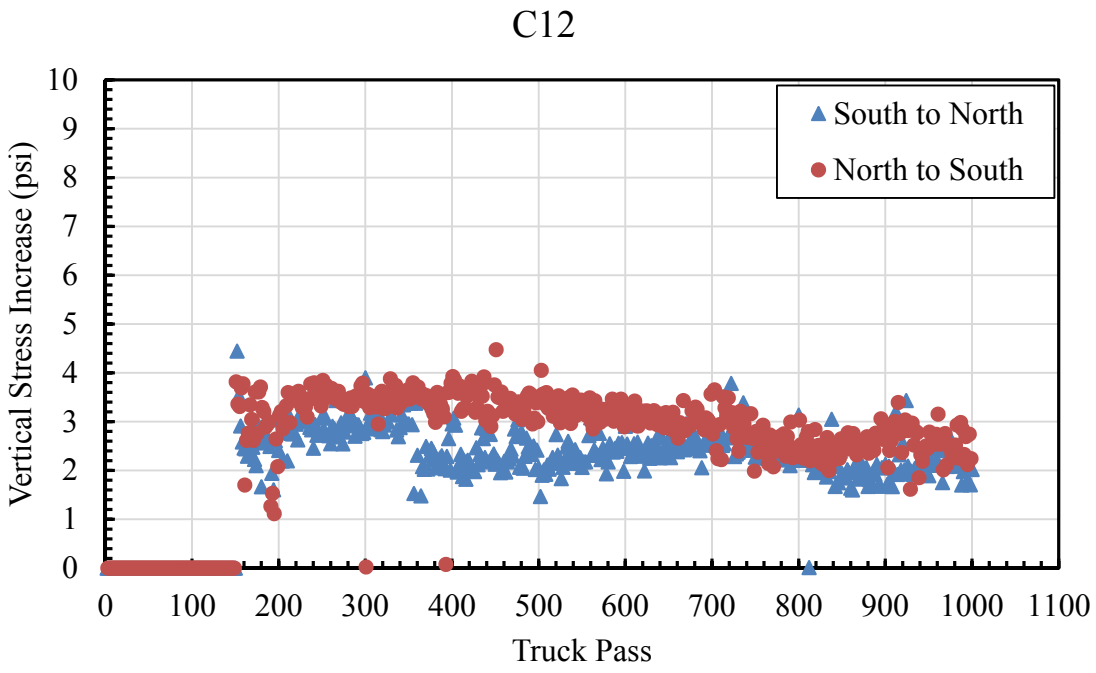

Figure E-2. Measured pressure by EPC C12

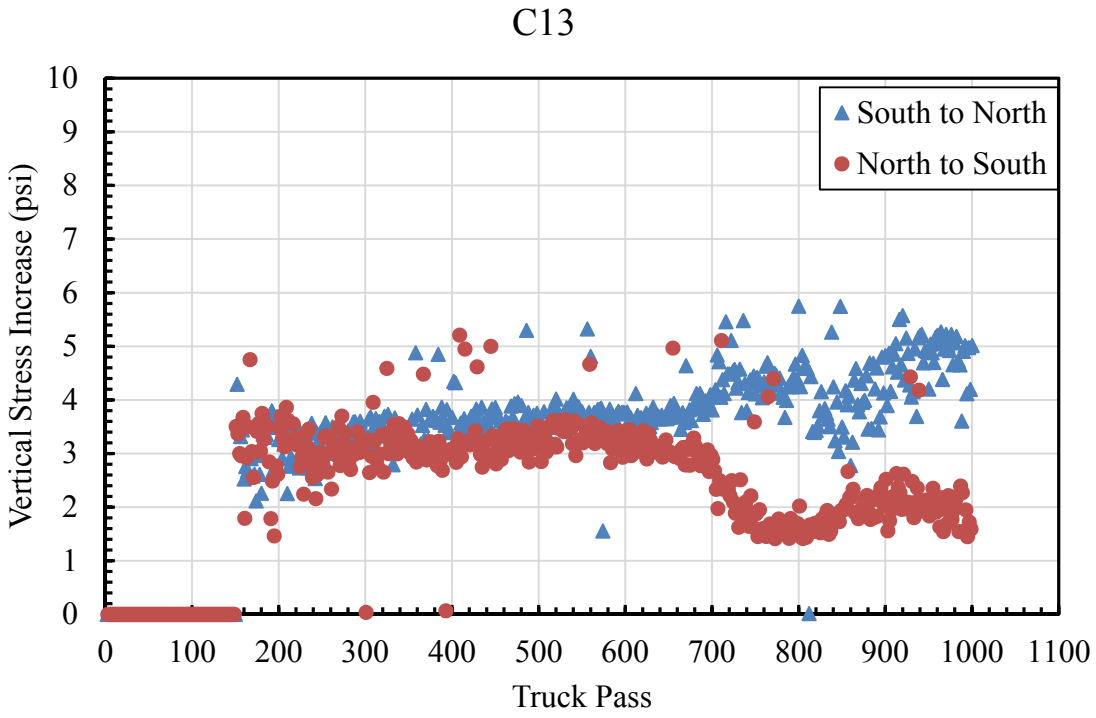

Figure E-3. Measured pressure by EPC C13

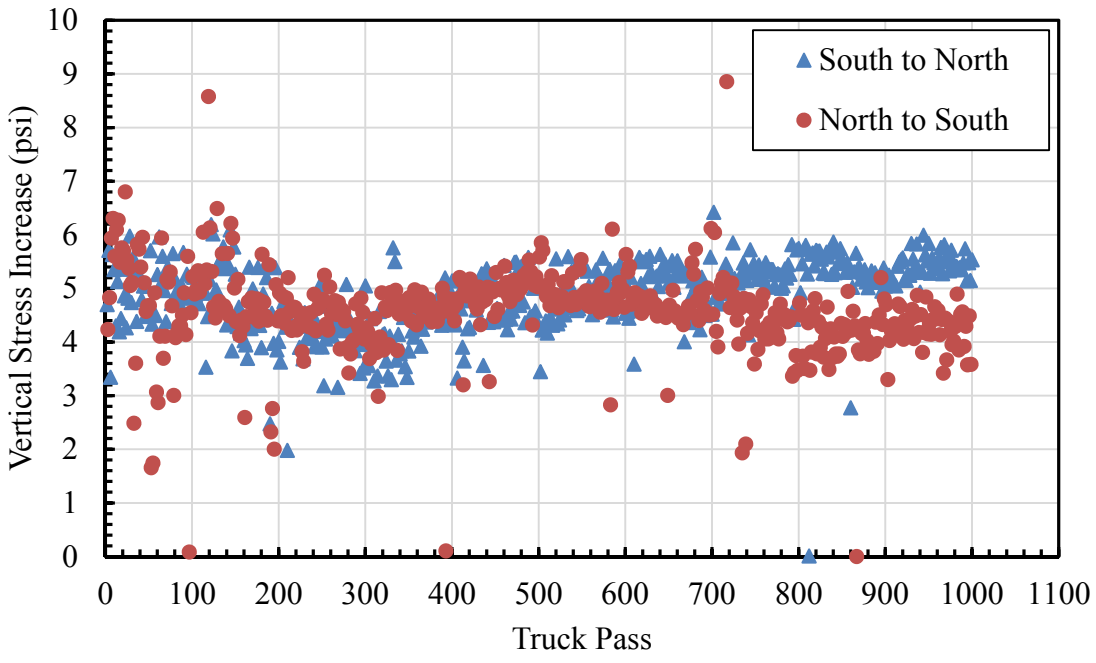

Figure E-4. Measured pressure by EPC C14

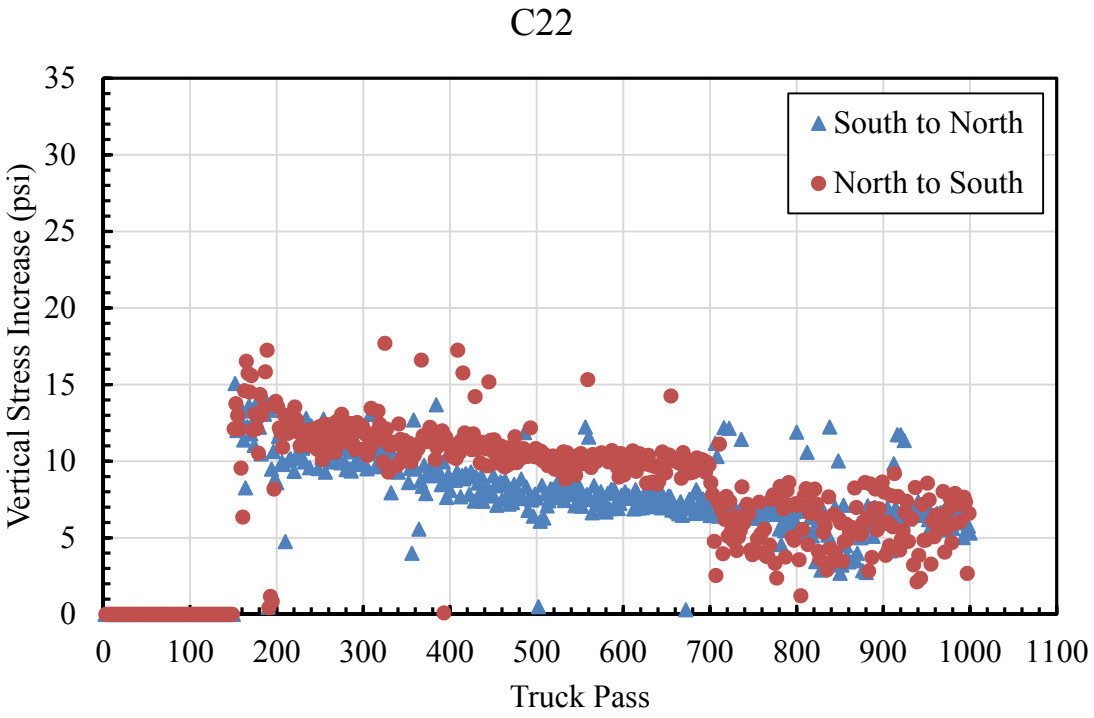

Figure E-5. Measured pressure by EPC C21

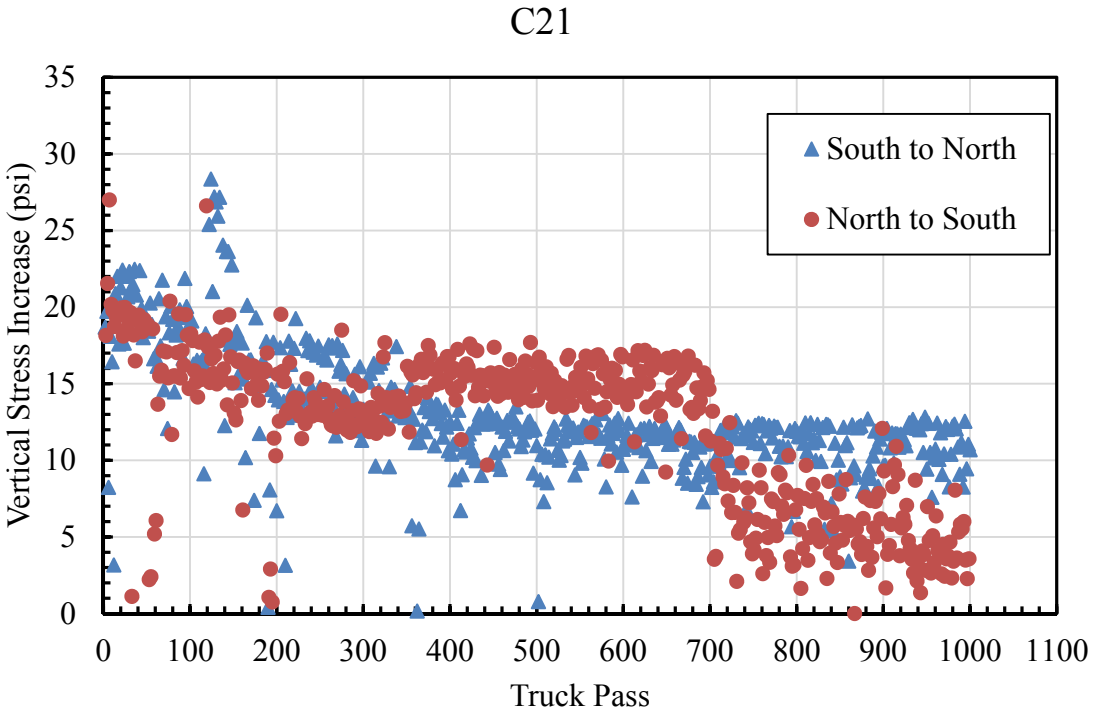

Figure E-6. Measured pressure by EPC C22

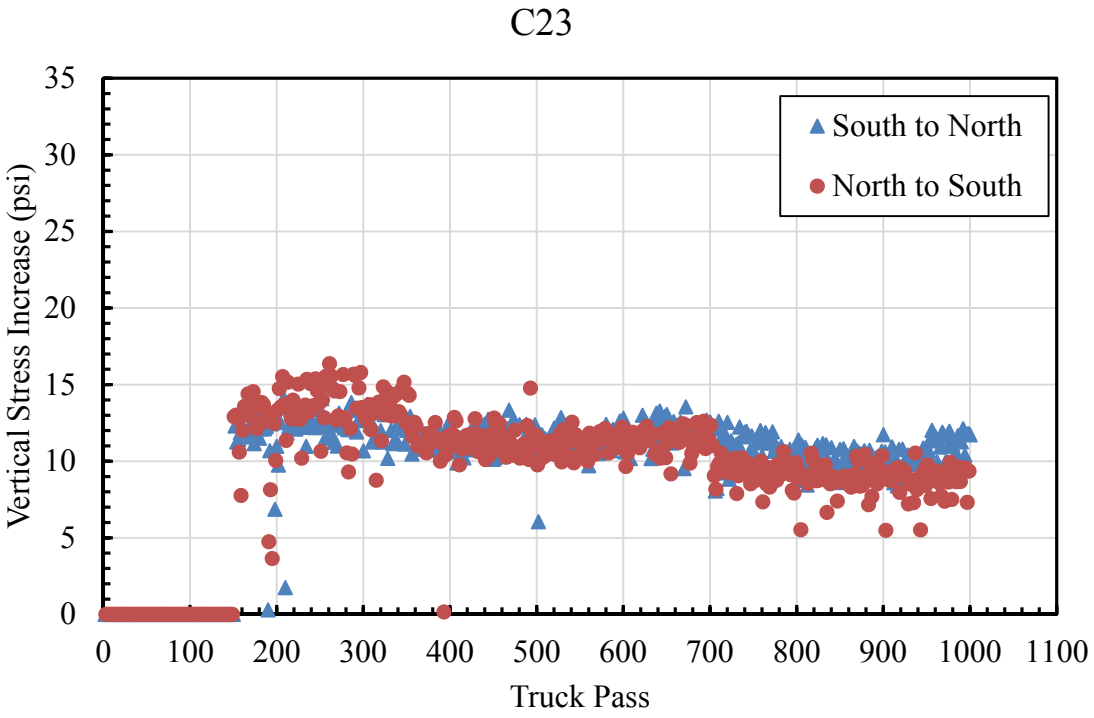

Figure E-7. Measured pressure by EPC C23

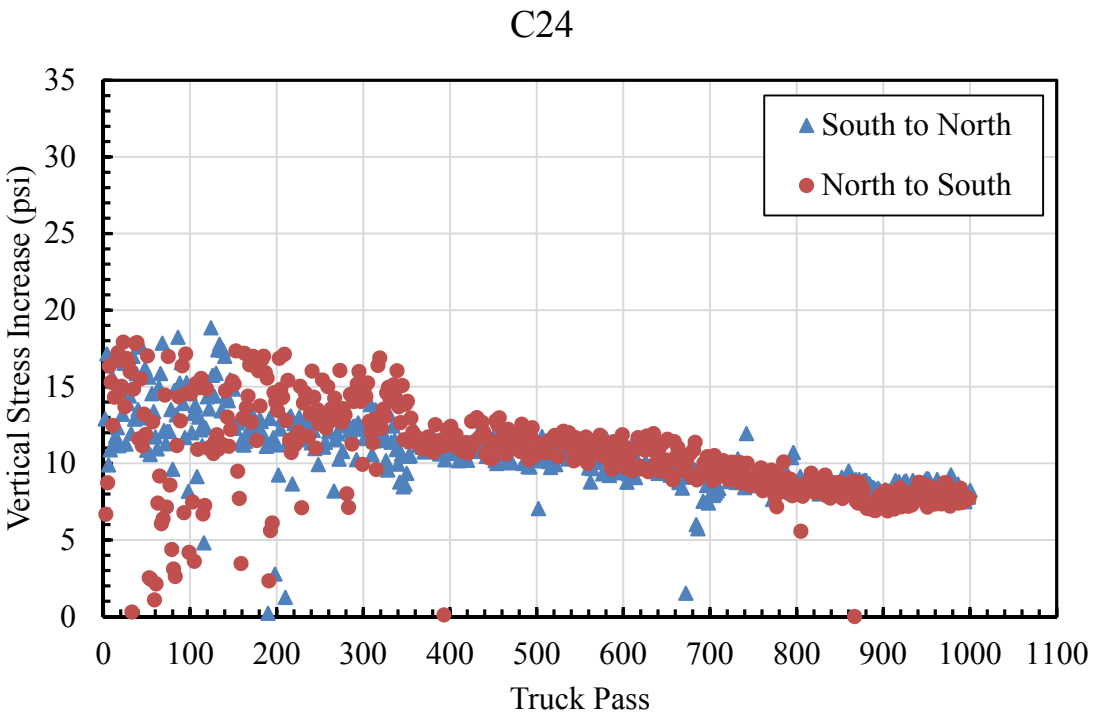

Figure E-8. Measured pressure by EPC C24

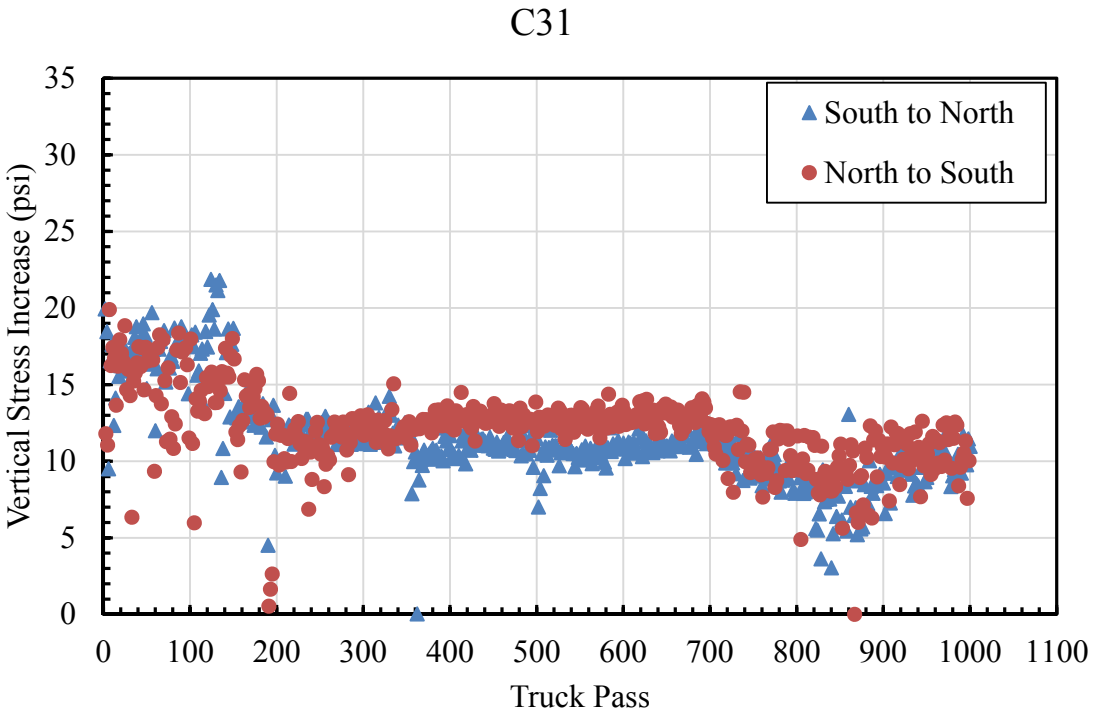

Figure E-9. Measured pressure by EPC C31

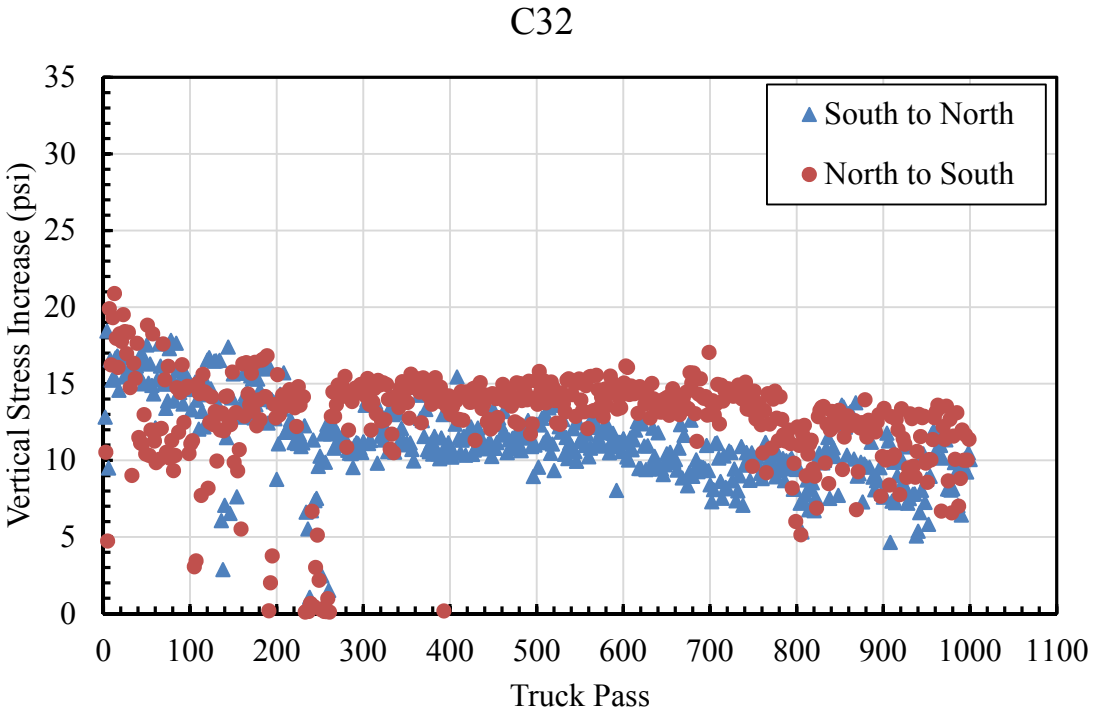

Figure E-10. Measured pressure by EPC C32

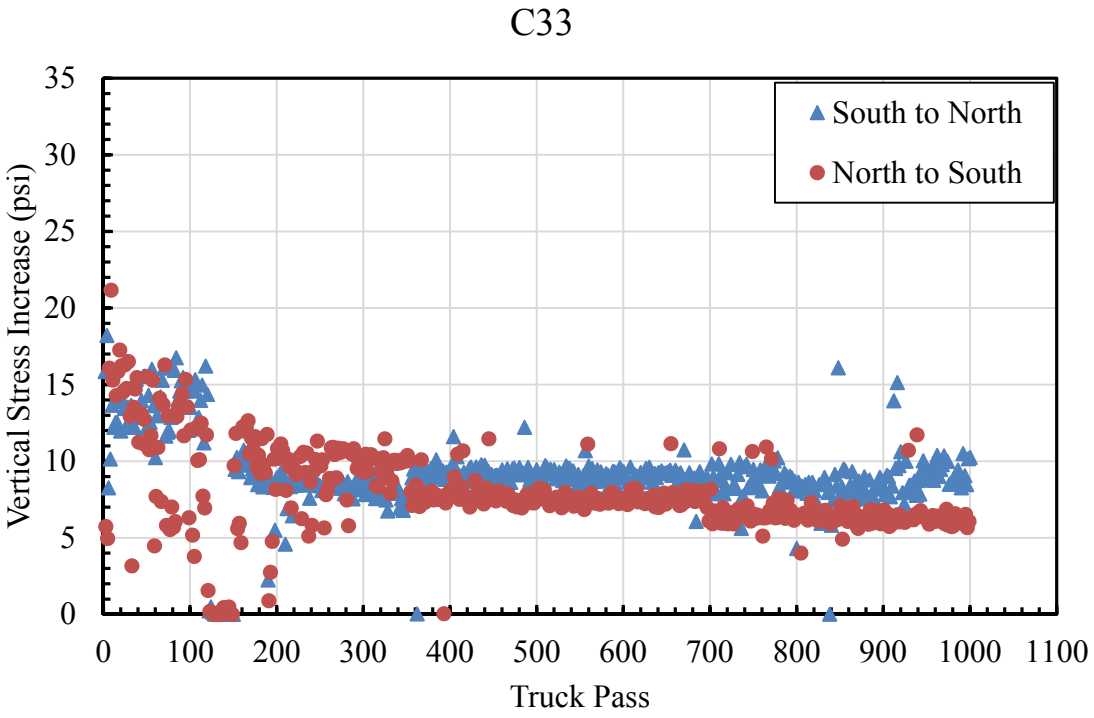

Figure E-11. Measured pressure by EPC C33

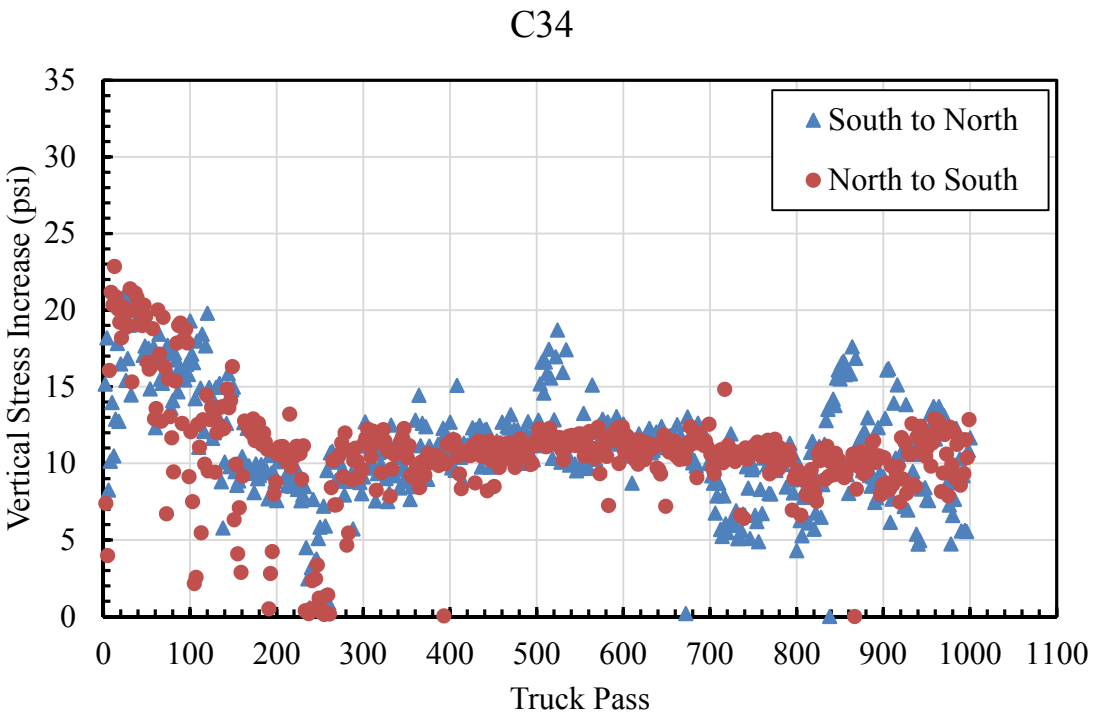

Figure E-12. Measured pressure by EPC C34